UNIVERSITAT DE BARCELONA

Role of the Tousled like kinases in maintaining genome and epigenome stability

Sandra Segura Bayona

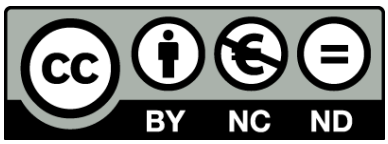

UNIVERSITAT DE BARCELONA

Universitat de Barcelona
Facultat de Farmàcia i Ciències de l'Alimentació
Programa de Doctorat en Biomedicina

Role of the Tousled like kinases in maintaining genome and epigenome stability

Sandra Segura Bayona

2018

Cover design and illustration: Hector Jenz

Layout design: Sandra Segura Bayona

Printing: Ridderprint BV, www.ridderprint.nl, partially funded by the Institute for Research in Biomedicine (IRB) Barcelona.

The research described in this thesis was performed from September 2013 until January 2018 at the IRB Barcelona, and was supported by a "la Caixa"-Severo Ochoa/IRB Barcelona International PhD fellowship and a YOUNG Biomedtec grant.

Barcelona, 2018

Role of the Tousled like kinases in maintaining genome and epigenome stability

Memòria presentada per **Sandra Segura Bayona**
per optar al títol de Doctor per la Universitat de Barcelona

Director
Dr. Travis H. Stracker

Autora
Sandra Segura Bayona

Tutor
Dr. Albert Tauler Girona

INSTITUT DE RECERCA
BIOMÈDICA (IRB)
DE BARCELONA

UNIVERSITAT DE BARCELONA
Facultat de Farmàcia i Ciències de l'Alimentació
Programa de Doctorat en Biomedicina

UNIVERSITAT DE
BARCELONA

Als meus quatre vèrtexs vitals,

Both catastrophe and utopia are possible from this moment, while the zone between them gets less and less likely. It's going to be one or the other, bad or good, catastrophe or utopia. A stark choice, and we're choosing it now by everything we do and don't do.

Kim Stanley Robinson,
Think of Yourself as a Planet

Table of contents

Summary 17

Resum 18

List of Abbreviations 21

Introduction 25

1. DNA replication & genome maintenance 27
    a. Control of DNA replication 27
    b. DNA damage response and cell cycle progression 29
    c. Causes and consequences of genomic instability 32

2. Chromatin assembly 33
    a. The histone chaperone ASF1 34
    b. DNA replication-dependent chromatin assembly 37
    c. DNA replication-independent chromatin assembly 38

3. DNA replication stress, chromatin assembly and human disease 41
    a. Hereditary diseases 41
    b. Replication stress in cancer 43
    c. Histone H3.3 and alternative lengthening of telomeres (ALT) in cancer 45

4. Identification of the Tousled like kinases 46

Objectives 51

Materials and Methods 55

Results 85

Chapter 1: Molecular determinants of Tousled like kinase 2 87

Characterization of the high-confidence interactome of human TLK2 89
Domain architecture, oligomerization and activity of human TLK2 91
TLK2 auto- and trans-phosphorylation in the kinase domain 94
Identification and docking of small molecule inhibitors of TLK2 activity 97
Design of an analog-sensitive allele for TLK2 kinase 99

Chapter 2: Differential requirements for Tousled like kinases 1 and 2 in mammalian development 103

TLK1 is dispensable for murine viability whereas TLK2 is an essential gene 105
TLK2 is essential for placental development 107
The influence of TLK2 deficiency on proliferation and gene expression in the placenta 107

TLK2 interacts with ASF1 and influences its phosphorylation in the placenta 110
TLK2 is dispensable for viability in embryonic and adult tissues 112
TLK1 and TLK2 cooperate to maintain cell viability and chromosomal stability 113

Chapter 3: Tousled like kinases stabilize replication forks and show synthetic lethality with checkpoint and PARP inhibitors 117

TLK2 is required for efficient DNA replication 119
TLK activity is required for chromatin assembly 121
Loss of TLK activity leads to DNA unwinding, checkpoint activation and loss of viability 123
TLK depletion is synthetic lethal with checkpoint inactivation and PARP inhibition 126
De novo nucleosome assembly defects synergize with checkpoint inhibition 127
TLKs do not fully phenocopy ASF1a role in promoting NHEJ 130

Chapter 4: Tousled like kinases as a target in cancer therapy 133

Alterations in *TLK1* and *TLK2* copy number and expression in human cancers 135
TLK loss is deleterious across a panel of human cancer cell lines 137
Defining a system for stable TLK loss in human cancer xenograft models 139
Defining a genetic system for stable TLK loss in a murine breast cancer model 144

Chapter 5 - TLK activity maintains histone density and suppresses ALT mediated telomere lengthening and an IFN response 149

TLK depletion leads to global changes in chromatin accessibility 151
Reduced TLK activity preferentially alters heterochromatin and TSS sites 153
TLK depletion causes impaired H3.3 deposition and DNA damage at heterochromatin 156
Total TLK depletion induces features of ALT 158
TLK suppresses noncoding RNA transcription and maintains heterochromatin silencing 161
Reduced chromatin density triggers an interferon response 163

Discussion 169

Conclusions 187

Supplementary Material 191

References 203

Summary

Histone deposition during DNA replication, transcription and repair ensures the faithful maintenance of genetic and epigenetic information. The histone H3-H4 chaperone ASF1 participates in both replication-dependent and independent nucleosome assembly. While much attention has been focused on the role of histone modifications, the significance of histone chaperones and their regulation in chromatin maintenance remains relatively unexplored. The Tousled like kinases 1 and 2 (TLK1 and TLK2) are evolutionarily conserved Ser/Thr kinases that regulate ASF1. TLKs have been implicated in DNA repair and chromosome stability but their cellular functions remain poorly defined. Apart from ASF1, the DNA damage signalling protein RAD9 is another proposed target of TLK activity but the extent to which they both rely on TLK1/2 has not been clearly established. The goal of this thesis is to characterize the relative functions of TLK1 and TLK2, identify their cellular targets, modes of regulation and consequences of their deficiency during development and in cancer. To this end, we have generated conditional mouse models with loss of function alleles, studied mouse-derived cells from homeostatic and cancerous tissues, and performed siRNA-mediated depletion of TLK1/2 in multiple human cell lines. *In vivo,* TLK1 and TLK2 play largely redundant roles in genome maintenance and cell viability in tissue homeostasis, with the exception of a placental specific requirement for TLK2. Depletion of TLK activity in cells leads to reduced histone deposition, DNA replication stress, extensive DNA damage accumulation and arrest or cell death. In addition, TLK deficient cells exhibit synthetic lethality with several DNA damage checkpoint inhibitors, consistent with a role for TLK activity in replication stress tolerance. Genome wide analysis indicated that TLK activity is required for heterochromatin maintenance, particularly in regions of repetitive DNA. This is consistent with defects in histone variant deposition and increased non-coding RNA transcription at these sites. While the phenotypes of TLK depletion support a major role in ASF1-mediated histone deposition, our data indicates that they likely control additional targets and suggests that the identification of small molecule inhibitors for these kinases could suppose a valuable target for cancer therapy to augment existing strategies for cancer treatment.

Resum

La deposició d'histones durant els processos de replicació, transcripció i reparació de l'ADN asseguren el manteniment de la informació genètica i epigenètica. ASF1 és una xaperona d'histones H3-H4 que participa en la deposició d'histones tant en processos de replicació com en processos independents de replicació. Mentre que les modificacions epigenètiques de les histones han estat molt estudiades, la importància de les xaperones d'histones i la seva regulació són àmbits menys explorats. Les Tousled like kinases 1 i 2 (TLK1 i TLK2) són quinases conservades evolutivament que regulen ASF1. Les TLKs tenen un paper en el manteniment de l'estabilitat del genoma malgrat les seves funcions cel·lulars no estiguin ben definides. A banda d'ASF1, un altre substrat de les TLKs és la proteïna RAD9, implicada en senyalització en resposta a dany de l'ADN. L'objectiu d'aquesta tesi és caracteritzar les funcions relatives de TLK1 i TLK2, identificar els seus substrats, entendre com es regulen i les conseqüències de la seva deficiència durant desenvolupament i en processos tumorals. Per assolir aquests objectius, hem generat models de ratolí amb al·lels de genoanul·lació condicional, hem estudiat la deficiència de les TLKs en cèl·lules derivades de ratolí i en línies cel·lulars humanes. *In vivo*, TLK1 i TLK2 tenen papers redundants en el manteniment dels teixits en homeòstasi, amb l'excepció de la placenta on hi ha un requeriment específic per la funció de TLK2. Depleció de l'activitat TLK en cèl·lules causa una reducció en deposició d'histones, estrès replicatiu, acumulació de dany a l'ADN i aturada del cicle cel·lular o mort cel·lular. La deficiència d'activitat TLK causa letalitat quan es combina amb inhibidors de CHK1 o de PARP, consistent amb un paper de les TLKs en la tolerància de l'estrès replicatiu. Un anàlisi a nivell genòmic ens demostra que l'activitat TLK és necessària per mantenir les regions d'heterocromatina, en particular regions repetitives. Aquest fenotip va acompanyat de defectes en la deposició d'una variant d'histona H3 i un increment de transcripció de RNA no codificant. Els nostres resultats recolzen un paper principal de les TLKs mitjançant el substrat ASF1, tanmateix considerem que les TLKs molt probablement controlin altres proteïnes. Finalment, suggerim que la identificació de molècules inhibidores de l'activitat TLK podrien suposar un avenç terapèutic en càncer per a augmentar l'efecte de teràpies existents. w

List of Abbreviations

9-1-1	RAD9-RAD1-HUS1
3D	Three-dimensional
4OHT	4-hydroxytamoxifen
A-T	Ataxia telangiectasia
A-T-LD	Ataxia-telangiectasia-like disease
ALT	Alternative lengthening of telomeres
APB	ALT-associated PML body
AS	Analog-sensitive
ASF1	Anti-silencing factor 1
ATAC	Assay for Transposase-Accessible Chromatin
ATM	Ataxia telangiectasia mutated
ATR	Ataxia telangiectasia and rad3-related
ATRX	Alpha thalassemia/mental retardation syndrome X-linked
BrdU	5-bromo-2'deoxyuridine
C-ter	C-terminus
CABIN1	Calcineurin-binding protein-1
CAF1	Chromatin assembly factor-1
CC	Coiled coil
CCLE	Cancer Cell Line Encyclopedia
CDAI	Congenital dyserythropoietic anemia type I
CDKs	Cyclin-dependent kinases
cDNA	complementary DNA
CFS	Common fragile site
cGAS	cyclic GMP-AMP synthase
ChIP	Chromatin immunoprecipitation
CIP	Calf intestinal alkaline phosphatase
CldU	5-chloro-2'-deoxyuridine
CMG	CDC45–MCM–GINS
CNAs	Copy number alterations
CND	Copy number decreases
CNI	Copy number increases
CPE	CPEB binding element
DAXX	Death domain-associated protein
DDK	DBF4-dependent kinase
DDR	DNA damage response
DDT	DNA damage tolerance
DFS	Disease free survival
DIPG	Diffuse intrinsic pontine gliomas
DMEM	Dulbecco modified eagle medium
DNA	Deoxyribonucleic acid
DNA-PK	DNA-dependent protein kinase
DNM	*De novo* mutations
ds	double stranded
DSB	Double strand break
ECL	Enhanced chemiluminescence
ECTR	Extra-chromosomal telomeric repeat
EdU	5-ethynyl-2'-deoxyuridine

ER	Estrogen receptor
ERV	Endogenous retrovirus / endogenous retroviral element
ES	Embryonic stem
FA	Fanconi anemia
FACT	Facilitates Chromatin Transcription
FBS	Foetal bovine serum
FF	Fluphenazine dihydrochloride
FISH	Fluorescence in situ hybridization
G1-phase	Gap 1 phase
G2-phase	Gap 2 phase
GBM	Glioblastoma multiforme
GO	Gene ontology
GSEA	Gene set enrichment analysis
HIRA	Histone regulator A
HJURP	Holliday junction recognition protein
HR	Homologous recombination
HTM	High-throughput microscopy
HU	Hydroxyurea
ICL	Inter-strand crosslink
ID	Intellectual disability
IF	Immunofluorescence
IFN	Interferon
IHC	Immunohistochemistry
IL-8	Interleukin-8
IP	Immunoprecipitation
IR	Ionizing radiation
KD	Kinase dead
LT	Long-telomere
M-phase	Mitosis phase
Mb	Megabase
MBP	Myelin basic protein
MD	Molecular dynamics
MEF	Mouse embryonic fibroblast
METABRIC	Molecular Taxonomy of Breast Cancer International Consortium
MMS	Methyl methanesulfonate
MMTV	Mouse mammary tumour virus
MNase	Micrococcal nuclease
MRN	Mre11–Rad50–Nbs1
MTM	Metaraminol
N-ter	N-terminus
NAP1	Nucleosome assembly protein-1
NASP	Nuclear Autoantigenic Sperm Protein
NBS	Nijmegen breakage syndrome
NHEJ	Non-homologous end Joining
NLS	Nuclear localization signal
ORC	Origin recognition complex
PARP	Poly(ADP)-ribose polymerase
PBS	Phosphate buffered saline
PCNA	Proliferating cell nuclear antigen
PEG	Polyethylene glycol
PEI	Polyethylenimine
PI	Propidium iodide

PML	Promyelocytic leukaemia
PMZ	Promazine hydrochloride
POLA	DNA polymerase Polα
POLD	DNA polymerase Polδ
POLE	DNA polymerase Polε
POLH	DNA polymerase Pol η
POLQ	DNA polymerase Polθ
PP1	Type 1 serine–threonine protein phosphatase
PPH	Perphenazine
PRC2	Polycomb regulatory complex 2
pre-RC	pre-replication complex
PTM	Post-translational modification
PVDF	Polyvinylidene fluoride
PyMT	Polyoma Virus Middle T antigen
qRT-PCR	Quantitative real time PCR
R-loop	RNA-DNA loop
RB	Retinoblastoma protein
RIF1	Replication Timing Regulatory Factor 1
RNA	Ribonucleic acid
RNR	Ribonucleotide reductase
ROS	Reactive oxygen species
RPA	Replication Protein A
rRNA	Ribosomal RNA
S-phase	Synthesis phase
SAHF	Senescence-associated heterochromatin foci
SD	Standard deviation
SEM	Standard error of the mean
SF	Strep-FLAG
siRNA	Small interfering RNA
ss	single stranded
ssDNA	single stranded DNA
STING	Stimulator of interferon genes
STS	Staurosporine
SV40	Simian virus 40
TCGA	The Cancer Genome Atlas
TERRA	Telomeric repeat-containing RNA
TFIID	Transcription initiation factor IID
THD	Thioridazine hydrochloride
TLK	Tousled like kinase
TNBC	Triple negative breast cancer
TSL	Tousled kinase
TSS	Transcription start site
TTS	Transcription termination site
UBN1	Ubinuclein 1
UTR	Untranslated region
UV	Ultraviolet radiation
WHS	Wolf-Hirschhorn syndrome
WT	Wild-type
XP	Xeroderma pigmentosum

Introduction

1. DNA REPLICATION & GENOME MAINTENANCE

a. Control of DNA replication

Faithful duplication of DNA and its organization into chromatin is essential to maintain genome integrity and function. During genome replication, progression of the replication machinery can be challenged by limitations in nucleotide supply and physical obstacles on the DNA template, including naturally occurring DNA lesions and difficult to replicate secondary structures. The identification of pathways that control the accurate execution of DNA replication, including those involved in genome stability upon replication stress, has been an active area of research for the last 30 years. Control of DNA replication is executed at several levels: the establishment of replication origins, the definition of replication domains that timely replicate and the control of origin firing and replication fork progression.

Replication origins are built into the genome by a first step of recruitment of origin recognition complex (ORC) to chromatin. Many more loci than the ones that will eventually become origins and fire are recognized by ORC. Some ORC-bound regions will become origins by forming the pre-replication complex (pre-RC), by a process called origin licensing (Figure 1A) (Fragkos et al., 2015; Técher et al., 2017). During licensing, there is a step-wise recruitment of DNA replication licensing factors CDC6 and CDT1, and the hexameric MCM2-7 DNA helicase. From the number of origins licensed, some origins will ensure the loading of factors that will allow activation of the replicative helicase, by the step known as origin firing (Figure 1A). During firing, pre-RCs require the loading of CDC45 and GINS that will form the active replicative helicase CMG (CDC45–MCM–GINS), MCM10 and DNA polymerase ε (POLE). CMG activation during origin firing requires multiple phosphorylation events by DBF4-dependent kinase (DDK), also known as CDC7–DBF4 kinase, and the S-phase Cyclin-dependent kinases (CDKs; in particular CDK2 together with Cyclin E/A) (Figure 1A) (Siddiqui et al., 2013; Yeeles et al., 2015).

DNA replication in eukaryotic cells is organized into discrete areas of similar replication timing. These areas are composed of multiple replication origins and associated replicons that are visualized in metaphase chromosomes as "replication bands" with Giemsa staining (Holmquist et al., 1982). Replication can be visualized by immunofluorescence (IF) by nuclear foci, and the location of these foci changes during the progression of S-phase (Figure 1B) (Rhind and Gilbert, 2013). In mammalian cells, the timely activation of origins follows a temporal program that allows early replicating regions, located in the interior of the nucleus, to be replicated first, while late replicating regions are mostly distributed around the periphery of the nucleus and nucleolus (Técher et al., 2017).

Nuclear organization has a major impact on replication timing: the complex 3D organization of chromosomes and regulation of transcription at the DNA sequence level heavily influence replication timing profiles. In each replication timing domain, consisting of regions on the scale of megabases (Mb), replication origins fire synchronously. Early replication domains lie in transcriptionally active regions, which are often gene-rich and

harbour active epigenetic marks (Figure 1B). These domains also display a higher amount of replication origins and increased occupancy of ORC binding, suggesting that ORC recruitment during G1 affects the probability of origin firing during S-phase (Dellino et al., 2013). Late replication domains lie on regions with a low density of genes, enriched for repressive histone marks and often devoid of replication origins, all of which are features of heterochromatin (Figure 1B). These late replication domains have been also associated with the presence of common fragile sites (CFS), regions that tend to form DNA secondary structures prone to breakage upon replication stress (Letessier et al., 2011; Rhind and Gilbert, 2013).

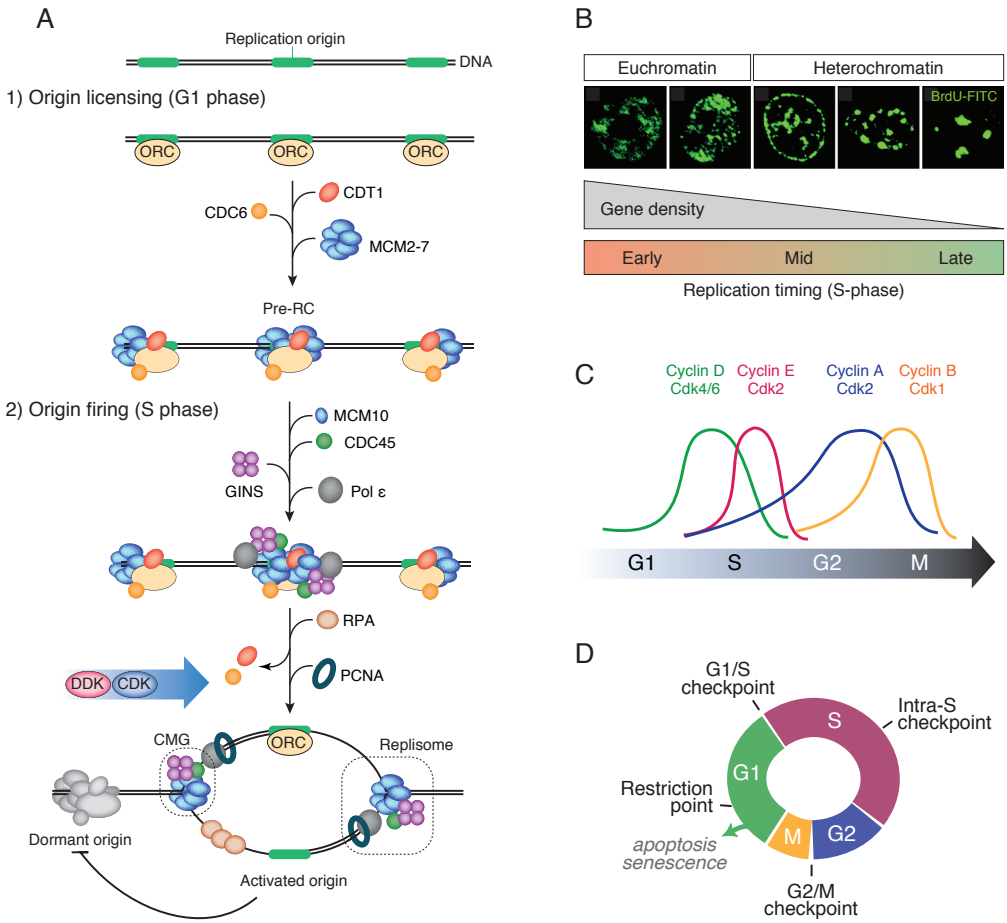

Figure 1. Control of DNA replication and cell cycle progression.

(A) Formation and activation of DNA replication origins within a replication unit. Licensing of replication origins, restricted to the G1-phase, results from sequential loading of pre-RC proteins on all potential origins in the genome. Origin activation requires the activation of the MCM helicase complex. DDK and CDKs, at the G1/S transition, trigger the assembly of functional replisomes by phosphorylating several replication factors (such as MCM10, CDC45, GINS or Pol ε) to promote their chromatin loading to origins. Besides, DDK and CDKs also directly phosphorylate the MCM2-7 complex to promote CMG activation and unwinding. On average, one out of three origins is activated, while the other remain licensed but silent. Figure adapted from Fragkos et al., 2015. (B) Relationship between chromatin properties and replication timing regulation. Replication timing changes during the progression of S-phase are linked to chromatin subnuclear position and transcription potential. First and

Replication timing has been reported to be affected mainly by two factors: DNA polymerase θ (POLQ) and Replication Timing Regulatory Factor 1 (RIF1). Cells depleted of Polθ display a normal density of activated origins in S-phase, but early-to-late and late-to-early shifts are produced in several replication domains via a mechanism that remains unknown (Fernandez-Vidal et al., 2014). RIF1 function in replication timing is conserved from yeast to humans. RIF1 is associated to late-replicating chromatin where it prevents DDK kinase activity by stimulating de-phosphorylation of key targets, such as the MCM helicase, by targeted activity of type 1 serine–threonine protein phosphatase (PP1). Thus, depletion of RIF1 in cells results in premature late-origin firing (Cornacchia et al., 2012; Hayano et al., 2012; Hiraga et al., 2014; Yamazaki et al., 2012).

Timely origin firing results in replication fork progression in a bidirectional manner from the activated origins (Figure 1A). DNA synthesis is achieved by DNA polymerases that are displaced from 5' to 3', allowing continuous DNA synthesis in the leading strand and discontinuous DNA synthesis in the lagging strand, which is formed by several Okazaki fragments of about 100-200 nucleotides that are later processed and ligated. The DNA polymerase Polα (POLA)–primase complex is in charge of starting DNA synthesis by assembling short RNA-DNA primers on both strands. These primers are then elongated by Polε and Polδ (POLD) in the leading and lagging strands, respectively. Proliferating cell nuclear antigen (PCNA) is a homotrimeric complex that acts as a DNA clamp to support the processivity of both Polε and Polδ, and is essential for DNA replication (Figure 1A) (Técher et al., 2017). During S-phase, cells need to cope with a myriad of situations that might perturb replication fork progression and activate a replication stress response (discussed in section 1.c). Thus, coordinated unwinding by the CMG helicase and synthesis of new DNA strands by DNA polymerases is central to allow correct replication fork progression.

b. DNA damage response and cell cycle progression

To ensure correct and complete duplication of the genome, cells have evolved a network of safeguards and repair mechanisms that protect genome integrity during the cell cycle (Zeman and Cimprich, 2014). CDKs are Ser/Thr kinases that drive cell cycle progression through S-phase and mitosis. Catalytic subunits of CDKs are inactive until they bind to the corresponding Cyclin subunits, which are tightly regulated by expression and ubiquitin-dependent degradation (Figure 1C) (Malumbres, 2014). Additional levels of regulation of CDK activity are provided by phosphorylation of the Cyclin-CDK complex. Wee1 phosphorylation of CDK1 or CDK2 (on Tyr 15) inhibits their kinase activity, therefore activation of CDKs requires their dephosphorylation by the CDC25 family of phosphatases (Figure 2) (Shaltiel et al., 2015).

second replication phases take place in the interior euchromatin, whereas in mid-late S-phase, replication takes place at the nuclear periphery, nucleolar periphery and internal heterochromatin blocks. Figure adapted from Rhind and Gilbert, 2013. (C) Stepwise activation of Cyclin dependent kinases ; different Cyclins activate different CDKs, and are expressed at different moments throughout the cell cycle. (D) Schematic representation of the cell cycle and its checkpoints. The cell cycle is divided in separate phases, the first gap phase (G1), the synthesis (S) phase and the second gap phase (G2) prior to mitosis (M). In response to genomic insults, cell cycle progression can be halted at several checkpoints.

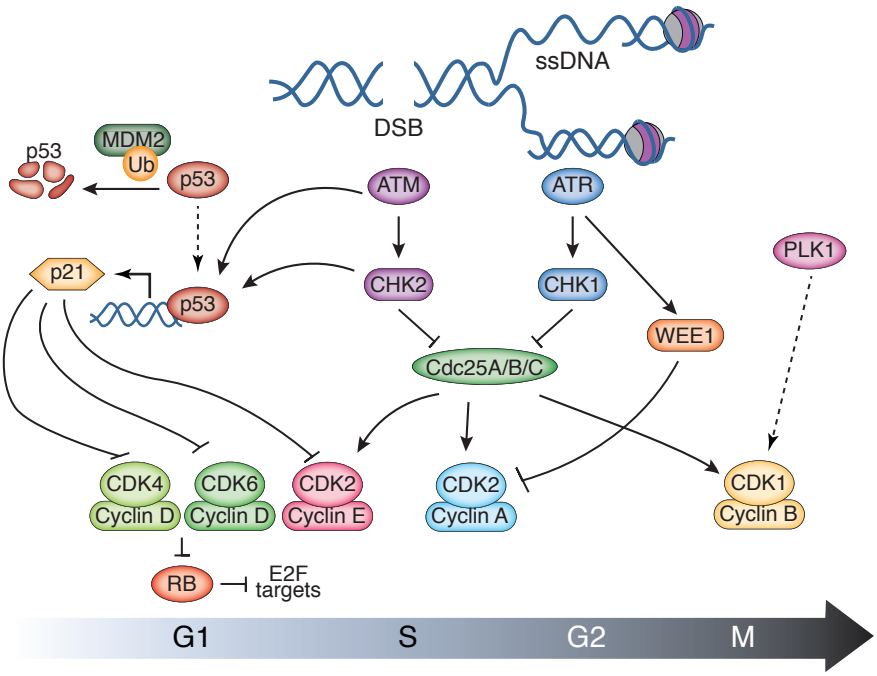

Figure 2. Simplified scheme of DNA damage-induced cell cycle checkpoints.

DNA DSBs and replication fork stalling result in the respective activation of ATM and ATR. ATM phosphorylates CHK2, which can prevent replication of damaged DNA by activating p53 and p21, which results in G1/S checkpoint arrest. Alternatively, ATR phosphorylates CHK1, which can arrest the cell cycle at the intra-S-phase or G2/M checkpoints by inhibiting CDC25A/B/C to allow DNA repair. CHK1 can additionally activate WEE1 in G2/M to maintain genomic integrity. Finally, DNA damage signalling is potently inhibited in mitosis as a result of the combined action of CDK1 and PLK1. Figure adapted from Bouwman and Jonkers, 2012; Shaltiel et al., 2015.

In early G1-phase, mitogenic signalling induces Cyclin D expression, which preferentially binds to and activates CDK4/6. Proliferating cells are committed to a new cell cycle once they pass through the "restriction point" (Figure 1C-D). Cyclin D-CDK4/6 dependent phosphorylation of the Retinoblastoma protein (RB) disrupts the interaction of RB with E2F and promotes the activation of the E2F transcriptional program, among which Cyclin E is one of the earliest genes. Transcription of E2F target genes includes the expression of genes involved in cell cycle control, DNA replication and DNA repair, thus facilitating the progression from G1 to S-phase (Bertoli et al., 2013). However, cell cycle checkpoints are able to halt or delay cell cycle progression in G1, S or G2 phases in response to different types of genotoxic stresses (Figure 1D and Figure 2). The presence of DNA double strand breaks (DSBs) in G1-phase activates the ataxia telangiectasia mutated (ATM) protein that subsequently activates many downstream substrates such as CHK2, p53 and p21 (Figure 2). P53 normally has short half-life due to binding of the ubiquitin ligase MDM2. Apart from activating p53, DNA damage via ATM/ATR also targets MDM2, contributing to the stabilization of p53 protein. Stabilization of p53 allows the transcription of genes involved in cell death and DNA repair mechanisms and promotes a permanent cell cycle arrest or senescence. A key target of p53 is the CDK inhibitor

p21, which prevents the G1/S transition by inhibiting Cyclin E-CDK2 and therefore causing G1 arrest (Figure 2). Additionally, CHK2 also mediates inhibition of CDC25A by phosphorylation as a mechanism to suppress CDK function. CDK inhibition further facilitates RB control of the E2F pathway, thereby provoking a sustained G1 blockade. Thus, the G1/S checkpoint response involves two critical tumour suppressor pathways, governed by p53 and RB, both of which are widely deregulated in human cancer (Bouwman and Jonkers, 2012; Kastan and Bartek, 2004; Shaltiel et al., 2015).

In a normal cell cycle where the checkpoint is inactive, Cyclin E preferentially binds and activates CDK2 further inhibiting RB, inducing E2F targets and progression into S-phase (Figure 1C-D and Figure 2). Throughout S-phase, Cyclin E levels drop and from S-phase until mitosis, Cyclin A becomes in charge of maintaining CDK2 activity (Figure 1C). During S-phase, when replication forks are challenged, long stretches of ssDNA can accumulate due to uncoupling of the CMG replicative helicase from stalled DNA polymerases (Byun et al., 2005; Dobbelstein and Sørensen, 2015; Zeman and Cimprich, 2014) and the single stranded DNA (ssDNA) binding protein Replication Protein A (RPA) coats ssDNA. Along with the 9-1-1 (RAD9-RAD1-HUS1) DNA clamp complex and TOPBP1, the ssDNA-RPA recruits and activates ataxia telangiectasia and rad3-related (ATR), the upstream kinase in the intra-S-phase replication checkpoint, through its interaction partner ATRIP (Figure 2) (Cortez et al., 2001; Saldivar et al., 2017; Zou and Elledge, 2003). ATR activation and subsequent activation of CHK1 act to stabilize arrested forks, suppress late origin firing and trigger activation of DNA repair machinery to deal with lesions. CHK1 mediated inhibition of CDC25A results in CDK2 inhibition, thus blocking the loading of CDC45 onto chromatin and preventing new origin firing (Falck et al., 2002; Saldivar et al., 2017). The intra-S-phase checkpoint also relies on the CHK1/2 dependent activation of WEE1 kinase, which phosphorylates CDK2 to inhibit its activity (Sørensen and Syljuåsen, 2012). In addition, Poly(ADP)-ribose polymerase (PARP) activity is required for CHK1 retention at stalled forks, activation of the S-phase checkpoint and the restart of stalled replication forks (Bryant et al., 2005; Min et al., 2013). Following completion of DNA replication, cells progress through G2-phase with the activity of Cyclin A-CDK2. Checkpoint control during G2 is dependent on the ATR-CHK1 axis with mechanisms similar to the intra-S-phase checkpoint, which also depends on the WEE1-dependent phosphorylation of CDKs (Figure 2). In contrast to the dependency of the G1/S checkpoint on ATM, p53 and p21, the G2/M checkpoint can promote a cell cycle arrest independently of p53 and is mostly activated by DNA lesions that engage with ATR activation, such as unreplicated DNA, aberrant fork structures or DSBs being repaired by homologous recombination (HR) (Shaltiel et al., 2015). Proper cell cycle progression promotes the expression of Cyclin B, which binds and activates CDK1 and is required for mitosis (Figure 1C). Activation of Cyclin B-CDK1 is controlled by feedback loops, for example the CDK1- and PLK1-mediated phosphorylation of WEE1 that targets it for degradation or PLK1-dependent activation of CDC25 phosphatases (Figure 2) (Gavet and Pines, 2010; Gheghiani et al., 2017; Shaltiel et al., 2015).

c. Causes and consequences of genomic instability

There are many situations that can perturb replication fork progression in unchallenged cells. Prolonged fork arrest poses a risk of fork collapse and generation of DSBs potentially due to nuclease attack (Zeman and Cimprich, 2014). During DNA replication, the exposure of ssDNA may be triggered when the polymerase slows down but the helicase continues unwinding, also known as polymerase and helicase uncoupling. This occurs for example when nucleotides or histone pools become limiting (Bester et al., 2011; Groth et al., 2007; Mejlvang et al., 2014; Poli et al., 2012; Técher et al., 2016). Alternatively, other situations may not involve uncoupling but imply that both polymerases and helicases pause at the same time, for example when replication forks face physical roadblocks (León-Ortiz et al., 2014; Mirkin and Mirkin, 2007). These situations prevent RPA exposure at first, but processing of stalled forks subsequently exposes ssDNA or generates DNA breaks that will eventually activate the checkpoint.

The most common features that may perturb fork progression are described in Figure 3 and these will often activate a replication stress response to protect cells from genome instability that may have deleterious consequences (Gaillard et al., 2015; Técher et al., 2017; Zeman and Cimprich, 2014). Several DNA secondary structures are able to hinder replication fork progression, and these are often induced in repetitive DNA sequences, such as palindromic sequences, trinucleotide repeats or minisatellites. These obstacles can be in the form of DNA hairpins, DNA triplexes, G-quadruplexes, RNA-DNA loops (R-loops) or torsional stress caused by altered DNA topology (Figure 3) (Gaillard et al., 2015). DSBs are generated endogenously in cells during active processes, such as V(D)J-recombination, meiosis, mobile genetic elements transposition and release of DNA supercoiling by Topoisomerase II (Tubbs and Nussenzweig, 2017). A shortage of replication factors such as nucleotide pools, histones pools or RPA at replication forks may also severely impair the progression of forks (Figure 3) (Groth et al., 2007; Mejlvang et al., 2014; Poli et al., 2012; Toledo et al., 2014). Many endogenous DNA lesions that can stall forks can occur as a result of the by-products of cellular metabolism, such as reactive oxygen species (ROS) or endogenous aldehydes that can generate DNA base oxidation (such as 8-oxoguanines), non-enzymatic methylation (producing 3-methyladenine and 7-methylguanine), DNA hydrolysis (thus generating apurinic sites) or histone demethylation (Figure 3) (Lindahl and Barnes, 2000; Rosado et al., 2011; Tubbs and Nussenzweig, 2017). During DNA replication, there can be sequences that are inherently difficult to replicate and generate mismatches, gaps or frameshifts, and these require specific repair mechanisms to ensure the integrity of genetic information (Figure 3).

The consequences of genomic instability in disease are heterogeneous, and range from hereditary disease, which arises in individuals deficient in replication stress response proteins, to the mutational landscape of cancer, that can include frequent base substitutions and chromosomal rearrangements (further discussed in section 3) (Tubbs and Nussenzweig, 2017; Zeman and Cimprich, 2014). The combination of environmental and endogenous

stresses in cells poses a threat to genome stability; thus, the detailed understanding of the cellular response to replication stress and the mechanisms of genome maintenance is of vital importance.

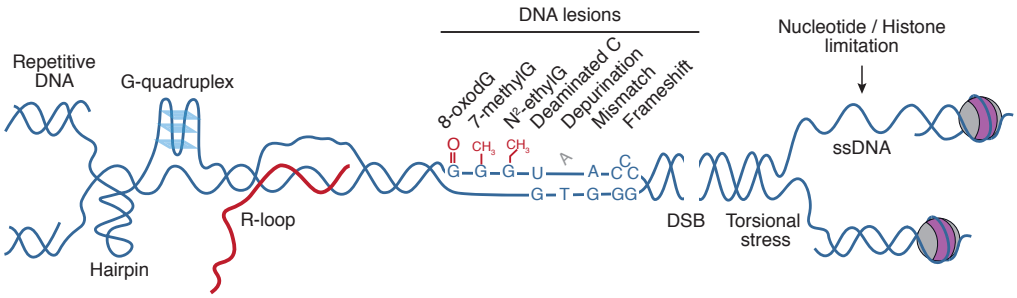

Figure 3. Sources of DNA replication stress.

There are various conditions or obstacles able to slowdown or impair replication fork progression, including repetitive DNA elements, hairpins, DNA secondary structures, RNA-DNA hybrids, ribonucleotide incorporation, DNA lesions, DSBs, torsional stress or altered DNA topology, limiting nucleotides or histone pools and oncogene-induced ssDNA accumulation. Adapted from Técher et al., 2017; Gaillard et al., 2015.

2. CHROMATIN ASSEMBLY

The plasticity of chromatin structure is critical for the regulation of essential cellular processes required for normal development and aging. As nucleosomes are perceived as barriers for DNA-related processes, they must first be disassembled to allow DNA replication, transcription and DNA repair machineries to access the DNA (Burgess and Zhang, 2014). The major subunit of chromatin is the nucleosome, a stretch of 145–147 base pairs of DNA wrapped around a histone core octamer. Each histone octamer consists of a histone $(H3–H4)_2$ tetramer and two histone H2A–H2B dimers (Hammond et al., 2017). Histones are regulated at the transcriptional level and through myriad post-translational modifications that occur both in complexes with histone chaperones and in the context of the nucleosome. The canonical histones, comprising H2A, H2B, H3.1, H3.2 and H4, are encoded by multiple genes that do not contain introns or polyadenylation signals and are organized as clusters in the genome. This ensures their timely transcription during S-phase to generate the pool of histones that is a source of chromatin packaging during DNA replication (Buschbeck and Hake, 2017). Histones are highly basic proteins that are associated with specific histone chaperones, which are required for the dynamic maintenance of chromatin structure and play multiple roles in the regulation of nucleosome formation, such as subcellular localization, storage, and deposition (Burgess and Zhang, 2014). During DNA replication, nucleosome assembly requires the incorporation of both parental histones and newly synthesized histones behind the replication fork, as well as histone eviction ahead of the fork. Nucleosome assembly also occurs independently of DNA replication, as for instance during gene transcription

throughout the cell cycle. Canonical histone H3 (H3.1 and H3.2) is assembled onto DNA by the histone chaperone Chromatin assembly factor-1 (CAF1) during DNA replication-dependent chromatin assembly. Conversely, the histone H3 replacement variant H3.3 (with 4-5 amino acids difference from canonical H3), is deposited by the histone chaperones Histone regulator A (HIRA) or death domain-associated protein (DAXX) in replication-independent nucleosome assembly (Drané et al., 2010; Goldberg et al., 2010; Lewis et al., 2010; Tagami et al., 2004).

a. The histone chaperone ASF1

Anti-silencing factor 1 (ASF1) is a central histone H3-H4 chaperone that mediates both replication-dependent and -independent pathways of histone deposition. The ASF1 gene was first identified as a silencing protein in budding yeast (Le et al., 1997; Munakata et al., 2000; Tyler et al., 1999). Yeast ASF1 cooperates with CAF1 in chromatin assembly (Tyler et al., 1999), and both human and *Drosophila* ASF1 interact directly with the medium CAF1 subunit, known as p60 in humans (Mello et al., 2002; Tyler et al., 2001). ASF1 also interacts with proteins involved in chromatin remodelling and transcription initiation, such as the SWI/SNF Brahma chromatin remodelling complex in *Drosophila* or the transcription initiation factor IID (TFIID) in both yeast and human (Chimura et al., 2002; Moshkin et al., 2002). Additionally, ASF1 has been implicated in maintaining heterochromatin silencing in yeast and *Drosophila* (Moshkin et al., 2002; Sharp et al., 2001; Yamane et al., 2011). Strikingly, the loss of ASF1 is not lethal in yeast, but slows cell proliferation and leads to global transcriptional deregulation, DNA replication defects, and results in an activated DNA damage response, gross chromosomal rearrangements and DNA damage sensitivity to a wide variety of lesions (Chen et al., 2008; Hu et al., 2001; Prado et al., 2004; Ramey et al., 2004; Zabaronick and Tyler, 2005). The fact that ASF1 is not lethal in yeast suggests that redundant pathways may compensate for the defects in replication-coupled nucleosome assembly or that yeast may have a higher tolerance to defective nucleosome assembly. Data generated in yeast supports the first option, since ASF1 deficient cells fail to display dramatic changes in nucleosome density or chromatin accessibility (Adkins and Tyler, 2004; Prado et al., 2004). Yeast ASF1 has also been shown to contribute to DNA repair. ASF1 forms a complex with the checkpoint kinase Rad53 (the yeast homolog to CHK2) that dissociates in response to exogenous DNA damage and replication blockage. Upon phosphorylation by the Rad53-dependent DNA damage checkpoint, released ASF1 can contribute to nucleosome reassembly following DNA repair (Emili et al., 2001; Hu et al., 2001). Interestingly, the overexpression of ASF1 is able to rescue the hydroxyurea (HU) sensitivity of Rad53 deficient mutants (Hu et al., 2001). These results indicate that ASF1 is an important player both in S-phase replication and in the cellular response to DNA damage.

While a single ASF1 gene is found in yeast, two isoforms, ASF1a and ASF1b, are encoded in higher organisms such as plants, *C. elegans* or mammals (Figure 4A-B) (Abascal et al.,

2013; Grigsby et al., 2009; Tripathi et al., 2015). ASF1a (or CIA), the major ASF1 isoform in mammals, is widely expressed across tissues throughout the cell cycle, whereas ASF1b (or CIA-II) displays a more restricted tissue distribution, being very highly expressed in proliferative tissues such as testis and thymus mostly during S-phase in a E2F-dependent fashion (Figure 4B) (Abascal et al., 2013; Umehara and Horikoshi, 2003). Overall sequence similarity between ASF1a and ASF1b is about 70% and even higher in the conserved histone chaperone domain where it is 92% (Figure 4A). ASF1 harbours a very conserved 156 aa N-terminal (N-ter) region across species, and a more variable C-terminus (C-ter). In yeast and *C. elegans*, the C-ter is very acidic, possibly favouring the interaction with histones. In mammalian homologs, the C-ter is instead rich in Ser and Thr residues, which have been shown to be phosphorylated by the Tousled like kinases (TLKs) or by DNA-dependent protein kinase (DNA-PK) (Figure 4A) (Huang et al., 2018; Klimovskaia et al., 2014; Silljé and Nigg, 2001). Thus, it is likely that the phosphorylated C-ter tail of human ASF1 might function similarly to the acidic C-ter tail of yeast ASF1.

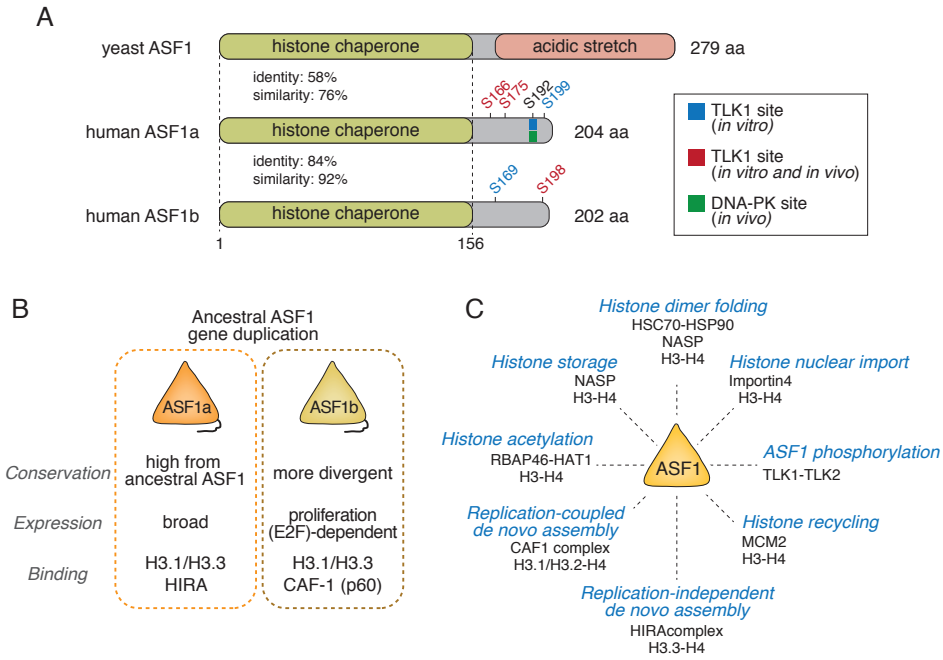

Figure 4. The histone chaperone ASF1.

(A) Comparison of yeast ASF1 with human ASF1a and ASF1b proteins. The green boxes show the region of over 70% similarity between human and budding yeast, the conserved histone chaperone domain. The red box shows the acidic region specific to yeast ASF1. The phosphosites identified in the C-ter tail of human ASF1a/b are indicated (Huang et al., 2018; Klimovskaia et al., 2014). The total number of residues of each protein is shown on the right. Sequence identity and similarity between the 1-156 aa of yASF1-hASF1a and hASF1a-hASF1b are displayed as a percentage, and was assessed by NCBI BLAST (blastp suite-2sequences). (B) Scheme summarizing the subfunctionalisation of the two ASF1 proteins present in vertebrates, regarding conservation similarity to the ancestral gene, expression patterns and the preferential interactions at the protein level. Adapted from Abascal et al., 2013. (C) Summary of ASF1 functions in histone supply. ASF1 is a central chaperone in the delivery of H3-H4 dimers, and TLKs phosphorylation promotes ASF1 histone binding. ASF1-H3-H4 complexes engage with multiple co-chaperone complexes that shield histone interfaces, facilitate their acetylation, nuclear import, storage, *de novo* deposition or recycling. Adapted from Hammond et al., 2017.

Mice deficient for ASF1a are embryonic lethal, whereas ASF1b is dispensable for embryonic development in mice and its deficiency only causes reduced reproductive capacity in females (Hartford et al., 2011; Messiaen et al., 2016). Consistent with the critical function of mammalian ASF1a, ASF1 is also essential for the viability of fission yeast (Umehara et al., 2002), *Drosophila* (Moshkin et al., 2002), and chicken DT-40 cells (Sanematsu et al., 2006). In mammalian cells, ASF1 regulates histone usage during DNA replication by promoting the incorporation of parental and newly synthesized histones, as well as buffering histone pools upon replication stress or arrest (Figure 4C) (Groth et al., 2003, 2005). Upon HU treatment, which depletes dNTP pools and blocks DNA replication through inhibition of the ribonucleotide reductase (RNR), the soluble pool of H3-H4 associates with ASF1 complexes, together with other histone chaperones such as p48 or NASP (Groth et al., 2005). These data suggest that ASF1 might be essential to buffer excess free histones that could potentially be toxic for cells. Depletion of ASF1 in *Drosophila* S2 cells, chicken DT-40 cells or human HeLa cells inhibits cell division due to slow progression through S-phase (Groth et al., 2007; Sanematsu et al., 2006; Schulz and Tyler, 2006). The accumulation of cells in S-phase is accompanied by defects in DNA unwinding through an interaction of ASF1 with the replicative helicase MCM2-7 (Groth et al., 2007). Thus, ASF1 functions by binding soluble H3-H4 dimers and promoting histone transit to the nucleus and downstream to additional histone chaperones (Figure 4C) (Jasencakova et al., 2010). Localization studies in mammalian cells revealed that ASF1 is not significantly bound to detergent-resistant chromatin, either before or after DNA damage, and the majority is soluble and nuclear (Mello et al., 2002).

The single ASF1 protein in yeast interacts with H3-H4 dimers, and these same dimers are deposited into chromatin both in a replication-dependent and independent manner (Green et al., 2005; Liu et al., 2012). Higher organisms have evolved with several histone H3 variants that are specifically recognized by some histone chaperones. CAF1 deposits canonical histones (H3.1 and H3.3) during DNA replication while HIRA deposits the replacement histone variant H3.3 throughout the cell cycle (Tagami et al., 2004). From the two ASF1 isoforms, ASF1a preferentially binds to HIRA, whereas ASF1b interacts preferentially with CAF1 (Figure 4B) (Abascal et al., 2013; Corpet et al., 2011; Tang et al., 2006). However, neither ASF1a nor ASF1b display a clear preference for canonical H3.1 or the variant H3.3, which implies that both ASF1a and ASF1b can function redundantly, at least in replication-coupled chromatin assembly (Abascal et al., 2013). This is supported by the fact that only depleting both ASF1 paralogues in human cells, and not by single depletion, is able to arrest DNA replication, similar to what happens upon depletion of CAF1 (Corpet et al., 2011; Groth et al., 2005, 2007; Hoek and Stillman, 2003). Recent reports have implicated solely ASF1a in DNA repair of DSBs, by a mechanism independent of its histone chaperone activity. ASF1a interaction with MDC1 upon non-homologous end joining (NHEJ)-mediated repair of DSBs promotes the recruitment of phosphorylated-ATM and facilitates the subsequent MDC1 phosphorylation at breaks (Lee et al., 2017). In addition, loss of CAF1 or ASF1 impaired the recruitment of TONSL-

MMS22L to DSBs, thus hindering the loading of RAD51 into DNA to be repaired by homologous recombination (Huang et al., 2018). For these reasons and despite the functional and regulatory differences of the yeast and mammalian ASF1 proteins, it is clear that ASF1 plays a key role in the histone chaperone network, as it is involved in both replication-dependent and –independent nucleosome assembly. In addition, studies from yeast to human place ASF1 at the crossroads of chromatin and cell cycle checkpoints.

b. DNA replication-dependent chromatin assembly

During DNA replication, parental nucleosomes must be disassembled ahead of the replication fork to enable the replisome to go through, and later, parental chromatin marks need to be restored on the new DNA. For this, both parental histone recycling and newly synthesized histones should be transferred to newly replicated DNA daughter strands to ensure the maintenance of epigenetic information (Figure 5). It has been shown that chromatin has a functional role during replication since Okazaki fragment size is limited by nucleosomes that impede Polδ progression (Devbhandari et al., 2017; Kurat et al., 2017).

Histone biosynthesis takes place in the cytoplasm, where H3-H4 and H2A-H2B associate in heterodimeric complexes. There are histone chaperones that promote histone recognition in the cytosol and assist in histone trafficking between the cytoplasm and nucleus. Several proteins facilitate histone folding in the cytoplasm, recognize histone dimers and shuttle them to the nucleus. The histone chaperone Nuclear Autoantigenic Sperm Protein (NASP) forms a complex with H3-H4 and the histone acetyltransferase RBAP46-HAT1, which acetylates histone H4 at Lys 5 and Lys 12, a mark of newly synthesized histones (Figure 4C) (Campos et al., 2010; Hammond et al., 2017). NASP provides histone buffering activity by providing storage of H3-H4 in both the nucleus and cytoplasm. This balances the reservoir of histones that will be later bound by ASF1 and keeps them protected from HSC70-HSP90 chaperone-mediated autophagy (Figure 4C) (Cook et al., 2011). ASF1-H3-H4 also interacts with Importin4, indicating that the cytoplasmic pool of ASF1 is implicated in nuclear histone trafficking (Figure 4C) (Jasencakova et al., 2010). Several histone chaperones are also involved in the nuclear import of H2A–H2B dimers. Nucleosome assembly protein-1 (NAP1) performs various functions in the nuclear import and delivery of H2A-H2B, including canonical H2A and the histone variant H2A.Z. NAP1 contributes to nuclear import of H2A-H2B dimers by handing histones to Importin9 (or KAP114) (Hammond et al., 2017). Additionally, NAP1 also delivers histones during transcription and DNA replication, and prevents the accumulation of H2A-H2B on DNA by shielding the DNA-binding interface of histones (Aguilar-Gurrieri et al., 2016; Andrews et al., 2010).

De novo replication-coupled histone deposition is often associated with the replication machinery (Figure 5). The best characterized histone chaperone for the H2A-H2B dimer is Facilitates Chromatin Transcription (FACT), which consists of two subunits, Spt16

and SSRP1, and FACT is required for efficient chromatin replication *in vitro* (Kurat et al., 2017). FACT mediates H2A-H2B binding through Spt16 and is also able to bind H3-H4 dimers through SSRP1, although with lower affinity than H2A-H2B (Winkler et al., 2011). Regarding *de novo* H3-H4 replication-coupled nucleosome assembly, the CAF1 complex, which is composed of three subunits p48, p60 and p150, mostly mediates histone assembly behind the replication fork. The large subunit p150 associates with the replisome sliding-clamp PCNA (Shibahara and Stillman, 1999).

Parental histone recycling must also occur in the context of DNA replication (Figure 5). It is believed that the force of the CMG helicase during DNA replication is the primary driver of nucleosome disassembly ahead of the fork (Hammond et al., 2017). The histone chaperone FACT may assist in this nucleosome disruption ahead of the fork since it stably associates with MCMs (Tan et al., 2006). The re-deposition of evicted histones behind the fork on newly replicated DNA probably requires the MCM2 subunit of the replicative helicase, which harbours chaperone activity and also binds ASF1 in a histone-dependent manner (Groth et al., 2007; Huang et al., 2015; Richet et al., 2015). MCM2 can bind H3-H4 tetramers, that when bound to ASF1 they dissociate in the form of H3-H4 dimers. Additionally, MCM2 can chaperone canonical H3 as well as H3.3 or CENPA replacement variants, making it amenable for histone recycling genome-wide (Huang et al., 2015). Analysis of histones bound to nascent chromatin revealed that old and new histones are present on nascent DNA in a 1:1 ratio, corroborating efficient histone recycling, and most of the histone post-translational modifications (PTMs) were restored within one cell cycle (Alabert et al., 2015).

c. DNA replication-independent chromatin assembly

Replication-independent incorporation of histones takes place during diverse processes that occur apart from S-phase, such as DNA repair or transcription, and also takes place in several specific distinct chromatin regions, such as centromeres or constitutive heterochromatin (Figure 5). Histones might be deposited through histone exchange or by a gap-filling process. Replication-independent incorporation of histones is often associated with the deposition of replacement histone variants that differ from canonical histones. Unlike canonical histones, that are encoded by gene clusters and transcribed in S-phase, histone variants are usually encoded by a single gene (as H2A.X) or two genes (as H2A.Z, macroH2A or H3.3) that are placed outside of the canonical histone gene clusters (Buschbeck and Hake, 2017). Thus, histone variants can be transcribed and deposited on chromatin throughout all the phases of the cell cycle.

The delivery of the histone variant H2A.Z has been shown to depend on specific chaperones in human cells, such as ANP32E and YL1, that deliver histone dimers to SWR-C histone remodelling complexes for deposition (SRCAP and/or p400–TIP60) (Latrick et al., 2016; Liang et al., 2016; Obri et al., 2014). Deposition of the H3 histone variant CENPA is necessary for centromere formation and chromosome segregation, and

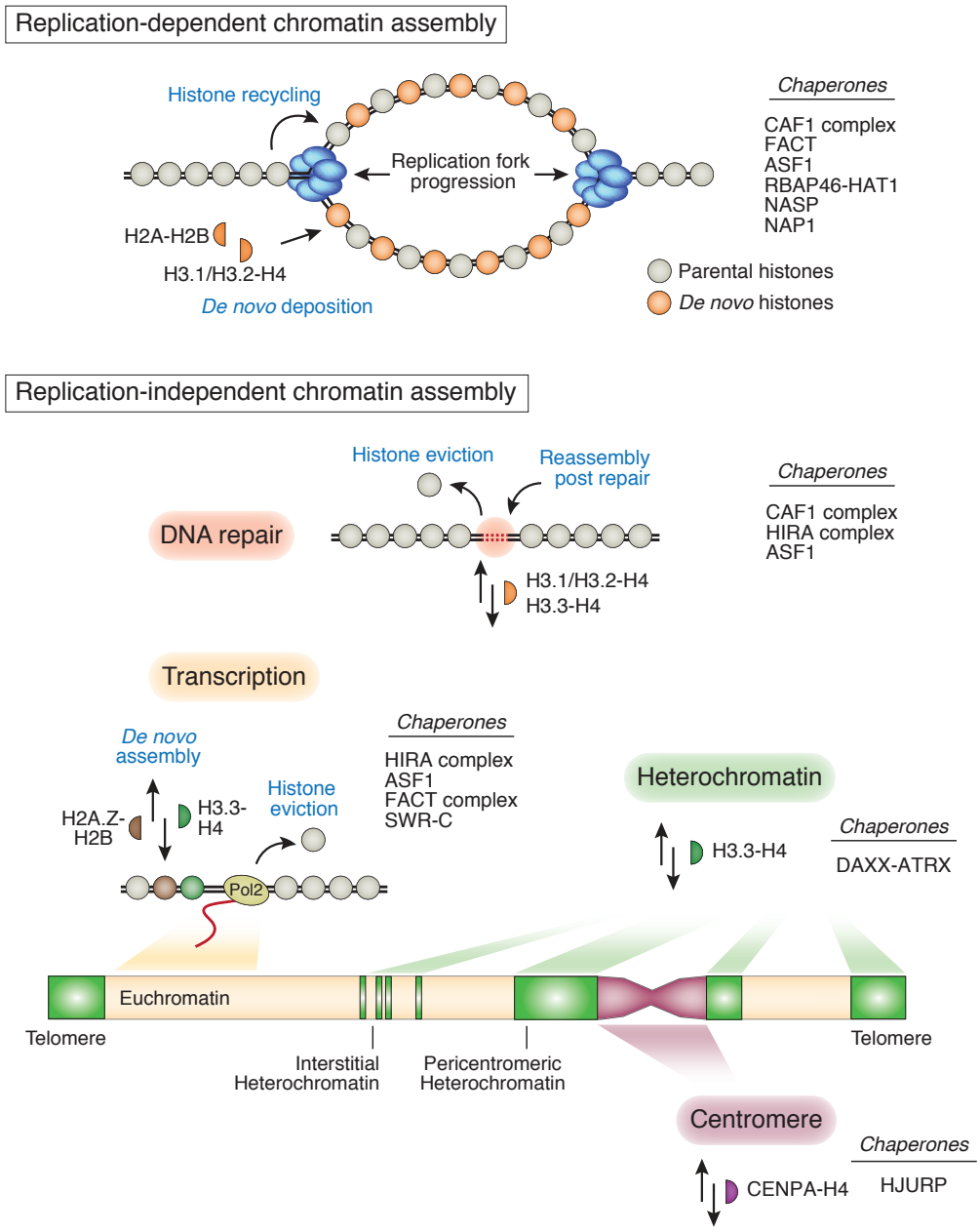

Figure 5. Overview of histone delivery and deposition mechanisms.

(Top panel) Replication-dependent chromatin assembly requires the incorporation of newly synthesized canonical histones as well as recycling of parental histones. (Bottom panel) Replication-independent chromatin assembly involves mechanisms of histone incorporation that occur globally and locally. The deposition of replacement histone variants occurs in specific cellular processes such as DNA repair or transcription, as well as in discrete genomic locations such as heterochromatin or centromeres. Adapted from Hammond et al., 2017.

its deposition is mediated by the histone chaperone Holliday junction recognition protein (HJURP) early in G1-phase (Figure 5) (Dunleavy et al., 2009; Foltz et al., 2009). This chaperone operates through a histone exchange reaction before the next round of DNA replication occurs, thus preventing further dilution during DNA replication, and ensuring centromere maintenance.

The H3 histone variant H3.3 is mostly enriched at active gene promoters, enhancers, gene bodies and heterochromatin regions such as telomeres (Goldberg et al., 2010). In mouse embryonic stem cells, H3.3 deposition at promoters and gene bodies is dependent on HIRA, whereas telomeres rely on ATRX–DAXX for H3.3 assembly (Figure 5) (Goldberg et al., 2010). The HIRA complex, composed of HIRA, ubinuclein 1 (UBN1) and calcineurin-binding protein-1 (CABIN1), dictates replication-independent H3.3-H4 chromatin assembly during DNA repair or transcription (Tagami et al., 2004). The HIRA complex is recruited to active chromatin regions through H3.3 and interactions with several regulators of transcription, such as RNA Polymerase II, PRC2 transcriptional regulators or RPA at promoters (Banaszynski et al., 2013; Ray-Gallet et al., 2011; Zhang et al., 2017). In addition, the HIRA complex promotes H3.3 deposition at the sites of UVC damage, thus enabling transcription restart (Adam et al., 2013). Also in the context of damage, specifically in the presence of DSB, the chromatin remodeller CHD2 triggers deposition of H3.3 at these sites together with chromatin expansion (Luijsterburg et al., 2016). Histone variant H3.3 is also located at heterochromatin and its specific deposition is mediated by the histone chaperone DAXX (Lewis et al., 2010). DAXX works together with the chromatin remodeller alpha thalassemia/mental retardation syndrome X-linked (ATRX). ATRX harbours a N-terminus cysteine rich domain called ADD, which promotes binding to H3K9me3, and a C-terminus ATP-dependent helicase SNF2 domain (Dyer et al., 2017). DAXX binds soluble H3.3-H4 dimers and localizes into promyelocytic leukaemia (PML) bodies together with ATRX, HIRA and ASF1a prior to histone deposition (Delbarre et al., 2013). Deposition of H3.3 is essential for the maintenance of heterochromatin in ES cells, both for endogenous retroviral element (ERV) silencing and for preventing telomere recombination (Elsässer et al., 2015; Udugama et al., 2015; Wong et al., 2009).

Interestingly, the two main H3.3 deposition pathways both localize to PML bodies, specific nuclear compartments marked by the PML protein. PML bodies are nuclear structures of up to 1.0 μM in diameter that contain numerous proteins involved in senescence induction, the antiviral response, DNA damage and telomere maintenance (Lallemand-Breitenbach and de Thé, 2010). During oncogene-induced senescence, PML bodies reorganize in senescence-associated heterochromatin foci (SAHFs), which depend on HIRA, ASF1 and the PML protein for their formation (Zhang et al., 2005b). HIRA, by depositing H3.3 at promoters and regulatory elements, controls a dynamic chromatin landscape in senescent cells (Rai et al., 2014). PML bodies, apart from serving as a platform for SAHFs during senescence, also function in proliferating cells as a scaffold for the assembly of DAXX-ATRX complexes in order to target H3.3 to heterochromatin and telomeres

(Chang et al., 2013; Delbarre et al., 2013; Drané et al., 2010). Recently, a novel role for PML in organizing chromatin domains was described: PML loss impairs H3.3 deposition by ATRX-DAXX but preserves H3.3 loading by the HIRA complex (Delbarre et al., 2017), further implicating PML as a scaffold during DAXX-ATRX mediated chromatin assembly. The PML-associated protein DEK also dictates chromatin supply of H3.3 to heterochromatin (Ivanauskiene et al., 2014), and DEK loss in ES cells impairs H3.3 loading at telomeres, affecting chromatin integrity.

It is worth mentioning that upon histone pool or histone chaperone unbalances, the histone chaperone network has been shown to mitigate some deleterious effects through redundancy. It has been specifically observed that upon overexpression of CENP-A, DAXX can mediate its deposition at non-centromeric sites (Lacoste et al., 2014) and in the absence of DAXX, H3.3 can bind the CAF1 complex (Drané et al., 2010). Thus, the flexibility of the histone chaperone network will become extremely important in disease states (further discussed below in section 3) where some of the modules that integrate the network may appear mutated or imbalanced.

3. DNA REPLICATION STRESS, CHROMATIN ASSEMBLY AND HUMAN DISEASE

a. Hereditary diseases

As discussed above, replication stress due to replication fork collapse, under-replicated DNA or alterations in DNA repair, can increase DNA damage and mutation rates and influence human disease. The intra-S-phase checkpoint is of great relevance to preventing genome instability arising from replication stress, and this is supported by the fact that both ATR and CHK1 kinases are essential for cell viability (Zeman and Cimprich, 2014). Human individuals that carry hypomorphic mutations in *ATR* suffer from Seckel syndrome, which presents with severe developmental problems such as intrauterine growth delay, dwarfism, microcephaly and mental retardation (Murga et al., 2009; O'Driscoll et al., 2003). Several other genes have been found mutated in Seckel-like syndrome, including the ATR partner *ATRIP*, the repair genes *CTIP* and *DNA2* and several genes implicated in centrosome biogenesis (*CENPJ*, *CEP152*, *CEP63* or *PCNT*) (Khetarpal et al., 2016; Qvist et al., 2011; Sir et al., 2011). Similar to Seckel syndrome, there are several genetic diseases resulting from inactivating mutations in checkpoint genes that present with significant phenotypic heterogeneity and often with a cancer-prone phenotype. I will briefly outline some of the main features of hereditary diseases that are caused by mutations in genes important for replicative stress, DNA repair and checkpoint activation. The loss of the central transducing kinase upon DSBs and apical regulator of G1/S checkpoint, *ATM*, underlies Ataxia telangiectasia (A-T) that is characterized by cerebellar ataxia, immune defects and cancer predisposition (Barlow et al., 1996). Similarly, loss of the MRE11–

RAD50–NBS1 (MRN) complex, which activates ATM upon DSB or ATR during replication stress, can be the cause of disorders such as Ataxia-telangiectasia-like disease (A-T-LD) (*MRE11* mutation), Nijmegen breakage syndrome (NBS) (*NBS1* mutation) or NBS-like disorder (*RAD50* mutation) (Stracker and Petrini, 2011). These deficiencies cause a similar spectrum of phenotypes as seen in A-T, including DSB-repair deficiencies and developmental defects affecting the central nervous system, immune system and germline. In addition to ATM and the MRN complex, the loss of the FANC family of proteins, implicated in inter-strand crosslink (ICL) repair and replication fork protection, results in Fanconi anaemia (FA) and is characterized by bone marrow failure, skeletal defects, hypopigmentation and cancer predisposition (Kim and D'Andrea, 2012). Deficiency in *RNaseH2*, *TREX1* or *SAMHD1*, which are involved in the removal of ribonucleotides or RNA–DNA hybrids such as R-loops can lead to a neurological disorder known as Aicardi–Goutieres syndrome (Crow et al., 2006a, 2006b; Rice et al., 2009). The loss of specialized DNA polymerases or helicases, that are crucial for the bypass of bulky lesions or DNA secondary structures, also results in various genetic diseases. Some illustrative example is the Xeroderma pigmentosum-variant (XP-variant) disorder caused by the loss of the DNA damage tolerance (DDT) polymerase Pol η (*POLH*), which presents with increased cancer-susceptibility condition similar to Xeroderma pigmentosum (Broughton et al., 2002). The loss of helicases important for the bypass of G-quadruplexes and for replication fork structure resolution, such as BLM, WRN or RECQL4, causes Bloom syndrome, Werner syndrome or Rothmund-Thomson syndrome, respectively. These disease states are characterized by premature aging, growth retardation and cancer predisposition (Suhasini and Brosh, 2013).

Interestingly, hereditary diseases have also been linked to mutations in genes involved in nucleosome deposition. Congenital dyserythropoietic anaemia type I (CDAI) is a disorder caused by mutation of *Codanin-1* and presents with chromatin abnormalities, such as chromatin bridges, spongy heterochromatin and invagination of the nuclear membrane in bone marrow erythroblasts, resulting in anaemia and skeletal abnormalities (Dgany et al., 2002). Codanin-1 was later identified as an interacting partner of ASF1 in the ASF1-H3-H4-Importin4 cytoplasmic complex. Codanin-1 negatively regulates ASF1 by sequestering it in the cytoplasm and preventing ASF1 binding to CAF1 or HIRA, since they compete for the same ASF1 binding domain. Mutations or loss of *Codanin-1* accelerate DNA replication rate and increase the chromatin-bound pool of ASF1, suggesting unscheduled chromatin replication (Ask et al., 2012). Wolf-Hirschhorn syndrome (WHS) is caused by different deletions of chromosome 4p16 and presents with growth retardation, mental retardation and various seizures. Chromosome deletions include genes involved in histone biogenesis such as *SLBP* or *NELFA*, and patient cell lines display delayed S-phase progression and reduced levels of chromatin-bound histones (Kerzendorfer et al., 2012). Germline mutations in the chromatin remodeller *ATRX* lead to ATR-X syndrome, characterized with severe intellectual disability, alpha thalassemia and myelodysplasia (Gibbons et al., 1995). ATRX plays a key role in several tandem repeat sequences within the genome,

including the deposition of H3.3, prevention of DNA replication fork stalling, and the suppression of recombination at telomeres (further discussed in section 3.c) (Clynes et al., 2013). More recently, a report implicated *de novo* mutations in the kinase domain of *TLK2* (H493R, H518R, D629N and R720A) in intellectual disability (ID) and these patients also presented with motor delay, behaviour problems and facial dysmorphisms (Lelieveld et al., 2016). Thus, it is likely that future large-scale exome sequencing studies will implicate additional genes involved in replication stress and nucleosome deposition in disease etiology of rare neurodevelopmental disorders. Last, it is key to mention that the most common human disease associated with problems in DNA replication stress and chromatin assembly is cancer, and the most relevant issues for this thesis will be discussed below in sections 3.b and 3.c.

b. Replication stress in cancer

Tumour cells are prone to replicative stress, and the first evidence for this was provided back in 2005, where seminal papers described that DNA damage markers were activated at early stages in carcinogenesis by oncogene-driven unscheduled DNA replication and cell division (Bartkova et al., 2005; Gorgoulis et al., 2005). This implies that DNA damage signalling poses a barrier to cancer evolution, and tumours may need to bypass this barrier to progress. One of this barriers is DNA damage-induced senescence (Bartkova et al., 2006) and the bypass of cell cycle checkpoints (Figures 1D, 2 and 6). The activation of oncogenes has been linked to the induction of replication stress and the accumulation of DNA damage in the so called oncogene-induced replication stress cancer model (Halazonetis et al., 2008). In this model, pre-cancerous lesions due to oncogene activation display unscheduled DNA replication that leads to exposure of ssDNA tracts, fork stalling and fork collapse. These are in turn substrates for endonuclease cleavage, which generate DSBs and the activation of the DNA damage response (DDR). Activation of the DDR induces p53 and provokes high levels of apoptosis and senescence, a barrier for tumour progression. Tumours need to circumvent this barrier, for instance with mutations in p53, in order to allow tumours to develop (Figure 6) (Cortez, 2015; Halazonetis et al., 2008).

The fact that enhanced DNA replication in tumour cells might generate replicative stress while other cell types that rapidly proliferate (such as hematopoietic progenitors, skin or intestine epithelia) do not display detectable levels of damage is intriguing. Some of the mechanisms that may account for enhanced replicative stress specifically in cancer cells is the uncontrolled activation of oncogenes that promote the G1/S transition, such as MYC, RAS, members of the E2F family, CDC25A or Cyclin E. Unscheduled S-phase entry may generate situations where nucleotides, replication factors or histones are limiting (Bartkova et al., 2005; Bester et al., 2011). The case of MYC or RAS overexpression, which promote gene expression of many active genes, may pose additional hurdles due to replication-transcription conflicts in addition to disrupted DNA replication (Kotsantis et al., 2016). Remarkably, MYC or Cyclin E overexpression induces firing of replication

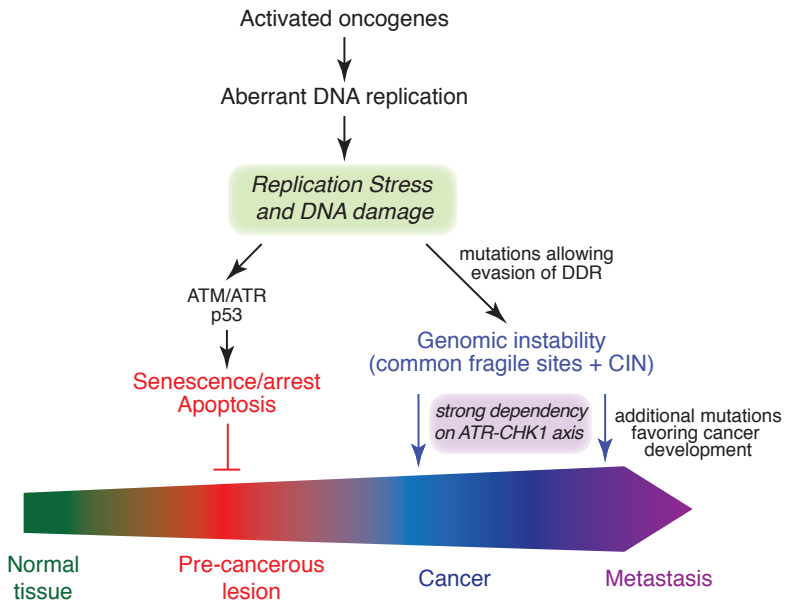

Figure 6. Oncogene-induced DNA replication stress model for cancer development and progression

Oncogene activation induces unscheduled DNA replication and as an outcome, generates endogenous replication stress and DNA damage in early cancer stages (pre-cancerous lesions). This activates cellular checkpoints and could lead to senescence or apoptosis, forming a tumorigenic barrier. However, such barrier can be bypassed by allowing evasion of the DDR, usually by impairing the p53 tumour suppressor pathway. This allows the transition from precancerous lesion to cancer, promoting tumorigenesis and creating a dependency on the functionality of the ATR axis to keep replication stress at non-toxic levels. Adapted from Halazonetis et al., 2008.

origins that locate within highly transcribed genes. Thus, premature S-phase entry prevents these origins from being suppressed by transcription during G1-phase, generates replication-transcription conflicts and severe chromosomal rearrangements (Macheret and Halazonetis, 2018). Another mechanism may be the reduced activity or inactivation of tumour suppressors, such as RB, p53 or the CDK inhibitor p16 (*CDKN2A*), which may promote premature G1/S transition (Dobbelstein and Sørensen, 2015).

The intra-S-phase checkpoint, controlled by the ATR-CHK1 pathway, plays a pivotal role in the oncogene-induced replication stress cancer model. Seckel syndrome patients do not present with increased cancer predisposition, and reduction in ATR activity is lethal in the context of oncogene-induced replication stress cancer models, regardless of p53 status (Figure 6) (Murga et al., 2011; Schoppy et al., 2012). On the other hand, CHK1 haploinsufficiency contributes to cancer predisposition (Lam et al., 2004). Regardless, high levels of replication stress in cancer cells causes them to acquire a strong dependency on functional ATR-CHK1 in order to tolerate such high levels to allow cell proliferation. This represents a very tight balance between replication stress promoting cellular transformation through a mutator phenotype early in tumorigenesis and providing a therapeutic window for targeting replication stress later in tumorigenesis, so the levels of DNA damage become so toxic for cancer cells that they enter in mitotic catastrophe.

This dependency allows exploiting the inhibition of ATR-CHK1 as a means to target cancer (Fokas et al., 2014). Inhibition of CHK1 promotes hypersensitivity to various DNA damaging agents in p53-deficient cancer cells (Stevens et al., 2011), and also selectively kills MYC-driven lymphomas (Murga et al., 2011). Similarly, ATR inhibition sensitizes ATM or p53-deficient cells to conventional DNA damaging agents used in the clinics (Reaper et al., 2011; Toledo et al., 2011). Thus, most of the data generated to date suggests a strong relationship between replicative stress, premature S-phase onset, nucleotide starvation and genomic instability in cells that overexpress oncogenes. ATR-CHK1 inhibition serves as a double-edged sword for cancer, while their insufficiency may promote tumorigenesis in the context of other mutations, their total inhibition is primarily toxic to cancer cells.

c. Histone H3.3 and alternative lengthening of telomeres in cancer

Tumour cells require that their chromosome ends, called telomeres, are elongated in order to bypass replicative senescence that is induced by telomere shortening (Shay and Wright, 2000). Most tumours induce Telomerase activation as a mechanism to maintain telomere length. Telomerase is a DNA polymerase that uses an RNA template to elongate chromosome ends and is highly expressed in embryonic tissues and stem cells but undetectable in most somatic cells (Kim et al., 1994). While around 85-90% of tumours reactivate Telomerase transcription, others lack Telomerase activity and instead maintain telomeres by a Telomerase-independent mechanism called Alternative lengthening of Telomeres (ALT). 10-15% of tumours rely on ALT for tumour maintenance, and these are often tumours of mesenchymal lineage, such as glioblastomas or osteosarcomas (Bryan et al., 1997). ALT+ tumours rely on recombination mechanisms at telomeres for lengthening, and these often display altered chromatin dynamics due to inactivating mutations in the H3.3 histone chaperone DAXX and even more frequently in the histone remodeller ATRX (Heaphy et al., 2011; Lovejoy et al., 2012). Although there is a subset of ALT+ tumours with reduced expression of ATRX or DAXX in the absence of mutations and some ALT+ tumours retain normal ATRX and DAXX expression, it is clear that loss of ATRX-DAXX pathway is strongly correlated with ALT. The molecular hallmarks of ALT comprise the presence of telomeres with heterogeneous length, telomere recombination, the production of extra-chromosomal telomeric repeat (ECTR) DNA species and the accumulation of ALT-associated PML bodies (APBs) (O'Sullivan and Almouzni, 2014). Moreover, the mutation of the *ATRX* gene or loss of ATRX protein strongly correlates with ALT. Cellular studies have revealed that re-expression of ATRX suppresses ALT activity in U-2-OS (ALT+ cells) (Clynes et al., 2015), indicating that ATRX is an ALT repressor. However, loss of ATRX by knockout or knockdown in SV40 immortalized BJ fibroblasts and HeLa cells is insufficient to trigger ALT activation (Lovejoy et al., 2012; O'Sullivan et al., 2014). Thus, despite the absence of ATRX is likely contributing to the ALT phenotype in a unique manner, it is probably not the only participating factor. In mouse ES cells, depletion of PML, ATRX or H3.3 causes a telomeric dysfunction

phenotype (Chang et al., 2013; Wong et al., 2009, 2010), implicating these factors in the regulation of telomere chromatin integrity. Additionally, other histone chaperones such as HIRA or ASF1 have been implicated in maintaining chromatin stability at ALT telomeres (Jiang et al., 2011; O'Sullivan et al., 2014); and in the case of ASF1, total ASF1 depletion strikingly induced ALT features in HeLa cells (O'Sullivan et al., 2014).

In addition to the common mutations of *ATRX* and to a lesser extent *DAXX* in ALT+ tumours, many paediatric diffuse intrinsic pontine gliomas (DIPG) and glioblastoma multiforme (GBM) contain heterozygous mutations in the histone H3.3 gene *H3F3A*. These mutations lead to substitutions at two critical amino acids at the histone H3.3 tail: K27M and G34R/G34V, Lys 27 being critical for its own methylation and Gly 34 for directly affecting Lys 36 methylation (Schwartzentruber et al., 2012; Wu et al., 2012). The K27M mutation in H3.3 is sufficient to inhibit the activity of EZH2, a member of the Polycomb regulatory complex 2 (PRC2) and methyltransferase that catalyses the H3K27me2/3 modification. Thus, K27M gain-of-function mutation acts as a dominant negative and is a mechanism to alter the epigenetic state of tumours (Bender et al., 2013; Lewis et al., 2013). Subsequent studies revealed that more than 90% of chondroblastomas contain heterozygous mutations in the K36M residue in the histone H3.3 gene *H3F3B*, while in giant cell tumour of bone mutations occurred in G34L/G34W in the histone H3.3 gene *H3F3A* (Behjati et al., 2013). Similar to the K27M gain-of-function, K36M mutation in H3.3 reduced H3K36me3 globally by inhibition of the two methyltransferases in charge of this modification, MMSET and SETD2, and this caused reprogramming of the epigenetic landscape (Fang et al., 2016). Although the status of telomere maintenance has not been investigated in detail in H3.3 mutated tumours, it is likely that the severe changes in the histone methylation landscape might affect telomeric chromatin and perhaps facilitate the activation of ALT. Therefore, it will be key to understand the mechanisms that drive ALT, since cancer therapies that target Telomerase could select for the emergence of ALT as a resistance mechanism. Specific treatments for the different telomere maintenance mechanisms are likely required to cope with recurrent tumours.

4. IDENTIFICATION OF THE TOUSLED LIKE KINASES

The Tousled kinase (TSL) and Tousled like kinases (TLKs) are nuclear Ser–Thr kinases that are absent in yeast but appear to be constitutively expressed in most cells and tissues from plants and animals, and they exhibit the highest levels of activity during S-phase. Both TSL and TLKs have a C-ter protein kinase catalytic domain and a large N-ter regulatory domain (Figure 7A) (Roe et al., 1997; Silljé et al., 1999). TSL was first identified in *Arabidopsis* where mutations in the gene led to pleiotropic defects in morphogenesis, including delays in flowering time and leaf development (Roe et al., 1993). Analysis of the TSL protein sequence revealed putative coiled-coil regions and three consensus nuclear localization signal (NLS) sequences in the N-ter. *In vitro* assays using TSL protein purified

from yeast showed that the coiled-coil regions influenced the ability of TSL to oligomerise and this was important for full kinase activity (Figure 7B) (Roe et al., 1997). Subsequent analysis of TSL in plants showed that TSL mRNA and protein expression levels are stable throughout the cell cycle (Ehsan et al., 2004), that TSL is required for the maintenance of transcriptional silencing and TSL mutants displayed hypersensitivity to UV-B radiation and methyl methanesulfonate (MMS) (Wang et al., 2007).

TSL homologues in human, *Drosophila*, *C. elegans* and *T. brucei*, have been implicated in DNA repair, DNA replication, transcription and mitosis (Carrera et al., 2003; Groth et al., 2003; Han et al., 2003; Li et al., 2007; Silljé et al., 1999). At the organismal level, the single TLK gene in *C. elegans* and *Drosophila* is essential for viability since its loss during early and rapid cell divisions leads to severe chromatin and proliferation defects and lethality during development (Figure 7B) (Carrera et al., 2003; Han et al., 2003). In *C. elegans*, the major defects observed following ceTLK-1 downregulation were transcriptional, reflecting reduced phosphorylation of RNA polymerase II, and mitotic, through interactions with Aurora B (Han et al., 2003, 2005). In *Drosophila*, the early arrest during embryonic development upon dTLK mutation was proposed to result from defective chromatin maintenance. Interestingly, the deleterious effects in eye development observed upon overexpression of a dTLK kinase-dead mutant could be rescued by the overexpression of the histone H3–H4 chaperone ASF1, a substrate of TLK (Carrera et al., 2003; Silljé and Nigg, 2001).

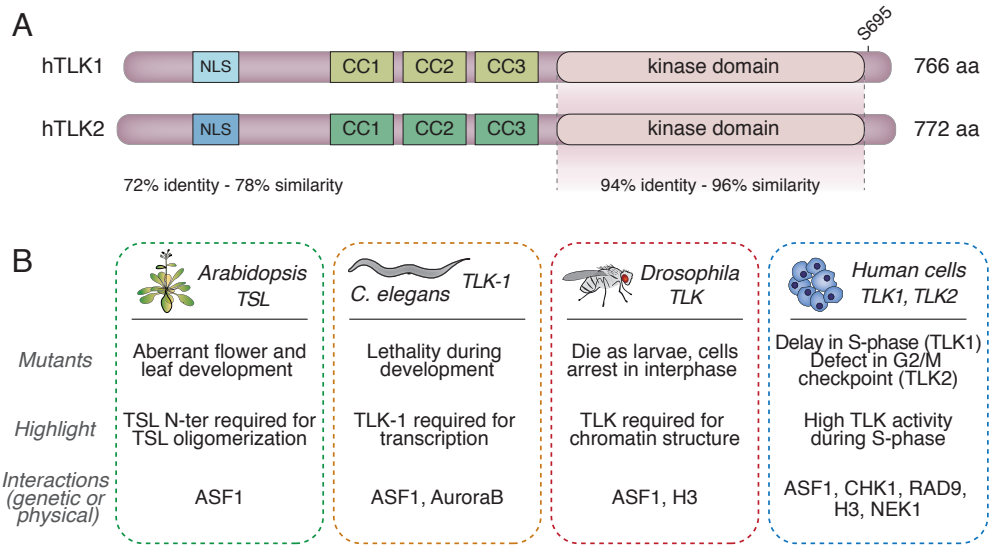

Figure 7. The Tousled like kinases.

(A) Comparison of the human TLK1 and TLK2 proteins. The pale purple boxes show the almost identical kinase domain. The blue box shows the nuclear localization signal (NLS), and green boxes the predicted coiled-coil domains (CC). The phosphosite identified in the C-ter tail of TLK1 upon DNA damage is indicated (Groth et al., 2003). The total number of residues of each protein is shown on the right. Sequence identity and similarity between the whole protein or the kinase domains are displayed as a percentage, and were assessed by NCBI BLAST (blastp suite-2sequences). (B) Scheme summarizing the most striking features described for TSL and TLK functions across different model organisms. References for original articles are found in the main text.

In mammals, there are two distinct TLK gene homologues, TLK1 and TLK2, which are highly similar (Li et al., 2001; Shalom and Don, 1999; Silljé et al., 1999; Yamakawa et al., 1997; Zhang et al., 1999). Human TLK expression is constitutive both at the mRNA and protein levels throughout the cell cycle, similar to what had been observed for TSL. However, TLK protein kinase activity (for both TLK1 and TLK2) oscillates during cell cycle, with a peak in S-phase (Figure 7B) (Silljé et al., 1999). Inhibition of DNA polymerase α by Aphidicolin causes a decrease in TLK kinase activity, suggesting that activation of TLKs is linked to DNA replication (Silljé et al., 1999). TLKs interact with each other and with both ASF1a and ASF1b, the primary established TLK1 and TLK2 targets (Silljé and Nigg, 2001). Although the precise mechanisms by which ASF1 is regulated remain unclear, in *Drosophila*, dTLK phosphorylation of ASF1 controls its stability, while in vertebrates, TLK1-mediated phosphorylation of several sites on the C-ter tail of ASF1 promote its binding affinity for the histone H3–H4 heterodimer (Figure 4A) (Klimovskaia et al., 2014; Pilyugin et al., 2009). These data suggest that TLK-mediated phosphorylation of ASF1a and ASF1b may promote histone delivery to downstream histone chaperones such as CAF1 and HIRA for replication-coupled and replication-independent chromatin assembly, respectively. ASF1 has been linked to checkpoint control in yeast, since it interacts with Rad53, the yeast homolog for CHK2 (Emili et al., 2001; Hu et al., 2001). However, this interaction is absent in human cells. In this case, following the activation of the DNA damage checkpoint in response to DSBs, the checkpoint kinase CHK1 does not interact with ASF1 but phosphorylates TLK1 at the C-terminal Ser 695 residue, transiently inhibiting its activity (Figure 7A). The CHK1 dependent modulation of TLK1 potentially coordinates global ASF1 histone-binding capacity with the checkpoint response and allows chromatin restructuring prior to chromatin reassembly during DNA repair (Groth et al., 2003; Krause et al., 2003). Subsequent studies have identified TLK1 at replication sites (Klimovskaia et al., 2014) and observed an S-phase delay in TLK1 depleted cells (Kelly and Davey, 2013). In addition to ASF1, TLK1 has been reported to phosphorylate RAD9, a component of the 9-1-1 alternative clamp loader that has multiple roles in the response to DNA damage, including the regulation of CHK1 activation, and this was linked to G2/M checkpoint release (Canfield et al., 2009; Kelly and Davey, 2013; Sunavala-Dossabhoy and De Benedetti, 2009). Other reports implicated TLK2, but not TLK1, in DNA damage-induced G2/M checkpoint recovery through ASF1a mediated transcriptional regulation (Bruinsma et al., 2016). Interestingly, TLKs modulate chromatin and act as repressors of reactivation of gamma herpesviruses from viral latency (Dillon et al., 2013).

A poorly translated splice variant of TLK1, named TLK1B, contains a long 5'UTR and its translation is regulated by eIF4E. Overexpression of TLK1B in mouse cells confers enhanced resistance to ionizing radiation (Li et al., 2001). Overexpression of dominant negative form of TLK1B causes missegregation of chromosomes, whereas siRNA-mediated suppression of TLK1 blocks cell cycle progression in mouse cells (Sunavala-Dossabhoy et al., 2003). Histone H3 has been described as another potential TLK

phosphorylation target site in *Drosophila* (Carrera et al., 2003) and in mammals, TLK1B phosphorylates Histone H3 *in vitro* and is capable of complementing a yeast mutant strain lacking the major yeast H3 kinase, IPL1 (Li et al., 2001).

Although TLK2 is less well characterized, copy number amplifications and increased expression of TLK2 have been recently reported in ER-positive breast cancer and linked to worse disease progression (Kelemen et al., 2009; Kim et al., 2016a, 2016b; Mertins et al., 2016) and TLK2 mutations have been implicated in intellectual disabilities (Lelieveld et al., 2016) suggesting that TLK activity influences human disease. Overall, TLK activity has been linked to DNA replication, DNA repair, transcription, chromatin structure, chromosome segregation, viral latency and cell cycle checkpoint control in various organisms. The TLKs could therefore act at the interface between DNA replication, chromatin assembly and genome integrity.

Objectives

Objectives

We hypothesised that absence of TLKs will lead to impaired cellular proliferation, chromatin abnormalities, and genome instability that would affect both at the cellular level and at the organism level.

The specific objectives of this thesis are:

1.– Characterise TLK2 biochemically and identify its domains, phosphorylation sites and interactions.

2.– Characterise the role of TLKs *in vivo*, using constitutive/germline knockout and conditional knockout mouse models.

3.– Establish the role of TLKs during DNA replication in cancer cells.

4.– Provide proof-of-principle of TLK inhibition in cancer models.

5.– Determine the effect of TLK depletion on chromatin assembly in cancer cells.

Materials and Methods

Cloning of human TLK2 domain-mutant or phospho-mutant/mimic constructs

The human TLK2 cDNA was obtained in a Gateway-compatible pENTR223 vector (Sigma Mission cDNA library) and introduced into the N-SF-TAP-DEST vector (a kind gift from J Gloeckner (Gloeckner et al., 2007)) by recombination reaction (300 ng TLK2-pENTR223, 300 ng N-SF-TAP-DEST, 4 µl Gateway buffer (Invitrogen) and 4 µl clonase LR (Invitrogen)) and incubated at 25°C for 1 h. Proteinase K (2 µl) (Sigma-Aldrich) was added and incubated at 37°C for 10 min to stop the reaction. Competent *E. coli* DH5α (Sigma-Aldrich) were transformed with the resulting recombination reaction and selected with kanamycin. Plasmids were checked by restriction digests and sequencing (Macrogen) and DNA prepared with MaxiPreps (Promega). All TLK2 constructs to be expressed in mammalian cells were made in a pcDNA3.1 vector with an N-terminal Strep-Flag (SF) tag. The wild type TLK2 cDNA was introduced into the pcDNA3.1 plasmid generating the TLK2-WT construct. The kinase-dead construct TLK2-KD (D592V), the phospho-site mutants or mimics S569A, S617A, S617D, S635A, S635D, S686A, S686D, S659A, T695A, S474A and the C-tail mutant S748stop were generated by QuickChange Lightning Site-Directed Mutagenesis (Agilent Technologies). The domain-deletion mutants were generated by restriction enzyme digest using unique restriction sites within the full TLK2 sequence of an initial pcDNA3.1 N-SF-TLK2-WT plasmid that had been previously modified to make unique EcoRI and ScaI restriction sites by introducing silent mutations using the QuickChange Lightning Site-Directed Mutagenesis (Agilent Technologies). ΔN-TLK2 and TLK2-ΔCC3 mutants were made by PCR-cloning using the high fidelity KOD Hot Start DNA Polymerase (EMD Millipore) and overhang primers containing the desired restriction sites. TLK2-ΔCC1 and TLK2-ΔCC2 mutants were made by cloning custom ordered GeneArt DNA-Strings (Thermo Fisher Scientific). Each DNA-String was cloned into a pCR Blunt End II-TOPO vector (Thermo Fisher Scientific) in order to allow storage and amplification. The resulting PCR product to generate ΔN-TLK2 and TLK2-ΔCC3 and the pCR Blunt End II-TOPO vectors containing DNA-Strings to generate TLK2-ΔCC1 and TLK2-ΔCC2 were digested using the restriction enzymes (New England BioLabs (NEB)) indicated in Table 2. The pcDNA3.1 N-SF-TLK2 plasmid was digested with the same restriction enzymes as the corresponding inserts and dephosphorylated with Calf intestinal alkaline phosphatase (CIP) (NEB). Digested insert and plasmid were purified by the PureLink Quick Gel Extraction & PCR Purification Combo Kit (Thermo Fisher Scientific) and ligated using the Quick Ligation Kit (NEB) in a 3:1 ratio. Restriction sites, primer pairs and DNA-Strings used are specified in Tables 1 and 2. All constructs were verified by DNA sequencing.

TABLE 1. Site directed mutagenesis primers

Mutant	Primer	Sequence 5'-3'
pcDNA3.1-N-SF-TLK2 ScaI site C>T	F	CTTTTCTGTGACTGGTGAGTATTCAACCAAGTCATTCTGA
	R	TCAGAATGACTTGGTTGAATACTCACCAGTCACAGAAAAG
pcDNA3.1-N-SF-TLK2 EcoRI site A>T	F	GGTGGCGGCGAATACCAGCACACTGGC
	R	GCCAGTGTGCTGGTATTCGCCGCCACC

Mutant	Primer	Sequence 5'-3'
TLK2-KD (D592V) GAC>GTC	F	AATATTACCTGGTTTGAGGACATAGTGTATGATGGGAGG
	R	CCTCCCATCATACACTATGTCCTCAAACCAGGTAATATT
TLK2-S569A TCC>GCC	F	GGAGAAAGAGGCCCGGGCCATTATCATGCAGAT
	R	ATCTGCATGATAATGGCCCGGGCCTCTTTCTCC
TLK2- S617A TCG>GCG	F	GATAAAAATTACAGATTTTGGTCTTGCGAAGATCATGGATGATGATAG
	R	CTATCATCATCCATGATCTTCGCAAGACCAAAATCTGTAATTTTTATC
TLK2- S617D TCG>GAC	F	GCTATCATCATCCATGATCTTGTCAAGACCAAAATCTGTAATTTTTATCTCTCCAC
	R	GTGGAGAGATAAAAATTACAGATTTTGGTCTTGACAAGATCATGGATGATGATAGC
TLK2-S635A TCA>GCA	F	TGGCATGGAGCTAACAGCACAAGGTGCTGGTAC
	R	GTACCAGCACCTTGTGCTGTTAGCTCCATGCCA
TLK2-S635D TCA>GAC	F	GTGGATGGCATGGAGCTAACAGACCAAGGTGCTGGTACTTATTGG
	R	CCAATAAGTACCAGCACCTTGGTCTGTTAGCTCCATGCCATCCAC
TLK2- S686A TCT>GCT	F	CTTTTGGCCATAACCAGGCTCAGCAAGACATCCTA
	R	TAGGATGTCTTGCTGAGCCTGGTTATGGCCAAAAG
TLK2-S686D TCT>GAT	F	TTGTAGGATGTCTTGCTGATCCTGGTTATGGCCAAAAGGC
	R	GCCTTTTGGCCATAACCAGGATCAGCAAGACATCCTACAA
TLK2- S659A TCA>GCA	F	CCACACATCAACTTTATTTGCGATCTTTGGTGGTTCTTTCC
	R	GGAAAGAACCACCAAAGATCGCAAATAAAGTTGATGTGTGG
TLK2-T695A ACG>GCG	F	GTAGCTTTAAGAATCGCATTCTCTTGTAGGATGTCTTGCTGAG
	R	CTCAGCAAGACATCCTACAAGAGAATGCGATTCTTAAAGCTAC
TLK2-S474A AGT>GCT	F	CTTTTGGGTAGAGGAGGTTTCGCTGAAGTTTACAAGGCATTTGA
	R	TCAAATGCCTTGTAAACTTCAGCGAAACCTCCTCTACCCAAAAG
TLK2-S748stop TCA>TGA	F	GTTGCCTCACATCCGAAAGTGAGTCTCTACAAGT
	R	ACTTGTAGAGACTCACTTTCGGATGTGAGGCAAC

TABLE 2. TLK2 deletion mutants primers and/or DNA-Strings

Mutant	Restriction sites used	Primer	Sequence 5'-3'
ΔN-TLK2	BamHI-NheI	F	CCCAAGCTTGGTACCGAGCT
		R	TGCTTAGCTAGCGGTCCCTTACTAACACCTA
TLK2-ΔCC3	HpaI-ScaI	F	TGCTTAGTTAACGTTTAAAGATCATCCAACGCTA
		R	GTTTTATTTCATTTAAGTACT

Mutant	Restriction sites used	DNA-String
TLK2-ΔCC1	EcoRI-HpaI	GAAAACAGTAAGAATTCAAAACAAGAGAAGATGGCGTGTAGAGATAAGAGCATGCAAGAC-CGCTTGAGACTGGGCCACTTTACTACTGTCCGACACGGAGCCTCATTTACTGAACAGTGG-ACAGATGGTTATGCTTTTCAGAATCTTATCAAGCAACAGGAAAGGATAAATTCACAGAGG-GAAGAGATAGAAAGACAACGGAAAATGTTAGCAAAGCGGAAACCTCCTGCCATGGGTCAG-GCCCCTCCTGCAACCAATGAGCAGAAACAGCGGAAAAGCAAGACCAATGGAGCTGAAAAT-GAAACGTTAACGTTAGCAGA
TLK2-ΔCC2	EcoRI-HpaI	GAAAACAGTAAGAATTCTGACTTAGAGAAGAAGGAGGGAAGAATAGATGATTTATTAAGAG-CCAACTGTGATTTGAGACGGCAGATTGATGAACAGCAAAAGATGCTCGAGAAATACAAG-GAACGATTAAATAGATGTGTGACAATGAGCAAGAAACTCCTTATAGAAAAGTCAAAACAA-GAGAAGATGGCGTGTAGAGATAAGAGCATGCAAGACCGCTTGAGACTGGGCCACTTTAC-TACTGTCCGACACGGAGCCTCATTTACTGAACAGTGGACAGATGGTTATGCCATGGGTCAG-GCCCCTCCTGCAACCAATGAGCAGAAACAGCGGAAAAGCAAGACCAATGGAGCTGAAAAT-GAAACGTTAACGTTAGCAGA

Generation of analog sensitive TLK2 allele by site directed mutagenesis

Mutations to obtain an analog sensitive TLK2 allele were introduced into the pcDNA3.1 plasmid containing the TLK2-WT construct by QuickChange Lightning Site-Directed Mutagenesis (Agilent Technologies). First, two alternative mutations in the gatekeeper residue, L544A and L544G, were introduced. Subsequently, three possible suppressor

mutations, C541V, T542E and S617A, were generated in the context of the gatekeeper mutant L544G. Primer pairs used are specified in Table 3, except for S617A mutant that is specified in Table 1.

TABLE 3. Site directed mutagenesis primers for analog sensitive TLK2

Mutant	Primer	Sequence 5'-3'
TLK2-L544A	F	CATTTCCCTCACAGTATTCTGCTACTGTACAAAACGAGTCAGTATCC
TTA>GCA	R	GGATACTGACTCGTTTTGTACAGTAGCAGAATACTGTGAGGGAAATG
TLK2-L544G	F	CATTTCCCTCACAGTATTCTCCTACTGTACAAAACGAGTCAGTATCC
TTA>GGA	R	GGATACTGACTCGTTTTGTACAGTAGGAGAATACTGTGAGGGAAATG
TLK2-C541V	F	CCCTCACAGTATTCTAATACTGTAACAAACGAGTCAGTATCCAGTGAAAAG
TGT to GTT	R	CTTTTCACTGGATACTGACTCGTTTGTTACAGTATTAGAATACTGTGAGGG
TLK2-T542E	F	CCCTCACAGTATTCTAATACTTCACAAAACGAGTCAGTATCCAGTGAAAA
ACA to GAA	R	TTTTCACTGGATACTGACTCGTTTTGTGAAGTATTAGAATACTGTGAGGG

Cloning of retroviral HA-HIRA construct

The plasmid pcDNA3-HA-HIRA coding for human HIRA was a kind gift from A. Groth laboratory and was used for transient transfection in mammalian cells. To clone HA-HIRA into a retroviral pLPC vector, the plasmid pcDNA3-HA-HIRA was first modified to make unique HindIII restriction site by introducing a silent mutation in HIRA coding sequence by QuickChange Lightning Site-Directed Mutagenesis (Agilent Technologies) using the primers HIRA_T>C_HindIII_site_F 5'-GGCTCCAGTGGTAAGCTCGCCAATGTGGAG-3' and HIRA_T>C_ HindIII_site_R 5'-CTCCACATTGGCGAGCTTACCACTGGAGCC-3'. pLPC backbone and pcDNA3-HA-HIRA were both digested using HindIII and XhoI restriction enzymes (NEB) and purified using the PureLink Quick Gel Extraction Kit (Invitrogen). Purified fragments were ligated using the Quick Ligation Kit (NEB) at an insert to backbone molar ratio of 3:1. OmniMAX competent *E. coli* cells were transformed with the resulting pLPC-HA-HIRA and colonies were selected in carbenicillin. All constructs were confirmed by DNA sequencing (Macrogen) using the primers pLPC_F_Seq: 5'-TAGGCGTGTACGGTGGGA-3', pLPC_R_Seq: 5'-TAGGCGTGTACGGTGGGA-3', HIRA_F650_Seq: 5'-GTTCCCAGAAATT CTAGCTAC-3', HIRA_F1300_Seq: 5'-ATGGCAAGAGCCTAGCCATCA-3' and HIRA_F1950_Seq: 5'-CAGAACCTTGTGAAAGAGCTG-3'.

Transfections and Strep immunoprecipitation (IP) in mammalian cells

AD293 cells were grown in DMEM media (Thermo Fisher Scientific) supplemented with 10% foetal bovine serum (FBS) (Sigma-Aldrich) and 50 U/mL penicillin/50 µg/ml streptomycin (Thermo Fisher Scientific) at 37°C in a 5% CO_2 incubator. Transient transfections of 20 µg plasmid per 15 cm plate were carried out using polyethylenimine (PEI) (Polysciences Inc.). Plasmids transfected were a series of pcDNA3.1-SF-TLK2 constructs described above and pEXPR IBA105-Strep-ASF1a or –ASF1b (kind gift from A. Groth). Cells were harvested 48 h after transfection and collected by scraping

in PBS. Pellets were lysed in 1 ml lysis buffer (50 mM Tris-HCl, pH 7.5, 150 mM NaCl, 1% Tween-20, 0.5% NP-40, 1x protein inhibitor cocktail (Roche) and 1x phosphatase inhibitor cocktails 2&3 (Sigma-Aldrich)) on ice for 20 minutes. Cells were freeze-thawed 3 times or sonicated at medium intensity for 10 minutes, and lysates were cleared by centrifugation at 16000g for 20 min at 4ºC. Proteins were quantified using the DC Protein Assay (Bio-Rad) and 100 µl was retained for input. 2-4 mg of total protein extracts were incubated with 100 µl pre-washed Strep-Tactin superflow resin (IBA GmbH) overnight at 4ºC using an overhead tumbler. Resin was spun down (7000g for 30 s) and transferred to Illustra MicroSpin Columns (GE Healthcare). Resin was washed 3 times with 500 µl wash buffer (30 mM Tris, pH 7.4, 150 mM NaCl, 0.1% NP-40, 1x protein inhibitor cocktail (Roche) and 1x phosphatase inhibitor cocktails 2&3 (Sigma-Aldrich)). Proteins were eluted from the Strep-Tactin matrix with 50 µl of 5x Desthiobiotin Elution buffer (IBA GmbH) in TBS buffer (30 mM Tris-HCl pH 7.4, 150 mM NaCl, 1x protein inhibitor cocktail (Roche) and 1x phosphatase inhibitor cocktails 2&3 (Sigma-Aldrich)) for 10 min on ice. For Western blotting, 30 µg of input and 25 µl of Strep-IP elute coming from AD293 cells were separated by SDS-PAGE and transferred to Nitrocellulose membrane (Amersham Protran; Sigma-Aldrich), except when probing with RAD9 primary antibody (BD Biosciences 611324) that PVDF membrane (Immobilon-P, Merck) was used. Primary antibodies (Table 13) were detected with appropriate secondary antibodies conjugated to HRP and visualized by ECL-Plus (GE Healthcare).

In vitro kinase assays from cell lysates pull-down

In vitro kinase assays were performed after Strep-IP purification of N-SF-TLK2 mutants coming from AD293 cells. The Strep-IP elute equivalent to 200 µg of total protein input was incubated with 12 µl of Buffer kinase (50 mM Tris-HCl pH 7.5, 10 mM $MgCl_2$, 2 mM DTT, 1x protein inhibitor cocktail (Roche) and 1x phosphatase inhibitor cocktails 2&3 (Sigma-Aldrich)), 100 µM cold ATP, 2 µCi ^{32}P-γ-ATP and 1 µg of substrate. After incubating the mixture during 30 minutes at 30ºC the reaction was stopped by adding 2-3 µl of Sample Buffer (6x SDS, 0.2% bromophenol blue and β-Mercaptoethanol) and boiled for 5 min. Samples were analysed on SDS-PAGE, stained with Coomassie Blue and dried for autoradiography. Substrates used for testing TLK2 mutants were 1 µg of Myelin basic protein (MBP) (Sigma-Aldrich) 1-16 µg of LC8 (kindly provided by D. Reverter) or 0.5 µg of GST-ASF1a (kindly provided by A. Groth). When treating with inhibitors, the Strep-IP elute containing the purified kinase was pre-incubated in Buffer kinase and cold ATP with the inhibitors at the desired concentrations for 30 minutes at room temperature, and then added the ^{32}P-γ-ATP and the substrate and proceeded with the regular reaction. The potential chemical TLK2 inhibitors tested in *in vitro* kinase assays are summarized in Table 4.

TABLE 4. Inhibitors tested in *in vitro* kinase assays

Inhibitor	Conc. in *in vitro* kinase assays	Source	Evidence	Reference
Staurosporine. Streptomyces sp.	10 µM	539745 PKi library II EMD Calbiochem	TLK2 score=1	(Gao et al., 2013) Kinase inhibitor screen.
K-252a. Nocardiopsis sp.	10 µM		TLK2 score=1	
Cdk1 Inhibitor. CGP74514A	10 µM		TLK2 score=31	
Indirubin Derivative E804	10 µM		TLK2 score=38	
Indirubin-3'-monoxime	10 µM		TLK2 score=60	
GSK-3 Inhibitor XIII	10 µM		TLK2 score=62	
Metaraminol (MTM)	3-10 µM	M4773 Sigma-Aldrich	Neg. inh. TLK1	(Ronald et al., 2013) *In vitro* kinase assays using TLK1.
Fluphenazine dihydrochloride (FF)	3-10 µM	F4765 Sigma-Aldrich	Neg. inh. TLK1	
Thioridazine hydrochloride (THD)	10 µM	R750603 Sigma-Aldrich	Pos. inh. TLK1	
Perphenazine (PPH)	1-3-5-10 µM	P6402 Sigma-Aldrich	Pos. inh. TLK1	
Promazine hydrochloride (PMZ)	10 µM	46674 Sigma-Aldrich	Pos. inh. TLK1	
Mol Dyn#1	10 µM	Z828624610 Enamine	Molecular dynamics simulation	M. Rueda collaboration
Mol Dyn#2	10 µM	Z318121832 Enamine		
Mol Dyn#3	10 µM	Z195528220 Enamine		
Mol Dyn#4	10 µM	Z200660424 Enamine		
Mol Dyn#5	10 µM	Z115674144 Enamine		
Mol Dyn#6	10 µM	STK082440 Vitas M Labs		
Mol Dyn#7	10 µM	STK209141Vitas M Labs		
Mol Dyn#8	10 µM	Z194474370 Enamine		
Mol Dyn#9	10 µM	Z112584264 Enamine		
PP1 Analog II 1NM-PP1	10 µM	529581 EMD Millipore	Inhibitor of analog sensitive kinase allele (Shokat allele)	
PP1 Analog III 3-MB-PP1	10 µM	529582 EMD Millipore		

Affinity purification of TLK2 and quantitative mass spectrometry

HEK293T cells were grown in DMEM (Thermo Fisher Scientific) supplemented with 10% FBS and penicillin–streptomycin at 37°C in a 5% CO_2 incubator. Transient transfections of 15 µg plasmid per 15cm plate were carried out using PEI (Polysciences Inc.). Cells were harvested 48 h after transfection and collected by centrifugation. Pellets were lysed in 1 ml lysis buffer (50 mM Tris-HCl, pH 7.5, 150 mM NaCl, 1% Tween-20, 0.5% NP-40 with 1x protease inhibitor cocktail (Roche) and 1x phosphatase inhibitor cocktail 2 (Sigma-Aldrich)) on ice for 20 min. Cells were freeze-thawed 3 times and lysates were cleared by centrifugation at 16000g for 20 min at 4°C. Proteins were quantified using the DC Protein Assay (Bio-Rad) and 100 µl was retained for input. Protein extracts were incubated with 100 µl prewashed Strep-Tactin superflow resin (IBA GmbH) at 4 °C for 2 h using an overhead tumbler. Resin was spun down (7000g for 30 s) and transferred to Illustra MicroSpin Columns (GE Healthcare). Resin was washed 3 times with 500 µl wash buffer

(30 mM Tris, pH 7.4, 150 mM NaCl, 0.1% NP-40, protease and phosphatase inhibitors). Fusion proteins were eluted from the Strep-Tactin matrix with 500 µl of Desthiobiotin Elution buffer (IBA GmbH) (30 mM Tris, pH 7.4, 150 mM NaCl, 1 mM EDTA, 2 mM Desthiobiotin, protease and phosphatase inhibitors) on ice for 10 min. 150 µl was retained for Western blot analysis and the remaining protein was concentrated in centrifugal filter units and taken to a final concentration of 6 M urea and 100 mM ammonium bicarbonate. Then they were reduced, alkylated and digested to peptides using sequence-grade trypsin at 1:10 ratio (w:w; enzyme:substrate) at 37°C overnight. Tryptic peptide mixtures were desalted using a C18 UltraMicroSpin (Thermo Fisher Scientific) column (Rappsilber et al., 2007).

Samples were analysed in a LTQ-Orbitrap Velos Pro Mass Spectrometer (Thermo Fisher Scientific) coupled to nano-LC (Proxeon) equipped with a reversed-phase chromatography 12-cm column with an inner diameter of 75 µm, packed with 5 µm C18 particles (Nikkyo Technos Co. Ltd). Chromatographic gradients from 93% buffer A, 7% buffer B to 65% buffer A, 35% buffer B in 60 min at a flow rate of 300 nl/min, in which buffer A: 0.1% formic acid in water and buffer B: 0.1% formic acid in acetonitrile. The instrument was operated in DDA mode and full MS scans with 1 micro-scans at resolution of 60000 were used over a mass range of m/z 250–2000 with detection in the Orbitrap. Following each survey scan the top 20 most intense ions with multiple charged ions above a threshold ion count of 5000 were selected for fragmentation at normalized collision energy of 35%. Fragment ion spectra produced via collision induced dissociation (CID) were acquired in the linear ion trap. All data were acquired with Xcalibur Software v.2.2.

Acquired data were analysed using the Proteome Discoverer Software suite (v.1.3.0.339; Thermo Fisher Scientific) and the Mascot search engine (v.2.3; Matrix Science) was used for peptide identification. Data were searched against an in-house generated database containing all proteins corresponding to human in the SwissProt database plus the most common contaminants, as described previously (Bunkenborg et al., 2010). A precursor ion mass tolerance of 7 p.p.m. at the MS1 level was used, and up to three miscleavages for trypsin were allowed. The fragment ion mass tolerance was set to 0.5 Da. Oxidation of methionine and protein acetylation at the N-terminal were defined as variable modification. Carbamidomethylation on cysteines was set as a fix modification. The identified peptides were filtered using a FDR <1%. For protein quantitation, the top 3 method was used (Silva et al., 2006). In brief, the average of the peptide areas for the three most intense peptides per protein was used a measure of protein abundance. Data is presented in Supplementary Table S1.

BioID analysis of proximity interactions

Human TLK2 was amplified with forward primer containing 5'-AscI (TLK2-AscI-F: 5'-AAAAAAGGCGCGCCTATGGAAGAATTGCATAGCC-3') or reverse primer containing 3'-NotI restriction sites (TLK2-NotI-R: 5'-AAAAAAGCGGCCGCTTA

ATTAGAAGAACTGTT-3') using KOD Hot Start DNA Polymerase (EMD Millipore) and cycling conditions recommended from the manufacturer (polymerase activation at 95°C for 2 min, denaturation at 95°C for 20 s, annealing at 55°C for 10 s and extension at 70°C for 50 s, repeated for 40 cycles). PCR products were purified using the PureLink Quick Gel Extraction Kit (Invitrogen) and cloned into pCR2.1-TOPO vector (Invitrogen). TOP10 competent *E. coli* cells (Invitrogen) were transformed with pCR2.1-TLK2 and colonies were selected in carbenicillin. Constructs were verified by restriction digestion and sequencing (Macrogen) with primers for the TOPO vector (T7 Promoter-F and M13-R). Afterwards, TLK2 was cut from the pCR2.1-TOPO vector by restriction digest with AscI and NotI-HF (NEB), purified using the PureLink Quick Gel Extraction Kit (Invitrogen) and ligated into pcDNA5/FRT/TO-N-FLAG-hBirA* (TLK2) using Quick Ligation Kit (NEB). TOP10 competent *E. coli* cells (Invitrogen) were transformed with pcDNA5/FRT/TO-N-Flag-hBirA*-TLK2 vector and carbenicillin selected. The constructs were confirmed by restriction digestion with AscI and NotI-HF (NEB) and sequencing (Macrogen).

AD293 cells were seeded and transfected the next day with either pcDNA5/FRT/TO-N-FLAG-hBirA*-TLK2 or pcDNA5/FRT/TO-N-FLAG-hBirA* using PEI (Polysciences Inc.) ±50 µM biotin (IBIAN Biotechnology; 2-1016-002). For mass spectrometry, 5x15cm plates per condition were harvested 24 h after transfection by scraping cells into PBS, washing two times in PBS and snap freezing on dry ice. Cell pellets were lysed in 5 ml modified RIPA buffer (1% TX-100, 50 mM Tris-HCl pH 7.5, 150 mM NaCl, 1 mM EDTA, 1 mM EGTA, 0.1% SDS, 0.5% sodium deoxycholate and protease inhibitors) on ice, treated with 250 U benzonase (EMD Millipore) and biotinylated proteins were isolated using streptavidin-sepharose beads (GE Healthcare). Proteins were washed in ammonium bicarbonate and digested with trypsin. Mass spectrometry was performed as described previously (Coyaud et al., 2015). Data is presented in Supplementary Table S2.

Generation of *Tlk1* and *Tlk2* deficient mouse models

Mouse embryonic stem (ES) cells containing a retroviral gene-trap cassette inserted between exons 1 and 2 of the *Tlk1* gene were purchased from the German Genetrap Consortium (clone ID E067A02). Cells were checked for a single insertion and injected into 3.5-day old mouse blastocysts derived from C57B6/j mice. Approximately 12-15 ES cells were injected into each blastocyst, and injected blastocysts were re-implanted back into the oviduct of 2.5-day pseudo-pregnant foster mice (CD1s). Chimeras born from these injections were scored for chimerism by coat colour analysis, and the chimeras showing the highest contribution from the ES cells were mated with C57BL/6J wild-type mice. Agouti offspring obtained from these test-matings were screened by PCR for the presence of the *Tlk1* allele. Subsequent pups were screened for the zygosity of the allele (*Tlk1*) by PCR using specific primers or by quantitative real time PCR (Transnetyx). The knockout-first *Tlk2* targeting construct was designed and constructed in the IRB Mutant Mouse facility using standard recombineering methods (Copeland et al., 2001). The targeting vector was

confirmed by sequencing and linearized vector was transfected into ES cells for targeting. Cells were selected with neomycin and digested genomic DNA analysed by Southern blot (performed by service in the Centro Ricerche Biotecnologiche of the Università Cattolica del Sacro Cuore, Milan, Italy) for correct targeting. For Southern analysis, 3 probes were used and correctly targeted clones were injected as described for *Tlk1*. Pgk1-*FlpO* (011065) and Sox2-*Cre* (008454) were purchased from Jackson laboratories (Bar Harbor, ME, USA) and ERT2-*Cre* mice were described previously (Hayashi et al., 2002; Indra et al., 1999; Wu et al., 2009). All animals were maintained in strict accordance with the European Community (86/609/EEC) guidelines at the animal facilities in the Barcelona Science Park (PCB). Protocols (CEAA13/0008) were approved by the Animal Care and Use Committee of the PCB (IACUC; CEEA-PCB) in accordance with applicable legislation (Law 5/1995/GC; Order 214/1997/GC; Law 1201/2005/SG). All efforts were made to minimize use and suffering.

Genomic DNA isolation and genotyping

Genomic DNA was extracted from samples of mouse/embryo tail lysed and digested with Proteinase K (0.4 mg/ml in 10 mM Tris-HCl, 20 mM NaCl, 0.2% SDS, 0.5 mM EDTA) overnight at 56ºC. DNA was recovered by isopropanol precipitation, washed in 70% ethanol, dried and resuspended in 10 mM TE for use in PCR reactions. Genotyping was performed by PCR reactions with Taq polymerase (Biotools) and run for 35 cycles with an annealing temperature of 58ºC. Primers used for mouse genotyping of the different *Tlk1* and *Tlk2* alleles, *Cre*, *FLP* and MMTV-*PyMT* are summarized in Table 5.

TABLE 5. Primers used for mouse genotyping

Mouse allele	Primer ID	Sequence 5'-3'	Fragments	Interpretation
TLK1-wt	TLK1-A02-F	ACTGAGTGTGTTATGCCCTTCGCA	~ 400 bp	Wild type allele
	TLK1-A02-R	GCGTACACATGTGCGTGTGAGTAT		
TLK1-trap	TLK1-A02-F	ACTGAGTGTGTTATGCCCTTCGCA	971 bp	Trap allele
	B32 diagnostic	CAAGGCGATTAAGTTGGGTAACG		
TLK1-cond	TLK1-A02-R	GCGTACACATGTGCGTGTGAGTAT	1770 bp	Conditional allele
	B32 diagnostic	CAAGGCGATTAAGTTGGGTAACG		
TLK2	TLK2-cond1-F	CTCTTAACCACTGAGCCATCTC	~1.3 kbp ~ 1 kbp ~ 450 bp	Conditional allele Wild type allele Knockout allele
	TLK2-cond2-R	CAGGACAGGGAAAGGCTAAA		
FlpO	FlpO-F	GCTATCGAATTCCACCATGGCTCCTAAGAAGAA	1293 bp	Flp allele
	FlpO-R	CAATGCGATGAATTCTCAGATCCGCCTGTTGATGTA		
Cre	Cre-F	GCGGTCTGGCAGTAAAAACTATC	~ 100 bp	Cre allele
	Cre-R	GTGAAACAGCATTGCTGTCACTT		
MMTV-PyMT	MMTV-PyMT TgF	CAACCCGAGTTCTCCAACAGATAC	63 bp	MMTV-PyMT allele
	MMTV-PyMT TgR	AACACAAGGATTTCGTCTTCTTCCA		

Immunohistochemistry (IHC)

Paraffin-embedded tissue sections (3 µm) were air dried and further dried at 60°C overnight. IHC was performed using an Autostainer Plus (Dako-Agilent) or manually (TPBPA). Before IHC, sections were dewaxed using Q6 the low pH EnVision FLEX

Target Retrieval Solutions for caspase-3 detection (Dako, ON, Burlington) at 97°C for 20 min using a PT Link (Dako-Agilent), or dewaxed and rehydrated and thereafter antigen retrieval was performed using a PT link (Dako-Agilent) at 97°C for 20 min with a citrate buffer (pH 6). Quenching of endogenous peroxidase was performed for 10 min with Peroxidase-Blocking Solution (Dako; REAL S2023). Primary antibodies used were as follows: rabbit polyclonal anti-Ki67 (Thermo Fisher Scientific; 1:75), rabbit polyclonal anti-CD31 (Abcam; ab28364; Q7 1:500), mouse monoclonal anti-phospho-histone H2A.X-pSer139 (clone JBW301; Millipore; 05-636; 1:600), rabbit polyclonal anti-cleaved caspase-3 (Asp175) (Cell Signalling; no. 9661; 1:300) and rabbit polyclonal anti-trophoblast-specific protein-α (Abcam; ab104401; 1:1500) were incubated at room temperature for 120 min. BrightVision Poly-HRP-Anti Rabbit IgG Biotin-free (Immunologic; DPVR-110HRP) was used as a secondary antibody. Antigen–antibody complexes were revealed with 3-3′-diaminobenzidine (Dako; K3468), with the same time exposure per antibody (5 min). Sections were counterstained with haematoxylin (Dako; S202084) and mounted with a mounting medium, toluene-free (CS705; Dako), using a Dako Q8 CoverStainer. Specificity of staining was confirmed by omission of the primary antibody. Slides were imaged using an Olympus DP25 camera mounted on a Q9 Olympus BX45 microscope or using a E600 Nikon epifluorescence microscope equipped with a x40 NA 0.75 objective lens and a charge-coupled Olympus DP72 device camera.

Histopathology

Embryos and placentas were harvested and fixed in 4% paraformaldehyde overnight at room temperature. Representative sections were trimmed, processed, embedded in paraffin, blocked, sectioned and stained with H&E and periodic acid/Schiff reagent. Stained slides were examined microscopically, unbiased by two experienced board-certified pathologists (Sameh A Youssef and Alain de Bruin). The different types of trophoblastic cell lineage (i.e. labyrinth trophoblast, syncytiotrophoblast, giant cell trophoblast and trophospongium) were identified based on the characteristic histologic features of every cell. The numbers and/or size of a particular cell from the trophoblastic cell lineage were compared between different genotypes and scored by an ordinal semiquantitative system as described (Gibson-Corley et al., 2013) where normal=no change in the numbers/size from control tissue, mild=decreased between 10 and 25%, moderate=decreased between 25 and 50% and severe=the number and/or size of a particular cell type is decreased more than 50% when compared with control tissue.

Isolation of mouse embryonic fibroblasts (MEFs)

MEF cultures were established from E13.5-14.5 embryos. Embryos were separated from the uterine wall and amniotic sac into fresh PBS. Head and soft tissues were removed from the embryos and the embryonic tissue was placed overnight at 4 °C in 5 ml 0.25% trypsin/EDTA (Life Technologies) solution. Following incubation at 37°C for 20 min, cells

were disaggregated with a serological pipette and supernatant plated for culture in DMEM supplemented with 15% (v/v) FBS (Sigma-Aldrich) and 50 U/mL penicillin/50 µg/ml streptomycin. Primary MEFs were transformed by transfecting a linearized p129 plasmid, containing an origin-less simian virus 40 (SV40) genome, using an Amaxa nucleofector with MEF reagent 2 (Amaxa). Transformed MEFs were maintained in DMEM supplemented with 10% (v/v) FBS and penicillin–streptomycin. For the induction of Cre recombinase in ERT2-Cre-expressing cell lines, cells were exposed to 4-hydroxytamoxifen (4OHT) (Sigma-Aldrich; H7904; 1 µM) for 72 h, washed and plated for experiments.

Protein extraction from mouse tissue for Western blotting

Dissected tissues were collected on ice, washed in PBS and resuspended in TNG-150 buffer (50 mM Tris-HCl, 150 mM NaCl, 1% Tween-20, 0.5% NP-40, 1x protease (Roche) and phosphatase inhibitors (Sigma-Aldrich)). Tissues were disrupted by zirconium beads in a mechanical tissue disruptor (Precellys 24; Bertin Technologies). Protein concentration was quantified using the DC Protein Assay (Bio-Rad), separated by SDS-PAGE and transferred to PVDF membrane (Immobilon-P, Merck). Membranes blocked with 5% milk/PBST for 1 h at room temperature and probed with primary antibodies (Table 13) overnight at 4°C. These were detected with appropriate secondary antibodies conjugated to HRP and visualized by ECL-Plus (GE Healthcare).

Endogenous co-Immunoprecipitation (co-IP) from mouse placentas

Dissected placentas were collected on ice and disrupted in Extraction Buffer (300 mM NaCl, 0.5% NP-40, 50 mM Tris-HCl pH 7.8, 0.2 mM EDTA, 5% glycerol, 1x protease (Roche) and phosphatase inhibitors (Sigma-Aldrich)) by zirconium beads in a mechanical tissue disruptor (Precellys 24; Bertin Technologies). After two centrifugation steps (10 min, max speed, 4°C and 5 min, max speed, 4°C), supernatants were collected, precleared and immunoprecipitated (overnight, 4°C, on rotation) with 10 µg of anti-TLK2 antibody (Bethyl Laboratories; A301-257A), 10 µl of polyclonal ASF1 serum (generated in the Groth Laboratory (Groth et al., 2005)) or 10 µg of rabbit IgG (Sigma-Aldrich) bound to 50 µl of Dynabeads Protein G (Invitrogen). Beads were washed five times with cold Wash Buffer (150 mM NaCl, 0.2% NP-40, 50 mM Tris-HCl pH 7.8, 0.2 mM EDTA, 5% glycerol, 1x protease (Roche) and phosphatase inhibitors (Sigma-Aldrich)), resuspended in 30 µl of Laemmli sample buffer and boiled for 20 min.

Isolation of RNA and quantitative real time PCR (qRT-PCR)

Dissected tissues were collected on ice, washed in PBS and snap frozen on dry ice. Tissues were disrupted in Tri-Reagent (Sigma-Aldrich) by zirconium beads in a mechanical tissue disruptor (Precellys 24; Bertin Technologies). Transformed MEFs or human cancer cell lines were collected after two cold PBS washes by scraping in Tri-Reagent. RNA was

isolated by chloroform extraction followed by centrifugation, isopropanol precipitation, washing two times in 75% ethanol and resuspension in DEPC-treated water. Nucleic acid quantification was performed with a Nanodrop 8000 Instrument (Thermo Fisher Scientific). Reverse transcription reaction for murine samples was carried out using High Capacity RNA-to-cDNA Kit (ABI), following the manufacturer's instructions, in a reaction volume of 20 µl and with the primers contained in the 2X RT buffer mix, which is composed of dNTPs, random octamers, and oligo$(dT)_{16}$. Reverse transcription reaction for human cancer cell lines was carried out using High Capacity cDNA Reverse Transcription Kit (ABI), following the manufacturer's instructions, in a reaction volume of 20 µl and with the primers contained in the kit, which are Random Primers. cDNA was stored at −20°C. For the detection on Telomeric repeat-containing RNA (TERRA), a first strand cDNA synthesis was first performed with the TERRA-specific RT-primer 5'-CCCTAACCCTAACCCTAACCCTAACCCTAA-3' (Feretzaki and Lingner, 2017) and a housekeeping gene-specific primer (Reverse) was included in the same reaction for normalization purposes. The reaction was carried out at 55ºC in the presence of RNA inhibitor SUPERase IN (Thermo Fisher Scientific) using the SuperScript III RT (Thermo Fisher Scientific). qPCR was performed using the comparative CT method and a Step-One-Plus Real-Time PCR Instrument (Applied Biosystems). SYBR Green and TaqMan reactions were carried out in technical duplicate or triplicate in a final volume of 10 µl. For SYBR Green 1X SYBR Green PCR Master Mix (no. 4364344; ABI) or 1X SYBR Select Master Mix (no. 4472908; ABI), forward and reverse primer (Sigma-Aldrich; 100-500 nM each) and 25 ng of template were used. For TaqMan reactions 1X TaqMan Universal PCR Master Mix (no. 4324018; ABI), 0.5 µl of probe and 25 ng of template were used. Thermocycling parameters used for SYBR Green reactions were: 95°C 20 s; 40 cycles 95°C 3 s, 60°C 30 s; melting curve and for TaqMan reactions were: 95°C 20 s; 40 cycles 95°C 1 s, 60°C 20 s. For TaqMan assays in mouse samples, *mACTB* probe was used as an endogenous control for normalization and for SYBR Green assays in mouse samples; primers for *18S* were used as endogenous controls for normalization. The 2−ddCT method was used for the analysis of the amplification products. Primer pairs used are indicated in Table 6. Mouse data are presented as the means±SD of at least three experiments, with at least three animals within each experimental group. Human cell line data are presented as the means±SEM of at least two independent experiments; exact N for each experiment is indicated in the figure legends. Statistical significance was determined using an unpaired t-test (****P <0.0001, ***P <0.001, **P <0.01, *P<0.05, NS=non-significant).

TABLE 6. Primer pairs used for qRT-PCR and TaqMan probe IDs.

Mouse primer target (SYBR Green)	Forward 5'-3'	Reverse 5'-3'	Reference (where relevant)
Igf2	GTGGCATCGTGGAAGAGTGC	GGGGTGGGTAAGGAGAAACC	(Zhu et al., 2011)
H19	AAGGTGAAGCTGAAAGAACAG	ATGGACGACAGGTGGGTACTG	
18S	ATGGTAGTCGCCGTGCCTAC	CCGGAATCGAACCCTGATT	

Mouse primer target (SYBR Green)	Forward 5'-3'	Reverse 5'-3'	Reference (where relevant)
Peg10	CATAGCTCGGACAAACAGGG	CAGAACGAATAAGGTCCCCA	(Cui et al., 2007)
Grb10	ATCTTCCGTTTCCCATTTCC	CTCCTTACCTCCTCCTCCGA	
Phlda2	TCCTGGGCTCCTGTCTGAT	CTGAAATGCCTTCCGAGC	
Cdx2	AGTGAAAACCAGGACAAAAG	ACCAAATTTTAACCTGCCTC	
Prl3d1 (Pl1)	CAATATACAACAGGACTCAGG	ATGGATGTCCCTTTTAATGC	
Prl3b1 (Pl2)	TATTCAATAGGGTTTACCCAGG	GACCTTGAGGTAATTGTCAAC	
Tpbpa	GACTACTGTTTTACACCCAATG	ATGTTACTGTGGCTGATTTG	
Cxcl15 (IL-8)	CGGCAATGAAGCTTCTGTAT	CCTTGAAACTCTTTGCCTCA	
Human primer target (SYBR Green)	**Forward 5'-3'**	**Reverse 5'-3'**	**Reference (where relevant)**
Satα	TAGACAGAAGCATTCTCAGAAACT	TCCCGCTTCCAACGAAATCCTCCAAAC	(Corpet et al., 2014)
Satellite 2	TCGCATAGAATCGAATGGAA	GCATTCGAGTCCGTGGA	(Ohzeki et al., 2012)
5S rDNA	ACGCTGGGTTCCCTGCCGTT	TGGCTGGCGTCTGTGGCACCCGCT	
Alu	GGCCGGGCGGTGGCTC	GAGACCGAGTCTCGCTCTGTC	
17 alphoid	CAACTCCCAGAGTTTCACATTGC	GGAAACTGCTCTTTGAAAAGGAACC	
HERV-H	CACGTTTTATCCGTGGACCC	AGGCATCCCTGCAATGATTAA	(Filipponi et al., 2013)
HERV-K	GAGAGCCTCCCACAGTTGAG	TTTGCCAGAATCTCCCAATC	(Izquierdo-Bouldstridge et al., 2017)
MER21C	GGAGCTTCCTGATTGGCAGA	ATGTAGGGTGGCAAGCACTG	
MLT1C49	TATTGCCGTACTGTGGGCTG	TGGAACAGAGCCCTTCCTTG	
MLT1J2	CCTGGGTCCCTGAGTCACTA	TGCCAGCTGCTGTAACAAAC	
MAVs	GGAGCAGCAGAAATGAGGAG	AAGGCCCCTATTCTCAGAGC	
MDA5	TCTGGGGCATGGAGAATAA	AAGGCCTGAGCTGGAGTTCT	
STING	CAGGCACTGAACATCCTCCT	GTTATCAGGCACCCCACAGT	
DDX60	AAGGTGTTCCTTGATGATCTCC	TGACAATGGGAGTTGATATTCC	
IFIT2	ACGGTATGCTTGGAACGATTG	AACCCAGAGTGTGGCTGATG	
IFI6	CTGTGCCCATCTATCAGCAG	GGGCTCCGTCACTAGACCTT	
TLR3	TCACTTGCTCATTCTCCCTT	GACCTCTCCATTCCTGGC	
OASL	GGGACAGAGATGGCACTGAT	AAATGCTCCTGCCTCAGAAA	
RSAD2	GTGAGCAATGGAAGCCTGAT	TCCCTACACCACCTCCTCAG	
ISG15	TGTCGGTGTCAGAGCTGAAG	GCCCTTGTTATTCCTCACCA	
15q TERRA	CAGCGAGATTCTCCCAAGCTAAG	AACCCTAACCACATGAGCAACG	(Arnoult et al., 2012)
hB-actin	TGTACGCCAACACAGTGCTG	GCTGGAAGGTGGACAGCGA	
hGAPDH	AGCCACATCGCTCAGACAC	GCCCAATACGACCAAATCC	
TaqMan		**Probe ID**	
mTlk1		Mm01328995_m1	
mTlk2		Mm01246220_m1	
mACTB		Mm00607939_s1	
hTLK1		Hs00367007_m1	
hTLK2		Hs00736802_m1	
hACTB		Hs99999903_m1	

Human cancer cell lines culture, DNA damaging agents and drug treatments

Human cancer cell lines summarized in Table 7 were grown in the indicated media (Thermo Fisher Scientific) supplemented with 10% FBS (Sigma-Aldrich) and penicillin–streptomycin at 37°C in a 5% CO_2 incubator. For 3T3 proliferation assays, cells were seeded every three days at the density of 3 x 10^5 cells per 6 cm plate. Total number of cells was counted at each passage and cumulative cell numbers were plotted ($Cells_{D2}$ x $TotalCells_{D1}$ / Cells seeded). HeLa long-telomere (LT) cells were a kind gift from J. Jacobs; GM847 cells, from J. Lingner; Saos-2 and BT-20, from K. Slobodnyuk (A. Nebreda laboratory); T-47D cells, from M. Guiu (R. Gomis laboratory); A549, NCI-H1395 and

NCI-H226, from J. Biayna (F. Supek laboratory); ACHN and 786-O, from C. Jeronimo; PLC/PRF/5, Hep G2 and SNU-449, from S. Ivanova (A. Zorzano laboratory).

For drug treatment, we used: Roscovitine (Sigma-Aldrich), 50 μM for 2 hours; Nocodazole (Sigma-Aldrich), 40 ng/ml for 10 hours; UCN-01 (Sigma-Aldrich), 0.3 μM for 2 hours; Chk1 inhibitor AZD7762 (Selleck Chemicals), 100 nM for 24 hours; PARP inhibitor Olaparib (Selleck Chemicals), 1 μM for 24 hours; ATR inhibitor ETP-46464 (Calbiochem), 5 μM for 24 hours.

TABLE 7. Established human cell lines used in this study.

Cell line	Tissue of origin	Cancer type	Culture conditions	Notes
U-2-OS	Bone	Osteosarcoma	DMEM	ALT+
HeLa LT	Cervix	Cervical adenocarcinoma	DMEM	derived from HeLa 1.2.11
GM847	Skin fibroblast	SV40 transformed from Lesch-Nyhan syndrome patient	DMEM	ALT+
Saos-2	Bone	Osteosarcoma	RPMI-1640	ALT+
MDA-MB-231	Breast	Adenocarcinoma TNBC	DMEM	
T-47D	Breast	Ductal carcinoma ER+ PR+	DMEM	
BT-20	Breast	Carcinoma TNBC	MEM	
A549	Lung	Carcinoma	DMEM	
NCI-H1395	Lung	Adenocarcinoma, stage 2	RPMI-1640	
NCI-H226	Lung	Squamous cell carcinoma, mesothelioma	RPMI-1640	
SW48	Colon	Colorectal adenocarcinoma, Dukes' type C, grade IV	DMEM	Ras WT, Braf WT
HT-29	Colon	Colorectal adenocarcinoma	DMEM	Ras WT, Braf mut
SW480	Colon	Colorectal adenocarcinoma, Dukes' type B	DMEM	Ras mut, Braf WT
ACHN	Kidney	Renal cell adenocarcinoma	MEM	
786-O	Kidney	Renal cell adenocarcinoma	RPMI-1640	
PLC/PRF/5	Liver	Hepatoma	DMEM	p53 deleted
Hep G2	Liver	Hepatocellular carcinoma	MEM + NEA	p53 mut
SNU-449	Liver	Hepatocellular carcinoma grade II-III/IV	RPMI-1640 + NEA	p53 WT

Clonogenic survival assay

For colony formation assays, MEFs and PyMT cells were seeded in duplicate on 6 cm plates and the number of seeded cells was adjusted to the plating efficiency. Cells were incubated at 37°C for 10–14 days and colonies stained with crystal violet (Sigma-Aldrich) and counted using ImageJ-plugin Trainable Weka Segmentation.

For sensitivity assays and colony formation assays, siRNA-transfected MDA-MB-231 and U-2-OS cells were seeded on 6 cm plates in technical duplicates. The number of the seeded cells was adjusted according to the plating efficiency. After 24 hours of plating, cells were treated with the indicated drugs for 24 hours and then washed and grown in fresh medium or kept in the drug media for the whole assay period in the case of Olaparib. Cells were incubated at 37ºC for 10-14 days. The colonies were stained with crystal violet (Sigma-Aldrich) and counted using an in-house built ImageJ macro using the Trainable Weka Segmentation plugin. Based on the colony number, plating efficiency (PE=number of colonies formed/number of cells seeded) and surviving fraction (SF=number of colonies formed after siRNA treatment/number of cells seeded x PE) were calculated and plotted.

Metaphase spreads

For metaphase spread preparations of MEFs, cells were treated for 2 h with 0.1 µg/ml colcemid (Demecolcine, Sigma-Aldrich). Cells were subsequently harvested by trypsinization, hypotonically swollen in prewarmed 0.075 M KCl for 20 min at 37°C and fixed (75% MeOH and 25% glacial acetic acid, ice cold). Metaphase preparations were spread on glass slides, placed for 5 minutes on a humidified 80°C heating block, dried and stained with DAPI in Vectashield mounting medium. Images were taken using a Leica DM6000 microscope and analysed using the Fiji Software.

Total denaturing protein extraction and Western blotting

Transformed MEFs or human cancer cell lines were collected after two cold PBS washes by scraping in 2X SDS Lysis Buffer (4% SDS, 20% Glycerol, 120mM Tris-HCl pH 6.8, 1x protease (Roche) and phosphatase inhibitors (Sigma-Aldrich)) on ice. Lysates were sonicated at medium-high intensity for 10 minutes in a Bioruptor Standard (Diagenode) placed at 4ºC and subsequently boiled for 10 minutes at 90ºC. Proteins were quantified using the DC Protein Assay (Bio-Rad), separated by SDS-PAGE and transferred to 0.2 µm pore Nitrocellulose membrane (Amersham Protran; Sigma-Aldrich). Membranes were blocked with 5% milk/PBST for 1 h at room temperature and probed with primary antibodies (Table 13) overnight at 4ºC. These were detected with appropriate secondary antibodies conjugated to HRP and visualized by ECL-Plus (GE Healthcare).

Lentiviral and retroviral stable cell lines

For retroviral transductions, AD293 producer cells were seeded at 3 x 10^6 cells per 10 cm dish and transfected using PEI (Polysciences Inc.) with 10 µg of vector of interest and with retroviral packaging vectors (1 µg VSV-G and 9 µg Gag-Pol). Medium was refreshed 8 h after transfection and viral supernatants were collected and filtered through a 0.45 µm filter at approximately 48 and 72 h post-transfection. For infection, cells were overlaid with filtered viral supernatant supplemented with 8 µg/ml Polybrene (Sigma-Aldrich) twice to achieve optimal infection efficiency. SNAP-Tag Histone cell lines were generated by retroviral transduction of U-2-OS cells using pBABE-Blast constructs containing H3.1, H3.3 and H4-SNAP-3XHA (kind gift from Lars Jansen (Bodor et al., 2013)). Selection with 2.5 µg/ml blasticidin was added 24 hours post-infection. U-2-OS cells transduced with pLPC-HA-HIRA were selected with 2 µg/ml of puromycin.

For lentiviral transductions, AD293 producer cells were seeded at 3 x 10^6 cells per 10 cm dish and transfected using PEI (Polysciences Inc.) with 10 µg of vector of interest and with lentiviral packaging vectors (2 µg REV, 6 µg RRE and 2 µg VSV-G). Medium was refreshed 8 h after transfection and viral supernatants were collected and filtered through a 0.45 µm filter at approximately 48 and 72 h post-transfection. For infection, cells were overlaid with filtered viral supernatant supplemented with 8 µg/ml Polybrene (Sigma-

Aldrich) twice to achieve optimal infection efficiency. For complementation experiments, U-2-OS cells were transduced with pLenti6/UbC/V5-Dest (Invitrogen) carrying TLK2 wild-type or kinase-dead mutant (D591A) resistant to siTLK2#1. Selection with 5 µg/ml blasticidin was added 24 hours post-infection. For stable shRNA knockdown, cells were transduced with the pLKO.1-puro shRNAs from the Sigma-TRC library and selected with 1-5 µg/ml of puromycin.

Cloning of CRISPR constructs

The plasmid pX330-CRISPR-Cas9-SV40prom-EGFP containing two expression cassettes, hSpCas9 and the chimeric guide RNA (a kind gift from C. Cortina (Cong et al., 2013)), was digested using BbsI (NEB) and gel purified. Guide RNA sequences were designed using the Zhang lab CRISPR design tool (http://crispr.mit.edu/) based on the target site sequence (20 bp) and flanked on the 3' end by a 3 bp NGG PAM sequence, so they could be cloned into the guide RNA already containing in the backbone a longer fragment of the tracrRNA (+85nt). Oligo pairs used are listed in Table 8. Oligonucleotides (Sigma-Aldrich) were phosphorylated with T4 PNK (NEB) and annealed in a thermocycler ramp down reaction. 50 ng of BbsI digested plasmid and 1 µl of annealed oligo duplex (80 nM) were ligated using the Quick Ligation Kit (NEB). All constructs were verified by DNA sequencing (Macrogen) using the primer U6 gRNA insert Seq F: 5'-ACTATCATATGCTTACCGTAAC-3'.

TABLE 8. CRISPR sgRNA oligonucleotides.

Target	Guide	Exon	Forward 5'-3'	Reverse 5'-3'
hTLK1	g#1 (H3-G1)	exon 10	CACCGTGCAAGATCGATTACGCCTC	AAAACGAGGCGTAATCGATCTTGCA
hTLK1	g#2 (H3-G2)	exon 10	CACCGTAACTGTTGTAAAGTGCCCG	AAAACCGGGCACTTTACAACAGTTA
hTLK2	g#4 (H2-G4)	exon 7	CACCGAGGGGCTGTTCTACTCGTCG	AAAACCGACGAGTAGAACAGCCCCT
hTLK2	GPP-g3	exon 4	CACCGAACCATATGAAACTAGCCA	AAACTGGCTAGTTTCATATGGTTC
hTLK2	GPP-g4	exon 11	CACCGAGCCTCATTTACTGAACAG	AAACCTGTTCAGTAAATGAGGCTC

Generation of CRISPR knockout cell lines

Knockout MDA-MB-231, U-2-OS and HeLa LT cell lines were generated using CRISPR/Cas9 genome editing. Cells were transfected using Lipofectamine 2000 (Thermo Fisher Scientific) with the corresponding pX330-CRISPR-Cas9-SV40prom-EGFP plasmids and 48 hours following transfection, single cells positive for GFP were FACS-sorted (BD FACSAria III) at a ratio of 1 cell per well in 96 well plates. For WT single cell clones, these were exposed to pX330-CRISPR-Cas9-SV40prom-EGFP without any targeting sequence cloned. Single cell clones were expanded and screened by Western blot for protein levels of TLK1 and TLK2.

Immunofluorescence (IF) and high-throughput microscopy (HTM)

For IF of chromatin-bound proteins, cells were grown on 8-well Lab Tek II chamber slides (Labclinics) to sub-confluence. For regular IF, cells were grown on Poly-L-Lysine coated

coverslips. For chromatin-bound proteins, pre-extraction was performed using cold 0.2% Triton X-100 in 1X PBS on ice for 5 minutes. Cells were fixed for 10 minutes in 4% paraformaldehyde at room temperature and permeabilised for 5 minutes in 0.2% Triton in 1X PBS at room temperature. After two washes in PBS, fixed cells were incubated for 1 h in blocking solution (3% BSA 0.1%Tween/PBS) and stained using the primary antibodies indicated in Table 13 diluted in blocking solution for 4 h at room temperature in a humid chamber. The secondary antibodies used were Alexa Fluor 488 (goat anti-rabbit IgG), Alexa Fluor 488 (goat anti-mouse IgG), Alexa Fluor 568 (goat anti-rabbit IgG), and Alexa Fluor 568 (goat anti-mouse IgG) from Thermo Fisher Scientific, and were used at a dilution of 1:500 in blocking solution. After primary and secondary antibody incubations, washes were performed with blocking solution. The last wash before mounting contained DAPI. Slides were air-dried, mounted in Vectashield (Vector Labs), sealed and stored in a cold dark chamber.

Confocal fluorescence images were obtained on a Leica DM2500 SPE confocal system. Images were taken with 40x NA 1.15 oil or 63x NA 1.3 oil objectives and the standard LAS-AF software. Possible crosstalk between fluorochromes was avoided by carefully adjusting laser intensities and HyD gain, thus avoiding false-positive colocalization signals.

For high-throughput microscopy (HTM), 24-48 images were automatically acquired from each well with a robotized fluorescence microscopy station (ScanR; Olympus) at 40× magnification and non-saturating conditions. Images were segmented using the DAPI staining to generate masks matching cell nuclei from which the corresponding signals were calculated using an in-house–developed package based on Cell Profiler. CellProfiler (www.cellprofiler.org), an open source software program, was used to develop a custom and automated approach to image analysis workflow. In collaboration with the Advanced Digital Microscopy Facility at IRB Barcelona, we developed a pipeline to load the stack of 8-bit images with 3 channels, generate nuclear masks with the DAPI channel and measure mean intensity of the two additional channels. Nuclei had a typical diameter of 60-150 pixel units, and background fluorescence in DAPI images below an absolute threshold of 0.20-0.35 was set to 0. These results were exported to Excel for further analysis and GraphPad-Prism was used for graphical representation.

EdU staining was performed by the laboratory of Prof. Dr. Anja Groth using Click-iT™ EdU Alexa Fluor 488/647 High-Throughput Imaging Assay kit (Thermo Fisher Scientific) according to the manufacturer's instructions. In brief, cells were labelled with 40 μM of 5-ethynyl-2'-deoxyuridine (EdU) for 15 min, pre-extracted, fixed and imaged. The treatment of cold methanol at -20°C for 15 min was used for antigen retrieval of endogenous PCNA. Images were collected using a DeltaVision system (Applied Precision) with UApo/340 40x/1.35 NA oil objective lens or ScanR system with UPlanSApo 20x/0.75 NA objective lens. All images in the individual panels were acquired under room temperature with the same settings and adjusted for brightness and contrast identically using Adobe Photoshop CS6. Analysis was done with SoftWoRx software (Applied Precision), Volocity image analysis software (Perkin Elmer) or ScanR analysis software.

SNAP-tag Histone based Pulse-Chase imaging

We used two SNAP-labelling strategies: quench-chase-pulse and pulse-chase, which allow for the analysis of new and old histone pools, respectively. Cells were plated in Lab Tek II Chamber slides (Labclinics) 24 hours post-siRNA transfection. SNAP-labelling was initiated 48 hours post-transfection (24 h after plating). For quench-chase-pulse experiments, cells were incubated with 5 µM SNAP-Cell Block (S9106S, NEB) for 30 min at 37ºC. After 2 PBS washes, cells were incubated in media for 30 min at 37ºC, followed by 2 extra PBS washes. Cells were incubated in media for the chase period (6-7 hours). After chase period for quench-chase-pulse experiments or for pulse-chase experiments, cells were incubated with 1 µM TMR-Star (S9105S, NEB) for 30 min at 37ºC. After 2 PBS washes, cells were incubated in media for 30 min at 37ºC, followed by 2 extra PBS washes, and proceeded to pre-extraction for 5 min in 0,2% Triton/PBS on ice and fixation for 10 min in 4% PFA at room temperature. Cells were analysed with standard immunofluorescence techniques by HTM (see above).

BrdU labelling for G1/S checkpoint assay by flow cytometry

For BrdU labelling, cells were plated 24 hours (U-2-OS) or 48 hours (MDA-MB-231) post siRNA transfection. 24 hours after plating, cells were pulsed with 10 µM BrdU for 20 min (transformed MEFs), 30 min-1 hour (U-2-OS) or 4 hours (MDA-MB-231) and cells were trypsinized and fixed overnight in ice-cold 70% ethanol. DNA was denatured by 0.1M HCl and then incubated at 100 ºC. S-phase cells were stained using the BD Pharmigen FITC Mouse Anti- BrdU Set antibody (BD Biosciences). Cells were resuspended in 400 µl PBS containing 25 µg/ml propidium iodide (PI) and 0.1 mg/ml RNaseA and subjected to FACS analysis in a Gallios Flow Cytometer (Beckman Coulter). The percentage of BrdU-positive cells and the cell cycle based on PI content was analysed with FlowJo software (Version 10.0.8).

Small interfering RNA (siRNA)-mediated knockdown

For siRNA transfection, cells were transfected with siRNAs at a final concentration of 100 nM (Sigma-Aldrich) using Lipofectamine RNAiMAX (Thermo Fisher Scientific). Transfections were done on attached cells that had been plated for approximately 18 hours, in media without antibiotics and the transfection mix was prepared in Opti-MEM (Thermo Fisher Scientific). Cells were transfected once and either split for several experiments after 24 hours and harvested after additional 24-48 hours or directly harvested 48 hours post-transfection. We used luciferase and GFP targeting as mock negative controls (see siGL2 and siGFP in Table 9). The sequences of the forward siRNAs are provided in Table 9. We used single siRNAs against the indicated target genes except for FLASH, ATRX and H3.3 genes where a pool of two siRNAs (siFLASH #1&#2, siATRX #1&#2 and siH3.3 #A&#B) was used to achieve optimal depletion.

TABLE 9. siRNA sequences used in this study.

siRNA ID (target)	siRNA sequence (5'-3') + [dT][dT]	Reference
siGFP	GGCUACGUCCAGGAGCGCCGCACC	(Rein et al., 2015)
siGL2	CGUACGCGGAAUACUUCGA	V. Constanzo lab
siTLK1 #1	GAAGCUCGGUCUAUUGUAA	
siTLK1 #2	GCAAUGACUUGGAUUUCUA	
siTLK1	#11: GAGUAUGCAAGAUCGAUUA #12: GAAGCUCGGUCUAUUGUAA #13: GCAAUGACUUGGAUUUCUA #14: GUUCAAAGAUCACCCAACA	Dharmacon ON-TARGET plus SMARTpool
siTLK2 #1	GGAGGGAAGAAUAGAUGAU	
siTLK2 #2	GGAAAGGAUAAAUUCACAG	
siTLK2	#7: AAGAUGGCGUGUAGAGAUA #8: UUACAAGGCAUUUGAUCUA #9: GAUAGAAAGACAACGGAAA #10: CCUCAAACCAGGUAAUAUU	Dharmacon ON-TARGET plus SMARTpool
siASF1a	AAGUGAAGAAUACGAUCAAGU	
siASF1b	AACAACGAGUACCUCAACCCU	
siFLASH #1	CCGCAAGGAUGAAGAAAUA	(Mejlvang et al., 2014)
siFLASH #2	AGAUAAAGACAGUAGGAAA	
sip53	GCAGUCAGAUCCUAGCGUC	
siDAXX #1	GGAGUUGGAUCUCUCAGAA	(Corpet et al., 2014)
siDAXX #2	CAGCCAAGCUCUAUGUCUA	
siATRX #1	GAGGAAACCUUCAAUUGUA	
siATRX #2	GCAGAGAAAUUCCUAAAGA	
siHIRA	GGAUAACACUGUCGUCAUC	
siH3.3 #A	CUACAAAAGCCGCUCGCAA	
siH3.3 #B	GCUAAGAGAGUCACCAUCA	

Statistical analysis of TCGA datasets

The results presented are in part based upon data generated by the TCGA Research Network (http://cancergenome.nih.gov/). TCGA data available as in February 2017 was downloaded from the cbioportal (Cerami et al., 2012) using the R programming language package "cgdsr" (http://www.R-project.org). GISTIC calls were used to estimate copy number variation and expression matrices from RNA-Seq z-scores were used for all available datasets. Mutation information was downloaded from the same portal. A gene was considered amplified if the GISTIC call was larger than 0. Mutual exclusivity of amplifications between gene pairs was computed using the Fisher's exact test. For each gene pair and dataset Pearson correlation coefficients and p-values of expression were computed using the function cor.test. Association of expression and survival was performed using the "survival" package in R (https://CRAN.R-project.org/package=survival). For the univariate analysis p-values were computed using no covariates and expression as a continuous variable through the coxph function. Groups of samples for Kaplan-Meier plots were divided by the median expression. For multivariate analyses the clinical variables gender, stage, age and proliferation (Ki67 expression terciles) were taken into account except for those datasets where only female samples were present.

The Molecular Taxonomy of Breast Cancer International Consortium (METABRIC) dataset (Curtis et al., 2012) was downloaded from the cbioportal (http://www.cbioportal.org/) for the genes of interest. Z-scores matrices were taken for expression analyses and clinical variables including the PAM50 classification were used as annotated in the clinical information associated with this dataset. The association of gene expression and disease-free survival was computed on ER+ samples with no therapy and considering cohort, age and PAM50 subtype as covariates. All routines were implemented in R.

Analysis of DSB repair pathways by I-SceI induced break reporters

U-2-OS cells bearing a single-copy integration of the reporters DR-GFP (Gene conversion) (Pierce et al., 1999), SA-GFP (Single strand annealing), EJ5-GFP (canonical NHEJ) or EJ2-GFP (alt-NHEJ) (Bennardo et al., 2008) were used to analyse the different DSB repair pathways. In all cases, 100 000 cells were plated in 12-well plates. One day after seeding, cells were co-transfected using Lipofectamine 2000 (Thermo Fisher Scientific) with the indicated siRNA and with constructs coding for I-SceI (0.8 µg of pCBA-SceI) and mCherry (0.4 µg pCAGGS-mCherry). The medium was changed after 6-8 h. After transfection, cells were maintained for 72 h and then trypsinized and fixed with 2-4% paraformaldehyde. The percentage of fluorescent cells was measured by flow cytometry in technical duplicate in a CytoFLEX platform (Beckman Coulter) and analysed by FlowJo software. The repair frequency was calculated as the percentage of green cells expressing GFP from the mCherry+ cell population that had been transfected. To facilitate the comparison between experiments, the GFP/mCherry ratio was set to 1 for the siRNA control condition in all the independent experiments.

RNA-Seq

U-2-OS cells were transfected in biological duplicate with siRNAs (siGFP, siTLK1, siTLK2, siTLK1+2) and 48 hours post-transfection were washed twice with cold PBS and collected by scraping in Tri-Reagent (Sigma-Aldrich). RNA was isolated using the PureLink RNA Mini Kit (Thermo Fisher Scientific) following the manufacturer's instructions for TRIzol Plus Total Transcriptome Isolation. Briefly, chloroform extraction followed by centrifugation resulted in a colourless upper aqueous phase that was mixed 1:1 with 100% ethanol. Sample containing RNA in 50% ethanol was bound to the spin cartridge, washed twice with Wash Buffer II and eluted in RNase-free water.

To avoid limiting our analysis in mRNA polyA+, we performed enrichment of whole transcriptome RNA by depleting ribosomal RNA (rRNA) species. Purified RNA samples were first quantified for integrity, size and purity by a 2100 Bioanalyzer Instrument (Agilent) and a RNA 6000 Nano Chip (Integrated Sciences). 2 µg of total RNA were processed for rRNA depletion by Ribozero Gold rRNA Removal kit (Human/Mouse/Rat) (Illumina) following manufacturer's instructions. rRNA-free RNA was subsequently fragmented and cDNA generated by NEBNext RNA First Strand Synthesis Module (NEB) and NEBNext mRNA Second Strand Synthesis Module (NEB). Resulting cDNA was purified, quantified and used for library generation for Next Generation Sequencing using the NEBNext Ultra II DNA library prep for Illumina (NEB). Each of the libraries was labelled by a specific barcode provided in NEBNext Multiplex Oligos for Illumina (Index Primers Set 1) (NEB) and amplified 7 cycles by PCR in the presence of SYBR Green in order to obtain an optimal yield. Libraries were quantified using DNA HS Qubit (Thermo Fisher Scientific) and size measured by a 2100 Bioanalyzer Instrument (Agilent) and a DNA HS Chip (Integrated Sciences). An equimolar pool was generated with the

eight libraries and the pool was sequenced in 2 lanes 50 nt single read in an Illumina HiSeq2500 (Illumina).

Single end reads of length 50 bp were aligned to the human genome version hg19 using bowtie v0.12.9 (Langmead et al., 2009) with default parameters. Alignments were sorted and indexed using Sambamba v0.5.8 (http://lomereiter.github.io/sambamba/). Gene differential expression was performed using DESeq2 (Love et al., 2014) with replicates as covariate. Pathway enrichment was assessed through the preranked version of Geneset Enrichment Analysis (GSEA) (Subramanian et al., 2005). GSEA was applied to the ranking defined by the log2 Fold Change of the differential expression analysis using DESeq2. Genesets for analyses were from the Gene Ontology (GO) terms (Ashburner et al., 2000) as collected in the GSEABase R package (version 1.40.1), or from the Hallmark collection (Liberzon et al., 2015) after retrieval from the MsigDB (Liberzon et al., 2011). Classification in coding and non-coding gene classes was performed according to the Gencode annotation version 19 (Harrow et al., 2012). For Repeat Masker analysis, sequences from repeat elements in the human Repbase database version 22.06 (Bao et al., 2015) were downloaded. Reads were aligned using bowtie with parameters --best and -k=1. Fold changes were computed between siTLK1+2 and siCont samples using normalised reads values of those repeat sequences that had at least 100 raw reads.

Assay for Transposase-Accessible Chromatin (ATAC)

The ATAC protocol was adapted from Buenrostro et al, 2015. U-2-OS or HeLa LT cells were transfected in biological duplicate with siRNAs (siGFP, siTLK1, siTLK2, siTLK1+2 for U-2-OS, and siGFP, siTLK1+2 for HeLa LT) and 48 hours post-transfection were collected by trypsinization and counted. 50 000 cells for U-2-OS or 75 000 cells for HeLa LT were resuspended in 50 µl of cold lysis buffer (10 mM Tris-HCl, pH 7.4, 10 mM NaCl, 3 mM $MgCl_2$, 0.1% (v/v) Igepal CA-630) for nuclei preparation and treated with Nextera Tn5 Transposase (Nextera DNA Library Preparation Kit, Illumina) at 37°C for 30 min. DNA was first purified using MinElute PCR Purification Kit (Qiagen). Samples were amplified by PCR using NEBNext High-Fidelity 2x PCR Master Mix (NEB) using PCR primers Ad1_noMX and Ad2_Barcode (Sigma-Aldrich, see Table 10, (Buenrostro et al., 2013)) for 5 initial cycles (1 cycle: 5 min 72°C, 30 sec 98°C; 5 cycles: 10 sec 98°C, 30 sec 63°C, 1 min 72°C). A qPCR side reaction was run on a tenth of the previous 5-cycle sample in order to determine the appropriate number of PCR cycles (N) and be able to stop amplification prior to saturation, in the presence of SYBR Green in an Applied Biosystems 7900HT Fast Real-Time PCR System (1 cycle: 30 sec 98°C; 20 cycles: 10 sec 98°C, 30 sec 63°C, 1 min 72°C). Then, the 5-cycle sample was run for an additional N=6 cycles, so the library had been amplified for a total of 11 cycles. Amplified libraries were purified using PureLink PCR Purification Kit (Thermo Fisher Scientific). The quality of purified libraries was assessed using a Bioanalyzer High-Sensitivity DNA Analysis kit (Agilent). For ATAC-seq, an equimolar pool was generated with the eight libraries of

U-2-OS biological replicates and the pool was sequenced in 2 lanes 50 nt paired-end in an Illumina HiSeq2500 (Illumina). ATAC-qPCR was performed with the same primers as in the ChIP-qPCR experiments (Table 11) on a 1:20 dilution of the eluted DNA after library amplification.

TABLE 10. Primers used for ATAC library amplification.

Primer ID	Sequence 5'-3'
Ad1_noMX	AATGATACGGCGACCACCGAGATCTACACTCGTCGGCAGCGTCAGATGTG
Ad2.1_TAAGGCGA	CAAGCAGAAGACGGCATACGAGATTCGCCTTAGTCTCGTGGGCTCGGAGATGT
Ad2.2_CGTACTAG	CAAGCAGAAGACGGCATACGAGATCTAGTACGGTCTCGTGGGCTCGGAGATGT
Ad2.3_AGGCAGAA	CAAGCAGAAGACGGCATACGAGATTTCTGCCTGTCTCGTGGGCTCGGAGATGT
Ad2.4_TCCTGAGC	CAAGCAGAAGACGGCATACGAGATGCTCAGGAGTCTCGTGGGCTCGGAGATGT
Ad2.5_GGACTCCT	CAAGCAGAAGACGGCATACGAGATAGGAGTCCGTCTCGTGGGCTCGGAGATGT
Ad2.6_TAGGCATG	CAAGCAGAAGACGGCATACGAGATCATGCCTAGTCTCGTGGGCTCGGAGATGT
Ad2.7_CTCTCTAC	CAAGCAGAAGACGGCATACGAGATGTAGAGAGGTCTCGTGGGCTCGGAGATGT
Ad2.8_CAGAGAGG	CAAGCAGAAGACGGCATACGAGATCCTCTCTGGTCTCGTGGGCTCGGAGATGT

TABLE 11. Primers used for ATAC-qPCR or ChIP-qPCR assays.

ATAC-ChIP target regions (SYBR Green)	Forward 5'-3'	Reverse 5'-3'	Reference (where relevant)
Tel	GGTTTTTGAGGGTGAGGGTGAGGGT-GAGGGTGAGGGT	TCCCGACTATCCCTATCCCTATC-CCTATCCCTATCCCTA	(Udugama et al., 2015)
HERV	CCCGCCAGAGAACAAACTCTCTTT	CCAAATTTCATGCGTGTCTGTGCG	(Filipponi et al., 2013)
KDM4B-prom	CAATACTGGCTCCTCTCTGTG	GACCGGCTCTGTTCTCATT	This study.
CFAP53-prom	AAGTCTGGTTGCCATGGTG	TCTCAGCTGGAAGAGGAAGT	
GSR-prom	CCATGCACGCGGAAGTG	CATGCTTAGTCACCGTGAGG	
up-Hit1	GTGACATGACCAACATGTGTTAC	GTGTCAGTCACGTGTCCATTA	
up-Hit2	CATAAGGAACCCAGCAGAGTAA	CCCATCAAAGCTGCAAGTTC	
up-Hit3	CAAGTAGGGCACAATGGGTATG	GCAGCAAGCGTGTAGAATAGAG	
hPOLII-prom	CTGAGTCCGGATGAACTGGT	ACCCATAAGCAGCGAGAAAG	S. Peiró lab

For ATAC-seq analysis, paired end reads of length 50 bp were aligned to the human genome version hg19 using bowtie v0.12.9 (Langmead et al., 2009) with default parameters except for n=1 to limit the maximum number of mismatches in the seed and m=1 to report the best possible alignment for a given read. Alignments were sorted and indexed using Sambamba v0.5.8 (http://lomereiter.github.io/sambamba/). Duplicated reads were removed using Sambamba. Peaks were called with MACS v1.4.2 (Zhang et al., 2008) for each sample without any control. All parameters were left as default except for read length. Peaks were annotated with the HOMER v2.8.2 (Heinz et al., 2010) software with the hg19 annotations. Consensus peaks were defined as the union of all peaks from all samples. For each sample, the number of reads per peak was computed using the countBam function from the Rsamtools R package (version 1.30.0, http://bioconductor.org/packages/release/bioc/html/Rsamtools.htm). Differential accessibility was computed using DESeq2 (Love et al., 2014) with replicate as covariate.

For ATAC-seq overlap with epigenetic marks, epigenetic information was downloaded from the Encode website (Dunham et al., 2012) (H3K9me3 [ENCFF001VDL], H3K36me3 [ENCFF001VDK]) and from the Gene Expression Omnibus (GEO) (Barrett et al., 2013) (Pol II [GSE73742], H3.3 [GSM1901950] and HIRA [GSM1095934]). Consensus peaks

were classified according to their overlap with each epigenetic track [minimum overlap length 100bp]. P-values were computed with a Mann-Whitney test as implemented in the function wilcox.test in R (R Development Core Team, 2016). For ATAC-seq FC correlation between replication time and methylation marks, the Repliseq track (wgEncodeUwRepliSeqNhekWaveSignalRep1.bigWig) was downloaded from the Encode website in Bigwig format. H3K36me3 and H3K9me3 corresponding to the U-2-OS cell line were also downloaded in Bigwig format from the same repository. Mean normalized signal was computed for 10kb bins along the genome. Spearman correlations coefficients were computed with the cor function in R. For Fig. 33D, Repliseq scores were binned in 25 quantiles. For ATAC-seq FC overlap with colors of chromatin, tracks were downloaded from Encode (wgEncodeAwgSegmentationChromhmmHelas3.bed) corresponding to the ChromHMM algorithm (Ernst and Kellis, 2012) in the HeLa-S3 cell line. Peaks were classified to the color with larger overlapping segment. For better visualization, colors were collapsed to 10 classes as follows: Active Promoter = {Tss, TssF}, Promoter Flanking = {PromF}, Inactive Promoter = {PromP}, Candidate Strong enhancer = {Enh, EnhF}, Candidate Weak enhancer/DNase = {EnhWF, EnhW, DnaseU, DnaseD, FaireW}, Distal CTCF/CandidateInsulator = {CtcfO, Ctcf}, Transcription associated={Gen5, Elon, ElonW, Gen3, Pol2, H4K20}, Low activity proximal to active states= {Low}, Polycob repressed = {ReprD, Repr, ReprW}, Heterochromatin/Repetitive/Copy Number Variation = {Quies, Art}.

Chromatin immunoprecipitation (ChIP)

U-2-OS cells were transfected in biological duplicate with siRNAs (siGFP and siTLK1+2) and 48 hours post-transfection were harvested by trypsinization. Cells were crosslinked with 1% Formaldehyde in DMEM for 10 min at room temperature. Excess formaldehyde was quenched with Glycine at a final concentration of 125 mM. Cells were washed with PBS twice, pelleted by centrifugation at 300 g and dry pellets were frozen at -80ºC. For nuclear extract preparation, cells were thawed on ice, resuspended in cold Swelling buffer (25 mM Hepes pH 7.9, 1.5 mM $MgCl_2$, 10 mM KCl, 0.1% NP-40, 1x protease (Roche) and phosphatase inhibitors (Sigma-Aldrich)) for 10 min and passed through a douncer 50 times. Nuclei were pelleted by centrifugation at 3000 g for 5 min at 4ºC, and resuspended in 300 µl of 1% SDS in ChIP buffer (10 mM Tris-HCl pH 7.5,150 mM NaCl, 1% Triton X-100, 5 mM EDTA, 0.5 mM DTT, 1x protease (Roche) and phosphatase inhibitors (Sigma-Aldrich)). The extracts were incubated for 15 min on ice, changed to 1.5 ml Bioruptor Pico Microtubes (Diagenode) and sonicated in a Bioruptor Pico sonication device (Diagenode) for 30 cycles 30'' on/30'' off. Chromatin was cleared by centrifugation at top speed 15 min at 4ºC and recovered in a low binding tube. Chromatin was checked for size after a phenol/chlorophorm extraction by an agarose gel and by a Bioanalyzer DNA HS Chip (Agilent; Integrated Sciences) so chromatin fragments have a size of 200 bp on average. For H3.3 and H3K9me3 ChIP, 5 µg of total chromatin was diluted 1:10 in ChIP buffer and incubated with 1 µg of antibody on rotation at 4ºC overnight. For

RPA ChIP, 25 µg of total chromatin was diluted 1:10 in ChIP buffer and incubated with 5 µg of antibody on rotation at 4°C overnight. 50 µl of prewashed Dynabeads Protein G (Thermo Fisher Scientific) were added on rotation for 2h at 4°C. Beads were washed with Low Salt buffer (50 mM HEPES pH 7.5, 140 mM NaCl, 1% Triton X-100, 1x protease (Roche) and phosphatase inhibitors (Sigma-Aldrich)), High Salt buffer (50 mM HEPES pH 7.5, 500 mM NaCl, 1% Triton X-100, 1x protease (Roche) and phosphatase inhibitors (Sigma-Aldrich)) and eluted by incubating in a thermomixer with Elution buffer (1% SDS, 100 mM $NaHCO_3$) for 30 min at 65°C and 1000rpm. Samples were reverse-crosslinked by incubating at 65°C overnight and incubated with Proteinase K for 1h at 45°C. Chipped DNA was purified using the MinElute PCR Purification Kit (Qiagen) and eluted in 40 µl. Purified ChIP DNA was used for library generation using the NEBNext Ultra II DNA Library Prep Kit for Illumina (NEB) following manufacturer's instructions. Each of the libraries was labelled by a specific barcode provided in NEBNext Multiplex Oligos for Illumina (Index Primers Set 1 and 2) (NEB) and amplified 9-13 cycles (depending on initial material amount) by PCR in the presence of SYBR Green in order to obtain an optimal yield. Libraries were quantified using DNA HS Qubit (Thermo Fisher Scientific) and size measured by a 2100 Bioanalyzer Instrument (Agilent) and a DNA HS Chip (Integrated Sciences). An equimolar pool was generated with all libraries and the pool was sequenced in 2 lanes 50 nt single read in an Illumina HiSeq2500 (Illumina). Libraries were also used as a template for qPCR using the primers corresponding to telomeric repeats (Tel) and the ATAC hit regions, summarized in Table 11.

For ChIP-seq analysis, single end reads of 50 bp length were aligned to the hg19 human genome version using Bowtie v0.12.9 (Langmead et al., 2009) with default parameters. Alignments were sorted and indexed using Sambamba v0.5.8 (http://lomereiter.github.io/sambamba/). Duplicated reads were removed using Sambamba. Peaks were called with MACS v1.4.2 (Zhang et al., 2008) for each sample with the corresponding input as control. All parameters were left as default except for read length. Peaks were annotated with the HOMER v2.8.2 (Heinz et al., 2010) software with the hg19 annotations. Consensus peaks were defined as the union of all peaks from all samples. For each sample, the number of reads per peak was computed using the countBam function from the Rsamtools R package (version 1.30.0, http://bioconductor.org/packages/release/bioc/html/Rsamtools.htm). Differential binding was computed using DESeq2 (Love et al., 2014) with replicate as covariate. Normalized densities for peaks were computed using the annotatePeaks function from the HOMER suite. Densities were plotted using the feature AlignedDistribution function from the ChIPpeakAnno R package (Zhu, 2013).

C-circle assay

The C-circle assay protocol was adapted from Henson et al, 2017. Genomic DNA from 200 000 cells was extracted by incubating cells with 50 µl of QCP lysis buffer (50 mM KCl, 10 mM Tris-HCl pH 8.5, 2 mM $MgCl_2$, 0.5% IGEPAL CA-630, 0.5% Tween-20)

and 3µl of QIAGEN protease shaking at 1400rpm at 56°C for 1 hour. The QIAGEN protease was inactivated by incubating the samples at 70°C for 20 min.

DNA concentration was measured by fluorimetry using the Qubit dsDNA HS Assay (Thermo Fisher Scientific). Samples purified from ALT+ cell lines were pre-diluted in QCP lysis buffer at 7.5 ng/µl whereas samples purified from ALT- cell lines were pre-diluted in QCP lysis buffer at 30 ng/µl. 7.5 ng or 30 ng of DNA (for ALT+ and ALT-, respectively) were diluted to 10 µl in 10mM Tris-HCl pH 7.6 and mixed with 9.25 µl of Rolling Circle Master Mix (RCMM) (8.65mM DTT, 2.16X 10X ϕ29 Buffer, 8.65ug/mL BSA, 0.216% Tween-20 and 2.16mM of each dATP, dCTP, dGTP and dTTP) and 0.75 µl of ϕ29 DNA Polymerase (NEB). Rolling Circle Amplification was performed by incubating samples in a thermocycler at 30°C for 8 hours, polymerase was inactivated at 70°C for 20 min and then kept at 8-10°C. Samples were kept at -20°C. For dot blot detection, samples were diluted with 2x SSC to 200 µl, then dot-blotted onto Nytran SuPerCharge (SPC) nylon blotting membranes (Sigma-Aldrich) under native conditions. After 254 nm UV-C crosslinking, the membrane was hybridized with γ-^{32}P labelled Tel-C oligo probe $(CCCTAA)_4$ at 37°C in hybridization buffer (1.5X SSPE, 10% polyethylene glycol (PEG) MW 8000, 7% SDS) for 16h. Membrane was exposed onto a storage phosphor screen (Molecular Dynamics) and scanned using Typhoon 8600 Variable Mode Imager (Molecular Dynamics). Membrane was stripped in wash solution (0.5X SSC, 0.1% SDS) at 65 ºC and re-hybridized with γ-^{32}P labelled Alu oligo probe 5'-GTAATCCCAGCACTTTGG-3' for loading control.

Fluorescence in situ hybridization (FISH)

After standard IF staining with primary and secondary antibody incubations, washes were performed with IF blocking solution. To continue with FISH, slides were fixed again in 4% formaldehyde for 5 min at room temperature, washed in PBS and dehydrated in increasing concentrations of ethanol (70%, 95%, and 100%). The slides were air-dried, incubated with Telomere PNA Probe/Cy3 (Dako-Agilent) and denatured on an 80°C hot plate for 5 minutes. Hybridization took place in the dark for 3-4 hours at room temperature. The slides were subsequently washed in Rinse Solution (Dako-Agilent), washed in pre-heated Wash Solution (Dako-Agilent) and dehydrated in increasing concentrations of ethanol (70%, 95%, and 100%). Slides were washed in DAPI, mounted in Vectashield (Vector Labs), sealed and stored in a cold dark chamber.

Isolation of polyoma middle-T (PyMT) mammary tumour cell lines

At 4-6 months after birth, mice with MMTV-PyMT allele *Tlk2*$^{F/F}$ ERT2-Cre were sacrificed and breast tumours were dissected. Tumours were chopped using razor blades and digested at 37°C rocking for 1 h in DMEM medium containing Collagenase A (1mg/ml; no. 10103586001, Roche) and Hyaluronidase (1.5 units/ml; no. H3506, Sigma-Aldrich). After digestion, cell suspension was filtered through a 70-µm cell mesh and

centrifuged for 5 min at 1500 rpm. Cell pellets were resuspended in 10 ml of media and pelleted again, and this step repeated for 4 times. The final cell pellet enriched in epithelial cells was plated. Cells were passaged until they entered senescence and they spontaneously immortalized. Immortalized cells derived from PyMT-induced breast tumours were maintained in DMEM supplemented with 10% (v/v) FBS and penicillin–streptomycin. For the induction of Cre recombinase in ERT2-Cre-expressing cell lines, cells were exposed to 4OHT (Sigma-Aldrich; H7904; 1 μM) for 48 h, washed and plated for experiments.

Inducible short hairpin RNA-mediated knockdown

Cloning of Doxycycline-regulated lentiviral miR-E expression vectors generated by Fellmann et al., 2013, in particular the LT3GEP vector (pRRL-T3G-tGFP-(Xho/Eco)-PGK-Puro), was done by PCR amplification of shRNA custom long oligonucleotides (97-mer, in Table 12) (Sigma-Aldrich) with the primers miRE-Xho-Fw (5'-TGAACTCGAGAAGGTATATTGCTGTTGACAGTGAGCG-3') and miRE-EcoOligo-Rev(5'-TCTCGAATTCTAGCCCCTTGAAGTCCGAGGCAGTAGGC-3'). Amplification products were XhoI/EcoRI digested and the resulting 125 nt shRNA fragments were cloned into LT3GEP vector using standard cloning techniques. Final vectors were sequenced (Macrogen) using the primer miRseq5' (5'-TGTTTGAATGAGGCTTCAGTAC-3'). The retroviral vector MSCV-rtTA3-IRES-Luc2-PGK-Hygro (kind gift of J. Zuber, (Fellmann et al., 2013)) was used for inducing shRNA expression upon Doxycycline (Sigma-Aldrich), which was used at 1-10 μg/ml.

TABLE 12. shRNA 97-mer oligonucleotides.

shTLK2 ID	Primer ID	Sequence 5'-3'
1	shTLK2 2138	TGCTGTTGACAGTGAGCGCGCAAGACATCCTACAAGAGAATAGTGAAGCCA-CAGATGTATTCTCTTGTAGGATGTCTTGCTTGCCTACTGCCTCGGA
2	shTLK2 1382	TGCTGTTGACAGTGAGCGCTCTACATATCAGGGAACTAAATAGTGAAGCCA-CAGATGTATTTAGTTCCCTGATATGTAGATTGCCTACTGCCTCGGA
3	shTLK2 1623	TGCTGTTGACAGTGAGCGACGGATTCATAAAGAGCTGGATTAGTGAAGCCA-CAGATGTAATCCAGCTCTTTATGAATCCGGTGCCTACTGCCTCGGA
4	shTLK2 1496	TGCTGTTGACAGTGAGCGCCAGTGAAGTTTACAAGGCATTTAGTGAAGCCA-CAGATGTAAATGCCTTGTAAACTTCACTGATGCCTACTGCCTCGGA
6	shTLK2 1174	TGCTGTTGACAGTGAGCGAAGGGAAGAGATAGAAAGACAATAGTGAAGCCA-CAGATGTATTGTCTTTCTATCTCTTCCCTCTGCCTACTGCCTCGGA
7	shTLK2 2348	TGCTGTTGACAGTGAGCGCTCCGAAAGTCAGTCTCTACAATAGTGAAGCCA-CAGATGTATTGTAGAGACTGACTTTCGGATTGCCTACTGCCTCGGA
8	shTLK2 4012	TGCTGTTGACAGTGAGCGCAAGGAGAAATAGATGTTTCAATAGTGAAGCCA-CAGATGTATTGAAACATCTATTTCTCCTTTTGCCTACTGCCTCGGA
9	shTLK2 919	TGCTGTTGACAGTGAGCGCCGGCAGATTGATGAACAGCAATAGTGAAGCCA-CAGATGTATTGCTGTTCATCAATCTGCCGTTGCCTACTGCCTCGGA

CD44/CD24 FACS staining for MDA-MB-231

Cells were trypsinized, pelleted, washed in PBS and incubated for 45 min on ice in the dark in 100 μl of FACS buffer (0.2% BSA in 1X PBS) containing the CD44-PE mouse anti-human (1:50; no. 555479, BD) and CD24-PERCP-Cy5.5 mouse anti-human (1:100; no. 561647, BD) antibodies. Cells were subsequently washed and resuspended in 300 μl of FACS buffer for analysis.

Xenograft orthotopic implantations in mammary fat pad

Several lines of MDA-MB-231 cells modified with CRISPR were previously transduced with a retroviral vector containing Luciferase (MSCV-rtTA3-IRES-Luc2-PGK-Hygro). Cells were selected with Hygromycin and tested to be free of *Mycoplasma*. For orthotopic implantations in the mammary fat pad, cells were harvested by trypsinization, washed twice with PBS and counted. Prior to injection, mice were anesthetized with ketamine (100 mg/kg of body weight) and xylazine (10 mg/kg of body weight). Resuspended cells (1 x 10^6 cells) were implanted 1:1 in Matrigel (BD Biosciences, growth factor-reduced) in a total volume of 50 µl into the fourth mammary fat pads (abdominal) of 8-week old BALB/c Nude mice using a 27G1/2 needle, with two mammary fat pad injections per mouse. A minimum of four tumours was generated per cell line. Animals were monitored at days 0, 1, 3, 7 and weekly for body weight, tumour size and luminescence imaging. For IVIS Spectrum *in vivo* imaging (PerkinElmer), animals were first anesthetized with isoflurane, luciferin was injected retro-orbitally using a 29G needle and images were taken within 5 minutes. Bioluminescence images indicating tumour growth were analysed with Living Image 2.60.I software by normalizing all obtained values to those obtained at day 0. Tumour size was analysed by measuring with a digital calliper tumour length (L) and width (W), and volume was calculated on the basis of the following formula: $\pi \cdot L \cdot W^2/6$. Mice carrying tumours of size greater than 400 mm^3 were sacrificed and tumours resected. All animal work was approved by the institutional animal care and use committee of IRB Barcelona.

Antibodies

TABLE 13. Antibodies used in this study.

Antigen	Species	Source	Dilution
TLK1	rabbit	Cell Signaling #4125	1:1000 (WB), 1:250 (IF)
TLK2	rabbit	Bethyl Laboratories A301-257A	1:1000 (WB), IP
ASF1	mouse	Sigma A5236, clone 4A1/3	1:800 (WB, in AD293)
ASF1	mouse	Santa Cruz sc-53171, clone 4A1/3	1:800 (WB, in AD293)
ASF1	rabbit	Groth Laboratory (Groth et al., 2005)	1:2000 (WB), IP
ASF1A	rabbit	Cell Signaling #2990, clone C6E10	1:250 (IF)
ASF1B	rabbit	Cell Signaling #2902, clone C70E2	1:250 (IF)
ASF1 pS166	rabbit	Groth Laboratory (Klimovskaia et al., 2014)	1:30000 (WB)
Actin	mouse	Sigma A4700, clone AC-40	1:3000 (WB)
FLAG	mouse	Sigma F3165, clone M2	1:5000 (WB)
Strep-tag	mouse	IBA GmbH 2-1509-001	1:1000 (WB)
LC8	rabbit	Abcam ab51603, clone EP1660Y	1:1000 (WB)
RAD9	mouse	BD Biosciences 611324	1:500 (WB)
GAPDH	mouse	Millipore MAB374, clone 6C5	1:10000 (WB)
H2AX pS139 (γH2AX)	mouse	Millipore 05-636, clone JBW301	1:250 (IF)
H2AX pS139 (γH2AX)	rabbit	Santa Cruz sc-101696	1:500 (WB), 1:250 (IF)
RPA2	mouse	Calbiochem NA19L, clone RPA34-20	1:1000 (WB), 1:250 (IF), ChIP

Antigen	Species	Source	Dilution
RPA2	rabbit	Bethyl Laboratories A300-244A	1:1000 (WB, murine cells)
RPA2 pS4/S8	rabbit	Bethyl Laboratories A300-245A	1:500 (WB)
RPA2 pS33	rabbit	Bethyl Laboratories A300-246A	1:500 (WB)
PCNA	mouse	Santa Cruz sc-56, clone PC-10	1:250 (IF)
Vinculin	mouse	Sigma V9264, clone hVIN-1	1:10000 (WB)
HA-tag	mouse	Santa Cruz sc-7392, clone F-7	1:500 (WB), IP
H3.3	rabbit	Millipore 09-838	1:1000 (WB), 1:250 (IF), ChIP
H3K9me3	rabbit	Abcam ab8898	ChIP
HP1α	mouse	Active Motif 39977, clone 2HP1H5	1:250 (IF)
PML	mouse	Santa Cruz sc-966, clone PG-M3	1:250 (IF)
TRF2	rabbit	Novus Biologicals NB110-57130	1:250 (IF)
ATRX	rabbit	Bethyl Laboratories A301-045A	1:1000 (WB)
HIRA	mouse	Active Motif 39557, clone WC119.2H11	1:1000 (WB)
STING	mouse	R&D Systems MAB7169, clone 723505	1:1000 (WB)
DAXX	rabbit	Bethyl Laboratories A301-353A	1:1000 (WB)
RPA194 (Pol1)	mouse	Santa Cruz sc-48385, clone C-1	1:250 (IF)
Alexa Fluor 488	Goat (anti-mouse)	Molecular Probes A11001	1:500 (IF)
Alexa Fluor 594	Goat (anti-mouse)	Molecular Probes A11005	1:500 (IF)
Alexa Fluor 488	Goat (anti-rabbit)	Molecular Probes A11008	1:500 (IF)
Alexa Fluor 594	Goat (anti-rabbit)	Molecular Probes A11012	1:500 (IF)
Anti-rabbit HRP	Goat (anti-rabbit)	Cultek 32490	1:15000 (WB)
Anti-mouse HRP	Goat (anti-mouse)	Thermo Scientific 31430	1:15000 (WB)

Results

Chapter 1

Molecular determinants of Tousled like kinase 2

Sandra Segura-Bayona[1], Cristina Jauset[1], Philip A. Knobel[1], Marina Villamor-Payà[1], Helena González-Burón[1], Aida Peña-Blanco[1], Anja Groth[2], Guillermo Montoya[3] and Travis H. Stracker[1]

[1] Institute for Research in Biomedicine (IRB Barcelona), the Barcelona Institute of Science and Technology, Barcelona, Spain.

[2] Biotech Research and Innovation Centre (BRIC) and Centre for Epigenetics, Faculty of Health and Medical Sciences, University of Copenhagen, Copenhagen, Denmark.

[3] Novo Nordisk Foundation Centre for Protein Research (CPR), Faculty of Health and Medical Sciences, University of Copenhagen, Copenhagen, Denmark.

Statement of contribution:

S Segura-Bayona designed, performed and analysed all the experiments with the exception of the BioID/IP-MS transfections for TLK2 network analysis.

C Jauset performed clonings in Figure 10A and 13A and initiated experiments that led to results showed in Figure 10B and 13C, under S Segura-Bayona supervision.

PA Knobel performed clonings in Figure 8B and the BioID experiment in Figure 8D-E.

M Villamor-Payà co-performed with S Segura-Bayona experiments shown in Figure 10B-C.

H González-Burón and A Peña-Blanco performed clonings in Figure 8A and IP-MS experiments in Figure 8E.

A Groth provided GST-ASF1a purified protein, pASF1a S166 antibody and information relevant to Figure 11A.

G Montoya provided autophosphorylation information relevant to Figure 11A, crystal structure in Figure 11E and performed docking in Figure 12C and 12E.

TH Stracker designed and supervised the whole project.

Characterization of the high-confidence interactome of human TLK2

TLK2 has been less studied than TLK1 in the literature, and whether it performs the same functions or has the same substrate spectrum as TLK1 remains elusive. ASF1a and ASF1b are the most clearly defined targets of TLKs but other substrates, such as RAD9 and NEK1, have been reported for TLK1 (Canfield et al., 2009; Kelly and Davey, 2013; Singh et al., 2017). For this reason, we wanted to address the potential substrate spectrum of TLK2 by defining the high-confidence interactome. We carried out immunoprecipitations of Strep-FLAG tagged TLK2 or kinase dead TLK2 (TLK2-KD) followed by quantitative mass spectrometry (IP-MS, Figure 8A). We could validate that the mutation D592V, corresponding to the aspartic in the HYD motif in the catalytic loop of the kinase domain, did abolish the catalytic activity of TLK2-KD in an *in vitro* kinase assay using TLK2 immunoprecipitated from AD293 cells and Myelin Basic Protein (MBP), a commonly used kinase substrate surrogate (Figure 8C). In addition, we overexpressed TLK2 fused to the BirA* biotin ligase to identify the proximity interactome of TLK2 using BioID (Figure 8B). We validated that most of the BirA*-FLAG-TLK2 localized to the nucleus of AD293 cells and biotinylation only occurred in the presence of external Biotin (Figure 8D). Only a small number of proteins were consistently identified by both approaches, including ASF1a and ASF1b, TLK1 and LC8 (DYNLL1) (Figure 8E and Supplementary Tables S1-S2). Additional proteins known to be involved in a variety of cellular processes, including DNA replication and chromatin assembly (ex. MCM helicase components, RIF1 and HIRA/UBN1-2), transcription (ex. GATAD2A, JUN) and translation (ex. EIF3F, EIF2S1) were identified in one or both approaches below our statistical thresholds (Figure 8E). We focused on the highest confidence interactions and could confirm the interactions of TLK1, ASF1 and LC8 by Strep immunoprecipitation of SF-TLK2 and TLK2-KD complexes followed by Western blot (Figure 8F).

Given that ASF1 has been the most well-defined target of TLK1, we wanted to address the TLK2-ASF1 interaction in more detail. For this, we performed co-immunoprecipitation experiments in AD293 cells by overexpressing the two ASF1 isoforms with a Strep tag, S-ASF1a and S-ASF1b. We could observe that both isoforms were expressed at the same levels and were able to immunoprecipitate similar amounts of endogenous TLK2 protein (Figure 9A). Similarly, co-immunoprecipitation of endogenous TLK2 efficiently pulled down both ASF1a and ASF1b proteins, thus confirming TLK2 interacts with both ASF1 isoforms (Figure 9A). Using an *in vitro* kinase assay with immunoprecipitated SF-TLK2 or TLK2-KD, we could confirm that ASF1 is a target of TLK2 expressed in mammalian cells (Figure 9B), as it had been shown before for TLK1 (Klimovskaia et al., 2014; Silljé and Nigg, 2001), and for TLK2 expressed in *Drosophila* S2 cells (Pilyugin et al., 2009).

Considering that we could verify the interaction with LC8 (Figure 8F), we next wanted to address whether LC8 could be a TLK2 target. We performed kinase assays with purified LC8 protein and did not observe any phosphorylation even with increasing concentrations of LC8 protein by autoradiograph, indicating that LC8 was unlikely to be a substrate of

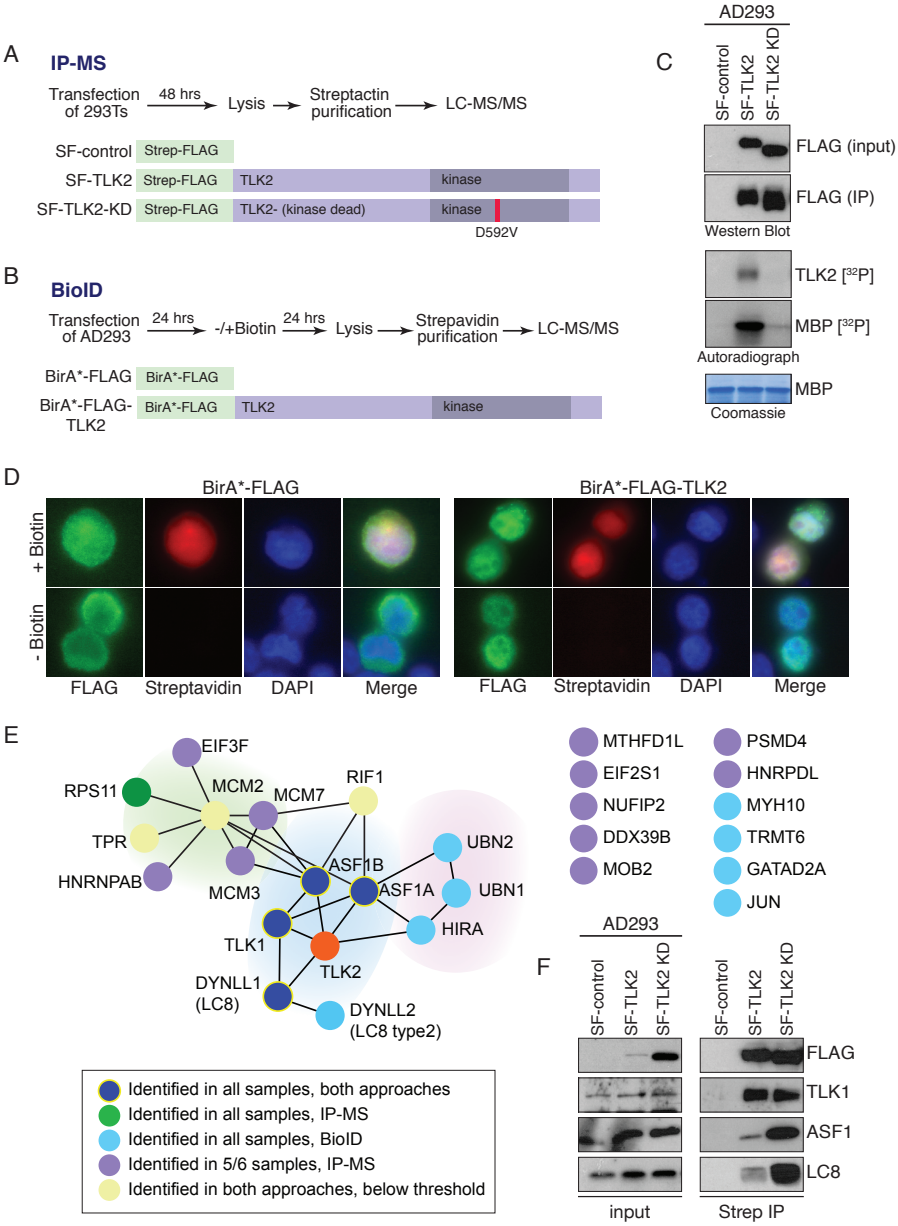

Figure 8. Characterization of the high-confidence interactome of human TLK2.

(A) Schematic of affinity purification strategy (IP-MS) for Strep-FLAG tagged TLK2 or a kinase dead allele, TLK2-KD (D592V). Replicates of the affinity purifications were digested with trypsin and subjected to LC-MS/MS to quantitatively identify interacting proteins. (B) Schematic of the BioID approach using TLK2 fused to the promiscuous biotin ligase BirA*. (C) Validation of TLK2 or TLK2 KD expression and affinity purification of TLK2 by Western blotting following transfection of AD293 cells (top panel). The effectiveness of the kinase dead mutation was also validated in IP-kinase assays (bottom panel). The TLK2 KD mutation abolished autophosphorylation and substrate phosphorylation (Myelin Basic Protein: MBP). (D) Validation of BirA*-TLK2 expression and activity in AD293 cells supplemented with biotin. Note that Streptavidin signal that was detected in the nucleus and cytoplasm for the BirA*-FLAG control, was exclusively nuclear in the case of BirA*-FLAG-TLK2. Biotinylated peptides were purified from cells expressing the BirA* constructs and identified by LC-MS/MS. (E) Graphic depiction of the combined results from multiple proteomics approaches to identify TLK2 interacting proteins from HEK293T or AD293 cells (IP-MS and BioID approaches, data presented in full in Supplementary Tables S1-S2). TLK1, ASF1a, ASF1b and DYNLL1 (LC8) were

TLK2 activity (Figure 9C). In addition, we also tried to identify phosphorylated peptides by LC-MS, and while we obtained very high coverage of all Ser, Thr or Tyr residues on the LC8 protein, we were unable to identify any phosphorylation in the analysed samples (data not shown).

In our interactome experiments using TLK2 as a bait, we have never detected the other main substrate of TLK1 that has been proposed, RAD9, a component of the 9-1-1 complex that has a role in the response to replication stress (Lieberman, 2006). Thus, we set out to determine if RAD9 interacted with TLK1 or TLK2 by overexpressing SF-TLK1 or TLK2 in AD293 cells followed by immunoprecipitation. We observed in multiple experiments that while RAD9 was pulled down by both TLKs, it was enriched equally in control samples, even when benzonase treatment was used (Figure 9D). As a control for these experiments, we used the *bona fide* interactor ASF1, whose interaction with TLK1 and TLK2 was evident with or without benzonase treatment and the control samples always showed no background. We have therefore not considered RAD9 further as a specific interactor or potential substrate of TLK1 or TLK2.

Additionally, all our BioID experiments identified components of the HIRA complex, such as HIRA itself or UBN1-2 (Figure 8E). In order to decipher whether TLK2 also interacted with HIRA directly, so it could potentially regulate directly a histone chaperone complex involved in replication-independent chromatin assembly, we generated a stable U-2-OS cell line expressing HA-HIRA and performed co-immunoprecipitation of HA-HIRA and endogenous ASF1. We could observe that HA-HIRA pulled down ASF1 and ASF1 pulled down both HA-HIRA and TLK2, indicating that the TLK2-HIRA interaction is likely indirect (Figure 9E). To further confirm this result, we transiently transfected HA-HIRA with or without SF-TLK2 in AD293 cells and analysed the co-immunocomplexes. Both HA-HIRA and SF-TLK2 could efficiently pull down endogenous ASF1 and were unable to pull down each other (Figure 9F), validating that TLK2-HIRA interactions occur via ASF1. Together, these data corroborate that ASF1a and ASF1b isoforms are the highest confidence TLK substrates and we have identified a novel interactor, LC8, that does not appear to be a target of TLK activity.

Domain architecture, oligomerization and activity of human TLK2

Human TLK1 and TLK2 proteins are composed of an N-terminal region, a middle region of helices predicted to contain three coiled coils (CC) and a C-terminal kinase domain that shows 94% identity between TLK1 and TLK2 (Figure 7A and 10A). The C-terminal regions of the kinase domains contain many possible phosphorylation sites in their

the only high confidence interacting proteins identified. (F) Validation of high confidence interacting proteins by IP-Western. The only proteins identified that were not detected in any controls and present in all 6 TLK2/TLK2-KD replicates were TLK1, ASF1a, ASF1b, LC8 (DYNLL1) and RPS11 (Supplementary Table S1). Of these, all but RPS11 were also found highly enriched in the BioID experiments (Supplementary Table S2). We could readily validate the interactions between TLK2 and endogenous TLK1 and ASF1 in AD293. In addition, we could detect binding to endogenous LC8.

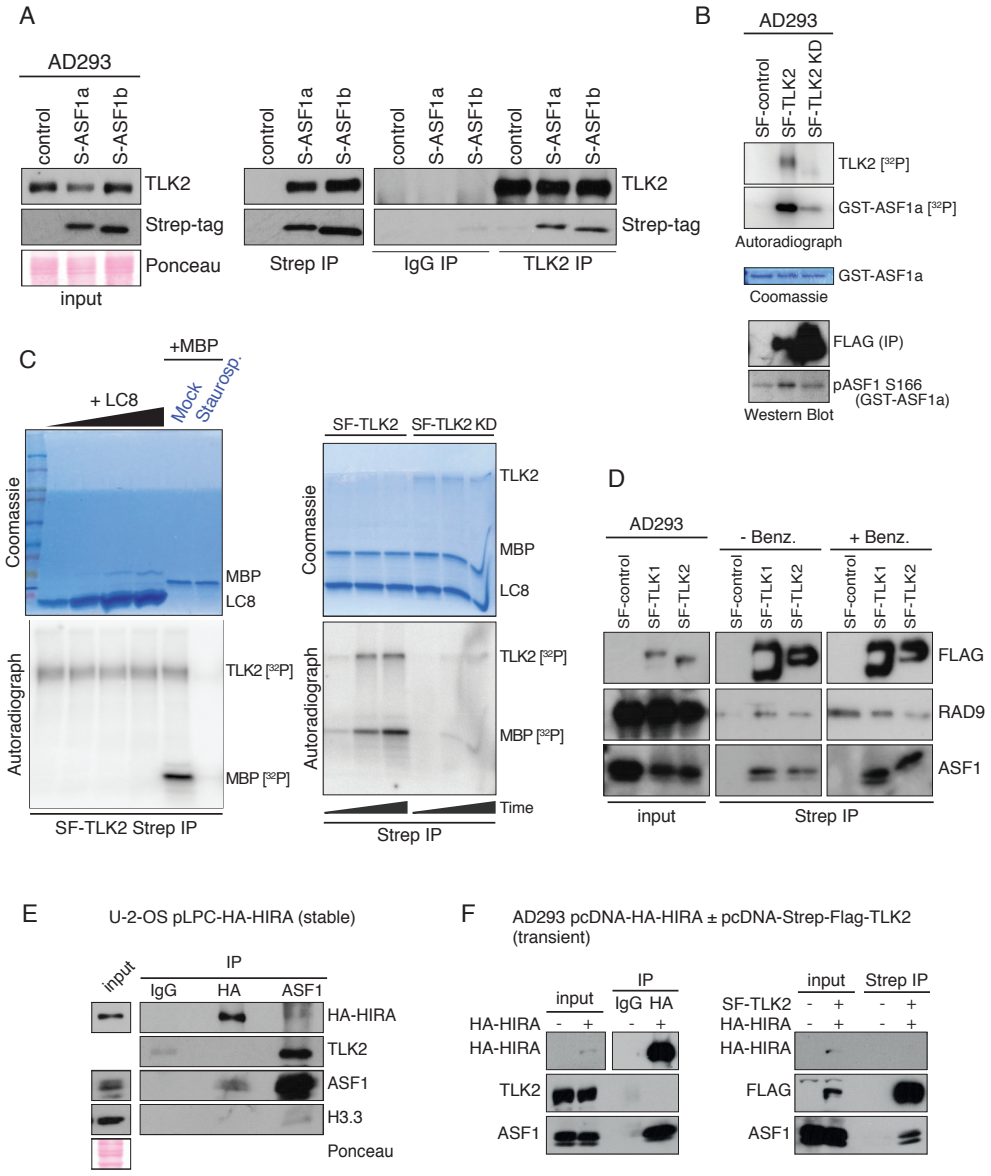

Figure 9. Characterization of the high-confidence interactome of human TLK2.

(A) Co-immunoprecipitation experiments with overexpressed Strep-ASF1a and Strep-ASF1b in AD293 cells. Both ASF1 isoforms interact with endogenous TLK2, while endogenous TLK2 also pulls down both isoforms of ASF1 to similar levels. (B) Validation of ASF1a as a TLK2 substrate. IP-kinase assays were performed with TLK2 or TLK2 KD affinity purified from AD293 cells using GST-ASF1a as a substrate. (C) LC8 does not appear to be a substrate of TLK2. Addition of LC8 did not influence the kinase activity of TLK2 (based on autophosphorylation) and recombinant LC8 was not phosphorylated by TLK2, suggesting that it is unlikely to be a substrate (left panel). Kinetic analysis of TLK2 or TLK2 KD activity on MBP and LC8. MBP phosphorylation is clearly increased over time while no signal is observed for LC8 in the phosphor imager, despite similar levels of protein loaded (right panel). (D) RAD9 is not a *bona fide* interactor. Immunoprecipitation experiments overexpressing SF-TLK1 and SF-TLK2 in AD293 cells consistently pull down ASF1. RAD9 is also pulled down by both kinases despite being equally present in control samples even in the presence of benzonase. (E) TLK2 and HIRA interaction is likely indirect. Immunoprecipitation experiments in U-2-OS cells stably expressing HA-HIRA confirmed HIRA-ASF1 interaction and endogenous ASF1 interaction with HIRA and TLK2. (F) Immunoprecipitation experiments overexpressing HA-HIRA and SF-TLK2 in AD293 cells consistently pull down ASF1 but do not pull down each other.

carboxyl terminus (C-tail), one of which has been reported to negatively regulate activity in TLK1 (Groth et al., 2003; Klimovskaia et al., 2014; Krause et al., 2003). The first 200 amino acids of the N-terminus are predominantly disordered and are predicted to contain a nuclear localization signal (NLS). The CC domains of *Arabidopsis* TSL, which contain an additional insertion in the first CC, have been reported to mediate oligomerization and activity (Roe et al., 1997). Sequence alignment from plants to mammals showed that both the kinase and the predicted coiled-coil domains are highly conserved (Supplementary Figure 1) and the last residues of the C-tail were predicted to be unstructured. Based on these sequence alignments and secondary structure predictions, we generated a series of constructs with N-terminal deletions to facilitate the analysis of the different sections of the TLK2 protein (Figure 10A).

The oligomerization of the *Arabidopsis* TSL has been suggested based on two-hybrid experiments but it has not been examined biochemically whether it occurred in mammalian cells to date (Roe et al., 1997). As previous work has linked the dimerization ability of TSL to its catalytic activity (Roe et al., 1997), we expressed a series of Strep-

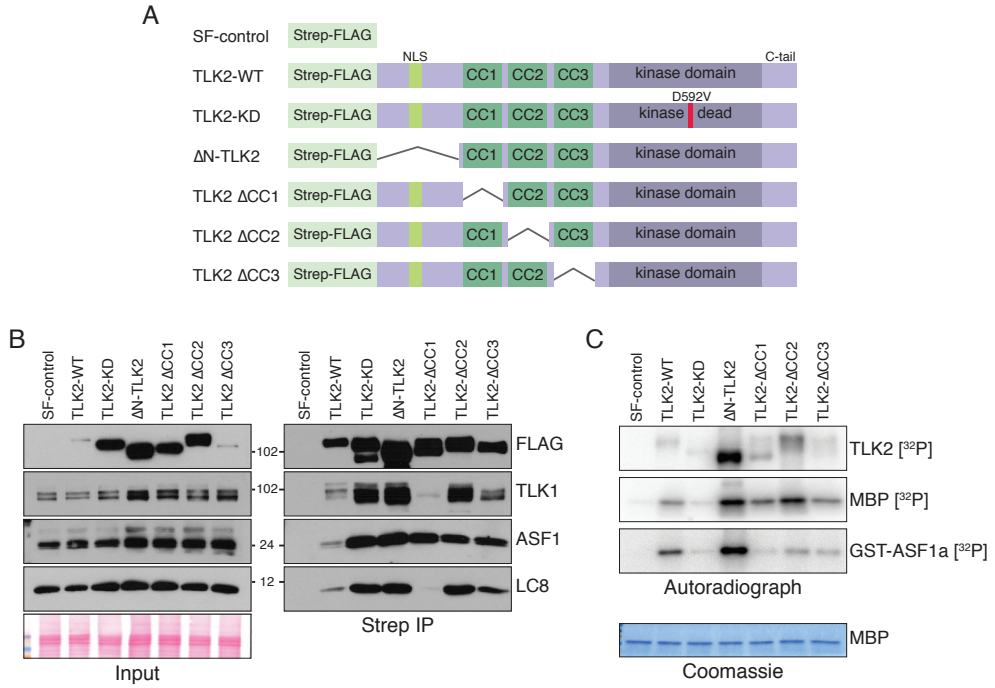

Figure 10. Domain architecture, oligomerization and activity of human TLK2.

(A) TLK2 domain architecture and constructs of N-terminal deletions used in this study. More details are available in Materials and Methods. (B) The indicated TLK2 mutants were overexpressed in AD293 cells by transient transfection and pulled down from cell lysates using Streptavidin resin. Protein-protein interactions were analysed by Western blotting for TLK2, TLK1, ASF1 and LC8 (right panel). Input levels are shown in the left panel including the Ponceau red stained membrane showing similar total protein levels. The figure shows one representative experiment of four biological replicates. (C) Kinase assays were performed from Streptavidin pull downs performed as in (B). Kinase complexes were incubated with either MBP or ASF1a in the presence of ^{32}P-γ-ATP and autophosphorylation (TLK2) and substrate phosphorylation assessed in dried SDS-PAGE gels exposed to a phosphor imager.

FLAG (SF) tagged TLK2 alleles with mutations in the N-terminus, CC domains or kinase domain in human cells and examined protein-protein interactions and kinase activity in pull-downs with streptavidin resin. In Strep pull-downs of tagged wild-type (WT) TLK2, we readily observed co-precipitation of TLK1, ASF1, the key TLK substrate, and LC8, another prominent interactor that is not a target of TLK2 activity (Figure 8F and 10B). All of these interactions were maintained in the N-terminal deletion (ΔN-TLK2) mutant lacking the first 161 residues, as well as the kinase dead (KD) protein. To address the potential roles of the CC domains, we generated deletion mutants lacking each of the 3 domains. Deletion of CC1 strongly impaired the interaction with both TLK1 and LC8 but did not appear to influence that of ASF1, suggesting that hetero-oligomerization between TLK1 and TLK2 may be mediated by LC8. In contrast, neither the CC2 nor CC3 domain had a clear influence on any of the protein-protein interactions (Figure 10B). We next examined kinase activity in the pull-downs using MBP as a substrate. The effect of the TLK2-KD mutation was clearly evident, as autophosphorylation and substrate phosphorylation were reduced to background levels compared to TLK2-WT (Figure 10C). The deletion of the N-terminus resulted in highly elevated autophosphorylation and substrate phosphorylation, suggesting that it may play a negative regulatory role and that it is not required for activity. Deletion of any of the individual CC domains did not abolish TLK2 activity on MBP, indicating that none of these domains, or the heterodimerization with TLK1, are required for TLK2 activity. However, when the kinase assay reaction was carried out with the specific substrate ASF1a, lower activity was observed with the CC domain mutants, especially ΔCC1, suggesting that ASF1a recognition may be dependent on the CC domains (Figure 10C) and that ASF1a is phosphorylated only by variants of TLK2 that are capable of oligomerization. With all these data, we concluded that TLK2 dimerization with TLK1 requires the predicted CC1 domain, that LC8 protein may promote hetero-oligomerization between TLK1/2 and assembly of higher order oligomers likely involving the CC domains may be an extra layer of regulation to fine tune phosphorylation of a physiological substrate such as ASF1a.

TLK2 auto- and trans-phosphorylation in the kinase domain

By generating recombinant TLK2 proteins in *E. coli* in the presence or absence of lambda phosphatase, we could identify which post-translational modifications (PTMs) would be a result of autophosphorylation. Biochemical studies performed by G. Montoya's laboratory indicated that dimerization enhances the activity of the enzyme (data now shown), showing that TLK2 can be activated without the need of an external triggering kinase, as is the case for CDKs and many other kinases (Malumbres, 2014). By performing competition assays with different ratios of TLK2-WT and TLK2-KD, we determined autophosphorylation sites that occur in the context of the protein dimer (Figure 11A). For homodimeric TLK2-WT, we identified 41 phosphosites out of 67 possible Ser/Thr phosphosites sites, 9 of which were in the structure of the kinase domain. The rest were

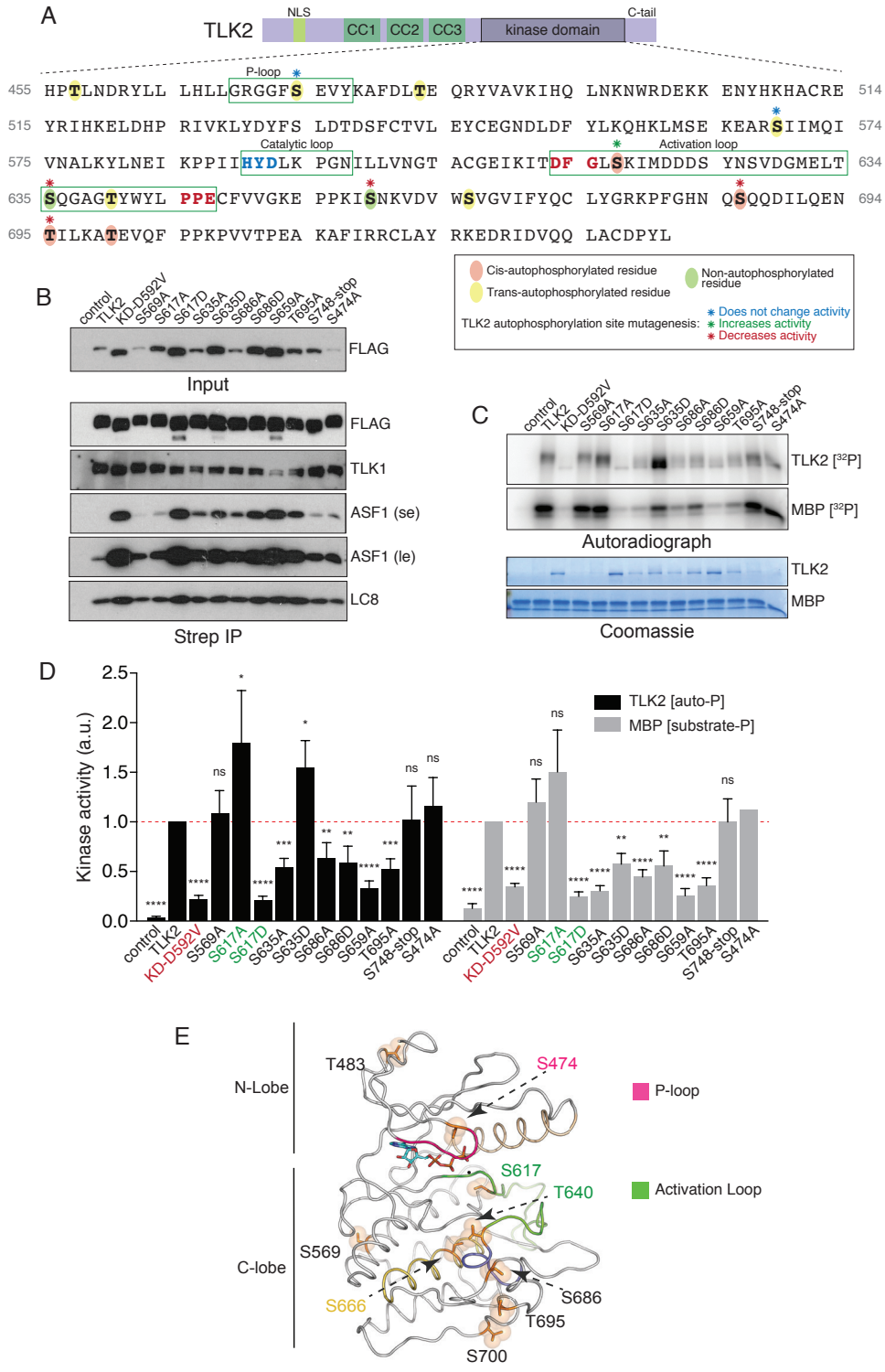

Figure 11. TLK2 auto- and trans-phosphorylation in the kinase domain. *(Legend in the next page)*

mostly found in the C-tail or the loops between the predicted CC domains. We focused our attention in the phosphosites belonging to the kinase domain. These phosphosites can be categorized into two groups, a first one including the phosphosites in the TLK2-KD resulting from inter-molecular phosphorylation (Trans), and a second group arising from intra-molecular phosphorylation (Cis) in the TLK2-WT. The active TLK2-WT monomer of the heterodimer undergoes Cis phosphorylations (S617, S686, T695 and T700) in the kinase domain. Active TLK2-WT homodimers displayed the Cis phosphosites mentioned above together with additional Trans phosphorylations (S474, T483, S569, T640, S666) in the kinase domain.

Most of the kinase domain phosphosites localize in the C-lobe, around the catalytic and activation loops (Figure 11E). Phosphorylations in the P-loop have been previously observed to influence the regulation of other kinases (Schumacher et al., 2012; Welburn et al., 2007). The modelling of a of a phosphoserine instead of S474 in the P-loop of the kinase domain structure suggests that this modification could affect ATP binding, leading to an activity reduction (data not shown). However, in *in vitro* kinase assays we have not observed significant reduction of activity with S474A mutant (Figure 11B-D). Generation of a phosphomimic mutant S474D will be needed to answer this question in the future.

From the phosphoresidues present in the C-lobe, S569 is located near the C-spine and its phosphorylation will likely aid in fixing the conformation of the catalytic loop through interactions with the main chain. Its mutation to alanine would not allow this interaction but it could be favoured by hydrophobic contacts with A605, thus not affecting the activity (Figure 11B-D). A very interesting phosphorylation occurs in S617, which is located just after the DFG motif. A phospho-mimic mutation (Asp, S617D) of this residue inhibited the kinase activity (Figure 11B-D). This is likely due to the fact that the presence of a phosphate will disturb the F614 conformation in the DFG motif, affecting the R-spine. A conserved residue between TLK1 and TLK2, T635, is in the position analogous to the activating phosphorylation of CDK2 and this residue was found phosphorylated in TLK1 in A. Groth's laboratory. This residue was found unphosphorylated in our mass spectrometry experiments (Figure 11A). Therefore, its phosphorylation does not seem to be essential for activity *in vitro* or likely to be the result of Cis or Trans-autophosphorylation. The S635A and S635D mutations in this residue reduced the activity of TLK2 on MBP but had converse effects on overall autophosphorylation. While S635A showed reduced autophosphorylation compared to TLK2-WT, it was increased by the S635D mutation.

(A) All the phosphorylation sites detected in the TLK2 kinase domain are mapped on the primary sequence and whether they are Cis, Trans or non-autophosphorylated sites is indicated. The essential structures of the kinase domain are highlighted in the primary sequence. Phosphosites whose activity has been tested in kinase assays are further designated with an asterisk. (B) Western blotting of input or Strep-pulldowns from AD293 cells transiently transfected with Strep-FLAG tagged TLK2 mutants. Levels of co-purified TLK1, ASF1 and LC8 are shown. Short or long exposure of the same film is indicated as (se) or (le), respectively. (C) Representative autoradiograms of *in vitro* kinase assays of Strep-pulldowns from cells expressing Strep-FLAG tagged TLK2 phosphorylation site mutants (S/T>A) or mimics (S>D). (D) Quantification of *in vitro* kinase assays of the indicated phosphorylation mutants of TLK2 isolated from AD293 cells by Streptavidin pull downs showing relative autophosphorylation and MBP phosphorylation. Data are quantified from N=2-7 independent experiments. (E) The nine phosphorylation sites in the kinase domain can be modelled on the structure. The sites are highlighted in stick and sphere representation and lie in the N-lobe, activation loop and C-lobe.

This could indicate that S635 is modified by another kinase *in vivo* to modulate TLK1/2 activity. Interestingly S686 and T695 most likely favour the kinase activity by stabilizing its structure and in fact, alanine mutations of these two residues decrease the activity of the enzyme (Figure 11B-D). Together, we have showed that TLK2 activation occurs through multiple Cis- and further Trans- autophosphorylations in the context of dimers or oligomers, and we have described key autophosphorylation sites critical for its activity.

Identification and docking of small molecule inhibitors of TLK2 activity

The implication of TLK2 in some types of cancer has suggested that small molecule inhibitors of its activity could be used as anti-cancer agents (Kim et al., 2016b). While specific inhibitors of TLK2 have not yet been identified, and given the high similarity both kinases TLK1 and TLK2 have in the kinase domain, we tested several compounds previously identified to inhibit TLK1 *in vitro* (Ronald et al., 2013). The compounds of the family of phenothiazine antipsychotics Metaraminol (MTM) and Fluphenazine dihydrochloride (FF) were shown not to inhibit TLK1 *in vitro*, whereas Thioridazine hydrochloride (THD), Perphenazine (PPH) and Promazine hydrochloride (PMZ) were shown to do so (Ronald et al., 2013). To test these small molecule inhibitors, we addressed substrate phosphorylation by immuno-precipitated SF-TLK1 and SF-TLK2 overexpressed and purified from AD293 cells and used the generic kinase substrate MBP. In our experiments, we used Staurosporine (STS) and the related Nocardiopsis as positive controls. These ATP-competitive kinase inhibitors bind to many kinases with high affinity and little selectivity. Treating with STS or Nocardiopsis completely abolished TLK1/2 catalytic activity (Figures 12A-B, 12D). We were unable to reproduce inhibition of TLK1 or TLK2 activity by THD, PPH or PMZ in *in vitro* kinase assays (Figure 12A-B).

Molecular dynamics (MD) simulations using the crystal structure of the TLK2 kinase domain was performed to predict small molecule inhibitors of TLK2. Some of these compounds were tested in *in vitro* kinase assays but did not show any activity against TLK2 (Figure 12B and data not shown). We tested additional compounds shown to have activity against TLK2 in a large screen of commercially available small molecules (Gao et al., 2013). Several of these inhibitors showed activity against TLK2, including CGP74541A (CDK1 inhibitor) and Inhibitor XIII (GSK3 inhibitor), as well as the Indirubin derivatives E804 and indirubin-3´-monoxime (Figure 12D). Indirubin is an active component of Danggui Longhui Wan, a traditional Chinese medicine formulation, whose encouraging clinical results in chronic myelocytic leukaemia patients have stimulated numerous studies on this compound (Hoessel et al., 1999). With the exception of the monoxime variant of indirubin, the other three compounds substantially inhibited TLK2 kinase activity (Figure 12D). We modelled the chemical compounds in our kinase domain structure using HADDOCK (Van Zundert et al., 2016) to rationalize the molecular bases of the inhibition (Figure 12C-E). The top 40 docking solutions were selected for each compound and analysed in detail. Out of them, the best docking solutions without steric clashes with

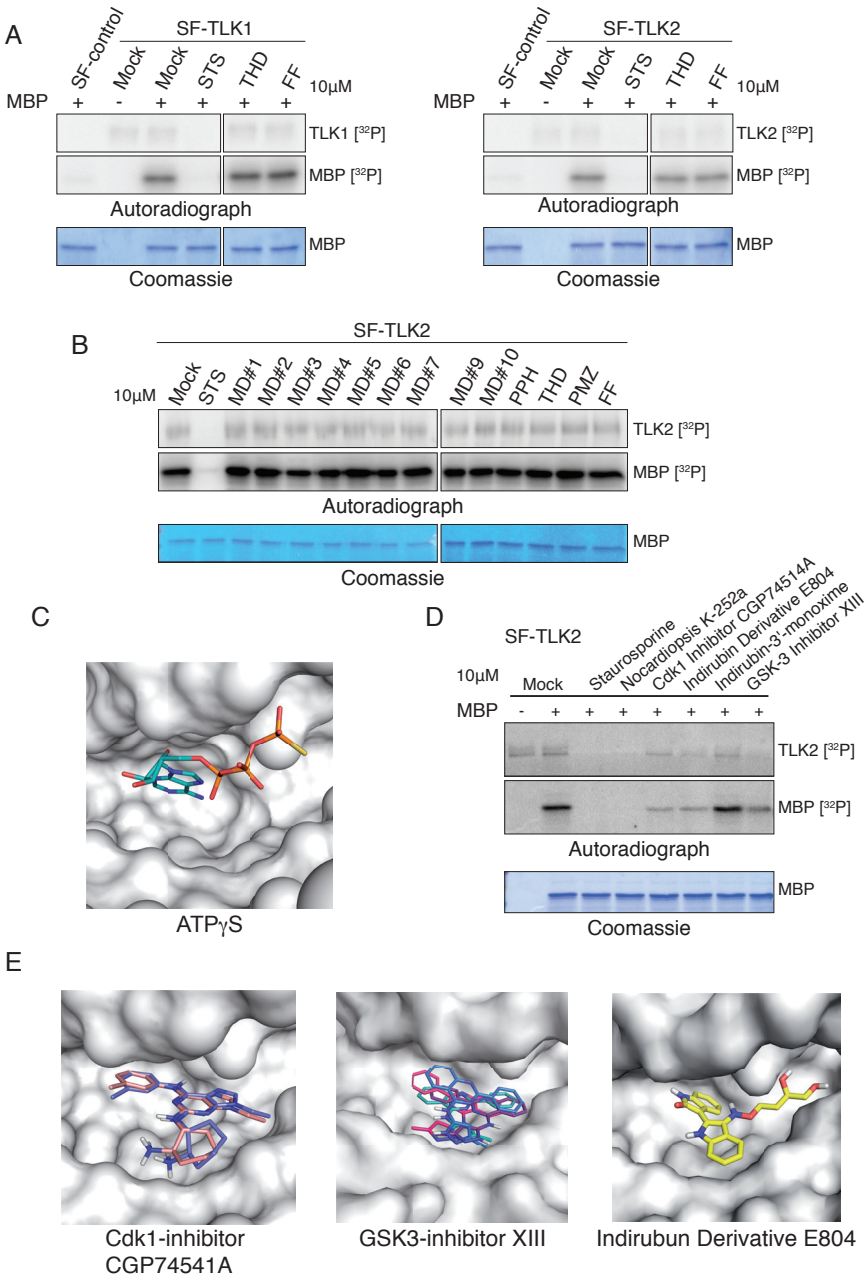

Figure 12. Identification and docking of small molecule inhibitors of TLK2 activity.

(A) *In vitro* kinase assay of TLK1 and TLK2 isolated from AD293 cells by Streptavidin pull downs in the presence or absence of the substrate MBP and the indicated kinase inhibitors. All inhibitors were used at 10 μM and the Coomassie stained gel shows equal loading of MBP. (B) *In vitro* kinase assay of TLK2 in the presence of several kinase inhibitors predicted from Molecular dynamics (MD) or previously described in Ronald et al., 2013. Coomassie stained gel shows equal loading of MBP. (C) Detailed view of the ATP binding pocket in the TLK2 kinase structure showing the bound ATPγS molecule. (D) *In vitro* kinase assay of TLK2 in the presence or absence of the substrate MBP and the indicated kinase inhibitors from Gao et al., 2013. All inhibitors were used at 10 μM and the Coomassie stained gel shows equal loading of MBP. (E) Zoom of the ATP binding pocket containing the modelled molecules shown to inhibit TLK2 kinase activity. The best score modelling results displayed no steric clashes.

the protein are shown. In the case of CGP74541, two solutions with minor differences were found, while for indirubin E804 only one solution did not show clashes with the protein. In the case of the GSK3 inhibitor XIII, four different solutions could be docked by HADDOCK in the nucleotide binding pocket of the kinase domain. Structural modelling indicated that the different behaviour of indirubin-3´-monoxime could be due to the absence of the aliphatic chain in 3' and the presence of a bulky iodine in the indol ring. The aliphatic region is engaged in interactions in the cavity while the iodine atom will clash with the protein moiety, thus avoiding binding and inhibition. These preliminary results show that the structure of the kinase domain of TLK2 can be successfully used in virtual screening for TLK2 inhibitors. However, further efforts need to be made in order to identify more specific and potent TLK inhibitors.

Design of an analog-sensitive allele for TLK2 kinase

Identifying specific small molecule inhibitors of TLK2 has proven to be challenging (Figure 12). The lack of a suitable specific TLK2 inhibitor, together with the long-term aim to identify novel TLK2 substrates, lead us to take a chemical genetics approach. A method for generating analog-sensitive (AS) kinase alleles was first developed by K. Shokat's laboratory (Bishop et al., 1998). The strategy consists of generating a silent "space-creating" mutation in the ATP binding pocket (gatekeeper residue) of the target kinase that sensitizes it to inhibition by a bulky ATP analog that is unable to inhibit wild type kinases. These two parts, the ATP binding pocket and the ATP analog, are also known as the "hole" and the "bump", respectively. The gatekeeper mutation is generated by using site-directed mutagenesis to change an amino acid harbouring a large side chain for an Alanine or Glycine, that have a small side chain, thus generating a unique open pocket in the target kinase.

In order to identify the putative gatekeeper residue of TLK2, we did a sequence alignment of TLK2 together with other kinase domains for whose an AS allele had been successfully made. The alignment revealed that the putative TLK2 gatekeeper residue was Leucine 544 (Figure 13A). Taking advantage of the crystal structure provided by G. Montoya's laboratory, we could confirm that this residue localized in the ATP binding pocket, specifically in the β5-sheet. Thus, we proceeded to mutate it to a Glycine or Alanine (L544G and L544A mutants). We next expressed and immunoprecipitated these AS mutants in AD293 cells and evaluated their binding to their physiological substrate, ASF1, and measured their kinase activity. We could observe that L544G and L544A mutants exhibited higher binding affinity to ASF1, similar to what we have previously observed with the kinase dead TLK2-KD mutant (Figure 8F and 13B), and we reasoned they may have less catalytic activity. This was confirmed by *in vitro* kinase assays with the L544G mutant: its catalytic activity towards the MBP substrate resembled that of the kinase dead TLK2-KD (Figure 13C).

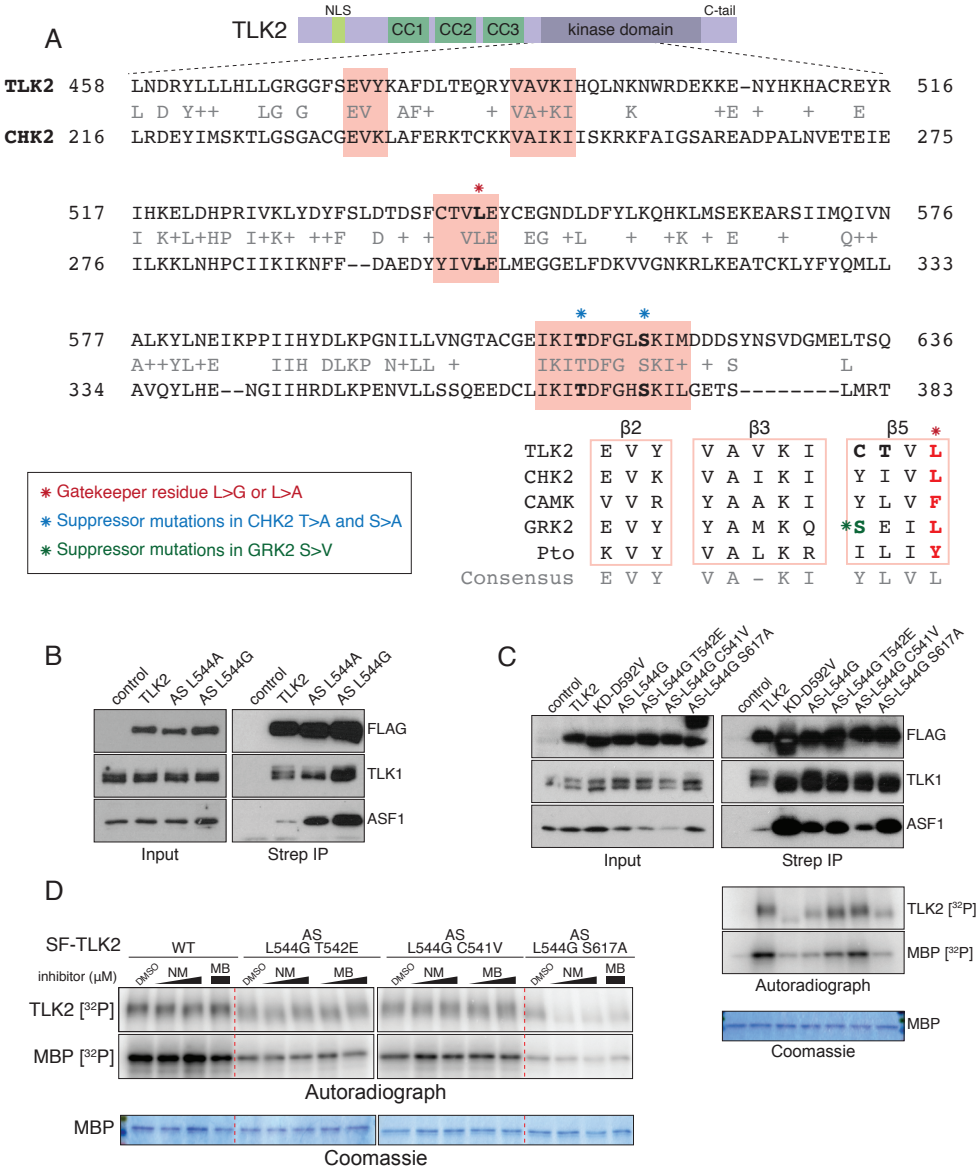

Figure 13. Design of an analog-sensitive allele for TLK2 kinase.

(A) Sequence alignment of TLK2 kinase domain with the one from CHK2. Highlighted in red boxes, the conserved secondary structures; marked with a red asterisk, the gatekeeper residue; marked with a blue asterisk, the suppressor mutations generated in CHK2 (top panel). Structure-based sequence alignment of some kinases for which an AS allele has been generated at selected positions in the three central β strands (β2, β3 and β5) (Zhang et al., 2005a). Marked with a green asterisk, the suppressor mutation generated in GRK2 (bottom panel). (B) Western blotting of input or Strep-pulldowns from AD293 cells transiently transfected with Strep-FLAG tagged TLK2 mutants. Levels of co-purified TLK1 and ASF1 are shown. (C) Western blotting of input or Strep-pulldowns from AD293 cells transiently transfected with Strep-FLAG tagged AS TLK2 mutants with gatekeeper with or without suppressor mutations. Levels of co-purified TLK1 and ASF1 are shown (top panel). Autoradiograms of *in vitro* kinase assays of Strep-pulldowns from cells expressing Strep-FLAG AS TLK2 mutants on the MBP substrate. Coomassie stained gel shows equal loading of MBP (bottom panel). (D) *In vitro* kinase assay of wild type TLK2 and AS TLK2 mutants in the presence of 1NM-PP1 (NM) or 3MB-PP1 (MB) bulky kinase inhibitors. Coomassie stained gel shows equal loading of MBP. Data is representative of three independent experiments.

According to Lopez et al., 2014, about 10-15% of kinases tested to date for chemical genetics do not tolerate the mutation of the gatekeeper residue and experience a severe loss of activity. In those cases, second site suppressor mutations are necessary to rescue kinase activity. CAMK is a kinase that tolerates the gatekeeper mutation (Zhang et al., 2005a), whereas CHK2, GRK2 or Pto are intolerant and need suppressor mutations. We tested three different suppressor mutations that were shown to rescue catalytic activity in CHK2 or GRK2, due to the higher similarity in the primary sequence in the β-sheet secondary structures (Figure 13A). To this end, we generated the S617A mutation, resembling the S>A suppressor mutation in CHK2, on top of a L544G backbone. We previously showed that this mutation increased autophosphorylation activity of wild type TLK2 (Figure 11C-D). We additionally generated the C541V mutation, resembling the S>V suppressor mutation in GRK2, and T542E mutation, resembling wild type sequence in GRK2, on top of a L544G backbone. From the three suppressor mutants, only L544G-C541V bound ASF1 with lower affinity in immunoprecipitation experiments, potentially indicating higher activity, and both L544G-C541V and L544G-T542E rescued the catalytic activity to levels comparable to wild type TLK2 in kinase assays (Figure 13C).

Once a functional TLK2 AS allele was successfully generated, the next step was to identify suitable inhibitors that would fit in the pocket of AS kinases and have minimal activity towards other wild type kinases. The most commonly used AS kinase inhibitors are Pyrazolo[3,4-d] pyrimidine inhibitors, derived from the promiscuous kinase inhibitor PP1. We tested side by side 1NM-PP1 (NM), a selective AS kinase inhibitor and the newly developed 3MB-PP1 (MB), that has improved selectivity and potency (Lopez et al., 2013). As expected, these inhibitors did not show any activity with the wild type allele of TLK2. Surprisingly to us, they also did not inhibit the AS TLK2 alleles L544G-C541V and L544G-T542E, even at high concentrations (up to 100 μM) (Figure 13D). Conversely, they showed some inhibitory activity against the L544G-S617A AS allele, especially on the autophosphorylation, despite this suppressor mutant could not overcome the loss of activity from the gatekeeper mutation (Figure 13D). Further characterization of these AS mutants will be needed to confirm sensitivity to ATP analogs. Then we will generate an AS allele using CRISPR to introduce the mutation in endogenous TLK2. This would provide a useful tool for reversible chemical inhibition of TLK2 in cells. Moreover, specific bulky ATP analogs bound to thiol groups (γ-S-ATP) would allow for specific substrate thiophosphorylation, which could then be enriched and analysed by LC-MS/MS to identify new TLK targets.

Chapter 2

Differential requirements for Tousled like kinases 1 and 2 in mammalian development

Sandra Segura-Bayona[1], Philip A. Knobel[1], Helena González Burón[1], Sameh A. Youssef[2], Lluís Palenzuela[1], Alain de Bruin[2] and Travis H. Stracker[1]

[1] Institute for Research in Biomedicine (IRB Barcelona), the Barcelona Institute of Science and Technology, Barcelona, Spain.

[2] Dutch Molecular Pathology Center, Department of Pathobiology, Faculty of Veterinary Medicine, Utrecht University, Utrecht, The Netherlands.

Statement of contribution:

S Segura-Bayona designed, performed and analysed most of the experiments.

PA Knobel maintained mouse cohorts, quantified IHC staining in Figure 16A-B, 16E and monitored Sox2-Cre mice in Figure 18A-C.

H González-Burón characterized TLK1 deficient mice and TLK2 embryonic lethality, shown in Figure 14.

L Palenzuela maintained mouse cohorts.

SA Youssef and A de Bruin assessed placental biology, shown in Figure 15.

TH Stracker designed and analysed experiments and supervised the whole project.

TLK1 is dispensable for murine viability whereas TLK2 is an essential gene

Despite their identification nearly 20 years ago, the role of the ubiquitously expressed TLK1 and TLK2 kinases in mammalian physiology remains unexplored. In particular, whether they have distinct, overlapping or entirely redundant roles in particular tissues or cell types during development or aging remains unknown. We set out to determine the roles of TLK1 or TLK2 during mammalian development by generating mice deficient for either *Tlk1* or *Tlk2*. Mice homozygous for a gene-trapped allele of *Tlk1* (*Tlk1*^{T}) (Figure 14A) showed efficient reduction of *Tlk1* expression and no TLK1 protein was detectable in Westerns from MEF lysates (Figure 14B). No compensatory changes in *Tlk2* mRNA or TLK2 protein levels were evident (Figure 14B and data not shown). Despite the implication of TLK1 in many critical cellular processes (Canfield et al., 2009; Groth et al., 2003; Kelly and Davey, 2013; Krause et al., 2003; Li et al., 2001; Sen and De Benedetti, 2006; Sunavala-Dossabhoy and De Benedetti, 2009; Sunavala-Dossabhoy et al., 2005), *Tlk1*$^{T/T}$ mice were born at normal Mendelian ratios (Figure 14C) and showed no obvious morphological or size differences at birth or during the first months of development. In addition, *Tlk1*$^{T/T}$ mice did not exhibit any obvious developmental phenotypes or accelerated morbidity over 18 months (Figure 14D). While we cannot rule out more subtle effects on repair processes or developmental programs, these data indicated that TLK1 was dispensable for murine development and aging in homeostatic conditions.

Based on previous data from lower organisms such as *Drosophila* or *C. elegans*, we expected that loss of TLK1 activity would result in severe phenotypes in the mouse (Carrera et al., 2003; Han et al., 2003). The lack of any clear phenotypes in *Tlk1*$^{T/T}$ animals suggested potentially redundant activities, with TLK2 being the most likely candidate. To address this, we generated a conditional, gene-trapped allele of *Tlk2* (Figure 14E) and interbred heterozygous mice to generate *Tlk2* deficient animals. In sharp contrast to *Tlk1*, we did not observe any live births of *Tlk2*$^{T/T}$ mice, indicating embryonic lethality (Figure 14G). To understand the cause of death, we examined embryos at different developmental stages. The number of *Tlk2*$^{T/T}$ embryos observed from E10.5 to E13.5 was consistent with expected Mendelian ratios (Figure 14H), although embryos were smaller in all cases (Figure 14I). *Tlk2*$^{T/T}$ embryos appeared anaemic (Figure 14I) and perished by E15.5, as no heartbeat was detectable. By E16.5 extensive tissue autolysis was evident. Fibroblast cultures from E14.5 embryos confirmed that *Tlk2* mRNA and TLK2 protein levels were reduced and that there was no compensatory increase of TLK1 (Figure 14F and data not shown). Further examination of *Tlk2*$^{T/T}$ embryos by conventional immunohistochemistry and lightsheet-based fluorescence macroscopy did not reveal any consistent defects and suggested that embryos were developmentally delayed, but in the majority of cases morphologically normal. Collectively, our data suggested that TLK2, but not TLK1, was essential for embryonic viability.

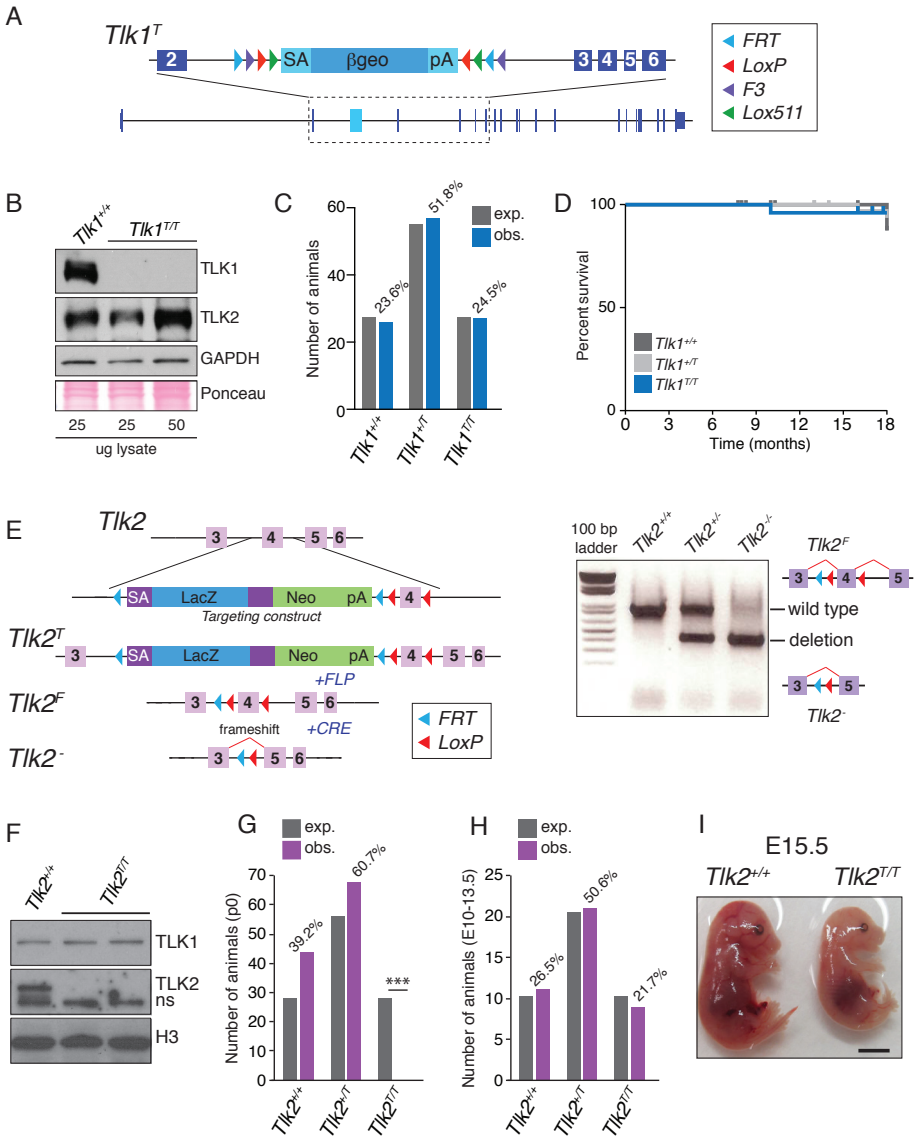

Figure 14. TLK1 is dispensable for murine viability whereas TLK2 is an essential gene.

(A) Schematic of the *Tlk1* genetrap allele (*Tlk1*^{T}), showing the position of the Flex-vector genetrap cassette in the *Tlk1* locus. (B) Western blotting of TLK1 and TLK2 protein levels in MEF cultures of the indicated genotype. Ponceau red stained blot showed equal loading. (C) *Tlk1*$^{T/T}$ mice are born at the expected (exp.) Mendelian ratios. Numbers of pups of the indicated genotype observed (obs.) from 32 litters of *Tlk1*$^{+/T}$ mice (110 pups total) are indicated. Percentage observed is indicated above the bar graphs. (D) Normal survival of *Tlk1*$^{T/T}$ mice. Kaplan Meier plot of animal survival over 18 months (n=25, 41 and 26 for *Tlk1*$^{+/+}$, *Tlk1*$^{+/T}$ and *Tlk1*$^{T/T}$ respectively). (E) (Left panel) Schematic of the *Tlk2* knockout first allele (*Tlk2*^{T}). The position of the genetrap cassette, the allelic configurations and their designations following FLP and CRE expression are shown. (Right panel) Example of the PCR-based genotyping of *Tlk2*$^{F/F}$ and *Tlk2*$^{-/-}$ alleles. (F) Western blotting of TLK1 and TLK2 protein levels in MEFs of the indicated genotype. Histone H3 is shown as a loading control and a non-specific (ns) band recognized by the TLK2 antibody is indicated. (G) *Tlk2* deficiency is embryonic lethal. The number of animals expected (exp.) from 27 *Tlk2*$^{+/T}$ breedings (112 pups total) assuming normal Mendelian inheritance is shown compared to the number of observed pups (obs.). Percentage observed is indicated above the bar graphs. Based on the genotypes of a total of 112 pups from 14 independent litters, a p-value of <0.0001 was determined using binomial distribution and indicated by ***. (H) Normal Mendelian distribution of genotypes was observed amongst 41 E10.5 to E13.5 embryos from 6 individual *Tlk2*$^{+/T}$ breedings. Percentage observed is indicated above the bar graphs. (I) Examples of littermate E15.5 embryos (scale bar = 2mm).

TLK2 is essential for placental development

As consistent defects in embryonic morphology were not observed, we examined placental function. At E14.5 *Tlk2*$^{T/T}$ placentas were smaller and we often observed a lack of blood circulation in the umbilical cord. To address this phenotype further without potential complications from the genetrap, we excised it by crossing to FlpO expressing mice, thus rendering Exon 4 floxable (*Tlk2*^{F}) (Figure 14E). Crosses with mice expressing Sox2-Cre, that is active in the embryonic epiblast cells, effectively deleted Exon 4 and yielded *Tlk2*$^{+/-}$ animals that were then interbred to generate *Tlk2*$^{-/-}$ embryos (Figure 14E).

The placenta acts as the interface between the maternal tissue and the foetus, from which the foetus acquires resources for growth such as nutrients or growth factors and needed for the exchange of gases and waste products. Defects in placental development have been previously associated to foetal growth retardation and death (Rossant and Cross, 2001). Placentas are composed of tissue derived from the embryo, the trophoblast; and maternal tissue, the decidua. The trophoblast is the main organized structure needed for correct placental function and is derived from the outer trophectoderm layer of the embryonic blastocyst. In mouse embryos, trophectoderm cells stop dividing and undergo DNA endoreduplication to give rise to trophoblast giant cells after implantation. In addition, the placental vascular network is organized through the labyrinth, a dense cellular structure that contains several differentiated lineages such as labyrinthine trophoblasts or syncytiotrophoblast cells. The labyrinth is supported by the spongiotrophoblast, which locates between the outer trophoblast giant cells next to de decidua and the labyrinth, closest to the embryo.

Considering the well described placental structure above, we next set out to histologically examine *Tlk2*$^{-/-}$ placentas from embryonic days E10.5 to E16.5. At all stages, *Tlk2*$^{-/-}$ placentas were moderately to severely smaller, thinner and less cellular compared to *Tlk2*$^{+/+}$ or *Tlk2*$^{+/-}$ littermates, and they were also poorly vascularized (Figure 15A-E). At E10.5 through E12.5 the labyrinths of *Tlk2*$^{-/-}$ placentas were disorganized and composed of less differentiated and less mature trophoblasts (Figure 15D). *Tlk2*$^{-/-}$ placentas had moderately to severely reduced numbers of labyrinth trophoblast, syncytiotrophoblast, spongiotrophoblast (including glycogen cells) and mildly to moderately reduced numbers of trophoblastic giant cells and vasculature (Figure 15C-E). These data indicated that TLK2 was required for normal placental development and function, and that its loss led to late embryonic lethality.

The influence of TLK2 deficiency on proliferation and gene expression in the placenta

As the regulation of ASF1 by TLK activity has been linked to ongoing DNA replication, we examined trophoblast proliferation by IHC using the marker Ki67 (Silljé et al., 1999). By E12.5 most cells of the trophoblastic lineage are differentiated and their rate of

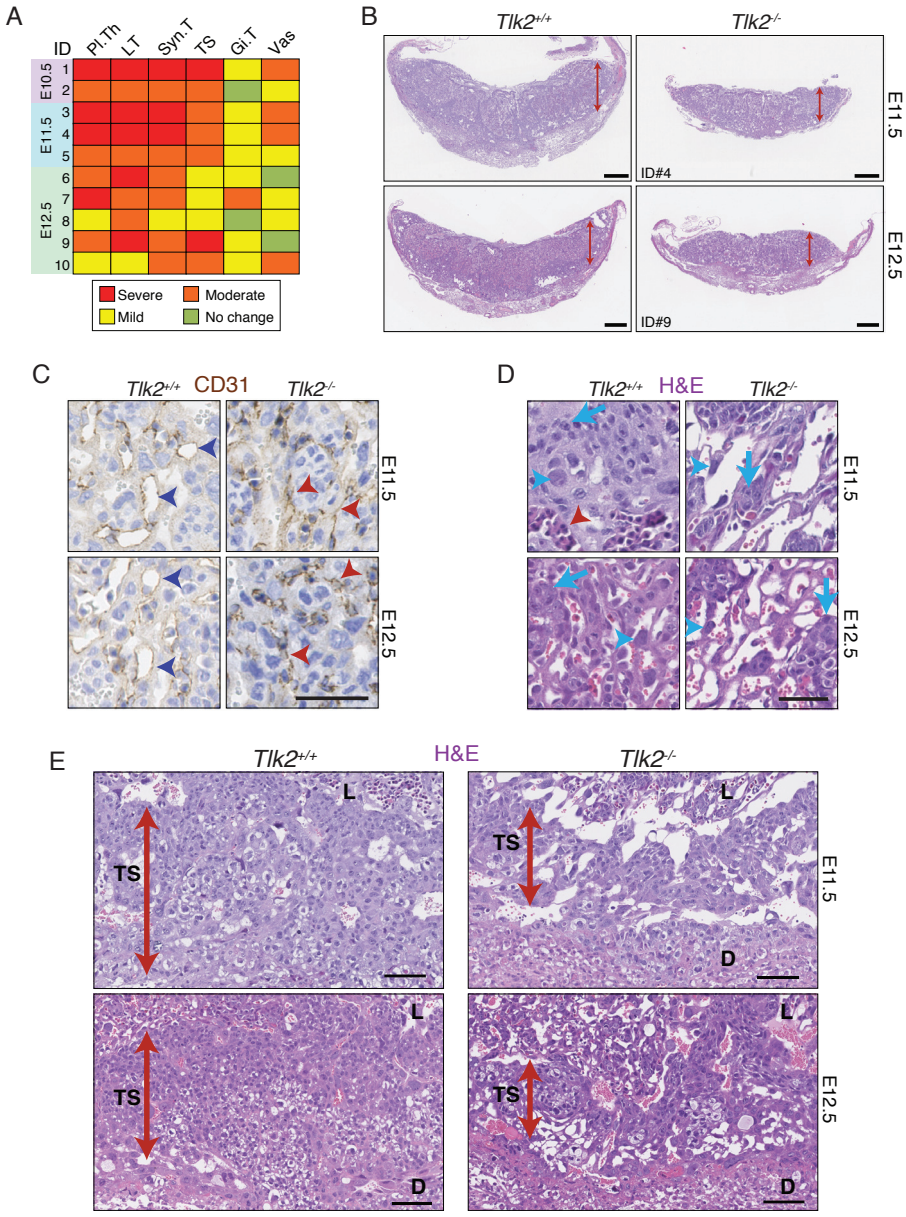

Figure 15. TLK2 is required for placental development.

(A) Semi-quantitative analysis of histological phenotypes in *Tlk2*$^{-/-}$ placentas. In each case, *Tlk2*$^{-/-}$ placentas (n=10) at the indicated age were compared to wild type littermates. Phenotypes are abbreviated as follows: Placental thickness (Pl. Th), numbers/size of Labyrinth trophoblasts (LT), Syncytiotrophoblasts (Syn.T), Spongiotrophoblasts including glycogen cells (TS), Giant cell trophoblasts (Gi.T) and Vasculature (Vas). Summary of the grading system used (Gibson-Corley et al., 2013) is provided in the Materials and Methods. (B) Sections from E11.5 and E12.5 littermate placentas stained with H&E. *Tlk2*$^{-/-}$ placentas are thinner, less cellular and poorly vascularized compared to *Tlk2*$^{+/+}$. Scale bars = 500 microns. (C) CD31 staining reveals that the vasculature of *Tlk2*$^{-/-}$ placentas is miniaturized, collapsed and appears slit-like (red arrowheads) compared to the well-developed, widely opened vasculature of *Tlk2*$^{+/+}$ (blue arrowheads). Scale bar = 20 microns. (D) H&E staining from the indicated age and genotype showing fewer and smaller trophoblasts (arrows) and Syncytiotrophoblasts (blue arrowheads) with an absence of foetal vasculature (red arrowhead) in *Tlk2*$^{-/-}$ placentas. Scale bar = 20 microns. (E) H&E staining of placentas showing a thinner Trophospongium (Spongiotrophoblasts and glycogen cells) in *Tlk2*$^{-/-}$ placentas. The Trophospongium (TS), labyrinth (L) and decidua (D) are indicated. Scale bar = 50 microns.

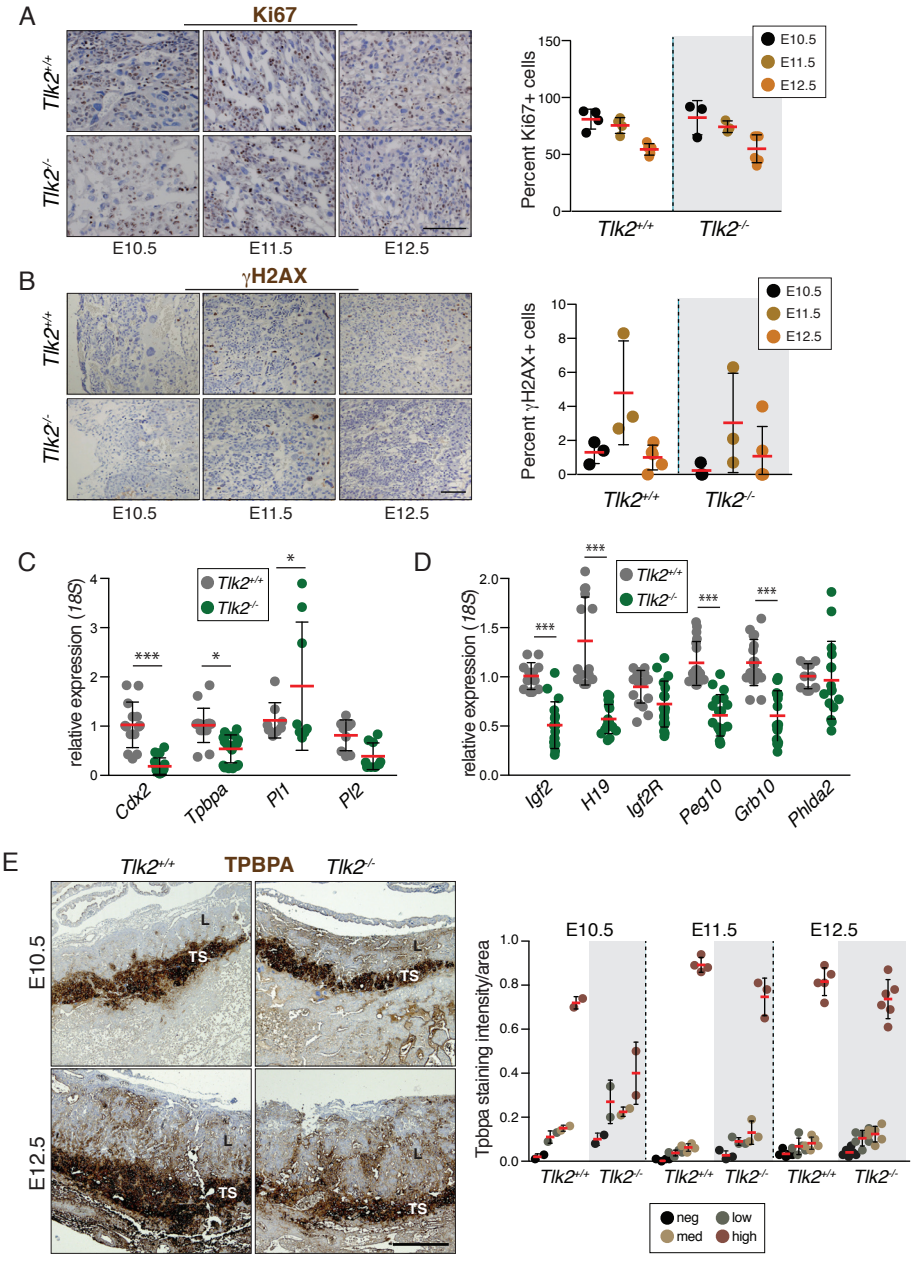

Figure 16. The influence of TLK2 deficiency on proliferation and gene expression in the placenta .

(A) Immunohistochemical staining of the proliferative marker Ki67 or (B) the DNA double-strand break marker γH2AX in E10.5, E11.5 and E12.5 placentas of the indicated genotype. Similar numbers of proliferative cells are visible in the labyrinth of *Tlk2*$^{-/-}$ placentas compared to wild type at each stage. Mean percent positive cells (red bars) and SD is graphed in right panels. n=3 and 2 at E10.5, n=3 and 3 at E11.5 and n=5 and 6 at E12.5 for *Tlk2*$^{+/+}$ and *Tlk2*$^{-/-}$, respectively. At least 200 total cells were counted for each individual and scale bar in (A) = 10 microns and in (B) = 100 microns. (C) and (D) Quantitative real time PCR analysis of genes expressed in trophoblast lineages from E12.5 placenta samples. Combined data represents the mean of triplicate samples from 3 individual animals of each genotype. Statistical significance was determined using an unpaired t-test (***p=<0.0001, **p=<0.001, * p=<0.05). (E) Immunohistochemical staining for TPBPA reveals a thinner trophospongium (TS) in the absence of TLK2 at both E10.5 and E12.5. The orientation of the labyrinth (L) is also indicated. Quantification of signal intensity distribution in the TS is shown in the right panel, normalized to area. Scale bar = 500 microns.

proliferation decreases (Cross, 2000; Simmons and Cross, 2005). Regardless of genotype, we observed similar percentages of Ki67 positive cells at each stage of development suggesting that the overall number of proliferating cells was similar (Figure 16A). In addition, we did not observe any significant increase in the DNA double strand break marker γH2AX (Figure 16B), suggesting that overall levels of proliferation and DNA damage were similar to wild type.

In addition to DNA replication, TLK2 has been implicated in transcriptional regulation through the phosphorylation of ASF1a (Abascal et al., 2013; Bruinsma et al., 2016). To address the possibility that transcription may be affected, we examined the mRNA expression levels of several genes required for trophoblast differentiation; *Cdx2*, *Tpbpa*, *Pl1* and *Pl2* (Simmons et al., 2007). We observed lower levels of *Cdx2*, *Tpbpa*, and *Pl2* in the *Tlk2*$^{-/-}$ placentas, reflecting reduced numbers and/or defective differentiation of trophoblast stem cells, spongiotrophoblasts and canal or sinusoidal trophoblast giant cells, respectively (Figure 16C). In contrast, the expression of *Pl1*, that is a marker for parietal trophoblast giant cells and is normally reduced by E11.5, was slightly upregulated compared to wild type placenta, although this was more variable amongst individual samples (Figure 16C) (Simmons et al., 2007). In addition, the expression of many imprinted genes that influence placental development, including *Igf2*, *H19*, *Peg10* and *Grb10*, was reduced in *Tlk2*$^{-/-}$ placentas, while others, such as *IgfR2* and *Phlda2*, were expressed at similar levels to that of wild type (Figure 16D) (Cleaton et al., 2014; Simmons et al., 2007). The reduced size of the *Tlk2*$^{-/-}$ labyrinth and reduced area of TPBPA positive cells was further confirmed with IHC (Figure 16E). Together, these data suggested that the loss of TLK2 did not cause clear defects in trophoblast proliferation or survival, but reduced the expression of numerous genes important for their normal function and led to impaired differentiation and placental function.

TLK2 interacts with ASF1 and influences its phosphorylation in the placenta

To understand why placental function was dependent on TLK2 and not TLK1, we examined their relative mRNA expression and protein levels. We found similar mRNA expression patterns of both genes in the wild type placenta at E13.5, E15.5 and E17.5 (Figure 17A). The protein levels of TLK2 were similar in placental tissue compared to tissue from the embryo (h-l, heart and foetal liver), while TLK1 protein levels were strongly increased in the embryonic tissues compared to the placenta, although TLK1 was detectable in placentas (Figure 17B-C). We next compared wild type placentas to *Tlk2*$^{-/-}$ placentas to exclude the possibility that there was any compensation of TLK1 in *Tlk2*$^{-/-}$ placentas. We observed that TLK1 followed the same pattern of protein expression in *Tlk2*$^{-/-}$ placentas as it did in wild type placentas, as it was significantly more abundant in the embryonic tissue (L, foetal liver) in both cases (Figure 17C). This suggested that TLK1 was significantly less abundant in the placenta than in the embryo, providing a potential explanation as to why placental development was particularly sensitive to *Tlk2* deficiency.

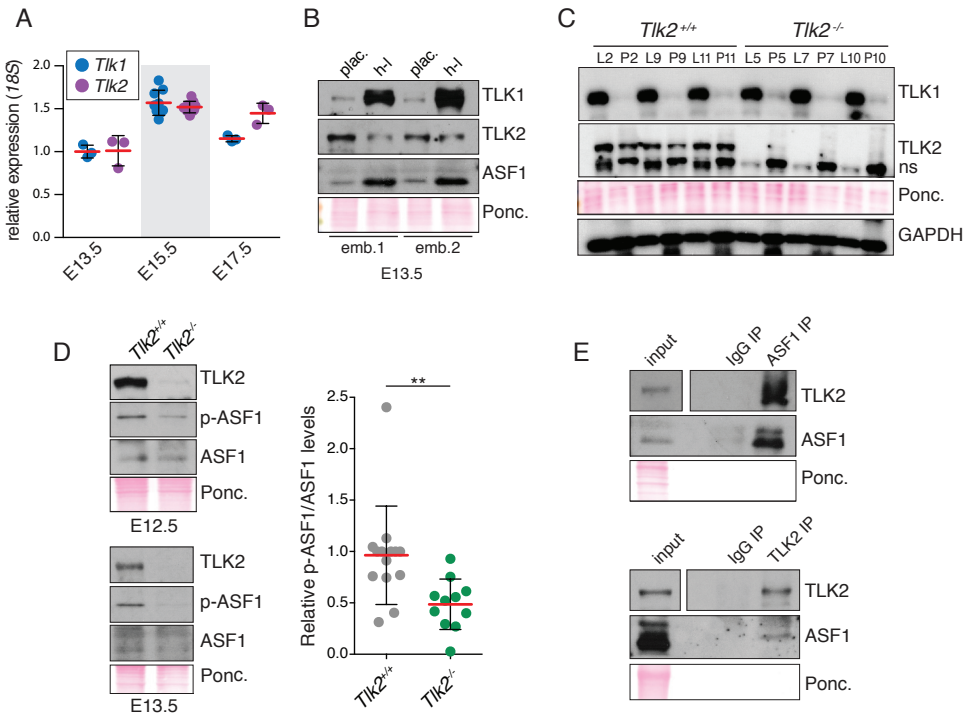

Figure 17. TLK2 interacts with ASF1 and influences its phosphorylation in the placenta.

(A) Quantitative real time PCR of *Tlk1* and *Tlk2* in wild type placentas of the indicated age. Mean (red bars) and SD of triplicate samples is graphed (n=1, 3 and 1 for each age indicated). (B) Western blotting of TLK1, TLK2 and ASF1 in lysates from E13.5 placenta (Ponc. = Ponceau red stained membrane). TLK2 levels are similar in either tissue (placenta = plac. and heart/foetal liver = h-l) while TLK1 levels are much higher in embryonic tissue relative to placenta. Samples from 2 littermate wild type placentas are shown. (C) Western blotting of lysates from embryonic tissue (foetal heart and liver = L) and placenta (P) from littermate animals of the indicated genotypes. While TLK2 protein levels are similar between tissues, TLK1 protein levels are much higher in the embryonic tissues relative to placenta, both in wild type and *Tlk2*$^{-/-}$ embryos. NS indicates a non-specific band. (D) Reduced ASF1-S166 phosphorylation (p-ASF1) in the E12.5 and E13.5 *Tlk2*$^{-/-}$ placentas. Western blotting of lysates for TLK2, ASF1 and p-ASF1 from littermates of the indicated age. In each case, blots shown are from the same membrane (Ponc. = Ponceau red stained membrane). Quantification of p-ASF1/ASF1 levels in multiple samples of the indicated genotype is shown in the right panel (additional Western examples are shown in Supplementary Figure 2A). Statistical significance (p=0.0064) was determined using an unpaired t-test and the mean (red bars) and SD are indicated (n=14 and 11, respectively). (E) Co-immunoprecipitation of endogenous TLK2 and ASF1 from wild type E13.5 placental lysates using antibodies for ASF1 (top panels) or TLK2 (bottom panels). Ponc. = Ponceau red stained membrane. Additional examples are shown in Supplementary Figure 2B.

Since ASF1a and ASF1b are the most clearly defined targets of TLK1 and TLK2 (Figures 8 and 9), we next focused on determining the level and phosphorylation status of ASF1 in normal and *Tlk2* deficient placentas. In *Tlk2*$^{-/-}$ placentas total ASF1 protein levels were similar to wild type controls but the phosphorylation of S166 (p-ASF1), a target site of TLKs, was reduced, suggesting reduced H3/H4 binding potential in the absence of TLK2 (Figure 17D and Supplementary Figure 2A) (Klimovskaia et al., 2014). To confirm that the interaction of TLK2 with ASF1 was also occurring in mouse tissue, and particularly in the placenta, we performed co-IPs of endogenous TLK2 or ASF1 from placental lysates. Following the IP of TLK2, we readily observed both ASF1 and TLK1 and reciprocal IPs with anti-ASF1 antibodies efficiently co-immunoprecipitated TLK2 (Figure 17E and Supplementary Figure 2B). Together, these results indicated that

despite some levels of detectable TLK1, TLK2 is required for full ASF1 phosphorylation in the placenta, potentially influencing the regulation of genes required for trophoblast differentiation and placental development.

TLK2 is dispensable for viability in embryonic and adult tissues

The differential protein levels of TLK1 between the placenta and embryonic tissue provided a potential explanation for placental dependence on TLK2 (Figure 17B). We considered that a similar situation in other cell types in the embryo could also contribute to the embryonic death of *Tlk2*$^{-/-}$ animals. To address this, we crossed female *Tlk2*$^{+/-}$ mice carrying the Sox2-Cre transgene, that expresses Cre in the epiblast, with males carrying the floxed conditional allele (*Tlk2*$^{+/F}$) to allow the generation of *Tlk2*$^{-/-}$ embryos, while maintaining at least 1 functional copy of *Tlk2* in the placenta (Figure 18A) (Hayashi et al., 2002). This strategy bypassed the embryonic lethality and we observed the birth of live, morphologically normal, *Tlk2*$^{-/-}$ animals (Figure 18A). These animals, although sometimes smaller than littermates, showed a similar growth capacity (Figure 18B) and no increased morbidity has been observed up to 18 months (Figure 18C), although we cannot yet rule out tissue specific or aging related phenotypes that are not overtly evident. Importantly, we could not detect TLK2 protein in any tissues examined by Western blotting, indicating that Sox2-Cre was effective at eliminating *Tlk2* expression (Figure 18D). These data demonstrate that, like TLK1, TLK2 is not required for organismal viability, despite its critical role in the development and function of the placenta.

As relative TLK1 and TLK2 protein levels were different between embryonic and placental tissues, we sought to determine if a similar situation existed in other adult tissues. We freshly isolated mRNA and protein from a panel of wild type tissues at 2 months of age. Using quantitative real time PCR, we determined the expression levels of *Tlk1* and *Tlk2* in different tissues (Figure 18E). In general, the expression of *Tlk1* and *Tlk2* followed a similar pattern across tissues, although the expression of *Tlk2* was particularly high in the testes, where the human TLK2 gene was originally identified (Shalom and Don, 1999). To determine if the mRNA levels reflected relative protein levels, we performed Western blotting from lysates prepared from some of the same tissues of both male and female mice (Figure 18F). These results were generally consistent with the mRNA expression levels and the patterns of TLK1 and TLK2 protein levels were similar relative to tissue type. One exception was the kidney, where both TLK1 and TLK2 protein were undetectable, despite similar levels of mRNA expression as other tissues (Figure 18E-F). These results suggested that the lack of clear phenotypes in adult animals deficient for either TLK1 or TLK2 could be due to their redundancy in most tissues, in contrast to the placenta where TLK2 is required due to the low levels of TLK1. Supporting this possibility, we found that *Tlk2* is haploinsufficient on a *Tlk1* deficient background, as all *Tlk1*$^{T/T}$ *Tlk2*$^{+/T}$ pups we observed displayed severe birth defects (data not shown).

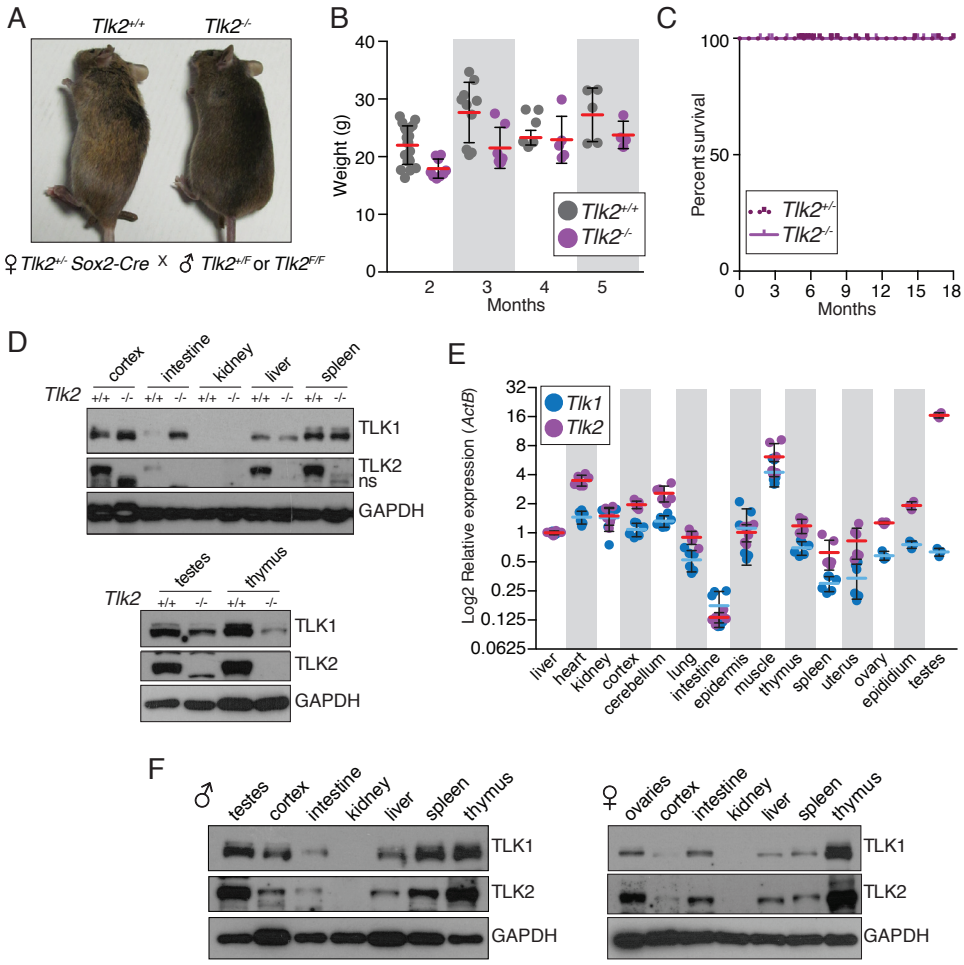

Figure 18. TLK2 is dispensable for viability in embryonic and adult tissues.

(A) *Tlk2*$^{+/+}$ and *Tlk2*$^{-/-}$ littermates are shown from breedings of female *Tlk2*$^{+/-}$, Sox2-Cre^{+} and male *Tlk2*$^{+/F}$ mice. (B) Weight of mice lacking TLK2 is slightly reduced but growth is similar to wild type. Mean (red bars) and SD are indicated (n=20 and 9 for 1 mo., n=10 and 7 for 2 mo., n=6 and 5 for 3 mo., n=5 and 4 for 4 mo. for *Tlk2*$^{+/+}$ and *Tlk2*$^{-/-}$, respectively) (C) Kaplan Meier survival curve of mice with the indicated genotypes (*Tlk2*$^{+/-}$ n=42, *Tlk2*$^{-/-}$ n=26). (D) Western blotting of TLK1 and TLK2 using lysates from selected tissues of *Tlk2*$^{+/+}$ and *Tlk2*$^{-/-}$ mice. NS refers to a non-specific band observed with the TLK2 antibody in many tissues and cell lines. (E) Similar expression patterns of *Tlk1* and *Tlk2* in adult mice. Taqman real time PCR analysis of *Tlk1* and *Tlk2* mRNA levels (Log2 transformed) relative to *ActB*. Mean (blue bars for *Tlk1* and red bars for *Tlk2*) and SD of triplicate reactions from at least 2 animals are plotted. In each case, levels are normalized to that of the liver (set to 1). (F) Western blotting of TLK1/2 protein levels in 2-month old male and female wild type tissues. GAPDH is shown as a loading control.

TLK1 and TLK2 cooperate to maintain cell viability and chromosomal stability

As TLK1 or TLK2 deficient animals appeared phenotypically normal, we wanted to investigate the effects of depleting both activities. To accomplish this, we generated single (*Tlk1*$^{+/+}$ *Tlk2*$^{F/-}$) and double conditional (*Tlk1*$^{C/C}$ *Tlk2*$^{F/-}$) transformed MEF lines that allow the 4OHT inducible trapping and deletion of *Tlk1* and *Tlk2*, respectively. Depletion of TLK1 and TLK2 protein levels following 4OHT induced Cre recombinase induction

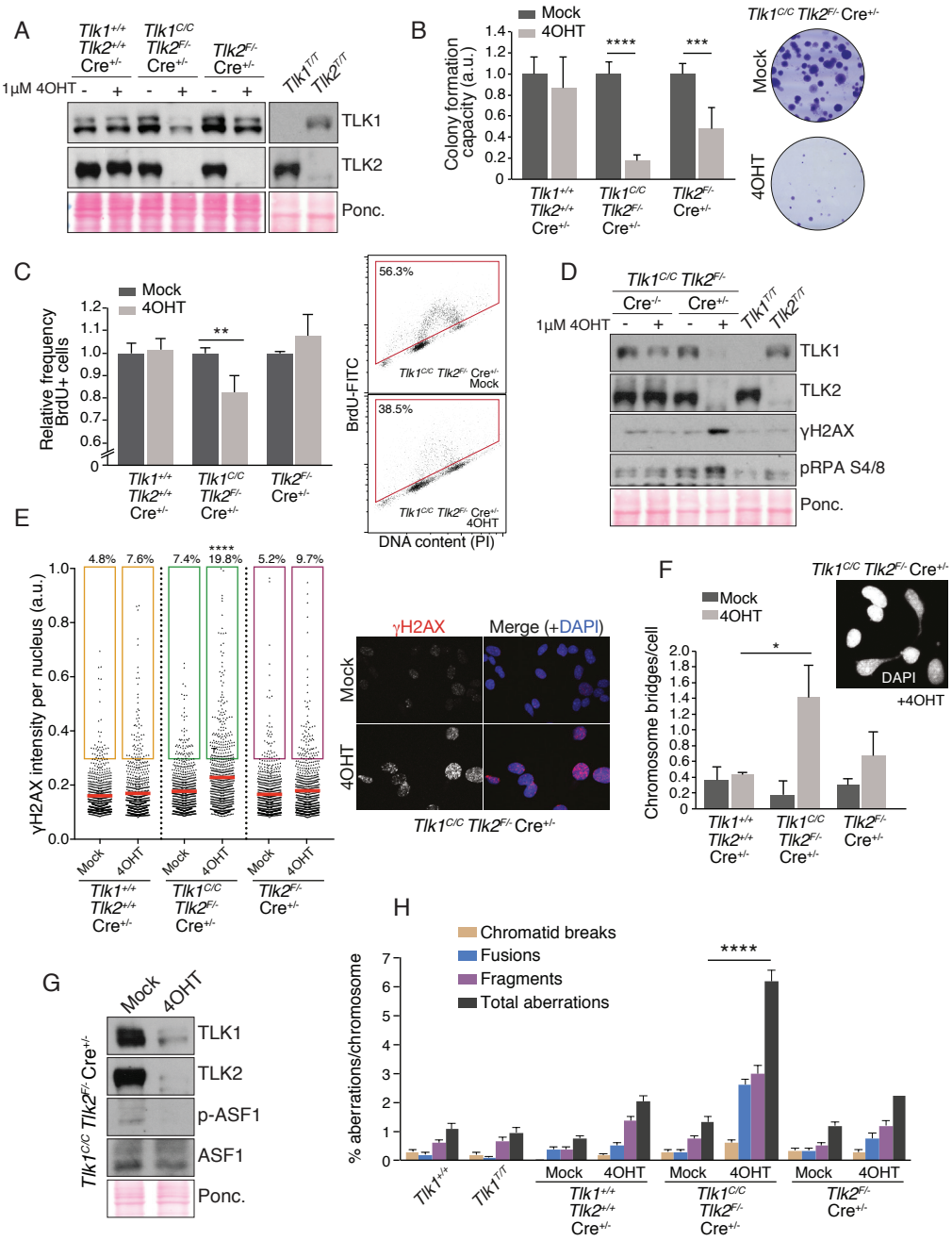

Figure 19. TLK1 and TLK2 cooperate to maintain cell viability and chromosome stability.

(A) Western blot with antibodies against TLK1 and TLK2 in whole cell extracts of transformed MEFs of the indicated genotypes mock treated or treated with 4OHT to induce trapping of TLK1 and/or deletion of TLK2 (Ponc. = Ponceau red stained membrane). (B) Deletion of TLKs reduces colony formation. MEFs were mock treated or treated with 4OHT for 72h, washed, plated and cultured for 10-14 days. Relative colony number to mock treated cells is displayed. *Tlk1*$^{+/+}$ *Tlk2*$^{+/+}$ *Cre*$^{+/-}$ n= 3; *Tlk1*$^{C/C}$ *Tlk2*$^{F/-}$ *Cre*$^{+/-}$ n=6; *Tlk2*$^{F/-}$ *Cre*$^{+/-}$ n=6. Results are shown as mean± SEM. Experiment was performed in technical duplicates. Statistical significance was determined using an unpaired t-test (****p=<0.0001, ***p=<0.001). (C) Deletion of both TLKs reduces short-term BrdU incorporation. MEFs were mock treated or treated with 4OHT for 72h, washed, plated and cultured for 24h. Relative percent

for 72 h was very effective for TLK2, that suffered a deletion of exon 4, and significantly depleted TLK1 but less effectively, since it consisted in trapping of an exon (Figure 19A, see Figure 14A and 14E for constructs). Double depletion of TLKs led to a severe reduction in colony formation when cells were seeded at very low density and left to grow over two weeks, compared to wild type or single mutants for *Tlk2* (Figure 19B).

In a short-term analysis of proliferation, we analysed the percentage of cells that incorporated the nucleotide analog BrdU as a surrogate of DNA replication. Only cells that were depleted for both TLKs displayed a significant reduction of the proliferating BrdU-positive population, indicating both kinases contribute to maintain DNA replication (Figure 19C). Defects in DNA replication can lead to replicative stress and various forms of DNA damage. We therefore simultaneously depleted TLK1 and TLK2 and observed a marked increase in the replicative stress marker pRPA S4/8 and the DNA double strand break marker γH2AX (Figure 19D). Similar results were obtained by analysing cells by immunofluorescence and quantifying the nuclear intensity of γH2AX foci, a predominant increase of γH2AX intensity was observed only in cells where both TLK1 and TLK2 had been depleted (Figure 19E). These cells also displayed mitotic defects, such as chromosome bridges (Figure 19F), as well as increased levels of chromosome aberrations scored in metaphase spreads, particularly chromosome fragments and fusions (Figure 19H). All these defects were accompanied by a reduction in total pASF1 S166 phosphorylation, similar to what was previously observed in the placenta (Figure 19G). Collectively, our *in vivo* and *in vitro* results indicated that TLK1 and TLK2 activities are largely redundant for cell viability and chromosome maintenance.

of positive cells to mock treated cells is displayed. *Tlk1*$^{+/+}$ *Tlk2*$^{+/+}$ *Cre*$^{+/-}$ n= 3; *Tlk1*$^{C/C}$ *Tlk2*$^{F/-}$ *Cre*$^{+/-}$ n=5; *Tlk2*$^{F/-}$ *Cre*$^{+/-}$ n=5. Results are shown as mean± SEM. Experiment was performed in technical duplicates. (D) Western blot with antibodies against TLK1, TLK2, the double strand break marker γH2AX and the replicative stress marker pRPA S4/8 in whole cell extracts of transformed MEFs of the indicated genotypes mock treated or treated with 4OHT. (E) Increased DNA double-strand break formation following the depletion of TLK1 and TLK2. High throughput microscopy of γH2AX levels per individual nucleus in response to TLK depletion in MEFs mock treated or treated with 4OHT. At least 800 nuclei were quantified per condition. Mean is shown as a red line; a.u., arbitrary units. Statistical significance was determined using Ordinary one-way ANOVA Tukey's multiple comparisons test (****p=<0.0001). In the right panel, representative images of IF experiments staining for γH2AX are shown from *Tlk1*$^{T/T}$ *Tlk2*$^{F/-}$ cells that were mock treated or treated with 4OHT. Nuclei were counterstained with 4',6-diamidino- 2-phenylindole (DAPI). (F) Increased chromosome bridges are evident in 4OHT induced double TLK deficient cultures relative to mock treated or *Tlk2* deletion alone. A minimum of 200 cells was scored in each independent experiment. *Tlk1*$^{+/+}$ *Tlk2*$^{+/+}$ *Cre*$^{+/-}$ n= 2; *Tlk1*$^{C/C}$ *Tlk2*$^{F/-}$ *Cre*$^{+/-}$ n=5; *Tlk2*$^{F/-}$ *Cre*$^{+/-}$ n=4. Results are shown as mean±SD. Statistical significance was determined using an unpaired t-test (*p=<0.05). (G) Western blotting of *Tlk1*$^{C/C}$ *Tlk2*$^{F/-}$ MEF lysates mock treated or treated with 4OHT for TLK1, TLK2, ASF1 and p-ASF1. Experiment performed in biological triplicate and a representative example shown. (H) Plot of chromosomal aberration types scored from multiple transformed MEF cultures depicted as percent aberrations per chromosome. Results are shown as mean± SEM. Statistical significance was determined using Fisher's exact test (****=p<0.0001).

Chapter 3

Tousled like kinases stabilize replication forks and show synthetic lethality with checkpoint and PARP inhibitors

Sandra Segura-Bayona[1], Sung-Bau Lee[2], Matthew A.M. Todd[2], Anja Groth[2] and Travis H. Stracker[1]

[1] Institute for Research in Biomedicine (IRB Barcelona), the Barcelona Institute of Science and Technology, Barcelona, Spain.

[2] Biotech Research and Innovation Centre (BRIC) and Centre for Epigenetics, Faculty of Health and Medical Sciences, University of Copenhagen, Copenhagen, Denmark.

Statement of contribution:

S Segura-Bayona designed, performed and analysed most of the experiments.

SB Lee performed and analysed experiments shown in Figure 20I and Figure 22K.

MAM Todd performed and analysed experiments shown in Figure 24D.

A Groth and TH Stracker designed experiments and supervised the whole project.

TLK2 is required for efficient DNA replication

It was established that TLK1/2 activity peaks during S-phase, when DNA is replicated and packaged into chromatin (Groth et al., 2003; Silljé et al., 1999). The fact that the two kinases are highly active during S-phase, together with the fact that inhibitors of DNA replication such as Aphidicolin inactivate both TLKs, suggests a role for these kinases during DNA replication (Silljé et al., 1999). We therefore set out to investigate the influence of TLK activity on DNA replication by measuring the incorporation of thymidine analogs such as 5-bromo-2'-deoxyuridine (BrdU). Incorporation of BrdU during active DNA synthesis can then be labelled with a specific antibody and in combination with propidium iodide (PI) staining detected by flow cytometry. The siRNA-mediated depletion of TLK1 in human osteosarcoma U-2-OS cells did not affect the number of BrdU positive cells (Figure 20A-B) and we could readily generate stable TLK1Δ CRISPR knockouts from the MDA-MB-231 breast cancer cell line (Figure 20C-D). These TLK1Δ cells exhibited similar proliferation rates and levels of BrdU incorporation as the parental cells (Figure 20E-F). In contrast, we were unable to stably propagate any TLK2Δ clones from MDA-MB-231 cells. However, in a first clone screening round by Western blotting, we scored a similar number of targeted TLK2Δ CRISPR knockout clones as for TLK1Δ (Figure 20C), suggesting a strong selective pressure for these cells to restore TLK2. Acute depletion of TLK2 by siRNA significantly reduced the overall number of cells in S-phase that incorporated BrdU in asynchronous culture of both U-2-OS and MDA-MB-231 cells (Figure 20A-B and Figure 20G-H), reflecting the need for TLK2 to support the rate of DNA replication.

Notably, the siRNA-mediated depletion of TLK2 also often resulted in the reduction of TLK1 protein levels, an effect that was more dramatic in U-2-OS cells than MDA-MB-231 cultures (Figure 20B), probably reflecting the ability of the two kinases to form heterodimers (Figure 8F) (Silljé et al., 1999). Thus, the relative abundance of TLK1 and TLK2 may be interdependent and could differ depending on the genetic background of each cell line, suggesting that care should be taken in interpreting knockdown and knockout data for these kinases.

The BrdU incorporation results were further validated with high-throughput microscopy nuclear intensity analysis of incorporation of another thymidine analog, 5-Ethynyl-2´-deoxyuridine (EdU), in U-2-OS cells (Figure 20I). SiRNA-mediated depletion of TLK2 resulted in reduced incorporation of EdU scored in S-phase cells identified by PCNA positivity. Importantly, stable expression of siRNA-resistant wild-type TLK2 (TLK2WT) rescued the replication defect of U-2-OS cells, whereas a kinase-dead mutant (D613A) (Silljé et al., 1999) of TLK2 (TLK2KD) failed to do so (Figure 20I). This demonstrates that TLK2 promotes DNA replication through its kinase activity. In addition, DNA combing analysis was performed in A. Groth's laboratory to monitor replication elongation and initiation at the single molecule level by measuring incorporated 5-chloro-2'-deoxyuridine (CldU) into newly replicating DNA. TLK2 depleted cells displayed reduced CldU track

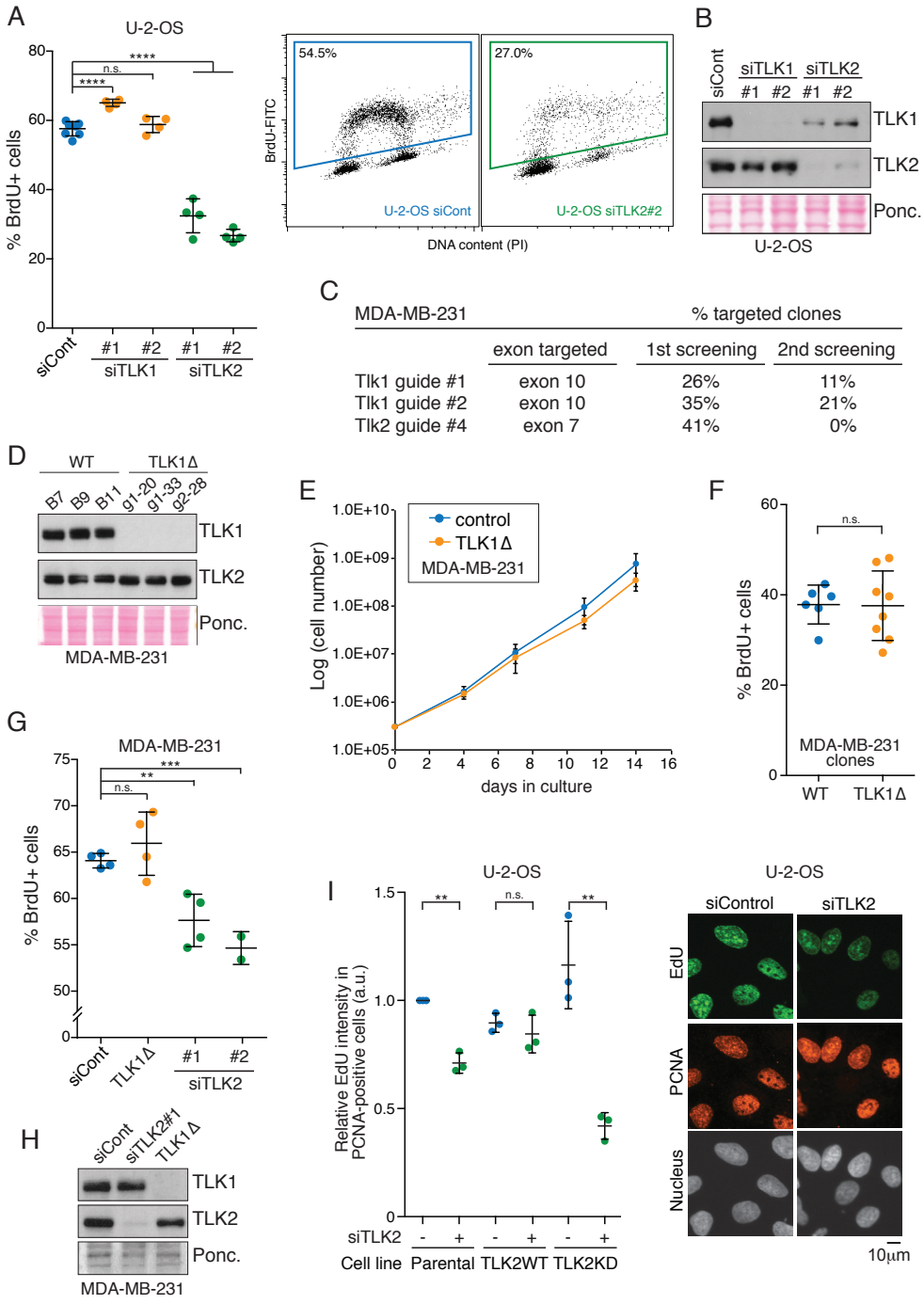

Figure 20. TLK2 is required for efficient DNA replication.

(A) U-2-OS cells were pulsed with BrdU 48 hours post-transfection with siRNAs against TLK1 or TLK2. The percentage of S-phase cells was subsequently quantified by analysis of DNA content using propidium iodide (PI) and staining for BrdU. Means and standard deviation (SD) from technical replicates performed in at least biological duplicate are shown. A two-tailed t test was used to determine statistical significance (left panel). Representative plots of BrdU staining are shown (right panel). (B) Western

length indicating a slow-down of fork progression (data not shown). Collectively, these results demonstrated that multiple cell lines are dependent on TLK activity for DNA replication and proliferation, and revealed that impaired replication fork progression underlies the replication defect in cells lacking TLKs.

TLK activity is required for chromatin assembly

The histone chaperone ASF1 is a well-established TLK substrate (Silljé and Nigg, 2001) and its phosphorylation by TLK is proposed to facilitate provision of canonical histones H3.1-H4 and H3.2-H4 to the histone chaperone CAF1 during DNA replication (Klimovskaia et al., 2014). Given that nucleosome assembly is required for replication fork progression (Mejlvang et al., 2014), we asked whether TLK depletion influenced the deposition of new histones. To answer this question at the cellular level, we used U-2-OS cells stably expressing SNAP-tagged histones (Clément et al., 2016) (Figure 21A). By combining siRNA depletion of TLKs and a quantitative microscopy approach, this method allowed us to visualize directly *de novo* histone deposition by cell imaging within individual nuclei in a cell population. The SNAP-tag itself is an enzyme that catalyses irreversible covalent binding to its own substrates. Thus, SNAP-tag fusion proteins stably expressed in cells can be labelled with cell-permeable non-fluorescent or fluorescent substrates to visualize target protein turnover or newly synthesized protein pools. In our analysis, we included both canonical histone H3.1 and the replacement variant H3.3, as ASF1 supplies histones to both replication-dependent and -independent pathways (Hammond et al., 2017).

Using quench-chase-pulse experiments, newly synthesized SNAP-tag histones can be tracked *in vivo*. First, an efficient "quench" step is needed so that all pre-existing SNAP-tag histones are labelled with a non-fluorescent dye (QCP 0h Block control, Figure 21A-B). Second, a "chase" period enables new SNAP-tag histones to be synthesized and incorporated into the chromatin. We found that after 6 hours the new pool of H3.1 or H3.3 could already be detected in the chromatin. Last, a "pulse" step labels all the newly synthesized proteins with a fluorescent dye, TMR (QCP 6h, Figure 21A-B). Importantly,

blot analysis of TLK1 and TLK2 from whole cell lysates of U-2-OS cells 48 hours post siRNA-transfection. (C) Table of CRISPR knockout targeting efficiencies scored by Western blot screening. 1st screening corresponds to 3rd passage. 2nd screening corresponds to approximately 6-10th passage. (D) Examples of Western blot screening of WT single cell clones and TLK1Δ single cell clones. Note that higher compensatory protein levels of TLK2 are not apparent. (E) Analysis of proliferation rates of MDA-MB-231 clones. Plots of the mean and SD of 3 independent clones performed in technical duplicate (n=3). (F) S-phase population analysis of WT and TLK1Δ MDA-MB-231 single-cell clones. Cells were pulsed with BrdU and analysed as in (A). Means and standard deviation from 6 independent WT clones and 8 TLK1Δ clones are shown. (G) The percentage of S-phase cells was quantified in MDA-MB-231 cells pulsed with BrdU 72 hours post-transfection and analysed as in (A). (H) Western blot analysis of TLK1 and TLK2 from whole cell lysates of MDA-MB-231 cells 72 hours post siRNA-transfection. (I) Immunofluorescence analysis of EdU incorporation in U-2-OS cells stably expressing siRNA-resistant wild-type (WT) or kinase-dead (KD) TLK2. Cells were pulsed with EdU 30 hours after TLK2 siRNA transfection and EdU nuclear intensities relative to parental cells from 3 independent biological replicates are displayed with mean and SD. One-sample and two-tailed t tests were used for statistical analysis of parental U-2-OS cells and complemented cell lines (TLK2WT and KD), respectively. Each independent experiment analysed a minimum of 400 nuclei per condition (left panel). Representative images are shown with PCNA as a marker for S-phase cells (right panel).

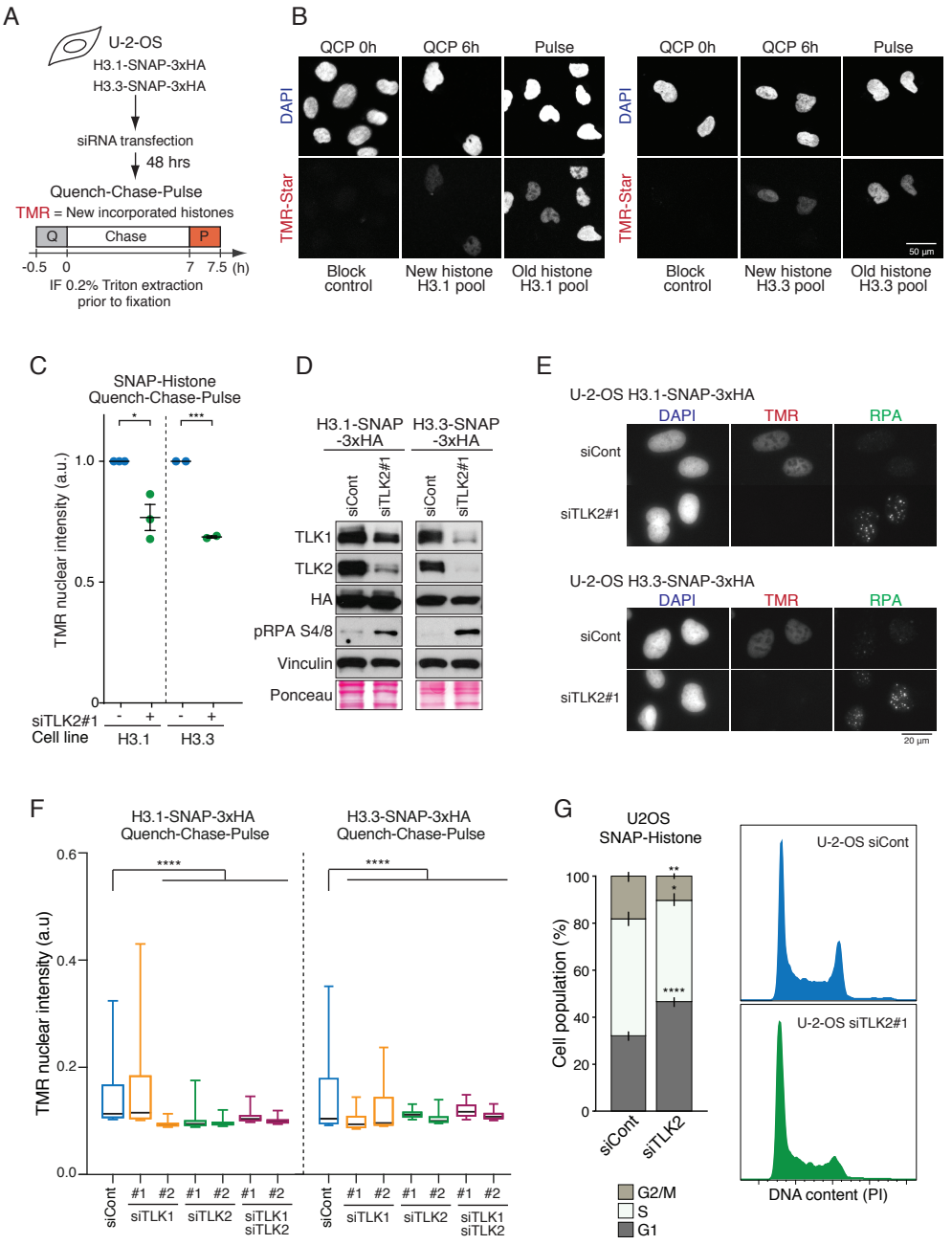

Figure 21. TLK activity is required for chromatin assembly.

(A) Experimental design for assaying histone incorporation in cell lines stably expressing SNAP-tag histones H3.1 and H3.3. For quench-chase-pulse (QCP) experiments, U-2-OS cells were pulsed with SNAP-Block and pulsed with TMR-Star after a chase period of 7 hours. (B) Controls for the SNAP-tag assay by immunofluorescence analysis. "QPC 0h" indicates the quenching control, "QPC 6h" indicates the de novo pool of histones and "Pulse" indicates all existing histones present in the chromatin. Representative images are shown for H3.1-SNAP-3xHA and H3.3-SNAP-3xHA cell lines. (C) Quantification of SNAP-tag histone incorporation from two or more independent experiments as described in (A). TMR intensity relative to mock transfected cells is plotted. For each data point, a minimum of 300 nuclei were analysed. Lines and error bars represent means and SEM, respectively. A two-tailed t test was used for statistical analysis. (D) Western blot analysis of whole cell lysates of U-2-OS cells

our analysis is centered in those histones that have been incorporated into chromatin, so a step of Triton pre-extraction prior to fixation for immunofluorescence is needed to remove all the soluble histones. In addition, pulse-only experiments that label all SNAP-tag histones without a previous quench step indicated that all the cells from our population were stably expressing the SNAP-tag histones (Pulse, Figure 21B). Performing quench-chase-pulse experiments with a chase period of 7 hours, we found that depletion of TLK activity strongly impaired *de novo* deposition of both histones H3.1 and H3.3 (Figure 21C-F).

Since TLK depleted cells also showed alterations in the cell cycle, with less cells in S-phase and G2, and more cells arrested in G1 (Figure 21G), we reasoned that incorporation of H3.1-H4, which is DNA replication-dependent, could be secondary to having less cells in the S/G2-phases. To resolve this point, experiments performed in A. Groth's laboratory specifically assayed chromatin assembly on newly synthesized DNA by labelling replicating DNA with radioactive thymidine and measuring the sensitivity of nascent chromatin to micrococcal nuclease (MNase) digestion (Mejlvang et al., 2014). Nascent chromatin of TLK depleted cells displayed hypersensitivity to MNase digestion (data not shown), confirming that indeed, TLK activity is required for efficient replication-coupled nucleosome assembly. Collectively, this argued that TLK activity is important for nucleosome assembly of both canonical and replacement histone variants and for maintaining chromatin organization, extending previous findings that TLK phosphorylation of ASF1 stimulates histone binding and interaction with CAF1 and HIRA (Klimovskaia et al., 2014).

Loss of TLK activity leads to DNA unwinding, checkpoint activation and loss of viability

Replication fork slowdown or stalling, origin hyper-activation and defects in chromatin assembly have all been implicated in replication stress, fork collapse and genome instability (Hoek and Stillman, 2003; Mejlvang et al., 2014; Ye et al., 2003; Zeman and Cimprich, 2014). Sustained depletion of TLK2 with two independent siRNAs in MDA-MB-231 cells, on either a WT or TLK1Δ background, significantly increased the levels of chromatin-bound RPA and H2AX phosphorylation at S139 (γH2AX) in immunofluorescence analysis, indicative of increased exposure of ssDNA accumulation and checkpoint activation (Figure 22A-D). In addition, Western blotting of whole cell protein lysates indicated an enhanced replicative stress checkpoint response, indicated by increased phosphorylation of RPA at S4/8 (Figure 22E). Similar results were obtained in U-2-OS cells where either

stably expressing SNAP-tag histones 48 hours after siRNA transfection. (E) Representative images of TMR signal in H3.1 and H3.3-SNAP-3xHA expressing U-2-OS cell lines. DAPI and RPA staining are also shown. (F) Representative measurements from one biological replicate of chromatin assembly analysis (QPC) using SNAP-tagged histones. Number of nuclei analysed is n>250. Median is shown with boxes and whiskers: 25-75 and 5-95 percentile ranges. A two-tailed t test was used for statistical analysis. (G) Cell cycle analysis of U-2-OS cells stably expressing SNAP-tag histones 48 hours after siRNA transfection. The means with SD of 4 independent experiments are shown. A two-tailed t test was used for statistical analysis (left panel). Representative histograms of PI staining are shown (right panel).

TLK1, TLK2 or double TLK depletion led to accumulation of chromatin-bound RPA in immunofluorescence analysis (Figure 22F-G), suggesting that DNA unwinding was taking place following fork stalling in TLK depleted cells. Moreover, Western blotting analysis in U-2-OS cells showed a prominent increase of phosphorylation of RPA at S4/8 and S33, markers of replication fork collapse upon residual stalled replication forks, and γH2AX, marker of DNA damage (Figure 22H).

We next set out to determine the colony forming ability of both cell lines, MDA-MB-231 and U-2-OS upon depletion of TLKs. In agreement with the activation of replicative stress checkpoint responses, MDA-MB-231 cells knockout for TLK1 or depleted of TLK2 displayed reduced colony-forming capacity, and the defect was further enhanced by depleting TLK2 in TLK1Δ cells (Figure 22I). Sustained depletion of TLK activity by siRNA-mediated knockdown of TLK2 in U-2-OS cells showed a considerable decrease in colony-forming capacity (Figure 22J). These results provide evidence of reduced viability and/or proliferative capacity following the reduction of TLK levels.

DNA damage signalling elicits a delay in cell cycle progression due to the activation of cell cycle checkpoints (Harper and Elledge, 2007). Upon sustained TLK2 depletion, we observed a moderate increase in p53, a major inducer of G1/S checkpoint arrest, along with a p53-dependent induction of the CDK inhibitor p21 in several different cell types, including U-2-OS (data not shown). Consistent with this, the number of S-phase cells was reduced in TLK depleted cells (Figure 21G). The ability of these cells to maintain a functional G1/S cell cycle checkpoint was analysed using a FACS-based nocodazole trap experiment. Cells treated with nocodazole were blocked prior to mitosis, as observed in siControl samples (Figure 22K). Sustained knockdown of TLK2 indicated that G1/S checkpoint transition was impaired (Figure 22K), suggesting that as DNA damage accumulates during prolonged TLK2 depletion the p53-p21 checkpoint is activated and blocks S-phase entry.

(A) Immunofluorescence analysis of MDA-MB-231 cells co-stained with antibodies against RPA, γH2AX and DAPI. (B) High throughput microscopy (HTM) analysis of chromatin-bound RPA in parental MDA-MB-231 (WT) or TLK1Δ cells (TLK1Δ) 72 hours after siRNA transfection. Data are representative of three independent experiments. The median is indicated and a two-tailed t test was used for statistical analysis. (C) Quantification of the MDA-MB-231 cells with >5 RPA foci. At least 300 nuclei were analysed and the mean with SEM is shown for independent cultures (n=10 for siCont; n=6 for siTLK2). A two-tailed t test was used for statistical analysis. (D) HTM-mediated quantification of the nuclear intensity of γH2AX in MDA-MB-231 WT or TLK1Δ cells 72 hours after siRNA transfection. Data are representative of three independent experiments. The median is indicated and two-tailed t tests were used for statistical analysis. (E) Western blot analysis of MDA-MB-231 cells 72 hours after TLK2 siRNA transfection. (F) HTM analysis of the chromatin-bound RPA in U-2-OS cells 48 hours after siRNA transfection. Data are combined from two biological replicates with more than 300 nuclei analysed in each replicate. The median is shown and a two-tailed t test was used for statistical analysis. (G) Representative immunofluorescence analysis of U-2-OS cells stained with RPA and DAPI. (H) Western blot analysis of U-2-OS cell lysates after 48 hours of siRNA transfection. (I) Colony formation assay in MDA-MB-231 WT or TLK1Δ cells transfected with TLK2 siRNAs. Data represents the average of two biological replicates, each done in technical duplicates. Error bars represent SEM and a two-tailed t test was used for statistical analysis. (J) Colony formation assay in U-2-OS cells transfected with TLK2 siRNAs. Data represents the average of two biological replicates, each done in technical duplicates. Error bars represent SEM and a two-tailed t test was used for statistical analysis. Representative images are shown in the right panel. (K) Cell cycle progression analysed by flow cytometry of cells treated with Nocodazole and stained with PI. The experimental design (left panel) and representative cell cycle profiles (right panel) from one out of three biological replicates are shown.

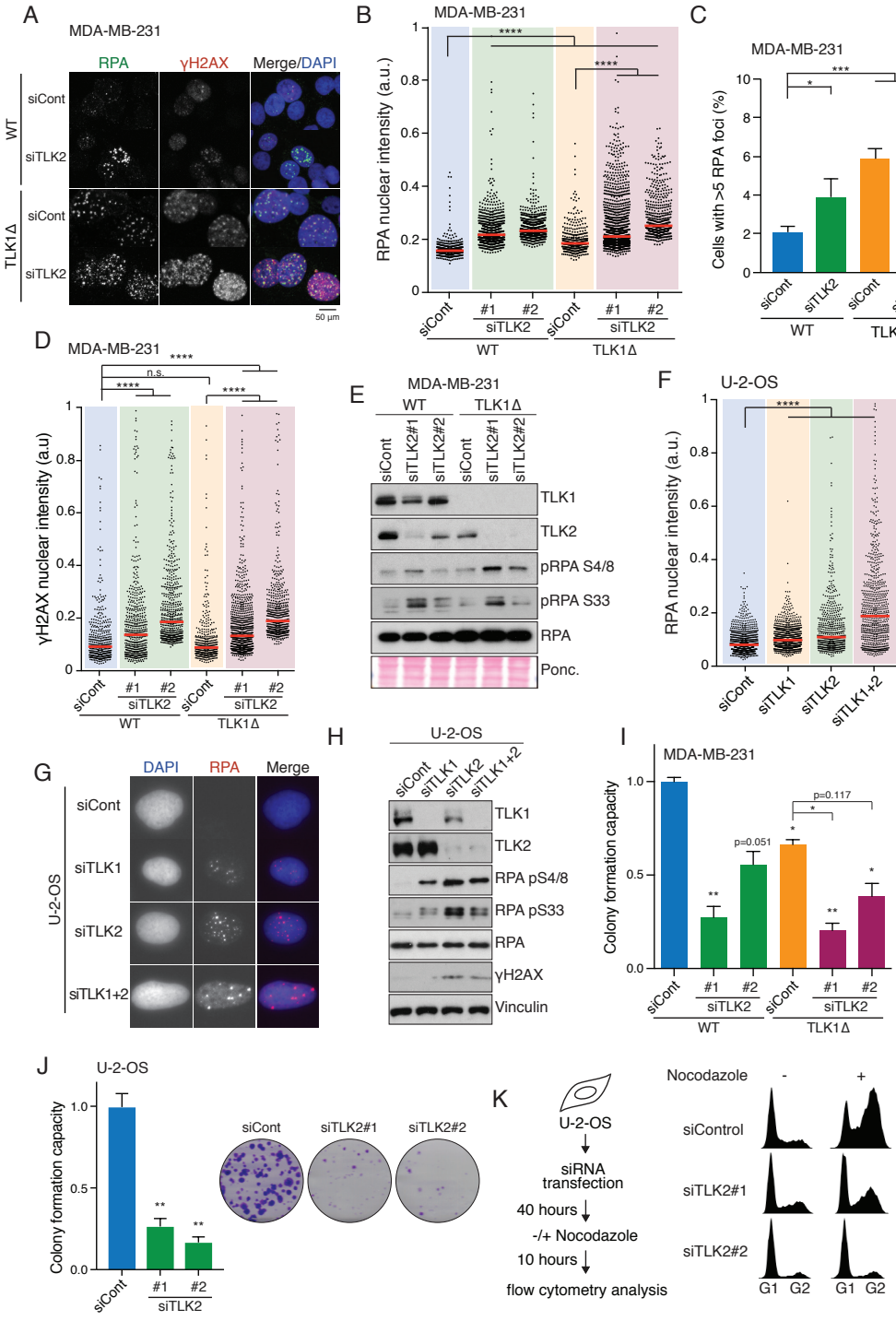

Figure 22. Loss of TLK activity leads to DNA unwinding, checkpoint activation and loss of viability.

(Legend in the previous page)

TLK depletion is synthetic lethal with checkpoint inactivation and PARP inhibition

Whereas sustained TLK depletion for 48-72 hours generated extensive replicative stress and DNA damage (Figure 22), short-term reduction of TLK activity impaired fork progression without eliciting a strong DNA damage response (data not shown). We reasoned that at early time points, when TLK depleted cells have not undergone a strong cell cycle arrest or cell death, TLK depleted cells that suffer DNA replication fork slowdown may strongly rely on the replication checkpoint to avoid DNA replication fork collapse. Therefore, we addressed the possibility of a synthetic sickness between these two pathways. Inhibition of the checkpoint kinase CHK1, which is activated by the presence of DNA lesions and replicative stress, results in increased replicative stress signalling in MDA-MB-231 cells (Figure 23A), as expected from previous work (Sørensen and Syljuåsen, 2012). Depletion of TLK2 concomitant to CHK1 inhibition by AZD7762 substantially enhanced this response (Figure 23A), elevating the phosphorylation of RPA2 at S4/8 and γH2AX. Consistent with this result, TLK2 depleted MDA-MB-231 cells displayed a further reduction in colony formation capacity following CHK1 inhibition by AZD7762 (Figure 23B). Similar results were obtained when MDA-MB-231 cells were treated with an inhibitor of ATR, which is activated upon the generation of lesions containing ssDNA. Depletion of TLK2 concomitant with ATR inhibition by ETP-46464 substantially enhanced phosphorylation of RPA2 at S4/8 (Figure 23C), and this effect was additive when ATR inhibition was combined with double TLK loss in TLK2 siRNA-depleted TLK1Δ cells.

In addition to CHK1 and ATR inhibitors, the PARP inhibitor Olaparib is of interest in current clinical studies, as it was shown to cause synthetic phenotypes with defects in homologous recombination mediated repair (Bryant et al., 2005; Farmer et al., 2005) and in combination with the loss of ARID1A, which induced replication stress (Shen et al., 2015). PARP is a NAD-dependent enzyme that catalyses PARylation of various substrates in response to an array of DNA lesions, stresses and replication fork impediments. Interestingly, replication fork stalling can lead to replication fork reversal, and this fork structure has been shown to be dependent on PARP activity (Ray Chaudhuri et al., 2012). Replication fork reversal may facilitate fork stabilization in a certain time window to allow mitigation of replication stress (Neelsen and Lopes, 2015). We therefore asked whether Olaparib would enhance the defects of TLK depleted cells in a similar manner as checkpoint inhibition. We strikingly found that the addition of Olaparib strongly decreased the survival of MDA-MB-231 cells depleted for TLK activity (Figure 23D-E) and this was accompanied by enhanced RPA phosphorylation and γH2AX in Western blotting analysis in both MDA-MB-231 and U-2-OS cells, suggesting toxic levels of replication stress and DNA damage (Figure 23F). Together, our results anticipate that treating TLK depleted cells with CHK1, ATR or PARP inhibitors leads to synthetic lethal phenotypes, including cell cycle arrest and/or cell death, and increased DNA damage. Thus, we envision that developing specific TLK inhibitors could have clinical utility and

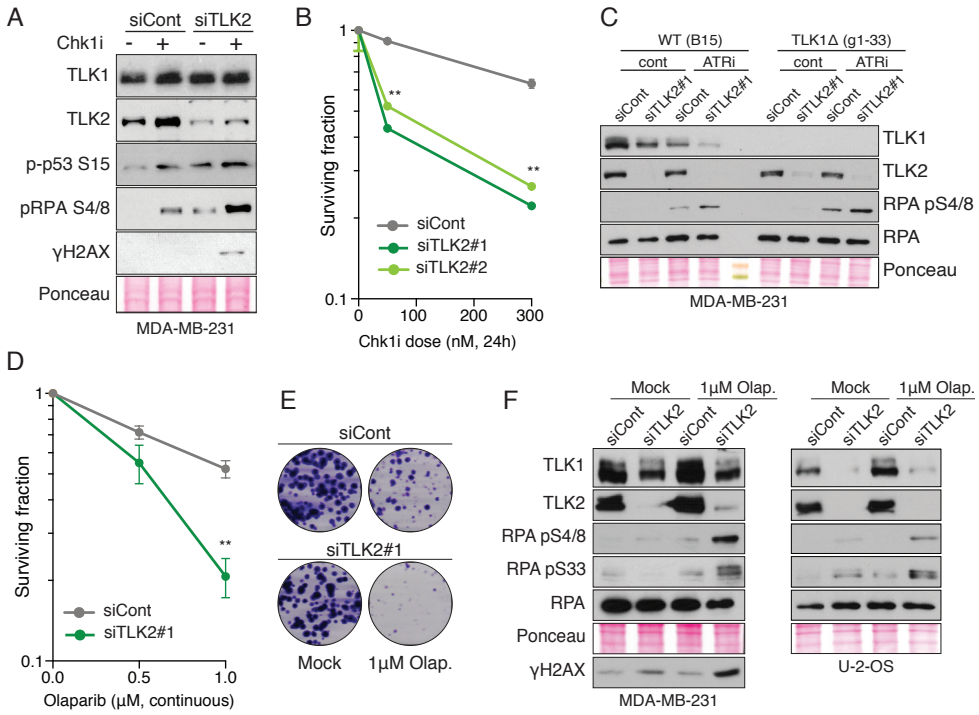

Figure 23. TLK depletion is synthetic lethal with checkpoint inactivation and PARP inhibition.

(A) Analysis of DNA damage signalling in MDA-MB-231 cells treated 72 hours post-transfection with AZD7762 (100 nM) for 24 hours, followed by Western blotting. (B) Sensitivity of TLK depleted cells to the CHK1 inhibitor AZD7762 measured by colony formation assay. (C) Analysis of DNA damage signalling in MDA-MB-231 cells treated 48 hours post-transfection with ATR inhibitor ETP-46464 (5 μM) for 24 hours, followed by Western blotting. (D) Sensitivity of TLK depleted cells to PARP inhibitor Olaparib measured by colony formation assay. (E) Representative images of colony survival assays in (D) are shown. (F) Western blotting of γH2AX, RPA and phospho-RPA following TLK depletion and Olaparib treatment in MDA-MB-231 cells (left panel) U-2-OS cells (right panel).

propose a new therapeutic concept by combining TLK inhibitors with existing agents such as CHK1/ATR/PARP inhibitors.

De novo nucleosome assembly defects synergize with checkpoint inhibition

New histone deposition and nucleosome assembly is required for replication fork progression (Mejlvang et al., 2014) and nucleosome assembly defects lead to a gradual decline in replication fork stability (Mejlvang et al., 2014), as observed in cells depleted for TLK activity. However, it has been described that DNA unwinding, that results in the generation of extensive ssDNA tracks, is strongly impaired in ASF1 depleted cells (Groth et al., 2005, 2007), in contrast to what we observed upon TLK depletion (Figure 22A-H). We confirmed this result by depleting TLK2, ASF1a and ASF1b in parallel for direct comparison. The response to TLK loss was characterized by extensive DNA unwinding

and replicative stress, indicated by activation of RPA phosphorylation at S4/8 and S33, and this response was absent in cells depleted for ASF1a or ASF1b (Figure 24A). It was therefore important to address whether the synthetic lethal relationships we observed with checkpoint and PARP inhibition were linked to the function of TLKs in chromatin assembly via ASF1 or to a distinct function that has yet to be identified.

We next compared TLK depletion (TLK1 and TLK2) to depletion of either ASF1 (both a and b isoforms) or FLASH, a key regulator of histone biosynthesis (Barcaroli et al., 2006), in a time course analysis. At 48 hours post-transfection, when extensive RPA phosphorylation was clearly evident in TLK depleted cells, little signalling was observed in cells depleted for both ASF1 (a and b) (Figure 24B). In contrast, FLASH depletion led to increased RPA S33 phosphorylation, albeit to lower levels than TLK depletion, indicating that replication stress was induced and some unwinding taking place (Figure 24B). In addition, epistasis analysis of TLK and ASF1 depletion phenotypes indicated that ASF1 function was required for DNA unwinding that occurs following TLK depletion. Hence, in the absence of ASF1, TLK depleted cells are not able to unwind DNA and fail to induce a strong replication stress response (Figure 24C).

Along these lines, we addressed whether defects in ASF1 function or new histone biosynthesis per se were sufficient to sensitize cells to treatment with checkpoint inhibitors. For this we used the checkpoint inhibitor UCN-01, which triggers hyper-activation of CDK2 kinase activity, and in combination with TLK2 depletion exacerbates UCN-01-induced DNA damage (data not shown and Figure 23). High content imaging showed that similar to TLK2 depletion, FLASH knockdown also exacerbated UCN-01-induced DNA damage, mainly in cells exhibiting an accumulation of RPA-coated ssDNA (Figure 24D). Surprisingly, this synthetic relationship was not recapitulated by depletion of ASF1 (a and b), further supporting that fork arrest differs in TLK and ASF1 depleted cells. In addition to delivering new histones to CAF-1 for *de novo* deposition, ASF1 has been implicated in histone recycling together with the replicative helicase MCM2-7 (Groth et al., 2007; Huang et al., 2015; Jasencakova et al., 2010). Given that inhibition of new histone biosynthesis by FLASH depletion mimics the hyper-sensitivity to checkpoint inhibitors that occurs in TLK depleted cells, the most parsimonious explanation is that this phenotype is linked specifically to *de novo* histone deposition, and not to other functions of ASF1 in histone dynamics. We cannot exclude that TLKs serve functions at the replication fork independent of histones, for example through other targets than ASF1 (Figure 8). However, we noted that the exacerbated DNA damage response in FLASH depleted cells could be suppressed by treatment with the CDK2 inhibitor Roscovitine (Figure 24D), suggesting that it was linked to origin hyper-activation, as in the case of TLK depletion.

accumulation and γH2AX in ASF1a/b or FLASH-depleted U-2-OS cells. One representative experiment out of two is shown (n>4800). (E) Complementation of TLK2 depletion with ASF1a 4A and 4D mutants. U-2-OS cells were induced or not with Tetracycline for 24 hours following transfection with siRNA against TLK2 and indicated proteins were monitored by Western blotting. Note that compared to the control, RPA S33 levels that are indicative of early replication stress signalling are enhanced by ASF1a 4A overexpression and reduced by ASF1a 4D. (F) HTM analysis of chromatin-bound RPA accumulation in ASF1a 4A cells. (G) HTM analysis of chromatin-bound γH2AX accumulation in ASF1 4A cells. Both signal of RPA (F) and γH2AX (G) was observed to increase to higher levels in cells overexpressing the ASF1a 4A mutant.

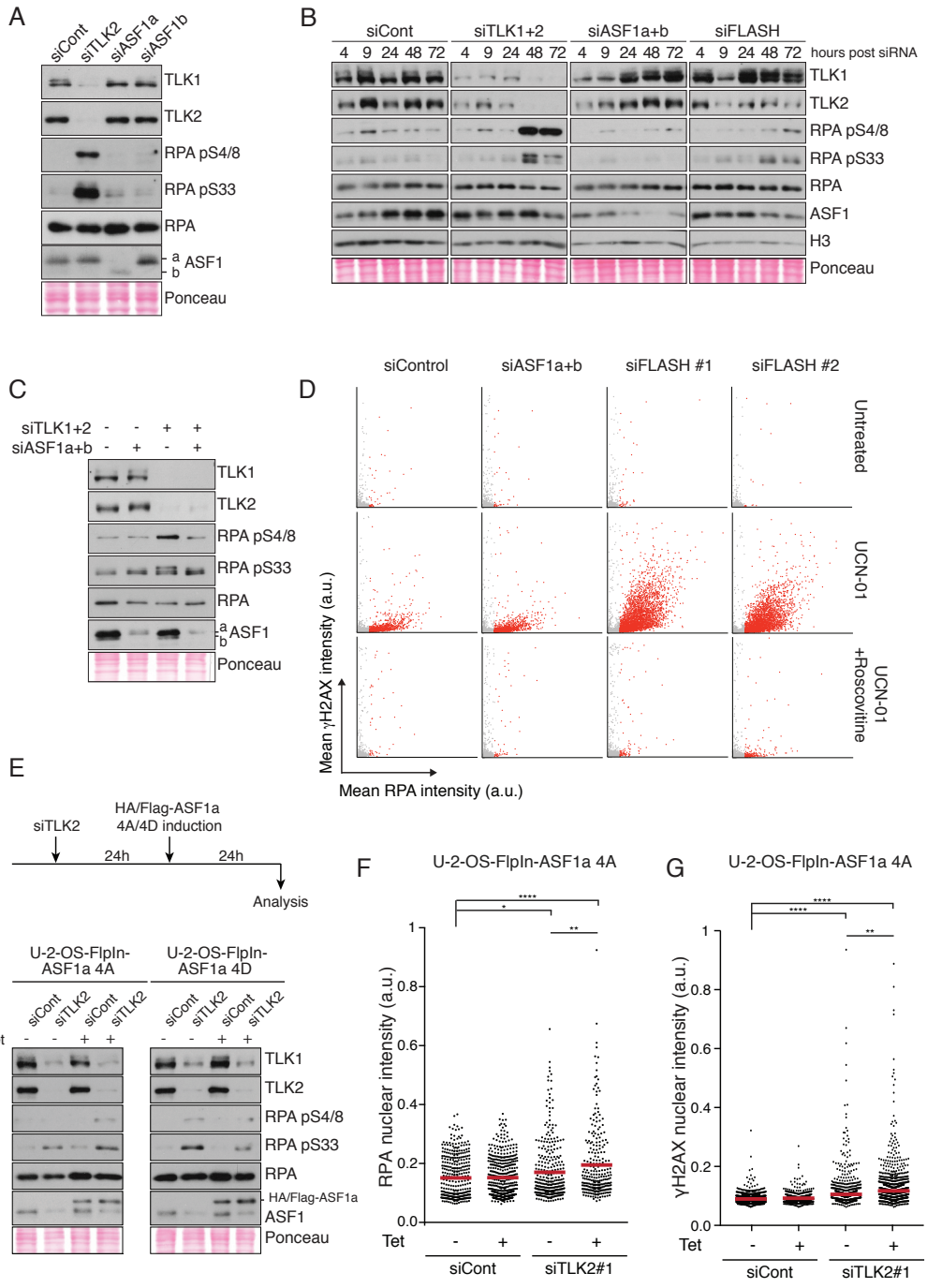

Figure 24. *De novo* nucleosome assembly defects synergize with checkpoint inhibition.

(A) Western blotting of RPA and phospho-RPA following TLK2, ASF1a and ASF1b depletion 48h post-transfection in U-2-OS cells. (B) Time course Western blot analysis of replication stress signalling following the siRNA depletion of TLK1/2, ASF1a/b and FLASH in U-2-OS cells. (C) Western blotting of RPA and phospho-RPA following either single TLK(1+2) or ASF1(a+b) depletions or combined TLK(1+2) and ASF1(a+b) depletions 48h post-transfection in U-2-OS cells. (D) HTM analysis of RPA

Previous work has shown that ASF1 phosphorylation by TLKs increases histone binding, histone-dependent interactions with chaperones such as NASP and RPAB46, interaction with replication-dependent histone chaperones such as CAF-1 and interaction with replication-independent histone chaperones such as HIRA (Klimovskaia et al., 2014), supporting that TLKs control histone delivery by ASF1. To further test this model, we attempted to complement TLK2 depleted cells with non-phosphorylatable and phosphomimetic ASF1a mutants previously described (Klimovskaia et al., 2014). We observed enhanced checkpoint signalling in TLK2 depleted cells expressing the ASF1a 4A mutant, and this was very consistent in several experiments (Figure 24E-G), presumably reflecting that TLK2 depletion is not fully removing the activity (notably these cells still have some TLK1, albeit at lower levels). However, expression of the ASF1a 4D mutant did not show a consistent rescue of the phenotype. We could observe reduced checkpoint signalling in Western blotting of TLK2 depleted cells expressing the ASF1a 4D mutant (Figure 24E), but high content immunofluorescence analysis did not recapitulate this rescue (data not shown). This probably reflects an inherent problem in this experiment because it does not allow for dynamic phosphorylation-dephosphorylation cycles presumably involved in histone binding and delivery by ASF1. This is in agreement with the fact that we cannot generate stable cell lines expressing either mutant. Taken together, all these results indicated that TLK depletion does not simply phenocopy the lack of ASF1, given that ASF1 is crucial for unwinding and this function is unlinked to its phosphorylation by TLKs. In addition, replication forks stalled due to *de novo* nucleosome assembly defects such as the ones occurring in the absence of TLKs or FLASH are vulnerable to collapse and these cells rely on basal levels of checkpoint signalling to prevent fork collapse, rampant genomic instability and cell death.

TLKs do not fully phenocopy ASF1a role in promoting NHEJ

Recently, it has been described that ASF1a has a role independent of its histone chaperone activity in promoting non-homologous end Joining (NHEJ) repair at double-strand breaks (Lee et al., 2017). It has been proposed that ASF1a does so by interacting with MDC1. This interaction is needed for activated ATM to interact with and phosphorylate MDC1, and for downstream recruitment of histone ubiquitination proteins RNF8/RNF168, which are in turn critical for recruitment of 53BP1 and promotion of NHEJ. To test whether TLK-mediated phosphorylation of ASF1a could be important for promoting double-strand break repair, we used U-2-OS cells that contain stably integrated reporters that can be activated by a DNA double-strand break (achieved by overexpression of the I-SceI endonuclease) followed by repair via several DSB repair pathways to produce expression a functional GFP gene (Bennardo et al., 2008).

We addressed DSB repair pathways by transfecting cells with the indicated siRNAs together with a plasmid expressing I-SceI endonuclease and a plasmid expressing mCherry as a transfection control. FACS analysis allowed us to normalize the number of cells expressing GFP (as a readout of cells having repaired the DSB with the indicated pathway) for the number of cells transfected expressing mCherry (Figure 25A). TLK activity depletion

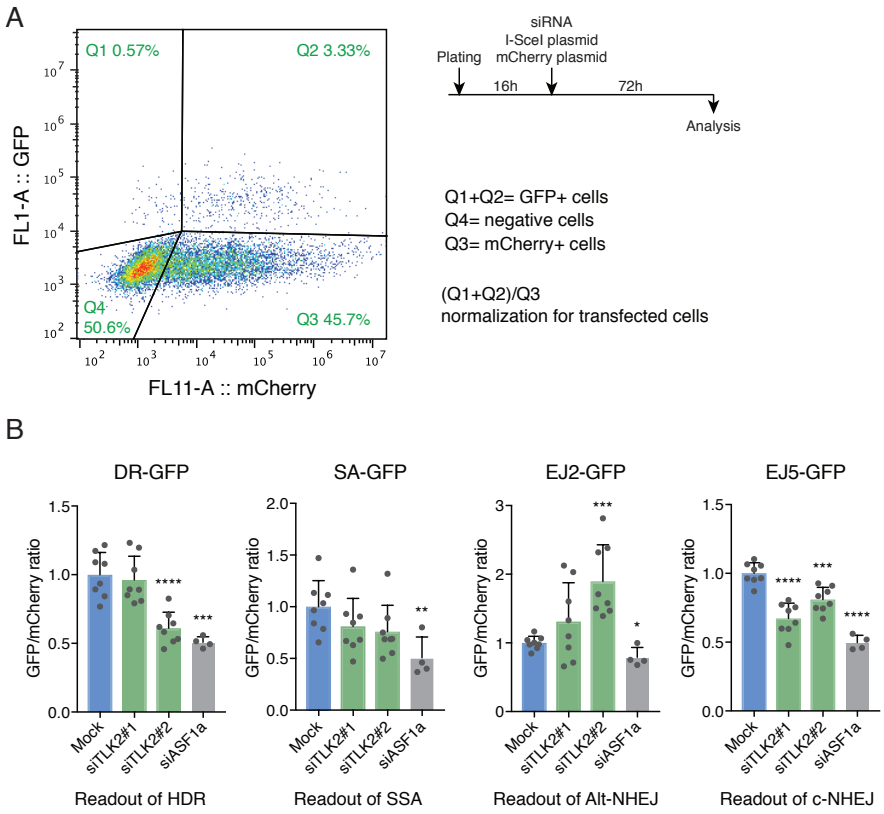

Figure 25. TLKs do not fully phenocopy the role of ASF1a in promoting NHEJ.

(A) Representative flow cytometry plot showing GFP and mCherry intensities (left panel). Experimental design scheme and quantification of positive cells for analysis (right panel). (B) DSB repair pathway efficiency is measured as described in (A) and represented as mean relative to Mock treated cells, which is set to 1. Individual data points of technical duplicates from 2-4 independent biological replicates are shown. Error bars represent SEM and a two-tailed t test was used for statistical analysis.

by knockdown of TLK2 with two different siRNAs, and ASF1a depletion consistently showed a reduction in classical NHEJ (EJ5-GFP reporter), although the extent of the phenotype showed by TLK2 depleted cells was less than the one observed by ASF1a knockdown (Figure 25B). Unexpectedly, ASF1a knockdown also showed a reduction in HDR and SSA, which was not recapitulated by knockdown of TLK2. The previous study demonstrated that in ASF1a CRISPR knockouts there was a prominent increase of HDR efficiency (Lee et al., 2017). Thus, care should be taken when interpreting our preliminary analysis. Additional experiments will be needed to shed light on whether TLK-mediated phosphorylation of ASF1a regulates double-strand break repair.

Chapter 4

Tousled like kinases as a target in cancer therapy

Sandra Segura-Bayona[1], Marina Villamor-Payà[1], Lluís Palenzuela[1], Marc Guiu[1], Camille Stephan-Otto Attolini[1] and Travis H. Stracker[1]

[1] Institute for Research in Biomedicine (IRB Barcelona), the Barcelona Institute of Science and Technology, Barcelona, Spain.

Statement of contribution:

S Segura-Bayona designed, performed and analysed all the experiments.

M Villamor-Payà co-performed with S Segura-Bayona experiments shown in Figure 28B-E.

L Palenzuela maintained mouse cohorts and assisted with xenograft injections.

M Guiu assisted with xenograft injections.

CSO Attolini performed bioinformatics analysis shown in Figure 26 and 27, with feedback from S Segura-Bayona and TH Stracker.

TH Stracker designed experiments and supervised the whole project.

Alterations in *TLK1* and *TLK2* copy number and expression in human cancers

Previous work has linked high expression levels of either *TLK2* or *ASF1B* with poor patient outcome in subsets of breast cancer patients (Corpet et al., 2011; Kim et al., 2016a, 2016b; Mertins et al., 2016). As our results indicated that TLK activity was critical for nucleosome assembly during DNA synthesis and for replication fork stability, we considered that it was likely to be maintained or amplified in many cancer cell types to support proliferation. We examined the available datasets from The Cancer Genome Atlas (TCGA) for copy number alterations (CNAs), mutations or relative expression of the *TLK1* and *TLK2* genes. As a basis of comparison, we also included *ASF1A/B*, *ATR* and *CHEK1* (encoding CHK1), as well as several genes related to proliferation (*MKI67*, *MCM2*, *E2F1*) and well-characterized tumour suppressors or oncogenes (*TP53*, *ATM*, *MYC*, *PTEN*, *EGFR*) to provide scale for comparison. Analysing data from over 7000 patient samples (n=7256), we found that *TLK1*, *TLK2* and *ASF1B* more frequently exhibited copy number increases (CNI) rather than copy number decreases (CND) or mutations (Figure 26). In contrast, CNDs were the most frequent type of alteration observed for *ASF1A*, consistent with recent reports (Figure 26A and 26C) (Lee et al., 2017).

As alterations in gene expression can also occur independently of CNAs, we examined gene expression in the datasets where it was available. We observed that *TLK1* and *TLK2* were expressed in most cancer types at different levels. Expression of both genes was particularly low in kidney chromophobe (kich_tcga) (Figure 27C-D). In addition, we could see gene expression levels corroborated some of the CNI results (Figure 26B), as *TLK1* was most highly expressed in uterine carcinosarcoma (ucs_tcga) and *TLK2* in kidney renal papillary cell carcinoma (kirp_tcga) (Figure 27C-D). We next asked whether there were correlations between the expression of *TLK-ASF1* and *ATR-CHEK1* genes, as well as the proliferation markers *MKI67* and *MCM2* (Figure 27A). At the expression level, *TLK1* and *ASF1A* showed a strong correlation with each other and neither gene was significantly correlated with the expression of proliferation markers (*MKI67* or *MCM2*). In contrast, expression of *ASF1B* and *CHEK1* showed a highly significant correlation with the expression of both *MKI67* and *MCM2* across nearly all TCGA datasets, supporting the proposed utility of *ASF1B* as a proliferation marker (Figure 27A) (Corpet et al., 2011). *TLK2* expression also correlated positively with proliferative markers across the pan-cancer dataset, albeit to a much lesser degree than *ASF1B*, and was significantly correlated with *MKI67* expression in a more limited subset of individual cancers, including breast invasive carcinoma (brca_tcga), liver hepatocellular carcinoma (lihc_tcga), brain lower grade glioma (lgg_tcga), kidney renal papillary cell carcinoma (kirp_tcga) or glioblastoma multiforme (gbm_tcga) (see Table 14 for a complete list).

We next wanted to examine the potential relationship between the genomic alterations or expression differences of *TLK1* and *TLK2* genes and patient outcome. We first carried out a univariate analysis to identify cancer types where *TLK1* or *TLK2* expression was significantly associated with survival or other clinical parameters. We then performed a multivariate analysis on several of these cohorts that showed high levels of CNIs (Figure 26B) or high expression of *TLK1* or *TLK2* (Figure 27C-D). We included age, sex, *MKI67* expression level (proliferation) and tumour stage as covariables in order to determine if

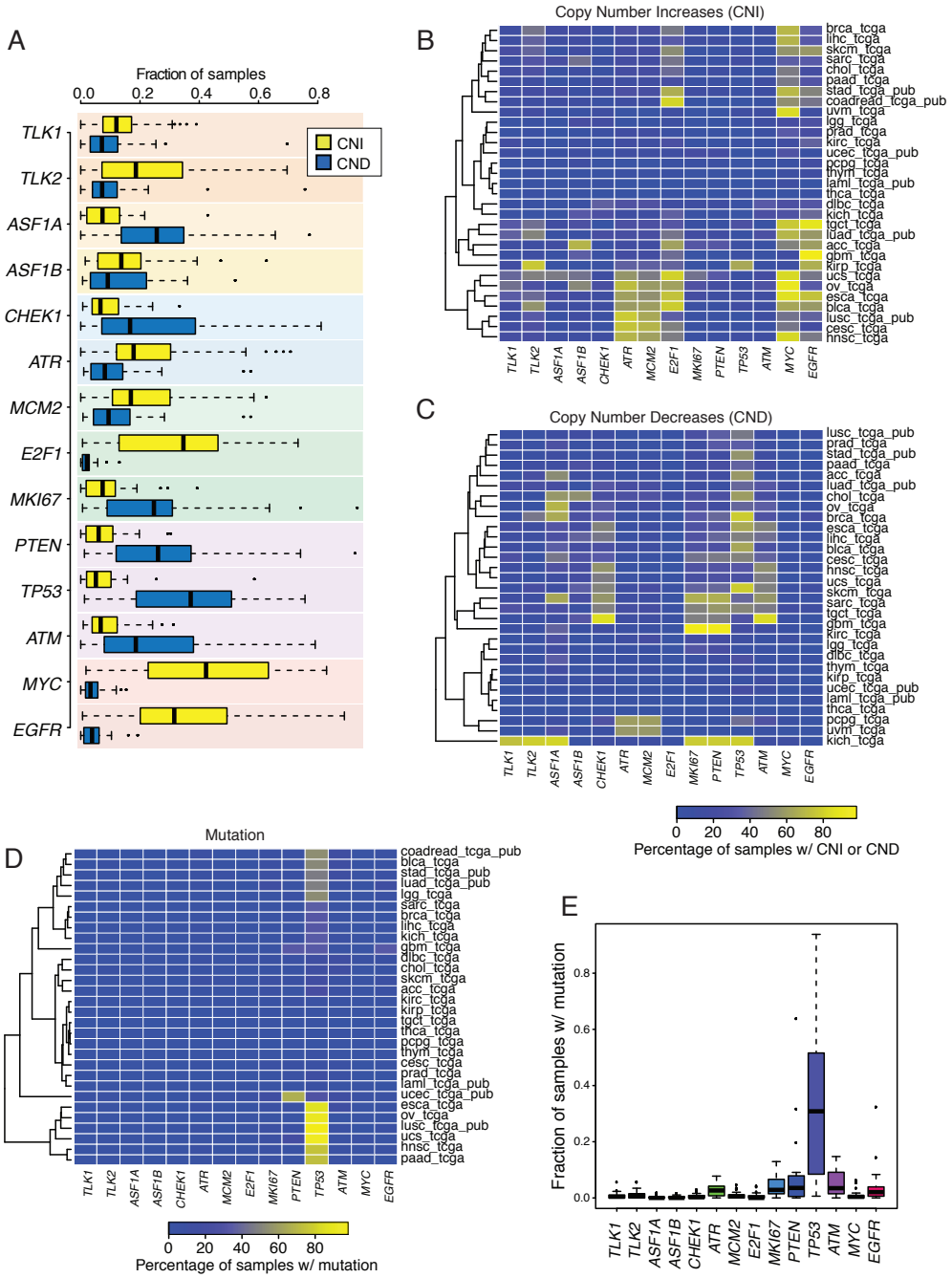

Figure 26. Pan cancer TCGA-cohort analysis of *TLK* and *ASF1* copy number alterations and mutations.

(A) Box plots of the fraction of patients with copy number increases (CNI) or decreases (CND) amongst TCGA cohorts for the indicated genes. (B) Heatmap showing the percentage of samples in individual TCGA cohorts with copy number increases for the indicated gene. TCGA cohort abbreviations and chromosome locations of each gene are provided in Supplementary Tables S3 and S4. (C) Heatmap showing the percentage of samples in individual TCGA cohorts with copy number decreases for the indicated gene. (D) Heatmap showing the percentage of samples in individual TCGA cohorts with mutation events in the indicated gene. (E) Boxplot of the percentage of patients with mutations identified for the indicated gene across TCGA datasets.

TABLE 14. Individual Pearson expression coefficients and log rank test (LRT) p-values for the expression of the gene pair *TLK2.MKI67*.

TLK2.MKI67 expression correlation		p-value	Pearson correlation
Thymoma	thym_tcga	0	0,501236879
Brain Lower Grade Glioma	lgg_tcga	0	0,393449564
Glioblastoma multiforme	gbm_tcga	2,40E-06	0,391882588
Liver hepatocellular carcinoma	lihc_tcga	0	0,344156388
Lung adenocarcinoma	luad_tcga_pub	2,40E-06	0,305362783
Kidney renal papillary cell carcinoma	kirp_tcga	4,00E-07	0,29618752
Lung squamous cell carcinoma	lusc_tcga_pub	0,0002305	0,272722055
Kidney renal clear cell carcinoma	kirc_tcga	0	0,256338027
Breast invasive carcinoma	brca_tcga	0	0,255193854
Uterine Corpus Endometrial Carcinoma	ucec_tcga_pub	9,32E-05	0,253702898
Stomach adenocarcinoma	stad_tcga_pub	3,89E-05	0,253155251
Prostate adenocarcinoma	prad_tcga	0	0,252810398
Bladder Urothelial Carcinoma	blca_tcga	0,0082366	0,23443377
Ovarian serous cystadenocarcinoma	ov_tcga	0,0015082	0,233553912

expression levels of *TLK1* or *TLK2* significantly correlated with patient outcomes. High expression levels of both *TLK1* and *TLK2* correlated with reduced disease-free survival in the uveal melanoma (uvs_tcga) and cervical squamous cell carcinoma and endocervical adenocarcinoma (cesc_tcga) cohorts (Figure 27E-F).

Further, high expression of *TLK2*, but not *TLK1*, was associated with reduced disease-free survival in kidney renal papillary cell carcinoma (kirp_tcga), that was among the cohorts that exhibited the highest number of *TLK2* CNIs amongst the TCGA datasets (Figure 27G), as well as ER+ breast cancer, as previously reported (Figure 27B) (Kim et al., 2016b). Collectively, these results show that *TLK-ASF* pathway genes (specifically *TLK1*, *TLK2* and *ASF1B*) are amplified frequently in many cancer types. In several cases, the expression of *ASF1B* and *TLK2* correlate with markers of proliferation to different degrees in some TCGA patient datasets and high expression of *TLK1* and *TLK2* correlates with poor patient outcome, further suggesting that TLK kinase activity may be a valuable therapeutic target that can enhance the efficacy of checkpoint or PARP inhibitors in a variety of cancer types.

TLK loss is deleterious across a panel of human cancer cell lines

Previous reports have indicated that *TLK2* overexpression is more prominent in luminal B breast tumours (Kim et al., 2016a). We then wanted to test if mRNA levels correlated with protein levels in a panel of breast cancer cell lines from different origins. We assayed TLK1 and TLK2 protein levels in the triple negative breast cancer (TNBC) cell lines BT-20 and MDA-MB-231, the HER2+ cell lines BT-474 and SK-BR-3, and the ER+ luminal cell lines T47D, ZR-75-1 and MCF7 (Figure 28A) compared to the osteosarcoma cell line

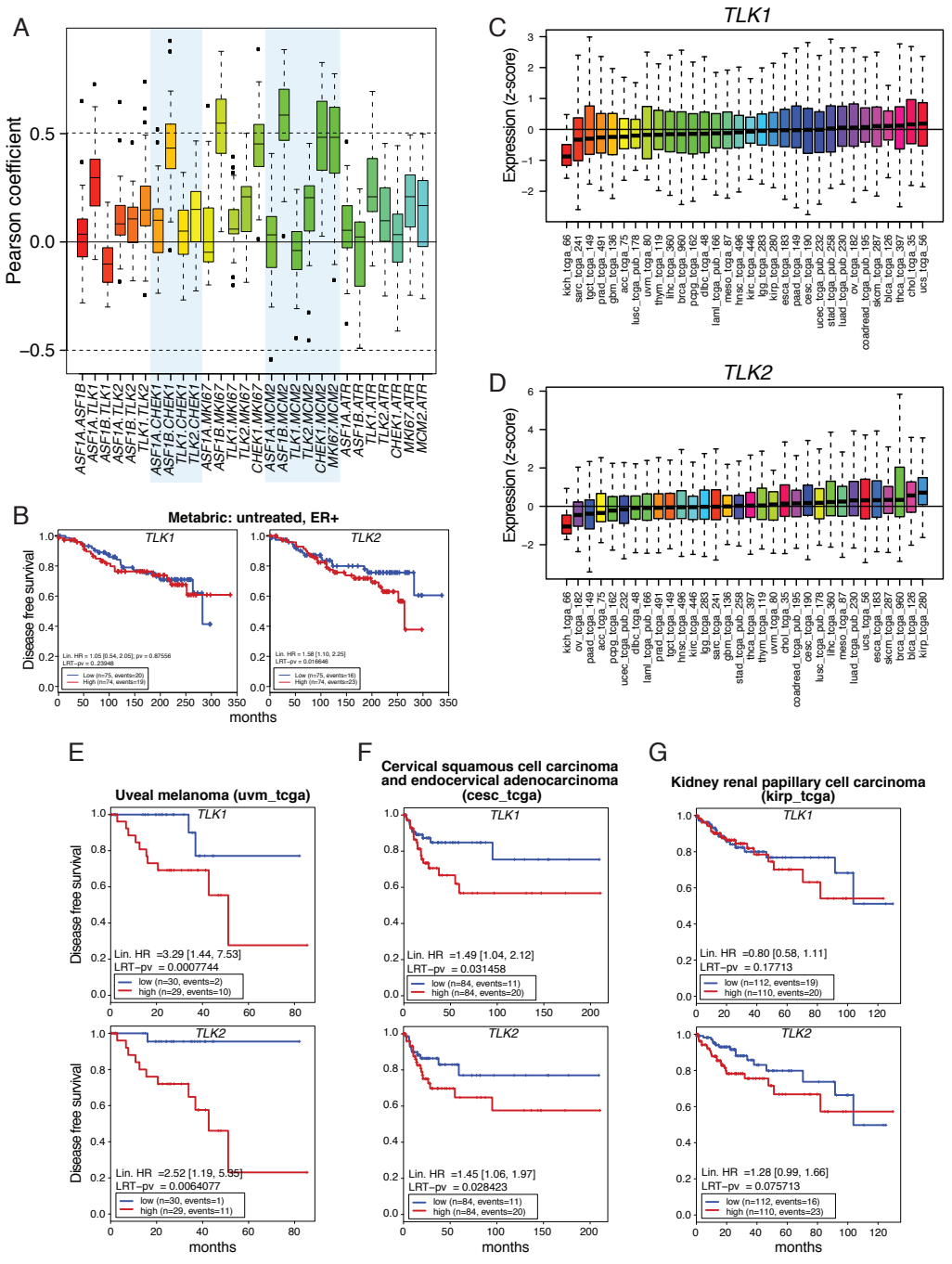

Figure 27. Pan cancer TCGA-cohort analysis of *TLK* and *ASF1* expression and disease-free survival.

(A) Correlation between the expression of the indicated gene pairs across the TCGA cohorts with expression data (n=5977). Individual Pearson expression coefficients and log rank test (LRT) p-values for the expression of the gene pair *TLK2.MKI67* is provided in Table 14. (B) Kaplan-Meier plot of disease free survival in ER+ untreated breast cancer patients in the Metabric cohort (http://www.cbioportal.org/study?id=brca_metabric#summary) based on *TLK1* or *TLK2* expression. The Hazard ratio (HR) and (LRT) p-value calculated using expression as a continuous variable is indicated for each plot. (C-D) Boxplots of gene

U-2-OS. This analysis revealed that all cancer lines expressed similar levels of TLK1 and TLK2, with some exceptions: BT-20 cells appeared to have more relative levels of TLK1, SK-BR-3 cells showed a prominent lower molecular weight TLK1 isoform and MCF7 cells presented with higher TLK2 levels, in agreement with expression data (Kim et al., 2016b). The fact that TLKs were overexpressed in many cancers beyond breast cancer suggested a dependency for TLK activity to suppress replication stress in tumours. We therefore examined the effects of total TLK depletion in a panel of human cancer cell lines from different tissues, including breast, lung, kidney, colon and liver. Depletion of both TLK1 and TLK2 in most of the cell lines examined led to increased DNA damage, indicated by phosphorylation of H2AX in HTM immunofluorescence analysis, although the extent of the response was variable (Figure 28B-D). In addition, whole cell protein lysates indicated that TLK depletion led to replication stress, indicated by phosphorylation of RPA at S4/8 and S33 in most cell lines (Figure 28E). One exception of this replication stress or DNA damage induction by TLK depletion was the PLC/PRF/5 liver hepatoma cell line. We also observed that while all cell lines seemed to respond to TLK depletion with replication stress signalling, those that had higher levels of basal replication stress tended to be more sensitive. For example, NCI-H226 lung cancer cells or SW480 colon cancer cells showed higher basal levels of γH2AX and a much stronger increase following TLK depletion (Figure 28B-C). This prominent DNA damage induction upon TLK depletion may indicate that those tumours that rapidly proliferate and exhibit higher levels of oncogene-induced replication stress could also be more susceptible to TLK inhibition, alone or in combination with checkpoint or PARP inhibitors.

Defining a system for stable TLK loss in human cancer xenograft models

Given the potential role of TLK activity in human cancer progression, we wanted to develop a system where we could assay the effects of TLK inhibition during tumour growth. The first step was to identify a suitable model that would mimic human cancer and allow the manipulations needed for reducing the levels of TLKs. We opted for xenograft injections of breast cancer cell lines (MDA-MB-231) in the mammary fat pad of BALB/c nude mice as a first approach, since it allowed tumour growth in a relatively short time and was a more affordable strategy than generating a genetic system. One of the primary limitations of this system is the lack of a competent immune system due to thymus atrophy, although BALB/c nude mice display innate immunity with NK cells activity, hence the study mostly focuses on the cell-autonomous effects of TLK depletion in tumour growth.

We used CRISPR to develop several human breast cancer cell clones in the MDA-MB-231 cell line with reduced or knockout TLK activity (Figure 20C-F) in order to address the influence of TLK activity on cancer growth and treatment. While we were able to obtain

expression (z-score) for the indicated genes in the indicated datasets. (E-G) Kaplan-Meier plots of multivariate disease-free survival analysis of the TCGA uveal melanoma (uvm, E), Cervical Squamous Cell Carcinoma and Endocervical Adenocarcinoma (cesc, F) and Cervical Kidney renal papillary cell carcinoma (kirp, G) cohorts based on the expression of the indicated gene. The Hazard ratio (HR) and (LRT) p-value calculated using expression as a continuous variable is indicated for each plot.

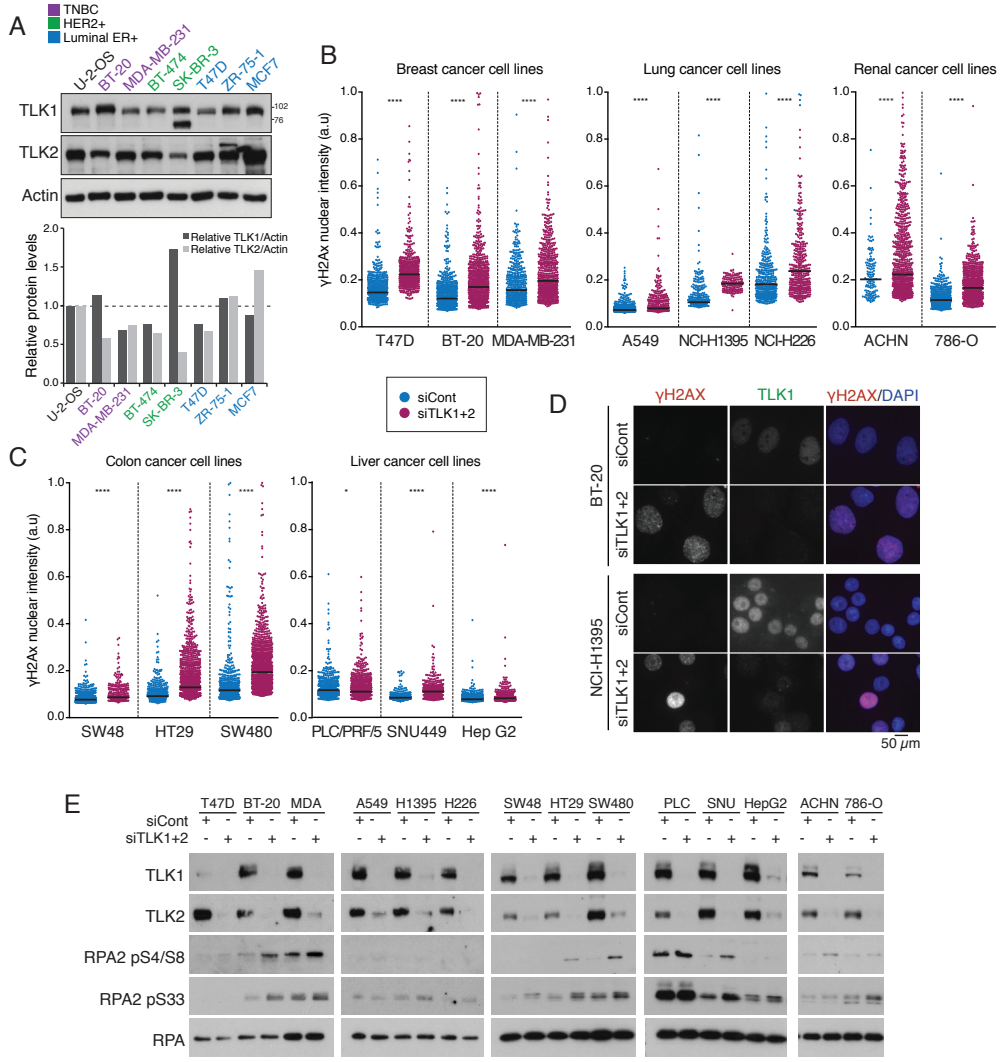

Figure 28. TLK loss is deleterious across a panel of human cancer cell lines.

(A) Western blotting showing TLK1 and TLK2 levels across a panel of breast cancer cell lines (top panel). Graph with quantification of protein levels relative to U-2-OS (bottom panel). (B-C) HTM analysis of γH2AX 48 hours post siRNA treatment in the indicated cell line. One representative experiment out of two is shown. Median is indicated by a black line and statistical significance analysed using a two-tailed t test. (D) Representative image examples for the quantification in (B-C). Staining for γH2AX and TLK1 (to assess depletion levels) are shown. (E) Western blotting 48 hours post siRNA treatment in the indicated cell lines.

stable TLK1 knockout clones, we were unsuccessful in generating stable TLK2 knockout clones, probably reflecting essentiality of this gene and selective pressure in this particular cell line (Figure 20C). Although TLK2 has not been reported to our knowledge as an essential gene in CRISPR screens, it has been postulated as "trans"-essential conditioned to tumours with certain CNA in breast cancer and to be a putative driver gene (Marcotte et al., 2016). We thus went ahead and infected the TLK1 knockout clones and parental MDA-MB-231 cell with retroviruses containing luciferase for tumour imaging and tested

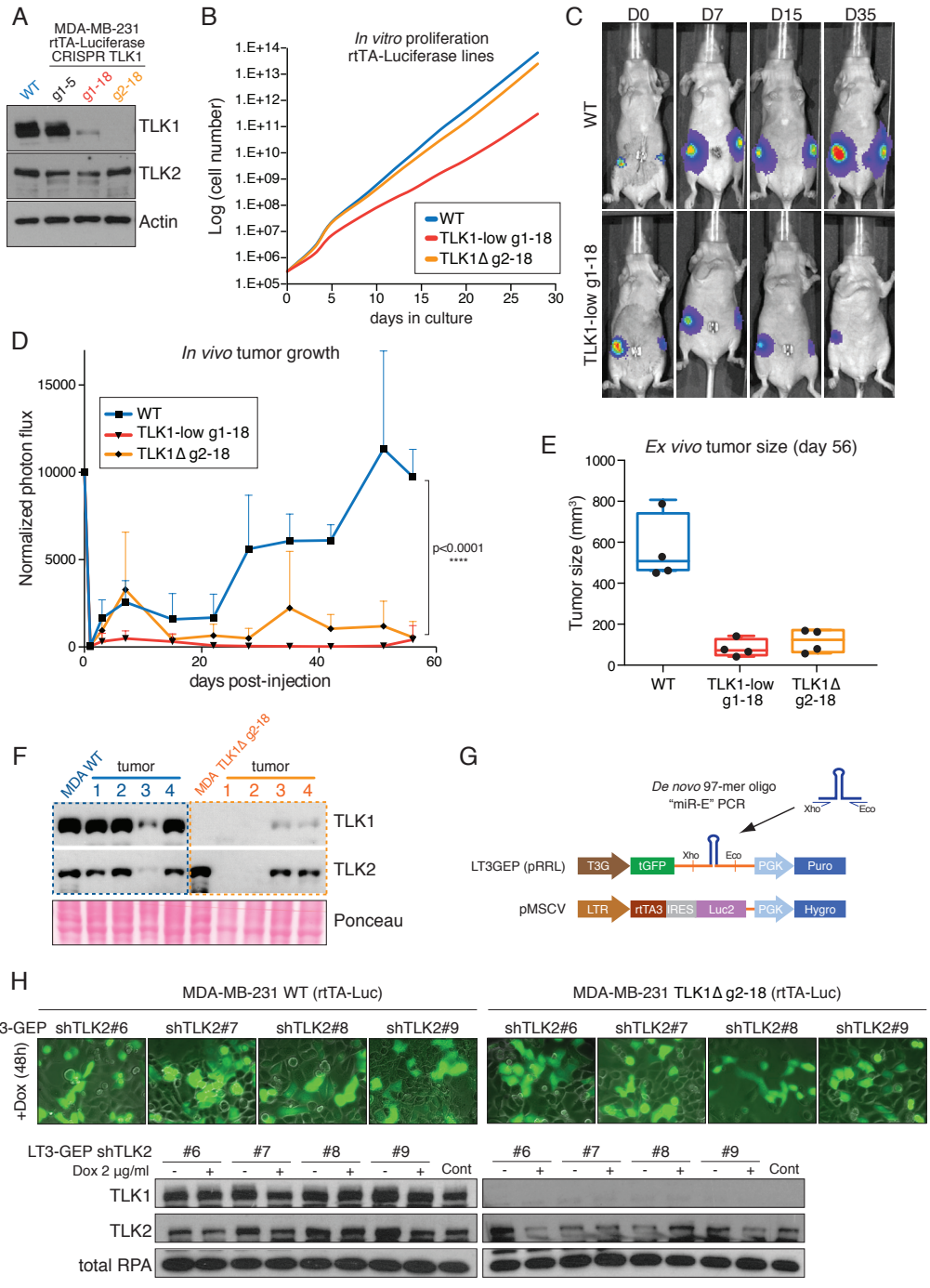

Figure 29. Defining a system for stable TLK loss in human cancer xenograft models.

(A) Western blotting showing TLK1 and TLK2 levels in parental (WT) MDA-MB-231 breast cancer cell lines and TLK1 CRISPR clones that had been infected with plasmids for stable expression of luciferase. (B) Analysis of proliferation rates of MDA-MB-231 clones. Plots are the mean of technical duplicates. (C) Representative bioluminescence images showing mammary tumour progression in xenograft mouse models. (D) Quantification of mammary tumour bioluminescence signal, each data point

that no compensatory levels of TLK2 protein were apparent in several TLK1 clones, that had not been targeted (i.e. clone g1-5), that had reduced levels of TLK1 (TLK1-low, i.e. clone g1-18) and that were TLK1 knockout (TLK1Δ, i.e. clone g2-18) (Figure 29A). We further assayed *in vitro* proliferation of the clones that would be later injected *in vivo*, and did not observe major differences between wild type and TLK1Δ clones, despite TLK1-low clone g1-18 was a bit delayed (Figure 29B). After injecting the cells into the abdominal mammary epithelium, with 4 seeded tumours per cell line, we monitored growth by luminescence imaging on a weekly basis and observed that depletion of TLK1 alone had a strong effect in tumour growth (Figure 29C-E). This was unexpected taking into account the results we previously obtained with these cell clones *in vitro*, in terms of proliferation, colony seeding and DNA damage induction (Figure 20D-F, Figure 22A-E, Figure 22I). When analysing protein levels of resected tumours by Western blotting, we could confirm tumours maintained TLK1 depletion, and in some cases, they had also reduced or lost the expression of TLK2 (Figure 29F).

Additional attempts beyond the use of CRISPR knockout technology were undertaken to achieve stable depletion of TLK2 for *in vivo* xenograft experiments. We attempted to set up an inducible shRNA system that had been developed by J. Zuber's laboratory (Fellmann et al., 2013). This uses the stable incorporation of two vectors, a retroviral vector with the transactivator and Luciferase and a lentiviral vector with inducible target shRNA and GFP expression (Figure 29G). Despite stringent antibiotic selection, induction of these shRNA upon Doxycycline treatment was always partial, observed by poor GFP expression and inefficient knockdown of TLK2 (Figure 29H), suggesting that the promoters were likely being silenced. Despite the outcome of the inducible shRNA trials, we performed histological analysis of the tumours obtained after xenograft injections and could readily observe distinct tissue morphology by H&E, specially for TLK1-low tumours which were very small, compact and composed of very small cells (Figure 30A). Most strikingly, staining with the proliferation marker Ki67 revealed a prominent decrease in TLK1Δ and TLK1-low tumours that was accompanied by a noteworthy increase in DNA damage, seen by staining with γH2AX (Figure 30A). TLK1Δ tumours also presented with some necrotic areas as observed in the γH2AX panel (Figure 30A). It is thus tempting to speculate that reduced tumour growth in TLK1Δ and TLK1-low tumours seeded by MDA-MB-231 clones is due to defective proliferation, replication stress and toxic levels of DNA damage.

Given the reduction of tumour growth we observed in TLK1 targeted tumours, we wondered whether we could be facing differences in tumour initiation potential, since we injected the parental MDA-MB-231 population for WT tumours and single cell derived MDA-MB-231 clones for TLK1Δ or TLK1-low tumours. Single-cell clone selection might reduce heterogeneity and thus could affect tumour initiation potential regardless of the TLK1 knockout effects. In order to test that, we first generated MDA-MB-231 wild type single cell clones and pooled five single cell clones for each genotype in two

represents n=4 independent tumours. (E) Measures of *ex vivo* tumour volume at the endpoint of the experiment in (C-D). (F) Western blotting of resected tumour protein lysates next to protein lysates of the injected cell line. (G) Scheme of the plasmids used in the inducible shRNA system (Fellmann et al., 2013). (H) Representative microscopy images of GFP-shRNA induction upon Doxycycline treatment (top panel). Representative Western blot of TLK1 and TLK2 levels with or without Doxycycline treatment in MDA-MB-231 cells (bottom panel).

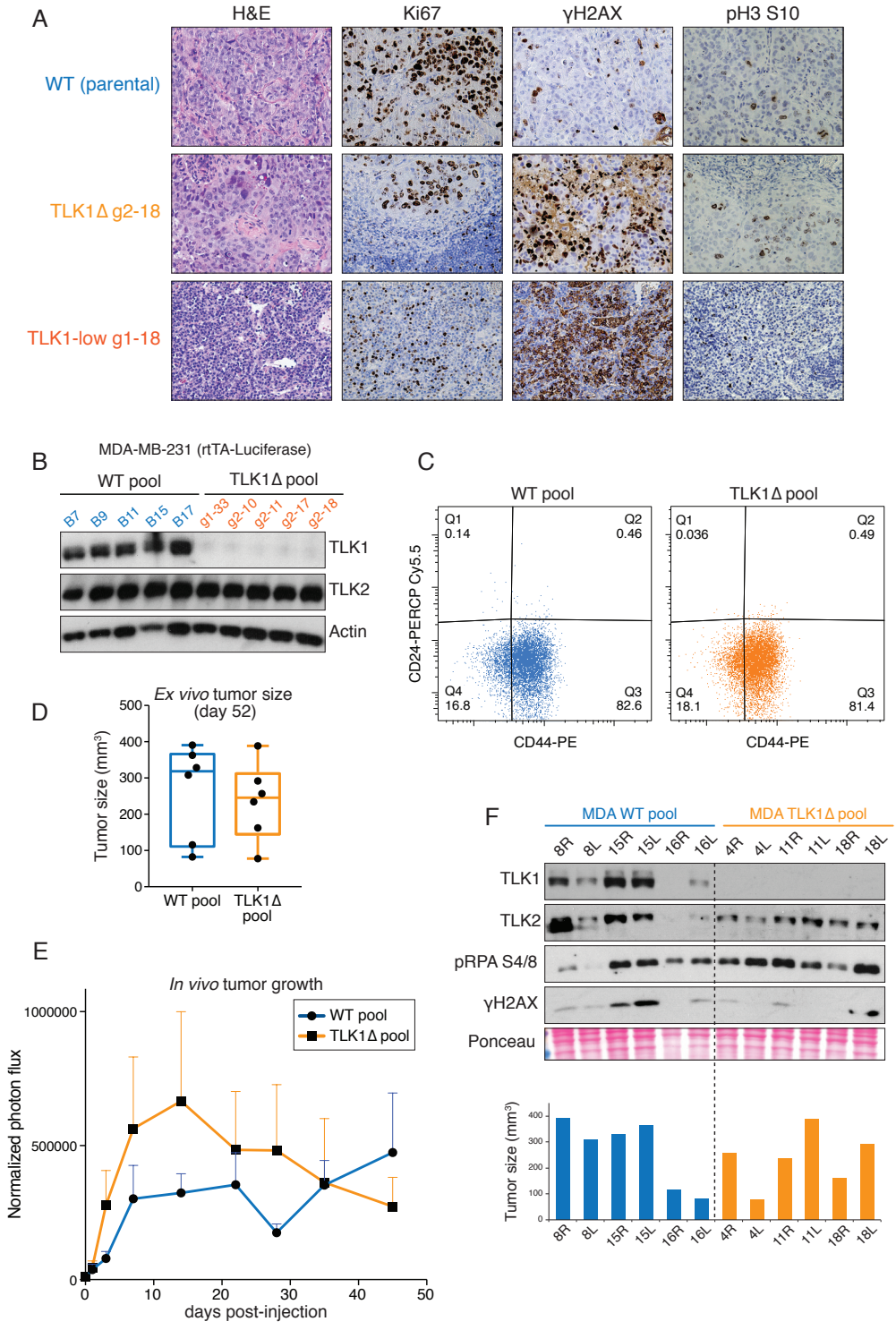

Figure 30. Defining a system for stable TLK loss in human cancer xenograft models. *(Legend in the next page)*

groups, WT and TLK1Δ (Figure 30B). The pool was generated right before injection, so the representation of all the clones would be selected *in vivo*, and not *in vitro*. In a parallel experiment, the two pools were examined for their tumour initiation potential by staining with the cell-surface markers CD24 and CD44. It has been described that in ER- breast cancer subtypes both CD24-/CD44+ and CD24+/CD44+ cell populations display self-renewal and primary tumour initiating capacity when injected into the mammary fat pad of immunodeficient mice (Meyer et al., 2010). Staining the WT and TLK1Δ pools resulted in similar populations of tumour initiating cells, precluding any differences in tumour formation potential (Figure 30C). Thus, we performed an additional *in vivo* experiment, but this time compared growth of the two cell lines that we named WT pool and TLK1Δ pool. After injecting the cells into the abdominal mammary epithelium, with 6 seeded tumours per cell line, we monitored growth by luminescence imaging in a weekly basis and observed that both groups grew with a similar rate, with no significant differences and a wide range of variability (Figure 30D-E). When analysing protein levels of resected tumours by Western blotting, we could confirm TLK1Δ pool tumours were still depleted of TLK1 and they rarely displayed reduced expression of TLK2 (Figure 30F), unlike what we had observed in our previous experiment (Figure 29F). We also noted a correlation in WT pool tumours, since WT bigger tumours exhibited higher levels of TLK1 and TLK2, whereas WT small tumours were devoid of TLK1 and TLK2 (Figure 30F), indicating that their expression likely correlates with the proliferation state of the tumour. Collectively, these results suggest that TLK1 inhibition does not impinge on tumour growth *per se*, and that small tumours that are presumably low proliferating may correlate with low levels of TLKs and higher levels of DNA damage. Moreover, we predict that highly proliferative cancers, particularly those with replication stress, may benefit from elevating TLK activity to a threshold level able to promote resistance to replication stress.

Defining a genetic system for stable TLK loss in a murine breast cancer model

In order to facilitate total TLK2 depletion *in vivo*, we set out to generate a genetic model of breast cancer in mice. The MMTV-PyMT model is a well-established genetic system where females harbouring a transgenic allele of the Polyoma virus Middle T antigen (PyMT) under the control of mouse mammary tumour virus (MMTV) promoter/enhancer. Females expressing PyMT develop with very high penetrance, and with early onset, palpable mammary tumours that often metastasize to the lung (Guy et al., 1992). We crossed MMTV-PyMT mice with our *Tlk1* and *Tlk2* conditional mice (Figure 14A and 14E) that control LoxP site recombination by expression of an ERT2-Cre inducible transgene. Previous to performing an *in vivo* experiment with this model, we first aimed at

(A) Representative images of H&E and Ki67, γH2AX and pH3 S10 immunohistochemical staining performed in xenograft tumours generated in Figure 29C-E. Scale bar: 50 microns. (B) Western blotting showing TLK1 and TLK2 levels in CRISPR single cell clone derived cell lines that constitute the WT pool and the TLK1Δ pool in MDA-MB-231 breast cancer cells. (C) Representative FACS profile of CD24/CD44 staining in WT pool and TLK1Δ pool lines. (D) Measures of *ex vivo* tumour volume at the endpoint of the *in vivo* xenograft experiment. (E) Quantification of mammary tumour bioluminescence signal, each data point represents N=6 independent tumours. (F) Western blotting of resected tumour protein lysates (top panel) accompanied by tumour size of each tumour at day 52 (bottom panel).

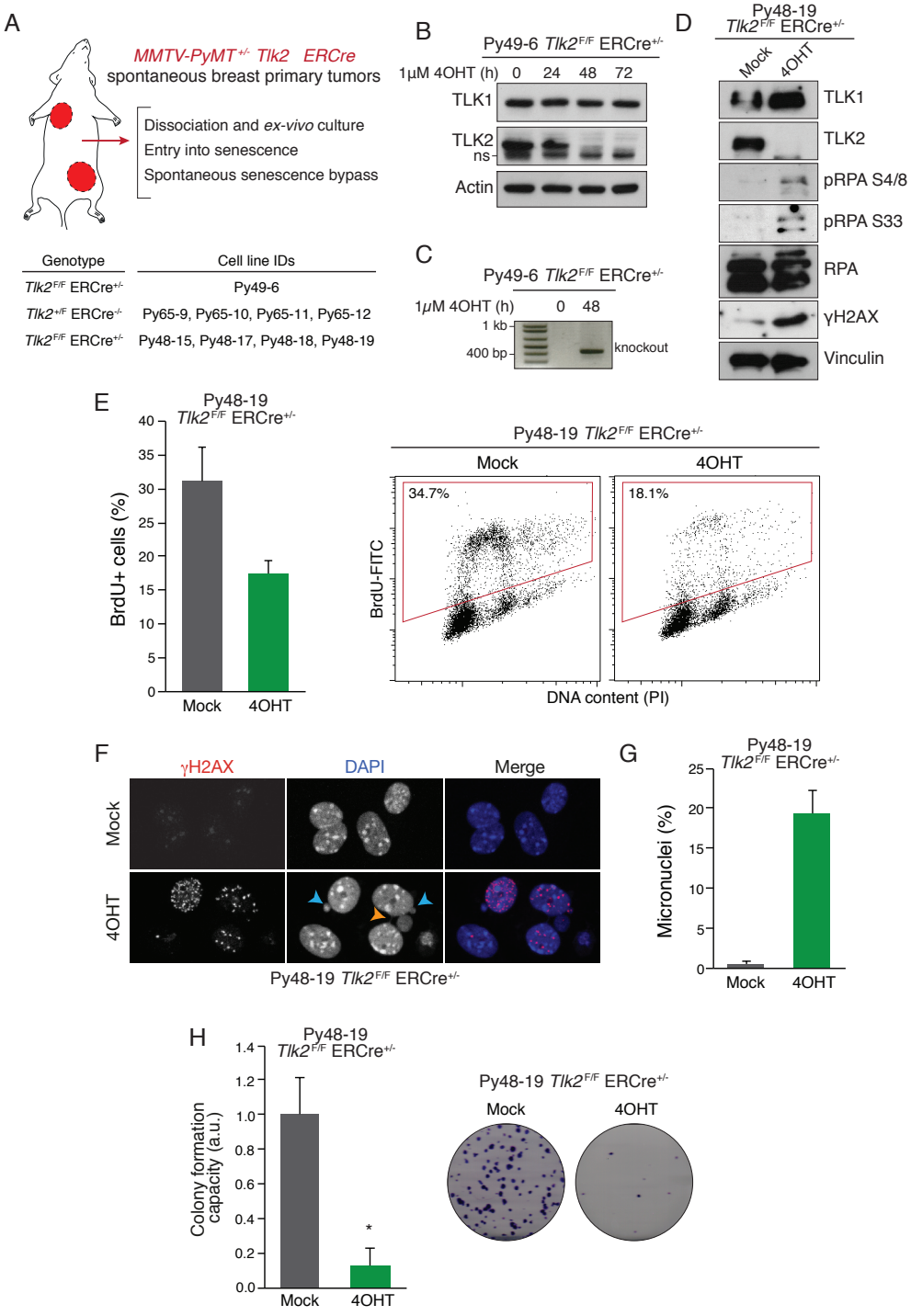

Figure 31. Defining a genetic system for stable TLK loss in a murine breast cancer model. *(Legend in the next page)*

validating the model *in vitro*. For that, we generated various *Tlk2* conditional murine breast cancer cell lines derived from the MMTV-PyMT mouse model. These primary lines were maintained by serial passaging *in vitro* until they entered replicative senescence. Only about half of these cell lines spontaneously transformed (9/19) and bypassed senescence (Figure 31A).

Treatment of these cells with 4-hydroxytamoxifen (4OHT) allowed for deletion of *Tlk2* at 48 hours, and this could be observed both at the protein and genomic DNA level (Figure 31B-C). First, it was very important to understand whether these murine tumour cells recapitulated the phenotypic traits we have previously described in human cancer cells (Chapter 3), since we know from studies in mouse embryonic fibroblasts that *Tlk2* deletion alone does not cause massive DNA damage and only a defect in colony formation capacity (Figure 19). To accomplish this, we depleted TLK2 protein levels following 4OHT induced Cre recombinase induction for 48 h and observed that a severe replication stress phenotype was induced, with a marked enhancement of RPA phosphorylation at S4/8 and S33 (and the phosphorylation shift could even be observed in the total RPA blot) and of the DNA double strand break marker γH2AX (Figure 31D). We analysed proliferation by evaluating the percentage of cells that incorporated the nucleotide analog BrdU and observed a significant reduction of the proliferating BrdU-positive population, indicating that TLK2 is required for DNA replication (Figure 31E). These defects were accompanied by a predominant increase in γH2AX foci evaluated by immunofluorescence as well as mitotic aberrations such as the presence of micronuclei (Figure 31F-G). Ultimately, *Tlk2* deletion led to a severe reduction in colony formation (Figure 31H), similar to the extent that we observed in MEFs when depleting both kinases (Figure 19B). Together, these results reiterate our findings in human cancer cell line models and anticipate that unlike in homeostasis, where TLK1 and TLK2 activities are largely redundant in the mouse, in breast cancer there is a dependency for TLK2 activity to increase robustness of DNA replication of tumour cells and make them resistant to replicative stress, potentially contributing to cancer aggressiveness.

These data thus provide a proof of principle for TLK inhibition in breast cancer and foresee that an *in vivo* genetic experiment would provide valuable information on specific roles of TLKs in cancer progression and metastasis beyond the resistance to replicative stress, such as the interactions with the tumour niche or with the immune system. Moreover,

(A) Scheme of the MMTV-PyMT mouse model (top panel) and table with the derived cell lines that successfully spontaneously transformed (bottom panel). (B) Western blot with antibodies against TLK1 and TLK2 in whole cell extracts of the Py49-6 line mock treated or treated with 4OHT at the indicated times. Actin blot shows equal loading. (C) Agarose gel showing the results of genotyping PCR after cells were treated with 4OHT for 48h. (D) Western blot with antibodies against TLK1, TLK2, the double strand break marker γH2AX and the replicative stress markers pRPA S4/8 and S33 in whole cell extracts of the Py48-19 line mock treated or treated with 4OHT to induce deletion of TLK2. Vinculin blot shows equal loading. (E) Deletion of *Tlk2* reduces short-term BrdU incorporation in Py48-19 cells. Cells were mock treated or treated with 4OHT for 72h, washed, plated and cultured for 24h. Results display technical replicates. (F) Representative images of IF experiments staining for γH2AX are shown from Py48-19 cells that were mock treated or treated with 4OHT. Nuclei were counterstained with DAPI. Blue arrowheads indicate micronuclei and orange arrowhead indicates an anaphase bridge. (G) Percentage of micronuclei scored in DAPI immunofluorescence as seen in (F). Results display technical replicates. (H) Deletion of *Tlk2* reduces colony formation in Py48-19 cells. Relative colony number to mock treated cells is displayed. Results display two biological replicates, each performed in technical duplicates. Statistical significance was analysed using a two-tailed t test.

an *in vivo* genetic experiment would allow us to test our therapeutic concept of synthetic lethality (Chapter 3) of inhibition of TLKs coupled with checkpoint or PARP inhibitors.

Chapter 5

TLK activity maintains histone density and suppresses ALT-mediated telomere lengthening and an IFN response

Sandra Segura-Bayona[1], Camille Stephan-Otto Attolini[1] and Travis H. Stracker[1]

[1] Institute for Research in Biomedicine (IRB Barcelona), the Barcelona Institute of Science and Technology, Barcelona, Spain.

Statement of contribution:

S Segura-Bayona designed, performed and analysed all the experiments.

CSO Attolini performed all bioinformatics analysis, with constant feedback from S Segura-Bayona and TH Stracker.

TH Stracker designed experiments and supervised the whole project.

TLK depletion leads to global changes in chromatin accessibility

Given that TLK depletion influenced the deposition of new histones (Figure 21), we wanted to determine whether TLK depletion had specific or stochastic genome wide effects in chromatin accessibility. How nucleosomes are positioned throughout the genome has a prominent regulatory function since it defines the available binding sites for transcription factors and the transcriptional machinery, as well as for DNA repair, replication and recombination factors. We thus evaluated chromatin accessibility in the absence of TLK1, TLK2 or both TLKs using the Assay for Transposase-Accessible Chromatin (ATAC) (Buenrostro et al., 2013) followed by deep-sequencing (ATAC-seq) in two biological replicates (Figure 32A). This method requires 50,000 unfixed cell nuclei that are used for chromatin preparation. These are then incubated with purified Tn5 transposase loaded with adapters for next generation sequencing (NGS) *in vitro*. The adapters are integrated primarily into regions of accessible (open) chromatin, as protected (closed) chromatin regions are inaccessible to the transposase. After library preparation and paired-end NGS, sequencing reads map to open chromatin providing a genome wide map of chromatin accessibility. For analysis of ATAC-seq results, we considered consensus peaks as those that appeared in at least one of our four conditions, so we could see chromatin accessibility changes. From those consensus peaks covering the whole genome, we could see that upon total TLK depletion, 10% of the genome became differentially accessible (Figure 32B). These significant changes involved regions that were depleted of accessibility peaks, with a negative fold change, and these were mostly promoter-TSS regions. Conversely, significant changes also involved regions enriched with accessibility peaks, with a positive fold change, and these were mostly intronic and intergenic regions (Figure 32B-C). Thus, the genomic distribution of accessibility peaks was not random. Our results suggested that single depletion of TLK1 or TLK2 follow the same trend, but differences were always more evident in the absence of both TLKs, with intergenic regions becoming more open and promoter-TSS becoming more protected (Figure 32D). This striking result immediately made us think about the histone variant H3.3, which is present at both chromosomal locations, in particular at active promoter regions and at pericentric heterochromatin (Buschbeck and Hake, 2017). We have previously shown that TLK activity is needed for *de novo* deposition of the replacement histone variant H3.3 (Figure 21). This histone variant is encoded by two genes, *H3f3a* and *H3f3b*, which are located out of the replication-coupled histone gene cluster. Its assembly into chromatin is thus replication-independent, being expressed and deposited throughout the cell cycle by two separate complexes, the HIRA complex and the DAXX-ATRX complex (Buschbeck and Hake, 2017). It has been previously shown that different chromatin environments require one or the other histone deposition pathway: promoters and active gene regions harbour HIRA-deposited H3.3 whereas heterochromatin regions encompass DAXX-ATRX-deposited H3.3 (Goldberg et al., 2010). Therefore, we next wanted to address the endogenous levels of H3.3 in chromatin in immunofluorescence by Triton pre-extracting soluble pools of histones. Quantification of chromatin-bound nuclear intensity of H3.3 staining by HTM revealed a significant reduction of H3.3 levels in TLK depleted cells (Figure 32E). These results were also confirmed by an alternative approach using U-2-OS

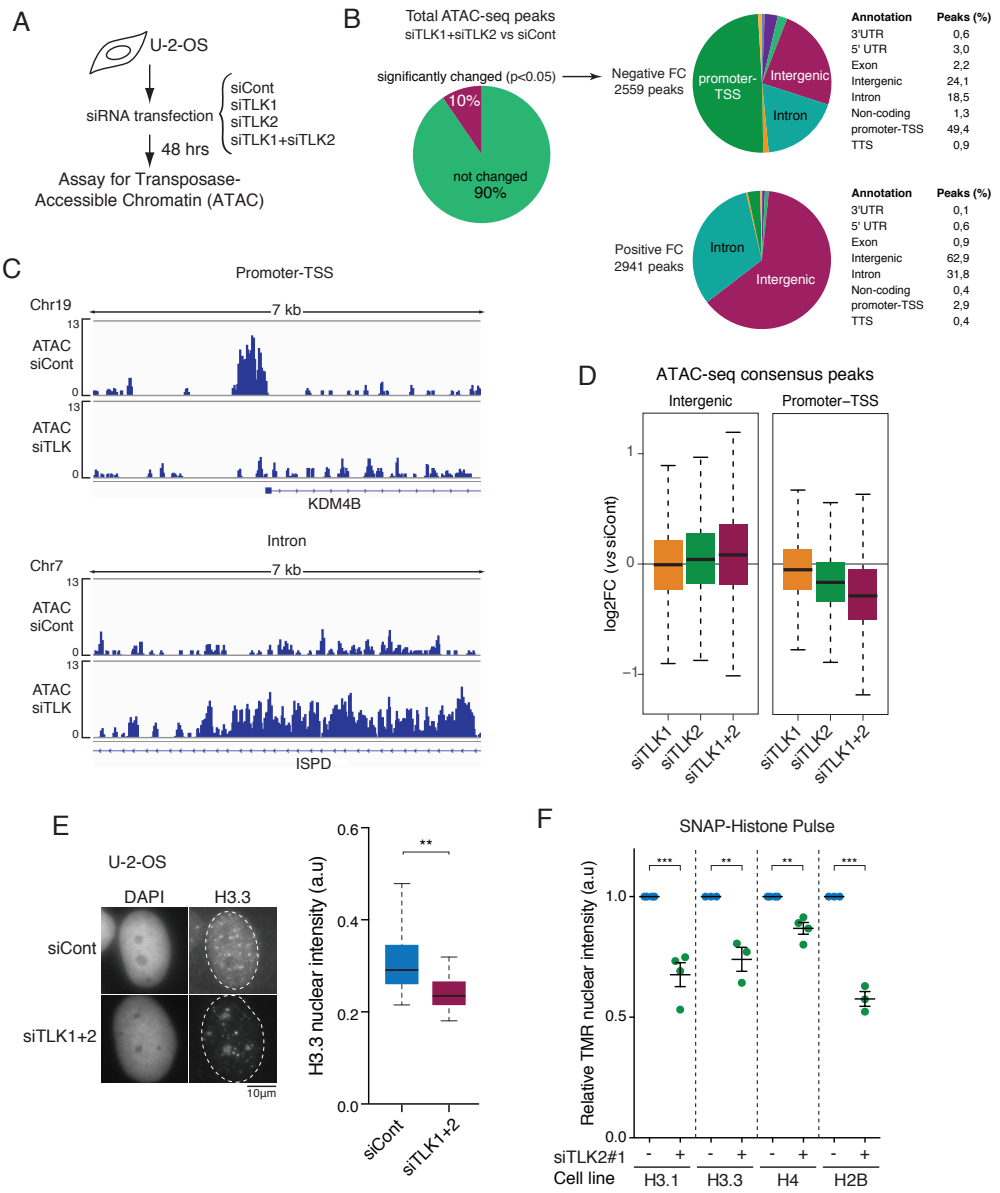

Figure 32. TLK depletion leads to global changes in chromatin accessibility.

(A) Experimental design of ATAC-seq experiment. (B) Changes on chromatin accessibility upon depletion of TLK1 and TLK2 are statistically significant in 10% of the genome (n=2) (left panel). Genome annotation of peaks with statistically significant negative or positive fold change upon TLK depletion (right panel). (C) Representative IGV tracks of ATAC-seq reads of a promoter-TSS (top panel) and intronic region (bottom panel) that become differentially accessible upon TLK loss. (D) Boxplots of ATAC-seq fold changes (FC) relative to siCont computed in intergenic and promoter-TSS regions. (E) Representative IF image stained by endogenous H3.3 after triton pre-extraction (left panel). Quantification of chromatin bound H3.3 levels, data are joint of 4 biological replicates with n>130 nuclei analysed per experiment. Median is shown with boxes and whiskers: 25-75 and Min-Max percentile ranges. An unpaired t test was used for statistical analysis of the average of each independent experiment. (F) Quantification of SNAP-tag histone incorporation by Pulse-fix analysis. TMR intensity relative to mock-transfected cells is plotted. Each data point represents an independent experiment, n>300 nuclei were analysed per each experiment. Lines and error bars represent means and SEM. A two-tailed t test was used for statistical analysis.

cells that expressed SNAP-tag histones. By doing Pulse-fix IF experiments, which label the pool of histones present at the chromatin 48 hours after siRNA transfection, we could observe the total levels of SNAP-tag histones. The total levels of chromatin bound SNAP-tag histones H3.1, H3.3, H4 and H2B were significantly reduced following depletion of TLK activity with TLK2 siRNA (Figure 32F). As TLK depletion activates a checkpoint response, the effects on histone biosynthesis could be indirect and a result of mRNA decay and less histone protein translation for the canonical histones H3.1, H4 and H2B (Figure 32F) (Rattray and Müller, 2012). However, unlike core histones, the H3.3 histone variant is not encoded by multi-copy gene clusters but by two single genes that contain introns and are constitutively transcribed throughout the cell cycle (Buschbeck and Hake, 2017; Talbert and Henikoff, 2017). Thus, the SNAP-tag histone result reinforces the likelihood that there is direct reduction of chromatin-bound H3.3 levels in TLK depleted cells. Together, our findings show that TLKs are required for the maintenance of chromosome accessibility at specific genomic regions, namely promoter-TSS and intronic-intergenic regions, and this could be mediated in large part by effects on H3.3 histone variant deposition.

Reduced TLK activity preferentially alters heterochromatin and TSS sites

We next wanted to evaluate how our chromatin accessibility changes correlated with certain regions of the genome characterized by histone modifications, histone variants or binding of specific chromatin factors. For that, we overlapped our ATAC results with published datasets of ChIP-seq performed in U-2-OS cells and assayed whether the overlapping peaks behaved differently from the non-overlapping peaks. We could prove that ATAC peaks overlapping with H3K9me3 mark (GSM788078) were enriched in TLK depleted samples, indicating that heterochromatic regions become more accessible upon TLK loss (Figure 33A). ATAC peaks overlapping with RNA Polymerase II binding sites (GSE73742 (Pradhan et al., 2016)) were negatively enriched in TLK2 and double-TLK depleted samples, corroborating the diminished accessibility of promoter-TSS observed upon TLK depletion (Figure 33A). The overlap of ATAC peaks with H3.3 histone variant (GSE73742 (Pradhan et al., 2016)) was negatively enriched in TLK depleted samples, illustrating that most of the peaks that overlapped likely correspond to promoter-TSS regions (Figure 33B). It is not surprising that we fail to see H3.3 changes in heterochromatic regions, since these are much less accessible than promoter-TSS sites on average and may not be fully annotated in the genome. We also overlapped ATAC peaks with the H3.3 histone chaperone HIRA, required for depositing H3.3 specifically at actively transcribed genes and promoters. For this we used a HIRA ChIP-seq dataset generated in HeLa cells (GSE45024 (Pchelintsev et al., 2013)) and observed the overlap with ATAC peaks was similar to the one of H3.3, indicating that HIRA-bound regions become less accessible upon TLK depletion (Figure 33B).

Subsequently, we aimed to validate some of the highest and lowest accessibility peaks upon total TLK depletion by ATAC-qPCR. We could readily validate the peaks that became

most accessible upon TLK loss (hit 1 to hit 3) by ATAC-qPCR, and these often overlapped with H3K9me3 regions and H3.3 in published datasets (Figure 33C and Supplementary Figure 3A). On the contrary, validating the lowest promoter peaks that became more protected upon TLK loss by ATAC-qPCR proved to be more difficult. Although we could see a tendency towards becoming less accessible after TLK depletion by ATAC-qPCR, the differences were not statistically significant (Figure 33C). Importantly, we did not observe a strong correlation between gene expression in RNA-seq and promoter accessibility, as this was only seen in about 10% of the genes (Supplementary Figure 3B). Thus, decreased chromatin accessibility is not sufficient to predict transcriptional repression in most of the promoter-TSS regions we observed upon TLK depletion.

Given the highly reproducible increase in accessibility in heterochromatic regions by ATAC-qPCR, we reasoned that reduced chromatin deposition in these regions could be the underlying mechanism for the changes in accessibility. In view of that, we assessed the statistical overrepresentation of the effects of TLK depletion on diverse genomic and epigenomic features previously associated with DNA damage and patterns of mutagenesis. Increased accessibility in TLK depleted cells was positively correlated with the heterochromatic mark H3K9me3 (Figure 33A and 33D) and negatively correlated with the euchromatin mark of active genes H3K36me3 and replication timing (Figure 33D). At a medium resolution of 10 kb, we did not observe any correlation with chromosomal locations such as distances to telomeres or centromeres (Figure 33D). Late replication timing is a well-known determinant of increased somatic mutation rates and correlates prominently with more closed chromosomal conformation (Rhind and Gilbert, 2013). In order to test whether increased accessibility in ATAC-seq upon TLK depletion is associated with replication timing, we used RepliSeq data from ENCODE (NHEK dataset as an average track) to correlate our ATAC fold changes. Interestingly, whereas we observed a flat trend line in siTLK1 depleted cells, we could observe an anti-correlation in siTLK2 depleted cells that was even more pronounced when depleting both TLKs (Figure 33E and data not shown). This indicated that the regions that become more accessible in TLK depleted cells correspond to late replication domains and the regions that become more protected correspond to early replication domains. In addition, when we used the ChromHMM tool where chromatin has been classified in several states (Ernst and Kellis, 2012) to correlate our ATAC fold changes, we manifestly observed that promoters (both active and inactive/poised) had decreased accessibility upon TLK loss, and heterochromatin (the "grey" repetitive/CNV chromatin state) had the most prominent increase in accessibility upon TLK loss (Figure 33F). Overall, these results strongly indicate that constitutive heterochromatin, which is restricted mainly to inert gene-poor regions, pericentromeres and telomeres, comprises the chromatin region most overrepresented in accessibility in the absence of TLKs, whereas promoter-TSS result strikingly protected.

(E) Boxplots of ATAC-seq FC (siTLK1+2 relative to siCont) through different replication timing chromatin regions from NHEK RepliSeq ENCODE dataset (NHEK was used an average track). (F) Boxplots of ATAC-seq FC (siTLK1+2 relative to siCont) through different ChromHMM chromatin states.

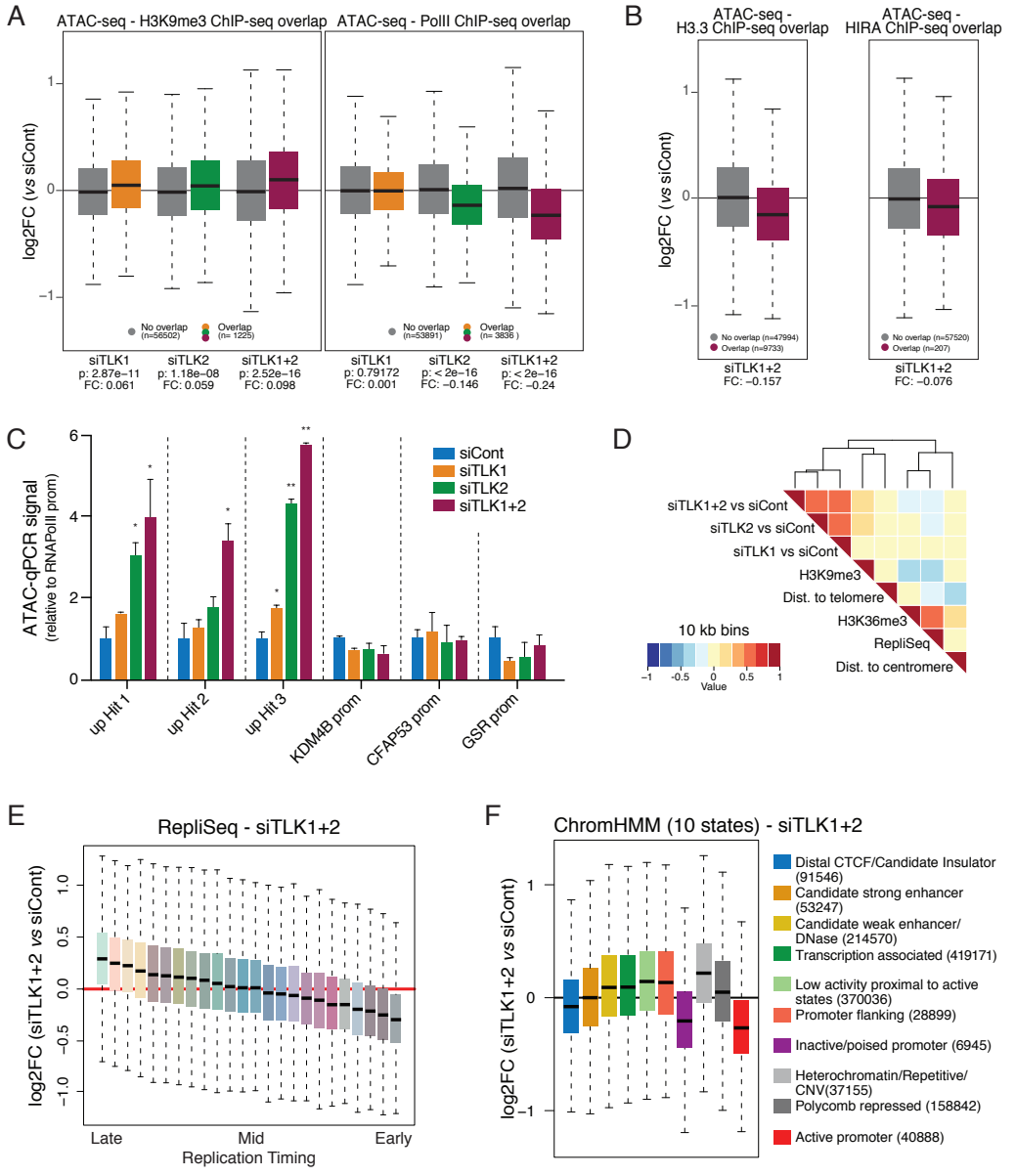

Figure 33. Reduced TLK activity preferentially alters heterochromatin and TSS sites.

(A) Boxplots depicting ATAC-seq FC relative to siCont computed in regions do or do not overlap with H3K9me3 ChIP-seq (GSM788078) and PolII ChIP-seq (GSE73742). (B) Boxplots depicting ATAC-seq FC of siTLK1+2 relative to siCont computed in regions do or do not overlap with H3.3 ChIP-seq (GSE73742) and HIRA ChIP-seq (GSE45024). (C) ATAC-qPCR was used to assess open chromatin at selected genomic regions in U-2-OS cells. Data of qPCR amplification were normalized to unchanging genomic region (RNAPol II promoter region) and represented as the fold-change relative to the signal obtained in siCont conditions, which were set to 1. Experiments were done in two biological replicates with technical replicates. Mean and SEM are shown, an unpaired t test was used for statistical analysis. (D) Heatmap that shows the correlation relationship grouped using hierarchical clustering between ATAC-seq FC (relative to siCont) and large-scale chromatin features at 10 kb resolution.

TLK depletion causes impaired H3.3 deposition and DNA damage at heterochromatin

Since we believed that TLK loss impinged on the deposition of H3.3, we next investigated H3.3 genomic locations upon TLK depletion using ChIP-seq. Analysis of H3.3 ChIP-seq peak differences among siCont and siTLK1+2 resulted in an average decrease of H3.3 occupancy in all genomic regions examined (Figure 34A). Moreover, integrated read density of all H3.3 peaks showed a prominent reduction of H3.3 occupancy, which was even more accentuated when looking at peaks that aligned to TSSs (Figure 34B). Thus, it is tempting to speculate that reduced H3.3 occupancy at promoter-TSSs may cause conformational changes in chromatin that cripple Tn5 transposase accessibility at those sites, potentially by allowing other factors to bind.

We next focused on how the accessibility changes we observed in TLK depleted cells, potentially due to the loss of H3.3, could affect the functionality of well-established heterochromatic sites. Telomeres are heterochromatic and endogenous sources of replicative stress. Given the increased chromatin accessibility of heterochromatin (Figure 33) and increased replicative stress (Figure 22) that appear upon TLK depletion, we reasoned that telomeres may be affected. It has been previously shown at mammalian telomeres that histone H3.3 is needed for trimethylation of H3K9 and formation of heterochromatin, and the absence of H3.3 generates DNA damage and sister chromatid exchange at telomeres (Udugama et al., 2015). We assayed accessibility at these sites by ATAC-qPCR and occupancy of H3.3 and H3K9me3 by ChIP-qPCR. Similar to the hits that become more accessible upon TLK loss (Figure 33C), we also observed that telomeres become more accessible upon TLK loss by ATAC-qPCR (Figure 33C). Additionally, ChIP-qPCR analysis revealed decreased occupancy of H3.3 and H3K9me3 at telomeres (Figure 33D).

It has been previously shown that defective H3.3 histone deposition by the ATRX-DAXX complex is a hallmark of recombination at telomeres (Dilley and Greenberg, 2015). We confirmed that the ssDNA binding protein RPA accumulated in discrete foci that co-stained with the shelterin subunit TRF2 or Telomeric FISH signal in U-2-OS cells upon depletion of TLK activity by TLK2 siRNA (Figure 34E-F). Alternative lengthening of telomeres (ALT), a telomerase independent mechanism of telomere maintenance, is often accompanied by inactivation of ATRX or DAXX, either by mutation or genomic loss. U-2-OS cells are ALT+ and ATRX-deficient. We hypothesized that in U-2-OS cells, in the absence of a functional ATRX-DAXX pathway for telomeric H3.3 maintenance, there might be a requirement of a TLK-ASF1-HIRA mediated pathway that was able to provide some level of redundancy in H3.3 deposition. As H3.3 is reported to be a major component of telomeric heterochromatin, we addressed whether heterochromatin formation was impaired by analysing the chromatin bound pool of H3K9me3 and HP1α. While we were unable to consistently observe differences in H3K9me3 staining (data not shown), we did observe reproducible reduction in chromatin-bound HP1α by immunofluorescence upon TLK depletion (Figure 34G). Collectively, we showed that TLKs are needed for H3.3 deposition and the reduced H3.3 occupancy at promoter-TSS sites may account for changes in accessibility at those sites. On the contrary, reduced H3.3

occupancy at heterochromatin regions, specifically in cells that rely on TLK-ASF1-HIRA, might cause increased chromatin accessibility, aberrant heterochromatin formation and replicative stress at those sites.

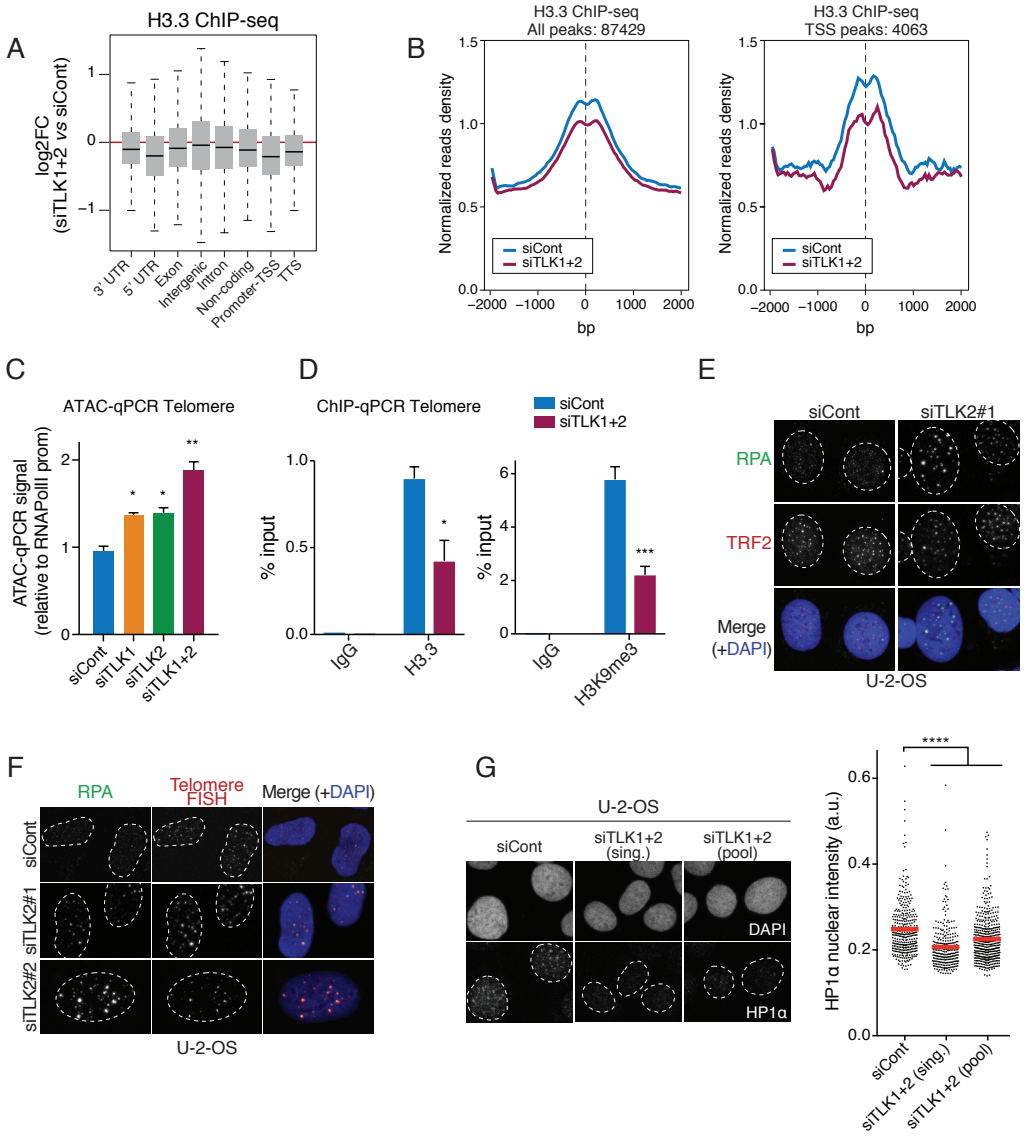

Figure 34. TLK depletion causes impaired H3.3 deposition and DNA damage at heterochromatin.

(A) Boxplots of H3.3 ChIP-seq FC (siTLK1+2 relative to siCont) through different genomic annotations. Data are from two biological duplicates. (B) Normalized read density at all H3.3 peaks centered at peak center and with +/- 2 kb (left panel). Normalized read density at H3.3 peaks located at TSS with +/- 2 kb (right panel). (C) ATAC-qPCR was used to assess open chromatin at telomeres in U-2-OS cells. Data are analysed as in Figure 33C. (D) ChIP-qPCR was used to assess occupancy of H3.3 and H3K9me3 at telomeres in U-2-OS cells. Data of qPCR amplification were normalized to input and represented as the percentage of input. Experiments were done in two biological replicates with technical replicates. Mean and SEM are shown, an unpaired t test was used for statistical analysis. (E) IF staining of RPA-TRF2 in U-2-OS cells. (F) IF-FISH staining of chromatin bound RPA and telomeres. (G) Representative IF images of HP1α staining in U-2-OS cells (left panel). Quantification of chromatin bound HP1α levels, data are from one biological replicate with n>300 nuclei analysed, and representative of four biological replicates. Average is shown in red and an unpaired t test was used for statistical analysis

Total TLK depletion induces features of ALT

The accumulation of RPA at telomeres in U-2-OS cells (Figure 34E-F) suggested the exposure of telomeric ssDNA, indicating replication stress and accumulation of potentially recombinogenic products at telomeres. U-2-OS is an ALT+ cell line, characterized by very long and heterogeneous telomeres, the presence of ALT-associated PML bodies (APBs) and altered DNA damage and recombination at telomeres, resulting in the presence of telomeric extrachromosomal circles (Lazzerini-Denchi and Sfeir, 2016). In U-2-OS, co-staining with the telomere marker TRF2 and PML revealed an enhancement of ALT associated PML bodies upon TLK2 or total TLK depletion (Figure 35A-B). We also noticed a remarkable increase in the fluorescent intensity of these PML bodies, and indeed that was the case when we quantified the nuclear intensity of PML staining (Figure 35C).

Next, we set out to determine whether TLK depletion was able to induce features of ALT in a non-ALT cell line. For this we used HeLa LT cells, a clone of the parental HeLa 1.2.11 cell line that was previously derived with long telomeres of about 20 kb (O'Sullivan et al., 2014) and where telomere elongation occurs via Telomerase. First of all, we tested whether in these cells, depletion of TLK activity would cause increased chromatin accessibility at the heterochromatic regions we identified by ATAC-qPCR. We could see that TLK depletion by siRNA caused an increase in accessibility at those regions (Figure 35D). We next focused on telomeres and generated some knockout clones of TLK1 by CRISPR (TLK1Δ). Total TLK depletion achieved by depleting TLK2 in TLK1Δ HeLa LT cells increased the presence of ALT-associated PML bodies and importantly, it also resulted in a prominent increase in the fluorescent intensity of PML bodies that was dependent on the loss of both TLKs (Figure 35E-F). Total TLK depletion caused massive replicative stress and DNA damage in these cells visualized in Western blot by phosphorylation of RPA at S4/8 and γH2AX (Figure 35G) and in immunofluorescence by accumulation of chromatin-bound RPA that often co-localized with telomeres (Figure 35H-I).

Given that HeLa LT cells have a proficient ATRX-DAXX pathway for H3.3 deposition, we thought that this could explain why we did not observe such a dramatic increase in accessibility of heterochromatic regions upon TLK loss compared to U-2-OS cells (Figure 35D and Figure 33C). Moreover, ATRX has been previously shown to suppress ALT (Clynes et al., 2015), although the depletion of ATRX alone does not fully recapitulate ALT (Chen et al., 2017; Lovejoy et al., 2012). Thus, we tested whether concomitant inhibition of ATRX-DAXX and TLK-ASF1-HIRA pathways would enhance features of ALT in HeLa LT cells. For that, we set up the C-circle assay that quantifies the presence of ALT specific extrachromosomal single-stranded C-rich (CCCTAA) telomeric circles (C-circles) (Henson et al., 2009, 2017). C-circles are partially double-stranded, and the

t test was used for statistical analysis (n=4 for siCont, n=3 for siTLK2, TLK1Δ siCont/siTLK2, n=1 for siASF1). (F) HTM-mediated quantification of IF staining intensity of chromatin bound PML bodies in HeLa LT cells, data are from one biological replicate with n>100 nuclei analysed, and representative of three biological replicates. Median is shown in red and an unpaired t test was used for statistical analysis. (G) Western blotting of DNA damage signalling markers upon TLK loss in HeLa LT cells, parental (WT) and TLK1 CRISPR knockout clones (TLK1Δ). (H) Representative IF image of RPA-TRF2 staining in HeLa LT cells. (I) Quantification of cells with more than 5 RPA discrete foci, with more than 200 cells evaluated per individual experiment. An unpaired t test was used for statistical analysis (n=6 siCont, n=5 for siTLK2, n=2 for TLK1Δ#5 siCont/siTLK2 and TLK1Δ#12 siCont/siTLK2, n=4 for TLK1Δ#8 siCont/siTLK2, n=2 for siASF1).

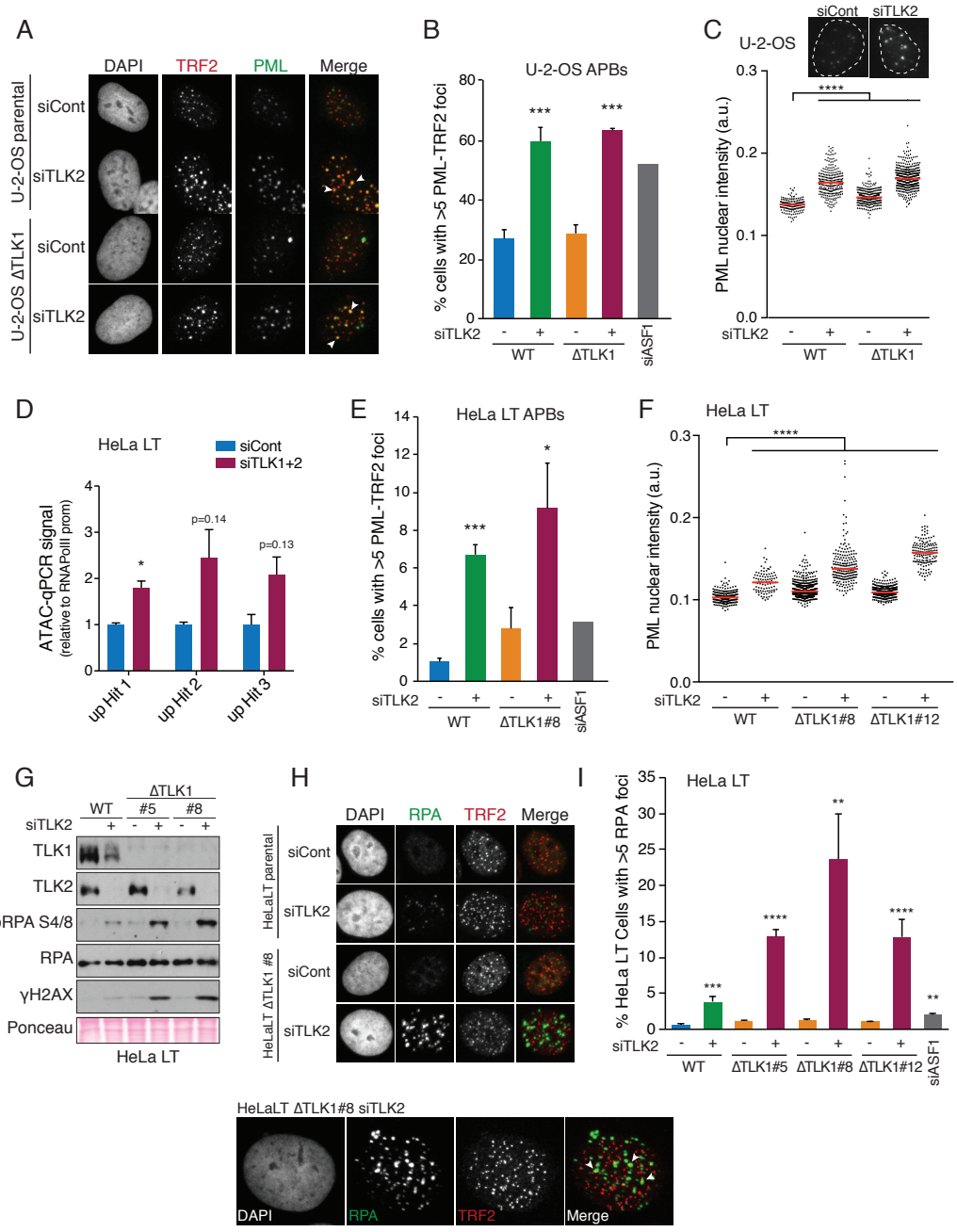

Figure 35. Total TLK depletion induces features of ALT.

(A) Representative IF image of APBs in U-2-OS cells. (B) Quantification of APBs (scored as cells with more than 5 TRF2-PML colocalizing foci) in U-2-OS cells, with more than 100 cells per individual experiment. An unpaired t test was used for statistical analysis (n=5 for siCont, n=4 for siTLK2, n=3 for TLK1Δ siCont/siTLK2, n=1 for siASF1). (C) HTM-mediated quantification of IF staining intensity of chromatin bound PML bodies in U-2-OS cells, data are from one biological replicate with n>180 nuclei analysed, and representative of four biological replicates. Median is shown in red and an unpaired t test was used for statistical analysis. (D) ATAC-qPCR was used to assess open chromatin at up-regulated "hit" regions in HeLa LT cells. Data are analysed as in Figure 33C. (E) Quantification of APBs in HeLa LT cells as in (B), with more than 100 cells per individual experiment. An unpaired

present ss/ds tails are sufficient for their self-priming in rolling amplification reactions. To test the relative contributions of TLK-ASF1-HIRA and ATRX-DAXX, we depleted them with siRNAs alone or in combination with TLK2 siRNAs in wild type or TLK1Δ HeLa LT cells and analysed the ALT phenotype. To our surprise, depletion of ATRX or DAXX did not enhance the production of C-circles observed following the loss of both TLKs, indicating they may act in the same pathway (Figure 36A). In addition, we failed to reproduce the induction of C-circles reported with the double depletion of ASF1a and ASF1b (O'Sullivan et al., 2014). However, the knockdown levels of ASF1 were not optimal, potentially accounting for some differences with the previously reported data (Figure 36B). In addition, we observed a mild reduction in ATRX and DAXX protein levels in TLK2 siRNA-depleted cells, indicating loss of TLKs may affect the stability of ATRX-DAXX complex, consistent with the added knockdown of ATRX or DAXX not enhancing the TLK-depletion induced ALT phenotype (Figure 36B). We will need to perform additional experiments to more precisely address the potential redundancy of these pathways in histone deposition at heterochromatic sites and particularly at telomeres, where chromatin composition has proven to be essential to maintain their functionality and genome stability. Our results however strongly implicate the loss of TLKs in the induction of ALT features in cells that maintain their telomeres through Telomerase and suggest that ALT+ cells with ATRX-DAXX deficiency may be hypersensitive to TLK inhibition.

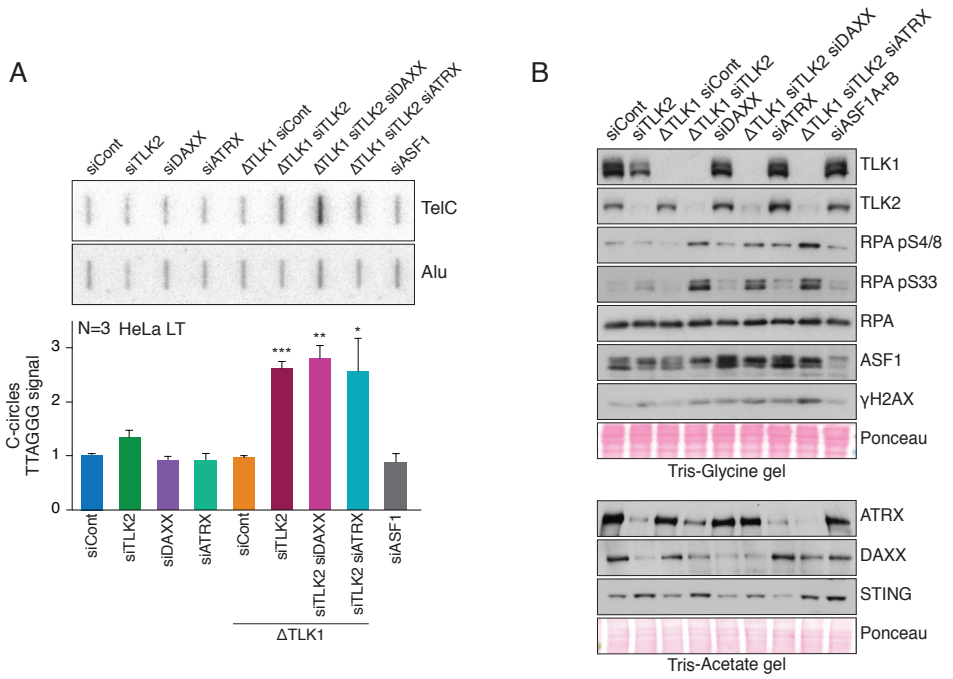

Figure 36. Total TLK depletion induces features of ALT.

(A) Dot blot of a representative C-circle assay in HeLa LT cells WT or TLK1Δ 72h after being treated with the corresponding siRNAs. Telomeric signal (TelC probe) was normalized by Alu signal. Quantification of three biological replicates is shown in the bottom panel. (B) Western blotting of DNA damage signalling markers in HeLa LT cells, WT or TLK1Δ 72h after being treated with the corresponding siRNAs.

TLK suppresses noncoding RNA transcription and maintains heterochromatin silencing

We next hypothesized that defective histone deposition of H3.3 could impair pericentric heterochromatin and telomeric chromatin formation and allow spurious transcription of silenced repeats, namely satellites or endogenous retroviruses (ERV) elements. Thus, we performed RNA-seq with rRNA depletion so that apart from mRNA analysis we could include the study of RNA species devoid of a poly-A tail. RNA-seq analysis revealed that global gene expression was not extensively altered upon TLK loss, and that with a fold-change cut-off of 2 there were more genes up-regulated than down-regulated (Figure 37A). Gene ontology (GO) analysis revealed that secretory pathways and antiviral responses were among the categories most enriched in the upregulated genes upon total TLK loss (Figure 37B). Gene set enrichment analysis (GSEA) revealed that among genes up-regulated in TLK depleted cells there were checkpoint response (p53 pathway) and apoptosis genes, whereas E2F targets and MYC targets were downregulated (Figure 37C), corroborating the G1/S cell cycle arrest and extensive DNA damage and cell death phenotypes we observed upon TLK depletion (Figure 22). In addition, GSEA extended the GO analysis, confirming that expression of many genes that fall into viral response signatures are over-represented in TLK depleted cells (Figure 37D).

Subsequently, we analysed differential RNA expression of samples by aligning to GENCODE annotated genetic variants (Harrow et al., 2012), which include protein-coding loci with alternatively spliced variants, non-coding loci and pseudogenes. From all the categories annotated in GENCODE, depletion of TLKs only significantly affected the expression of antisense RNA and long intergenic noncoding RNA (lincRNA) and interestingly the double depletion of both TLKs caused an additive phenotype. Both antisense and lincRNA appeared upregulated upon TLK loss (Figure 37E), indicating that TLKs specifically suppress noncoding RNA transcription and not that of protein-coding genes. We next wanted to focus our attention on constitutive heterochromatin, which is mostly repressed and comprises mostly repetitive DNA. Disrupted heterochromatin formation may account for desilencing of these regions, so we aligned our RNA-seq data to the annotated database for repetitive elements Repbase (Bao et al., 2015). We focused our analysis on those repeat elements that had at least 100 raw reads, and then computed their normalized fold changes relative to siCont condition. We could observe that expression of satellite RNA, together with some ERVs, were significantly increased upon depletion of TLKs (Figure 37F). Preliminary ChIP-qPCR analysis indicated that some of these endogenous retrovirus elements, such as HERV, have decreased occupancy of H3.3 and a mild decrease in H3K9me3 (Figure 37G), providing a plausible explanation as to why there is desilencing upon TLK depletion. Together, our results indicated that loss of TLKs causes cell cycle arrest, the expression of p53 response genes and a decline of E2F targets. Moreover, loss of TLKs causes a prominent induction of an interferon antiviral response, potentially due to spurious transcription of noncoding RNAs and silent repeat elements from heterochromatic regions.

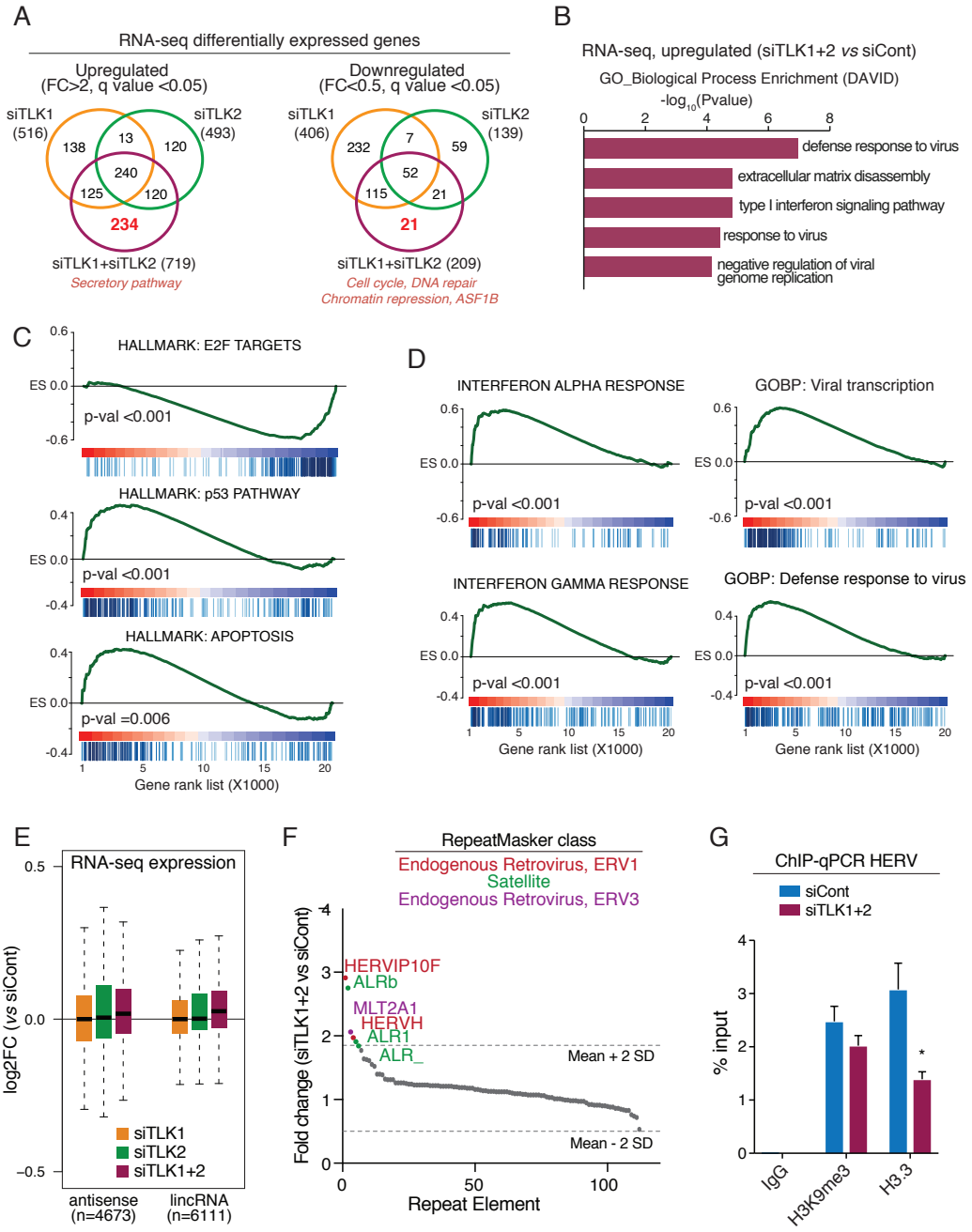

Figure 37. TLKs suppress noncoding RNA transcription and maintain heterochromatin silencing.

(A) Venn diagrams showing the overlap among differentially expressed genes in RNA-seq analysis of siTLK1, siTLK2 and siTLK1+2 conditions relative to siCont. The experiment was done in biological duplicate. (B) GO analysis (enrichment Biological Process) of RNA-seq differentially up-regulated genes upon double TLK knockdown (siTLK1+2). (C and D) GSEA of RNA-seq differentially expressed genes corresponding to the samples siTLK1+2 vs siCont, done in biological duplicate. (E) Boxplots of RNA-seq noncoding expression such as antisense RNA or lincRNA relative to siCont (n=2). (F) Analysis of repetitive RNAs expression (n=2). Fold change in RNAs (siTLK1+2 vs siCont) transcribed from different repeat types were plotted as a rank order from highest to lowest. Only repeat types with over 100 reads were included. The horizontal dotted line represents a cut-off

Reduced chromatin density triggers an interferon response

It has been described previously that perturbation of the epigenetic landscape results in transcription of endogenous RNA from heterochromatin, including ERVs and other non-coding repeat elements. This has been described in mouse ES cells to be dependent on H3.3 (Elsässer et al., 2015), in human ovarian cancer cell lines to be dependent on DNA methylation (Chiappinelli et al., 2015) and in human breast cancer cell lines to be dependent on linker histone H1 (Izquierdo-Bouldstridge et al., 2017). Moreover, desilencing of endogenous repeats was accompanied by activation of an antiviral response in some of these cases (Chiappinelli et al., 2015; Izquierdo-Bouldstridge et al., 2017). We set out to validate whether in the absence of TLKs some spurious transcription was taking place from heterochromatic repeats such as satellites, ERVs or telomeric repeat-containing RNA (TERRA) thus activating the interferon response. We assessed expression of several repeats by RT-qPCR in U-2-OS cells upon total TLK inhibition and observed up-regulation of several repeats such as satellites (Sat-α, Satellite2, 17-alphoid), ERVs (HERV-H, HERV-K, MER21C, MLT1C49, MLT1J2) and TERRAs (15q TERRA) (Figure 38A), whereas other repeats we assayed did not change expression levels (5S rDNA or Alu repeats). We confirmed our RNA-seq results, as we found the significant activation of an antiviral response (Figure 38B and 37D) by assessing the expression of numerous genes by RT-qPCR. The cytoplasmic long-dsRNA sensing receptor MDA5/IFIH1 and the endosome short-dsRNA sensing receptor TLR3 were found up-regulated in TLK-depleted cells, although the MAVs/IPS-1 signalling effector downstream of these RNA receptors was not significantly changed (Figure 38B). Moreover, stimulator of interferon genes (STING), an important mediator of the response against cytosolic DNA, was found significantly upregulated (Figure 38B). Several IFN-stimulated genes, including IFI6, ISG15, IFIT2, OASL, DDX60 and RSAD2, that execute various antiviral functions were also significantly up-regulated upon TLK depletion (Figure 38B-C).

In order to determine whether reduced chromatin density in heterochromatic regions was responsible for triggering an IFN response, we tried to mimic the defects in histone deposition by depleting the histone chaperones ASF1(a+b) and HIRA, which function downstream of TLKs in replication-independent H3.3 deposition, or by impairing histone biosynthesis itself by FLASH depletion. For this analysis we used two ALT+ cell lines, U-2-OS and GM847, that have defective ATRX (Lovejoy et al., 2012). Induction of STING expression and of the IFN-stimulated genes IFIT2, OASL and RSAD2 was always more severe upon depletion of TLKs, however, depletion of FLASH, ASF1(a+b) and HIRA showed a less pronounced, but still significant, up-regulation of these genes in most of the cases (Figure 38C-D). The fact that we were unable to observe this phenotype upon knockdown of H3.3 suggests that spurious transcription from heterochromatin may

of 2 standard deviations from the mean. Grey dots represent repeat types that fall under two standard deviations from the mean. Repeats that were enriched more than two standard deviations from the mean are labelled, and colours represent the RepeatMasker broad repeat class to which that repeat type belongs. (G) ChIP-qPCR was used to assess occupancy of H3.3 and H3K9me3 at HERV in U-2-OS cells. Data of qPCR amplification were normalized to input and represented as the percentage of input. Experiments were done in two biological replicates with technical replicates. Mean and SEM are shown, an unpaired t test was used for statistical analysis.

not be the main inducer of this IFN response (Figure 38C-D). However, care should be taken since the achieved knockdown for H3.3 was always incomplete and at best, we observed only a 50% reduction of protein levels (Figure 38F). We believe the strong phenotype of TLK depletion is explained both by the effect of TLKs on suppressing replication stress, which may eventually generate DNA damage and release cytosolic DNA byproducts (evidence for this is that FLASH depletion also induced STING and IFN-stimulated genes (Figure 38D)) and by the effect of TLKs on suppressing heterochromatic non-coding RNA transcription, which may result from aberrant H3.3 deposition at these sites (evidence for this is that ASF1(a+b) or HIRA depletion also induced IFN-stimulated genes (Figure 38D)). Additional studies in the HeLa LT cell line, which is proficient for H3.3 deposition via ATRX-DAXX, support the fact that STING and IFN-stimulated genes may be induced by replicative stress and cytosolic DNA damage. Depletion of ATRX or DAXX alone in this cell line, which should impair H3.3 deposition at heterochromatin, were unable to activate the IFN response in contrast to depletion of TLKs (Figure 38E).

Cytosolic DNA sensing via cyclic GMP-AMP synthase (cGAS) and STING mediate interferon signalling and activate mechanisms of innate immunity. It has been previously shown that reverse transcribed RNA from ERV transcription may result in cDNA that, in the absence of the exonuclease TREX1, is sensed by the cGAS-STING pathway (Stetson et al., 2008). Moreover, activation of the interferon response via DNA damage and micronuclei has recently been shown to be induced by irradiation of cancer cells (Harding et al., 2017; MacKenzie et al., 2017). These studies suggested that micronuclei and genome instability-mediated cytosolic DNA harbour a source of immunostimulation and could act as a surveillance mechanism to recruit immune cells to tumours by releasing inflammatory cytokines. Therefore, tumours that harbour high levels of genome instability per se, or those that maintain their telomeres via ALT and generate extrachromosomal telomeric circles, would need to circumvent this pathway in order to minimize immunostimulation levels and withstand immune surveillance. In fact, it has been shown that ALT+ cancer cells exhibit defective cytosolic DNA sensing, suggesting that loss of cGAS-STING is required for maintenance of ALT (Chen et al., 2017). We hypothesized that TLK inhibition would be a strategy to re-sensitize ALT+ cells to telomeric circles by activation of STING expression. Depletion of H3.3 or the TLK-ASF1-HIRA pathway by siRNAs against TLK1+2, ASF1a+b and HIRA was able to induce STING protein expression in the ALT+ cell line U-2-OS (Figure 38F). This was supported by the fact that expression of *TLK2* and *TMEM173*, gene encoding for STING, anticorrelated in the dataset from

(A) Expression of DNA repetitive elements by RT-qPCR in U-2-OS cells. Data were normalized to unchanging expression gene levels (B-actin) and the signal obtained in siCont conditions was set to 1. Mean and SEM are shown, an unpaired t test was used for statistical analysis (n=4 for all except 15q RT primer "TERRA" for which n=2). (B) Expression of RNA and DNA sensors and interferon response genes by RT-qPCR in U-2-OS cells. Data were analysed as in (A), (n=4). (C-E) Expression of STING and the interferon response genes IFIT2, OASL and RSAD2 by RT-qPCR in U-2-OS cells (C), GM847 cells (D) and HeLa LT cells (E). Heatmaps represent the mean of n biological replicates. Data were normalized to unchanging expression gene levels (B-actin) and the signal obtained in siCont conditions was set to 1. For U-2-OS, n=4 for all except for siTLK1+2(pool) where n=3. For GM847, n=3 for all except for siH3.3 where n=2. For HeLa LT, n=3. (F) Western blotting of STING in U-2-OS cells, 48 h after being treated with the corresponding siRNAs. Graph in bottom panel is a quantification of protein levels relative to siCont from two biological replicates, mean and SD are shown. (G) Correlation dot plot of RNA-seq levels of *TLK2* and *TMEM173* (encoding for STING) genes in the cell lines from the CCLE. Green dots represent cell lines that have TLK2 levels above than 3.5 and negative levels of STING.

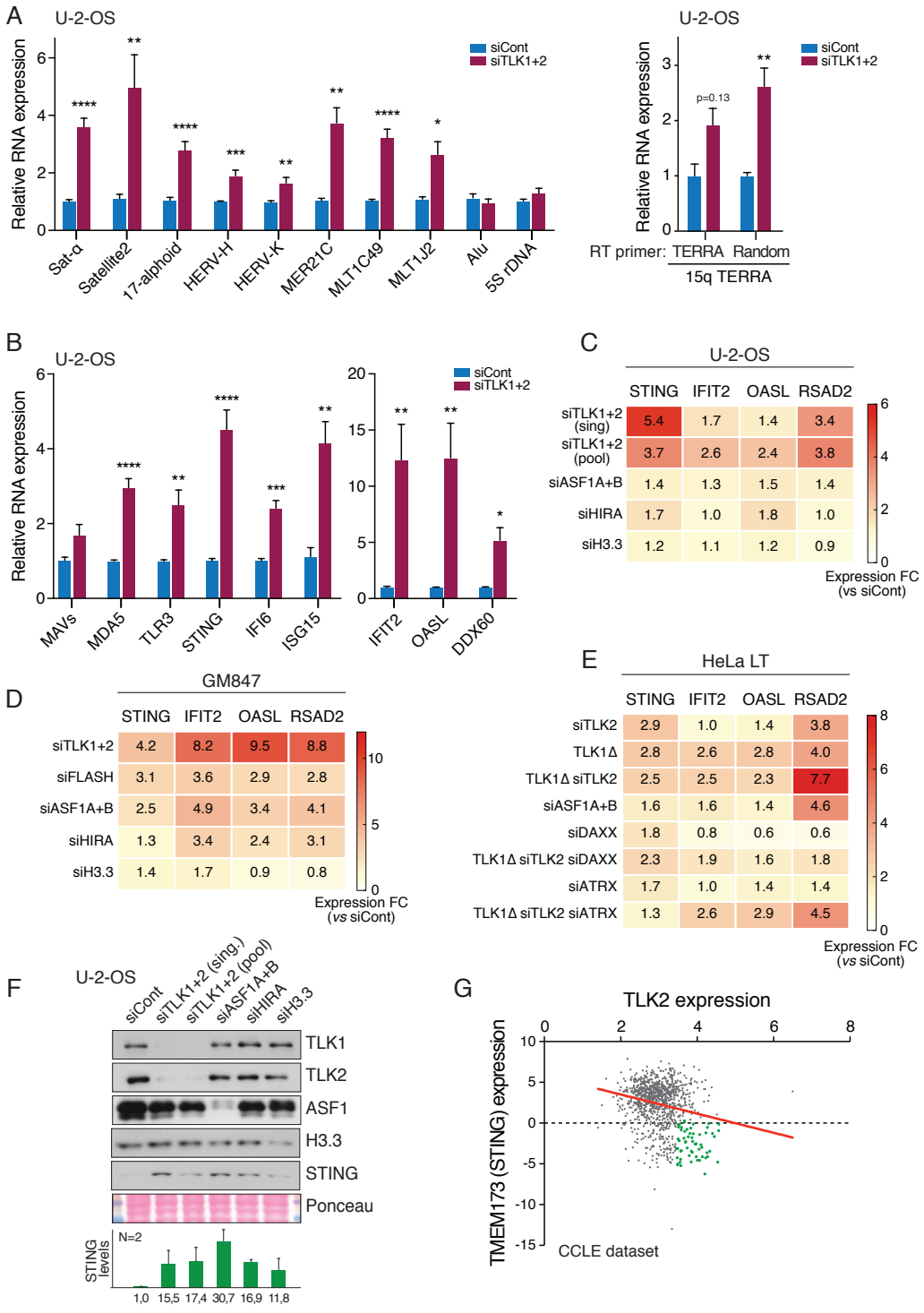

Figure 38. Reduced chromatin density triggers an interferon response. *(Legend in the previous page)*

the Cancer Cell Line Encyclopedia (CCLE) (Figure 38G). These data open up the possibility that tumours that have defective cytosolic DNA sensing by STING inactivation or *TMEM173* epigenetic silencing, potentially mostly ALT+ or highly genomic unstable tumours, would benefit from inhibition of TLK activity, activity that is probably high in these specific cases in order to promote proliferation and survival.

Discussion

The work presented in this thesis provides several novel concepts and insights into the molecular mechanisms that could be used to exploit TLKs as a target in cancer therapy. In the first chapter, we describe the molecular determinants of TLK2 and the high confidence interactors that likely contribute to its molecular function. In the second chapter, we describe the functions of TLK1 and TLK2 in homeostasis in mouse tissues and derived cells. We show that TLKs are highly redundant in homeostasis in most tissues to maintain genome stability, unlike the placenta, where TLK2 is essential to maintain specific transcriptional programs required for specialized cell type differentiation. In the three last chapters, we address how TLKs maintain proliferation and epigenome stability in a disease state, specifically in cancer. In chapter 3, we identify widespread defects in DNA replication in the absence of TLKs, resulting in genomic instability and decreased proliferative capacity. We show that the role of TLKs in maintaining replication fork integrity is synthetic lethal with the replication checkpoint and mechanisms that stabilize stalled forks, such as PARP activity. In the fourth chapter, we investigate TLK genes status in cancer genomes and explore the potential of TLKs as a therapeutic target in cancer using multiple cancer lines and two *in vivo* cancer models. Last, chapter 5 provides an additional novel role of TLKs in maintaining heterochromatin and suppressing an antiviral IFN response. We propose this role of TLKs could be exploited to target specifically tumours with defects in H3.3 deposition, such as ALT+ tumours.

1. Upstream regulators of TLKs and how its functions can be mediated by targets beyond ASF1

In this thesis, we have provided strong evidence that the most relevant functions of TLKs are to prevent defects in histone assembly through the phosphorylation of ASF1. However, we have not determined whether other TLK interactors are substrates and if they contribute to the described phenotypes. While some of these interactors may represent *bona fide* substrates, our attempts to validate HIRA as a direct interactor of TLKs was not successful (Figure 9E-F) and it is likely that many of the other proximity interactors represent indirect interactions that take place through ASF1, or other proteins. Thus, in future work, it will be important to validate these potential interactors in cells where we have knocked down ASF1 in order to determine if TLK act to some extent in a manner parallel to ASF1. One of the interactors that we were able to readily validate was LC8 (Figure 8F and 9C). LC8 comprises a family of dynein light chain factors, DYNLL1 and DYNLL2, which were originally identified as components of the axonemal dynein motor protein complex (Rapali et al., 2011a). Several discoveries have revealed that LC8 associates with multiple interaction partners independently of its motor protein functions, including the kinase NEK9 and 53BP1, consistent with LC8's proposed role as a general multimerization hub that organizes different protein partners (Lo et al., 2005; Rapali et al., 2011b; Regue et al., 2011). LC8 light chains recognize short linear motifs located in intrinsically disordered protein segments and these were originally divided into two classes: (K/R)XTQTX and XG(I/V)QVD. The binding motif for NEK9 is KGTQTA, whereas in the case of 53BP1 the motifs are IGIQTM and AATQTI (Rapali et al., 2011a,

2011b). Our results indicate that the LC8 binding domain for TLK2 either lies within the CC1 domain or that it requires dimerization, that is also dependent on CC1. It is also possible that LC8 binding is required for heterodimerization with TLK1 or it may stabilize the interaction (Figure 10B). Within the vicinity of CC1, a possible binding motif for LC8 might be RQTQSD for TLK2 and FKIQTD for TLK1. Future studies will be needed to explore whether mutations of this motif, rather than deletion of the whole CC1, impairs TLK1-TLK2 heterodimerization. Moreover, whether loss of LC8 interaction impairs other TLK2 interactions or modifies affinity to potential substrates will be interesting to determine, given the observed reduced phosphorylation of ASF1a by TLK2-ΔCC1 *in vitro* (Figure 10C). Biophysical studies on the higher order oligomerization of TLKs in the presence of LC8 might shed light on these interesting questions regarding the upstream regulation of TLKs and their activation mechanism. Although LC8 does not influence kinase activity *in vitro* (Figure 9C), we suspect that LC8 can regulate TLK complex formation, and direct consequences of this on TLK substrate spectrum will be interrogated in future studies.

Our MS experiments have not detected CHK1, RAD9 or histone H3, which have been previously proposed to be upstream regulators or human TLK substrates (Figure 8E and data not shown) (Groth et al., 2003; Kelly and Davey, 2013; Li et al., 2001). Very little is known about the regulation of TLKs beyond the CHK1-dependent phosphorylation of TLK1 at S695 in response to DNA damage by IR or inhibition of DNA replication by HU (Groth et al., 2003; Krause et al., 2003). The inhibition of TLK1 activity upon checkpoint activation is transient, and since our interactome studies have been done in unchallenged cells growing in asynchronous conditions, this may explain why we have not detected CHK1 as a potential interactor. Although the inhibition of TLK activity was CHK1-dependent, it has not been demonstrated these two kinases interact in cells in the abovementioned conditions, and it could very well be that a downstream target of CHK1 that harbours kinase activity could mediate this phosphorylation event. However, a chemical genetic approach performed to identify CHK1 substrates identified TLK1, arguing against the latter possibility (Blasius et al., 2011). Inhibition of TLKs during checkpoint activation might not affect ASF1 function in buffering histones but may affect ASF1 in coordinating fork progression and histone dynamics by *de novo* histone deposition (Groth et al., 2003, 2005; Klimovskaia et al., 2014).

The validated substrate spectrum of TLKs is rather limited beyond ASF1, RAD9 or histone H3, although the proposed spectrum of TLK1 comprises more than 150 proteins (Singh et al., 2017). RAD9, as a component of the 9-1-1 complex is required for damage-induced checkpoint activation (Delacroix et al., 2007). The interaction between TLK1 and RAD9 is enhanced by DNA damage, and phosphorylation of RAD9 at T355 is also enhanced upon genomic insults and regulates the checkpoint response (Kelly and Davey, 2013). Whereas our data points to RAD9 as a non-specific TLK interactor (Figure 9D), it will be important to explore in the future whether this or other interactions are more apparent following DNA damage. In addition, DNA damage and other stresses may reveal a new set of interactors/substrates. The phosphorylation of histone H3 has been proposed to be mediated by TLKs in various organisms. In human cells, the splice variant

TLK1B potentially phosphorylates H3 at Ser10 (Li et al., 2001) whereas in *C. elegans*, ceTLK-1 interacts with Aurora B, and this interaction promotes phosphorylation of ceTLK-1 and Aurora B activation (Han et al., 2005), potentially explaining why higher TLK activity indirectly promotes more H3 Ser10 phosphorylation. Phosphorylation of histone H3 at Ser10 is a hallmark of mitosis and required for chromatin condensation (Crosio et al., 2002), and so far, we have not observed any TLK phenotype that could be central to mitosis that would not be explained by the cell cycle arrest and genomic instability observed upon TLK depletion. Given the defects we observe in heterochromatin formation (Figure 34G), TLK-mediated histone phosphorylation could potentially account for some less characterized modifications with a role in chromatin maintenance. The histone variant H3.3, which differs from H3.1 in five amino acids, contains an Alanine to Serine replacement at position 31 (Ser31). This residue is phosphorylated late in mitosis in specific chromosomal regions such as those immediately adjacent to centromeres and telomeres (Chang et al., 2015; Hake et al., 2005). While p-H3.3 Ser31 is restricted to pericentric regions during mitosis in most somatic and cancer cells, p-H3.3 Ser31 is spread through the entire chromosome in ALT+ cells, and this has been proposed to be due to a delay in mitotic progression and CHK1-dependent (Chang et al., 2015). Treatment with CHK1 inhibitors reduced this phosphorylation and caused an increase of γH2AX in mitotic chromosomes accompanied by a decrease in cell viability. One may speculate that this phosphorylation event could be a target of TLKs, since the effects of TLK depletion specifically in ALT+ cells are very severe, cause DNA damage and a strong decrease in cell viability (Figure 22), similar to what is observed in cells overexpressing H3.3 S31A mutants. Thus, it will be important to investigate whether TLK1/2 interact with H3.3 in G2/M synchronized cells and whether one of the underlying mechanisms by which TLKs maintain heterochromatin specifically in ALT+ cells is through p-H3.3 Ser31, since very little is known about the functional implications of this phosphosite in chromatin assembly.

One of the most reproducible interactors of TLKs identified by unbiased analysis (both by IP-MS and by proximity ligation using BioID) is the heterochromatin associated protein RIF1 (Figure 8E). RIF1 is conserved from yeast to mammals, and it was first identified in yeast as a regulator of telomere length (Shi et al., 2013). In mammals, there is not a specific telomere role for but it is implicated in the control of DNA repair and regulation of replication timing, the latter being a conserved function across species (Buonomo et al., 2009; Chapman et al., 2013; Cornacchia et al., 2012; Hayano et al., 2012; Hiraga et al., 2014; Di Virgilio et al., 2013). RIF1 serves as a PP1 scaffold and governs PP1 substrate targets. RIF1 has been implicated in the regulation of replication timing by its ability to promote the dephosphorylation of the MCM replicative helicase, keeping late replication origins dormant to control replication timing. Interestingly, both TLK1 and TLK2 were also identified in RIF1-associated complexes from mouse ES cells in 2 out of 3 replicates (Sukackaite et al., 2017). Our analysis indicates that there is a positive correlation between DNA replication timing and ATAC accessibility. In TLK depleted cells, early replicating timing regions become less accessible whereas late replicating regions become more accessible (Figure 33D-E). These data open the hypothesis that the replication stress observed at heterochromatin and its transcriptional desilencing may be partly a consequence of alterations in replication timing regulation. It was recently reported

that RIF1 is required for ERV silencing in mouse ES cells through the establishment of repressive chromatin marks (Li et al., 2017). Alternatively, there is the possibility that differences in DNA unwinding at replication forks between TLK and ASF deficient cells could be explained by the interactions with RIF1-PP1. This complex and the TLKs could represent opposing forces that regulate histone flow at the fork. Additionally, there is the possibility that RIF1 may be a regulator of TLKs by targeting PP1 to TLKs to switch off their autophosphorylated activation state. We have evidence that in serum starved HeLa cells, the proximity interaction detected by BioID between TLK2 and RIF1 is strongly enhanced (P. Knobel, data not shown), opening up the possibility that RIF1 targets PP1 to TLK2 for its inhibition when cells stop cycling. It will be important in future work to address whether the RIF1-TLK2 interaction is direct, whether it occurs in specific nuclear compartments and to perform mechanistic interventions to understand its role as a potential regulatory circuit.

2. Defects in placenta development in the absence of TLK2 and its potential links to intellectual disability and the immune system

The results presented in chapter 2 were recently published and describe for the first time the relative contributions of TLK1 and TLK2 to mammalian embryogenesis (Segura-Bayona et al., 2017). Although TLK1 and TLK2 may have specific roles, our results indicate that TLK1 and TLK2 are largely redundant in tissue homeostasis and individually dispensable for mammalian viability, with the exception of TLK2's role in placental development. TLK2 is strictly required for embryogenesis through its role in supporting the proper differentiation of trophoblast lineages, likely through transcriptional regulation through ASF1 phosphorylation (Figure 15-17). However, we cannot rule out the possibility that loss of TLK2 impairs DNA replication to some extent, leading to either cellular attrition or indirect defects on transcription in the placenta, although we failed to observe any indications that proliferation was strongly affected (Figure 16A). The fact that ASF1a mouse knockout leads to lethality by E9.5 (Hartford et al., 2011), notably earlier than we observed with TLK2 deletion, is potentially consistent with the incomplete effect we observed on total ASF1 phosphorylation. We found that mRNA levels of *Tlk1* and *Tlk2* in the placenta were similar from E13.5 to 17.5. TLK1 protein levels are much reduced in placenta compared with embryonic tissue, whereas TLK2 protein levels are similar regardless of the tissue (Figure 17A-C). We propose that there is a translational mechanism that regulates TLK1 protein levels in the placenta, and the low TLK1 levels provide an explanation as to why TLK2 is essential in this tissue, although we cannot rule out another unknown, essential role during development. We have identified a consensus CPEB binding element (CPE) that overlaps with the 3'UTR of TLK1. Thus, perhaps TLK1 could be regulated at a translational level during placental development. Together, the proposed model for the contribution of TLK1 and TLK2 activity to the placenta and adult tissues in homeostasis considers that TLK2 is the prevalent activity and required to maintain a threshold of signalling required for viability in placental tissue. This likely involves ASF1a/b and potentially other substrates. Alternatively, in most adult

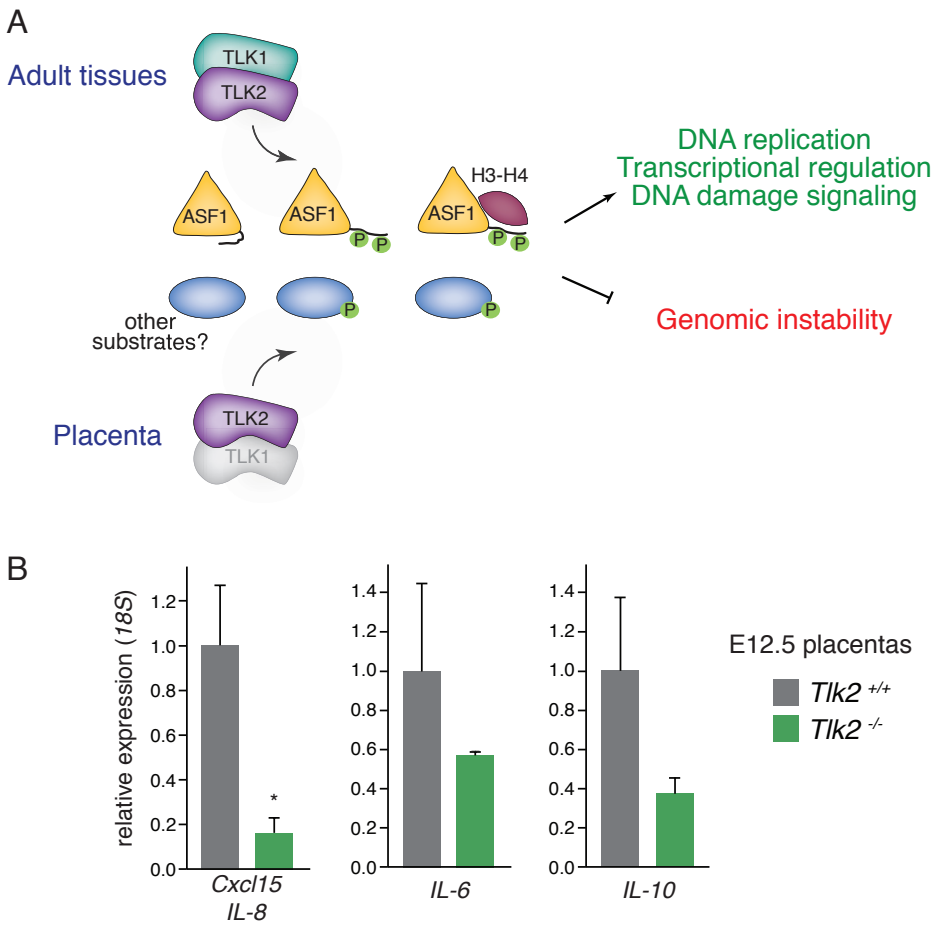

Figure 39. TLK1 and TLK2 cooperate to maintain cellular functions in most somatic tissues.

(A) Proposed model for the contribution of TLK1 and TLK2 activity to the placenta and adult tissues. In the placenta, and possibly other cell types or tissues, TLK2 is the prevalent activity and is required to maintain a threshold of signalling required for viability. This likely involves ASF1a/b and potentially other substrates. In most adult tissues, TLK1 and TLK2 are largely redundant and the presence of either is sufficient to provide the necessary activity to support cellular functions required for the maintenance of genome integrity and viability. (B) Quantitative real time PCR analysis of cytokine genes from E12.5 placenta samples. Combined data represents the mean of triplicate samples from 3 individual animals of each genotype. Statistical significance was determined using an unpaired t-test (* p=<0.05).

tissues, TLK1 and TLK2 are largely redundant and the presence of either is sufficient to provide the necessary activity to support cellular functions required for the maintenance of genome integrity and viability in homeostasis (Figure 39A).

A recent meta-analysis of data from over two thousand patients identified *TLK2* as one of ten new candidate genes for intellectual disability (ID) and other neurodevelopmental disorders (Lelieveld et al., 2016). These patients have *de novo* loss of function mutations (DNM) and exhibit severe clinical features, such as facial dysmorphisms. It is tempting to speculate that the effects of these *TLK2* mutations could reflect placental defects, although we would expect them to be less marked than what we have observed in mice

with a full *Tlk2* knockout. In collaboration with the laboratory of Guillermo Montoya, we have investigated the implications of the ID mutations in TLK2 kinase activity *in vitro* and found that all mutants display reduced kinase activity (data not shown, manuscript under revision). Given that kinase-dead or -mutant versions of TLK2 display a dominant negative effect due to their ability to homo- and heterodimerize with TLK1, we presume that harbouring a single allele mutation may significantly alter substrate recognition and the phosphorylation dynamics of ASF1 during placental development, thus affecting embryonic development and potentially accounting for neurodevelopmental seizures.

An important aspect during placental development is the interplay with the immune system. In cancer cells, we have unveiled that depletion of TLKs activates innate immunity by the interferon pathway (Figure 37 and 38). Moreover, RNA-seq analysis in U-2-OS cells revealed that interleukin-8 (IL-8) gene *CXCL8* is one of the more downregulated genes upon TLK depletion following single TLK1 or TLK2 depletion or double TLK1+2 loss (Figure 37A). The expression of cytokines such as IL-8 may influence angiogenesis in the placenta by directly acting on cell growth and differentiation or by indirectly inducing secondary cytokines that may mediate angiogenesis (Pereira et al., 2015). We investigated the expression levels of several cytokines such as IL-8 (*Cxcl15* gene in mice), as well as IL-6 (*Il6* gene) or IL-10 (*Il10* gene) at E12.5 placentas and saw a significant downregulation of IL-8 in *Tlk2* null placentas, which correlates with abnormal vasculature in these placentas (Figure 39B and Figure 15A-C). Thus, one could speculate that in the absence of TLK2 there is a suppression of the inflammatory response needed for angiogenesis, vascular permeability and beneficial to placentation, whereas there is an induction of detrimental inflammation that could potentially stimulate immune cell infiltration. Placental vascularization defects during embryonic development have been recently related to compromised embryonic defects in heart, brain and the vascular network (Perez-Garcia et al., 2018). Thus, placental insufficiency through vasculature defects may underlie postnatal consequences, such as congenital neurodevelopmental abnormalities.

3. TLKs and ASF1 are required for replication fork progression and differentially affect DNA unwinding

The results presented throughout this thesis and mainly in chapter 3 demonstrate a key role for TLK activity in promoting chromatin assembly and maintaining replication fork stability. The depletion of TLK activity impaired nucleosome assembly and led to replication-coupled ssDNA accumulation and fork stalling. Over time, DNA damage accumulated and induced a G1 arrest. In cells that experience short-term TLK depletion or histone deprivation, basal checkpoint responses and PARP activity are required to maintain the stability of stalled forks and prevent new origin firing that would accelerate fork collapse and increase levels of DNA damage. TLK depletion concomitant with inactivation of the replication checkpoint led to massive accumulation of DSBs and loss of viability. This line of evidence argues that TLK activity governs replication fork integrity and chromatin restoration on newly synthesized DNA, with checkpoint kinases and PARP activity being crucial to prevent the collapse of forks arrested with chromatin

assembly defects in the absence of TLK activity. Thus, there is a combined influence of chromatin assembly and checkpoint signalling in the protection of stalled replication forks (Figure 40).

Our work shows that proper control of TLK activity is critical for chromosomal integrity and survival in cancer cells. Further, it also provides a potential explanation as to why the loss of TLK activity during early and rapid cell divisions in *Drosophila* and *C. elegans* causes severe chromatin and proliferation defects and cell death (Carrera et al., 2003; Han et al., 2003). Chromatin is central to all DNA-based processes and governs cell fate specification, as well as genome integrity. Failure to assemble the newly synthesized DNA into chromatin, as a result of histone deprivation (Mejlvang et al., 2014) or loss of CAF1 (Hoek and Stillman, 2003), ASF1 (Groth et al., 2007) or TLK1/2 (this work), causes severe DNA replication defects. Despite available evidence indicating that ASF1 is the prime TLK target in metazoans (Silljé and Nigg, 2001), it is intriguing that TLK depletion does not simply recapitulate the phenotype of ASF1 loss of function. Loss of total ASF1 activity reduces replication fork speed and leads to a strong S-phase arrest. The cells that accumulate in S-phase lack accumulation of RPA or checkpoint activation. In this setting, exposure of ssDNA is not evident at stalled forks. Treatment of ASF1 deficient cells with HU more dramatically shows that DNA unwinding and γH2AX induction are inhibited (Groth et al., 2007). In contrast, this is not phenocopied by lack of TLK activity, since TLK depletion reduces fork speed concomitant with accumulation of RPA on ssDNA, checkpoint activation and eventually a G1 arrest. These data indicate that TLKs and ASF1a/b serve distinct functions at replication forks. This is consistent with two different scenarios that are not mutually exclusive: TLKs regulate additional targets besides ASF1, or ASF1 serves both TLK-dependent and independent functions.

Our data and the published evidence supports the latter explanation, although we cannot completely rule out the effects on DNA replication can be mediated by additional targets beyond ASF1. ASF1 is physically required for unwinding through a function that is independent of its phosphorylation by TLKs (Figure 24C). The fact that TLKs are dispensable for ASF1 function in unwinding is further corroborated by the overexpression of a non-phosphorylateable ASF1a mutant (ASF1a-4A) that enhanced the levels of RPA phosphorylation observed following TLK depletion (Figure 24E-G). Aside from ASF1 function in *de novo* histone delivery, which is modulated by TLK1/2 phosphorylation promoting ASF1 histone binding capacity (Klimovskaia et al., 2014); ASF1 forms a histone-dependent complex with the MCM2-7 helicase that is required for the control of DNA unwinding and ssDNA exposure (Groth et al., 2007; Huang et al., 2015). Thus, we favour the idea that TLK independent functions of ASF1 in helicase regulation explain the differential phenotype of TLK and ASF1 depleted cells. TLK-mediated phosphorylation likely regulates a subset of ASF1 functions, namely the supply of new histones to the replication fork. Importantly, we find that in contrast to ASF1 depletion, inhibition of new histone biosynthesis by FLASH depletion leads to low levels of replication stress (Figure 24B) even though it also reduces replication fork speed and arrests cells in S-phase (Mejlvang et al., 2014). Most remarkably, we provide further evidence of this difference by showing that FLASH depletion, which leads to DNA unwinding, mimics the

hypersensitivity of TLK depleted cells to checkpoint inhibitors, whereas ASF1 depletion does not synergistically increase UCN-01 induced RPA accumulation and DNA damage (Figure 24D). This argues that replication forks arrested by lack of ASF1 function are not dependent on checkpoint signalling for stability in contrast to forks in TLK depleted cells.

It has been demonstrated that TLK activity is transiently inhibited by CHK1 phosphorylation upon DNA damage (Groth et al., 2003; Krause et al., 2003), indicating that the responses are interlinked. Nevertheless, it is remarkable that concomitant depletion of TLKs and inhibition of CHK1 or ATR activity showed strong synergistic effects, leading to genome breakage and lethality. Given that new histones incorporated during DNA replication, via H4K20me0, provide a signature of post-replicative chromatin and recruit the TONSL-MMS22L homologous recombination complex (Saredi et al., 2016), we propose that impaired nucleosome assembly in TLK deficient cells hampers TONSL-MMS22L recruitment and sensitizes replication forks for collapse upon CHK1-dependent new origin firing and RPA exhaustion (Toledo et al., 2014). This idea is consistent with our finding that Roscovitine, by inhibiting CDK2-mediated new origin firing, prevents fork collapse in TLK depleted cells (data not shown), and the recent finding that long term depletion of CAF1 and ASF1 for 72 hours impairs recruitment of TONSL- MMS22L to DNA double strand breaks (Huang et al., 2018).

Both TLK1 and TLK2 target ASF1 (Silljé and Nigg, 2001), but specialized functions for TLK1 and TLK2 have been proposed (Bruinsma et al., 2016; Kelly and Davey, 2013; Kim et al., 2016b; Sunavala-Dossabhoy and De Benedetti, 2009). We could generate TLK1Δ MDA-MB-231 cell lines, but were unable to propagate lines that initially appeared to have lost TLK2 (Figure 20C). Thus, we cannot exclude a TLK2 specific function important for cell viability. However, our data are most compatible with redundant functions of TLK1/2 in chromatin assembly and maintenance of replication fork stability, with their relative levels and potentially regulation varying across different cell types. A plausible scenario is that the genetic background of each cell line and the alterations carried in every genome most often dictate a higher dependency on TLK2 than on TLK1. This scenario is not representative of mouse embryonic fibroblasts, which resemble a more homeostatic condition and TLK1 and TLK2 play redundant roles on the maintenance of genome stability (Figure 19). We anticipate that different thresholds of TLK activity are required in different cell lines, depending on the replicative potential of the cells. In our hands, cells that are p53 wild-type, like U-2-OS, are more sensitive to TLK depletion than p53 mutant MDA-MB-231 cells when examining cell viability or colony formation capacity (Figure 22). This could be explained by the checkpoint status but also because U-2-OS cells are ALT+ and it is possible that they rely on TLK activity to support ALT (further discussed below). Additionally, ALT+ cells are highly genome unstable and display complex karyotypes (Marzec et al., 2015), thus they probably have a higher basal level of replication stress.

Taken together, these results point towards defective new histone deposition as a major contributor to fork instability in TLK depleted cells, and suggest that highly proliferative cancer cells may generally require the integrity of TLK-ASF1 signalling to support

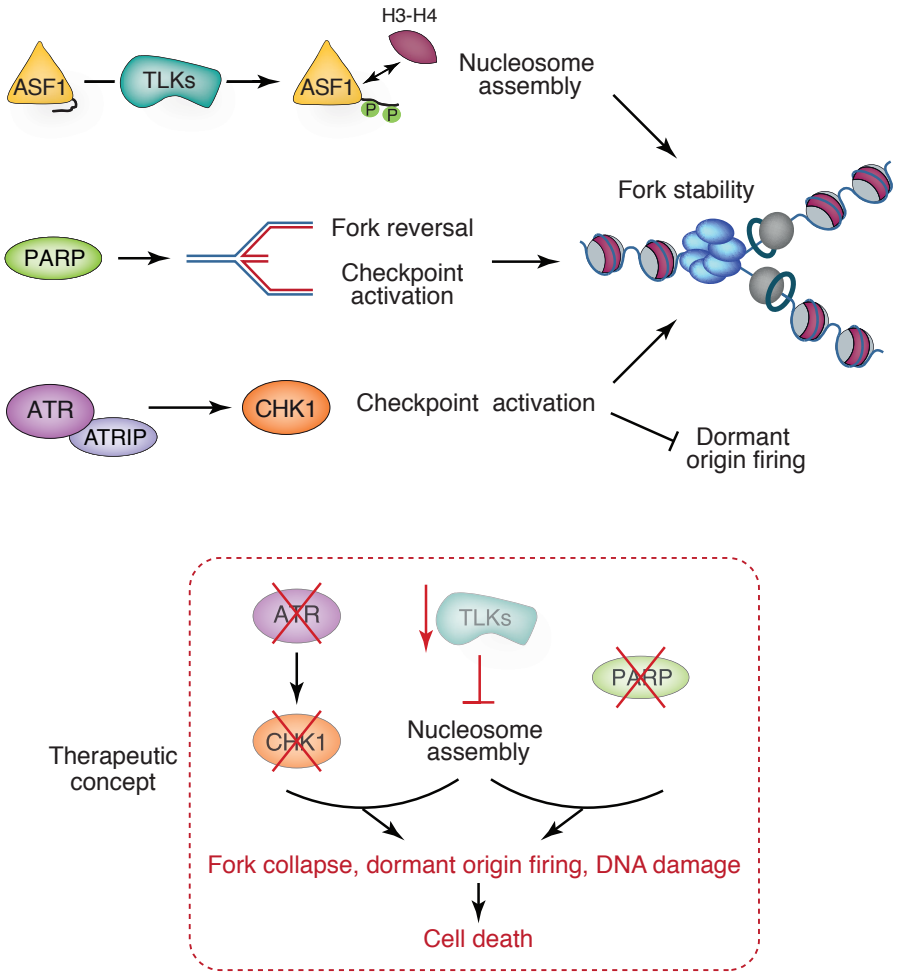

Figure 40. TLKs stabilize replication forks and show synthetic lethality with checkpoint and PARP inhibitors.

(Top panel) Model for the combined influence of chromatin assembly and checkpoint signalling in the protection of stalled replication forks. Assembly of new nucleosomes on replicating DNA is required for fork progression and dependent on ASF1 mediated histone provision. PARP activity acts to promote fork reversal to stabilize stalled replication forks and promotes checkpoint activation. Checkpoint activation by ATR-CHK1 axis maintains the stability of stalled forks and prevents new origin firing that would accelerate fork collapse and increased levels of DNA damage. (Bottom panel) Reduced TLK activity impairs *de novo* nucleosome assembly, slowing down replication forks and reducing their stability. Under these circumstances, basal checkpoint and PARP activity are required to prevent fork collapse, dormant origin firing and DNA damage that will eventually lead to cell death.

elevated levels of DNA replication and reduce toxic replication stress. Importantly, we also uncovered that cells with reduced TLK activity become highly dependent on the ATR-CHK1 mediated replication checkpoint and PARP activity for survival (Figure 40).

4. The emergence of TLKs as a target for cancer therapy

Our analysis of genomic data from nearly 6000 patients in the TCGA datasets revealed that amplifications were the most common genomic alteration observed for both *TLK1* and *TLK2*, as well as *ASF1B*, while few mutations or deletions were found in any of these genes. We have extended previous observations from the analysis of breast cancer (Kim et al., 2016b) and showed that high expression of both *TLK1* and *TLK2* is associated with reduced disease-free survival in additional cancer types from multiple tissues. The correlation of *TLK2* expression with that of proliferation marker *MKI67* is much weaker than the correlation between *MKI67* and *ASF1B*, which is a direct E2F target. The correlation between *TLK2* and *MKI67* is not observed in all cancer types, in contrast to *ASF1B* or *CHEK1* that have a near absolute correlation with multiple proliferation markers in nearly all TCGA datasets. Particularly in cervical squamous cell carcinoma and endocervical adenocarcinoma (cesc) and uveal melanoma (uvm), where *TLK2* expression correlates with DFS, there is not a significant correlation between *MKI67* and *TLK2* expression. This correlation with proliferation is not observed with *TLK1*, which is also elevated in some cancer types and in some cases also correlates with patient outcome. Regardless of the correlation with the proliferation state of the tumour, given the previous publication that has postulated TLK2 to be a subtype specific biomarker and target (Kim et al., 2016b), we propose to balance this statement with a more objective view of the cancer data. *TLK1* and *TLK2* expression correlates with patient outcome in multiple cancer types, in some cases it also correlates with the expression of proliferation markers, but more importantly, the TLKs may be relevant targets in many cancers regardless of expression levels. This is similar to the dependency of cancers on CHK1 and ATR, as our data demonstrates that TLKs play a fundamental role in supporting DNA replication integrity. Given the central role of TLKs in promoting histone provision during DNA replication, we propose that TLK activity is likely to be important for genomic stability in most proliferating cells, and thus a potentially valid target in many types of highly proliferative cancers, regardless of the association between expression and patient outcome. This proposition is further supported by the observation that TLK depletion leads to increased replication stress in cells from across a wide variety of cancer types (Figure 28). In addition, we propose that highly proliferative cancer cells may generally not only require the integrity, but in some cases the amplification, of *TLK-ASF1* pathway to support elevated replication stress.

The results presented in chapter 4 provide proof of principle that TLKs may be a target in cancer. We have attempted to address the role of TLKs in breast cancer by allografting human cells transduced with retroviruses in the mammary gland of nude animals for tumour formation. While we concluded that TLK1 loss alone did not impinge on cancer formation, we encountered issues with single cell selection of our knockout cell clones. Allografting TLK1 deficient cells that had been single cell selected resulted in decreased tumour formation when comparing to a parental cell population that had not been single cell selected (Figure 29). Thus, care should be taken in xenograft studies and one must ensure the maintenance of clone heterogeneity and tumour initiation capacities. Since we failed to obtain a xenograft system where we could stably eliminate TLK2, we next set up a genetic model. The validation of the model suggests that unlike in MEFs, murine

breast cancer cells depend on TLK2 activity for maintaining proliferation (Figure 31). Experiments that are already ongoing in our laboratory will analyse the effects of TLK loss in already established tumours *in vivo* in the MMTV-PyMT breast cancer model. These analyses not only will allow us to see whether TLKs are required for tumour initiation or progression but also for metastasis, and will allow us to test *in vivo* the synthetic lethality we described in chapter 3 between TLK loss and checkpoint or PARP inhibitors. To develop specific TLK1 and 2 inhibitors, we have recently started a collaboration with biological chemists and tested some kinase inhibitors that appear to exhibit specificity towards TLK1 and TLK2 in *in vitro* kinase assays, unlike the potential inhibitors tested to date (Figure 12A-B). Optimization of these compounds will allow us to test these inhibitors in cancer models and provide new therapeutic opportunities in a broad range of cancers, particularly in conjunction with ATR, CHK1 and PARP inhibitors (Figure 40).

5. TLKs impact on chromatin accessibility, telomere maintenance and heterochromatin silencing

Our work demonstrates that TLKs play a critical role in maintaining chromatin density and therefore affect the status of well-established sites of heterochromatin, such as telomeres and other repeat elements (see chapter 5). The effects of TLK depletion impinge on chromatin accessibility in a non-random manner, reducing chromatin accessibility at promoter-TSS regions and increasing it at heterochromatin. We can associate the defective chromatin deposition upon TLK depletion to reduced H3.3 at telomeres, and this is associated to the loss of heterochromatin marks such as H3K9me3 at these sites (Figure 34D), as it has been previously proposed to occur in mouse ES cells (Udugama et al., 2015). However, one of the most intriguing questions that remains to be answered is what are the causes and implications of the chromatin accessibility loss at promoter-TSS regions upon TLK depletion. While we have observed reduced H3.3 occupancy at promoter-TSS (Figure 34B) and the presence of H3.3 has been associated with active transcription (Zhang et al., 2017), we failed to observe a significant correlation between chromatin accessibility and gene expression. Thus, additional mechanisms and not solely chromatin accessibility are responsible for transcriptional repression in most of the promoter-TSS regions we observed to be more protected upon TLK depletion. It will be important to investigate whether more subtle transcriptional defects that we were not able to capture in our RNA-seq analysis apply in this situation, and we propose that nascent RNA analysis could perhaps better address these questions.

The loss of TLK activity leads to increased chromatin accessibility at several intronic and intergenic loci that correlate with heterochromatin marks, and we believe this results in the spurious transcription of non-coding RNA. RNA-seq analysis revealed a prominent activation of the innate immune response that may be due to both chromosomal instability, by releasing cytoplasmic DNA fragments or telomere circles, and spurious transcription resulting from chromatin desilencing due to defective histone deposition at critical silent loci (Figure 41). On the one hand, activation of innate immunity via DNA damage and micronuclei has recently been shown to be induced by irradiation

of cancer cells (Harding et al., 2017; MacKenzie et al., 2017). This activates a cytosolic sensor of double-stranded DNA, cGAS, and STING, which mediate interferon signalling. This work suggests that micronuclei are a source of immunostimulation and can act as a surveillance mechanism to recruit immune cells to tumours by releasing inflammatory cytokines. This also suggests that a rationale for treatment would be the combination of ionizing radiation together with immune checkpoint blockade. An important concern is how tumours with very high levels of genome instability circumvent this pathway and avoid immune surveillance. It has been recently shown that ALT+ cancer cells, which generate extrachromosomal telomeric circles in the cytosol, display defective cytosolic DNA sensing by epigenetic silencing of cGAS-STING expression (Chen et al., 2017). This suggests that loss of cGAS-STING would be required for the maintenance of ALT. On the other hand, activation of innate immunity via non-coding RNA transcription, such as ERV desilencing, has been previously shown to be induced by the inhibition of DNA methyltransferases with Aza (5'-azacytidine) (Chiappinelli et al., 2015). Loss of DNA hypermethylation upregulates the expression of several sense and antisense silent ERV transcripts and this results in dsRNA that is sensed by cytosolic sensors such as TLR3, MDA5 (IFIH) and RIG-I (DDX58). Similarly, this activation of the IFN response sensitized melanoma cells to immune checkpoint inhibitors, such as anti-CTLA-4 or anti-PD-1/PD-L1. Thus, targeting TLKs with specific inhibitors, via switching on the IFN response, could be an effective strategy to prime cells for immune checkpoint blockade therapy (Figure 41). To this end, we will pursue *in vitro* proof of principle experiments to determine if PD-L1 expression is enhanced in TLK deficient cells and xenografts. The next step will be to determine whether TLK depleted cells can be more efficiently killed in T-cell cytotoxicity assays in the presence of immune checkpoint blockade.

Our results show that TLKs suppress ALT features in HeLa LT cells, which are ALT-cells. TLK depletion enhances RPA accumulation at telomeres, increases APBs and C-circles in HeLa LT cells (Figure 35). It will be important to address whether other ALT characteristics, such as telomere fragility and telomere sister-chromatid exchange, are affected upon TLK depletion in HeLa LT cells. Although loss of total TLK activity resembles ALT phenotypes, we do not believe TLK loss is likely to be a driver of ALT in cancer, since both TLK1 and TLK2 appear very rarely mutated or deleted in cancer genomes and are required for DNA replication (Figure 13 and 26). We favour the idea that ALT+ cells may have a severe addiction to TLK activity in order to support heterochromatin maintenance in the absence of ATRX-DAXX (Figure 41). TLKs likely suppress ALT by regulating chromatin assembly via ASF1-HIRA. However, our BioID experiments also identified GATAD2A as a TLK2 proximity interactor in all our experiments (Figure 8E). GATAD2A, also known as p66α, is a subunit of the transcriptional repressor nucleosome remodeling and histone deacetylation (NuRD) complex. Although our BioID experiments are done in AD293 cells and not in an ALT+ cell line, perhaps there is an interplay between TLK2 and GATAD2A that is required for the maintenance of ALT. The NuRD complex is recruited to ALT telomeres as a scaffold for HR, creating an environment for telomere-telomere recombination (Conomos et al., 2014). Additional studies have revealed that the NuRD complex is required for S-phase progression and pericentric heterochromatin maintenance (Sims and Wade, 2011) and

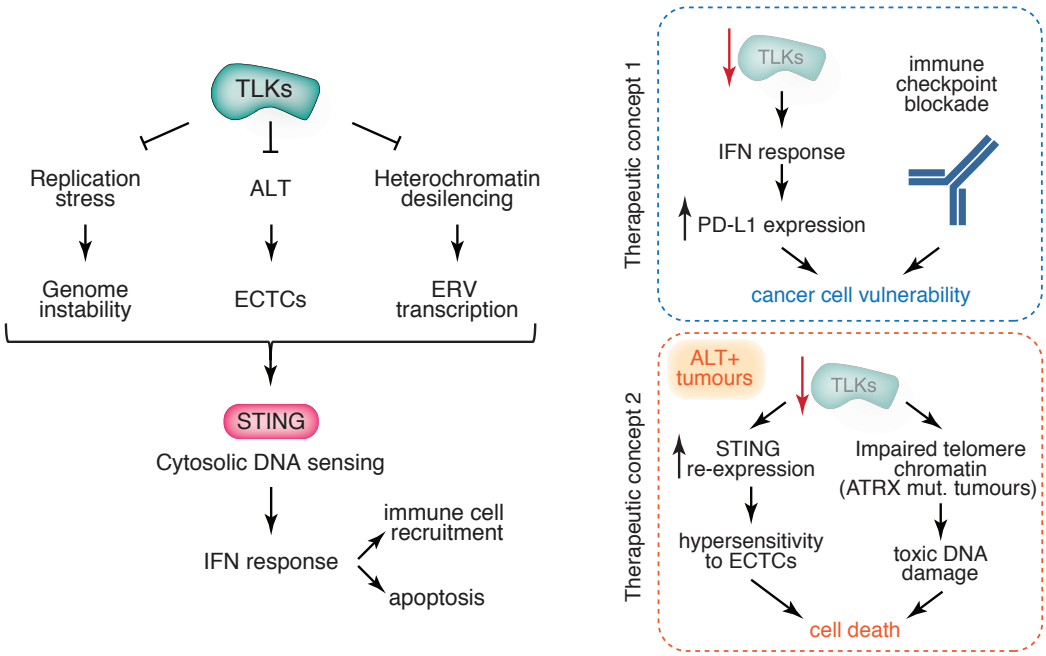

Figure 41. TLK activity maintains histone density and suppresses an antiviral response that could be exploited in cancer cell vulnerabilities.

TLK mediated chromatin changes suppress replication stress, ALT and heterochromatin maintenance. In the absence of TLKs, these situations result in genome instability, ECTCs and ERV transcription that in turn activate an innate immune response. These interactions could result in cancer cell vulnerabilities that anticipate windows for therapeutic intervention together with immune checkpoint blockade (therapeutic concept 1) and in ALT+ tumours (therapeutic concept 2).

NuRD recruitment to DSB via ZMYND8 promotes their repair by HR (Spruijt et al., 2016). It is thus tempting to speculate that in ALT cells TLKs-GATAD2A would facilitate heterochromatin maintenance and create a HR-permissive state at telomeres. It will thus be important to determine whether TLK2 and GATAD2A interact, whether this is enhanced in ALT+ cells, whether GATAD2A could be a TLK substrate and if NuRD occupancy at telomeres in ALT cells is diminished in the absence of TLKs.

It has been previously proposed that ATR inhibition would be a highly selective strategy for cancer cells that rely on ALT (Flynn et al., 2015), although these findings are controversial (Deeg et al., 2016). Inhibiting ATR in ALT+ cells is capable of disrupting recombination and RPA accumulation at telomeres, triggering chromosome fragmentation and apoptosis (Flynn et al., 2015). Our results suggest that reactivation of STING expression in ALT+ cancer cells upon TLK depletion would be a strategy to re-sensitize ALT+ cells to immune surveillance that detects telomeric circles and cytoplasmic DNA fragments (Figure 41). Defective sensing of cytosolic DNA by the cGAS-STING pathway may be required to evade telomere circles in ALT+ cells (Chen et al., 2017). In addition, an enhanced cGAS-STING response upon treatment with STING agonists leads to the induction of apoptosis (Gulen et al., 2017). It is tempting to speculate that treating cancers that rely

on ALT with TLK inhibitors might induce an antiviral IFN response, reactivate STING and induce cell death, thus attenuating ALT and the proliferative capacity of these cancer types (Figure 41). We will pursue in future work whether blocking STING signalling by CRISPR knockout is capable of rescuing the toxicity of TLK inhibition, demonstrating that one of the causes of cell death is the induction of IFN response upon severe genome instability and ERV desilencing.

Taken together, we have provided an appealing connection between chromatin maintenance, genomic stability and an antiviral response. This potentially provides a novel concept to target cancer regardless of their telomere maintenance mechanism: upon TLK depletion, defective chromatin maintenance promotes genome instability and transcriptional desilencing, which activate an IFN response and potentially prime cancer cells for anti-PD-L1 immune checkpoint blockade (Figure 41, first concept). More significant for the ALT+ subset of tumour types is the dependency they have to TLK-mediated telomere chromatin maintenance in the absence of a functional ATRX-DAXX axis. This added to the requirement of ALT+ cells to elude DNA cytosolic sensing likely makes them addicted to TLK activity (Figure 41, second concept). Thus, TLK inhibition could represent a novel rational targeted therapy to render ALT+ cancers more vulnerable to the induction of cell death and provides a window of opportunity to switch chromatin state to dictate tumour regression.

Conclusions

Conclusions

The first N-ter coiled-coil domain of TLK2 is required for TLK1 dimerization and LC8 interaction but not ASF1 interaction.

Auto-phosphorylation of S617 is a crucial regulatory site that inhibits TLK2 activity. Phosphorylation of S635 indicates an active kinase and may be generated by another kinase *in vivo* in order to modulate its activity.

TLK1 and TLK2 are largely redundant in tissue homeostasis and individually dispensable for mammalian viability.

Depletion of total TLK activity in MEFs leads to severe growth impairment and elevated chromosomal instability.

Loss of TLK activity in cancer cells leads to widespread defects in DNA replication, resulting in genomic instability and decreased proliferative capacity.

Loss of TLK activity in cancer cells impinges on histone dynamics of both canonical histones (H3.1) and replacement variants (H3.3).

TLK depletion causes synthetic lethality with checkpoint and PARP inhibitors.

TLK genes are frequently upregulated in human cancers and this associates with poor patient outcome in several cancer types beyond breast cancer.

Targeting TLK activity could prove effective for ablation of cancer cells.

Loss of TLK activity impacts on chromatin accessibility genome-wide.

TLKs suppress alternative lengthening of telomeres.

TLKs suppress an antiviral/IFN response that could be exploited in cancer cell vulnerabilities.

Supplementary Material

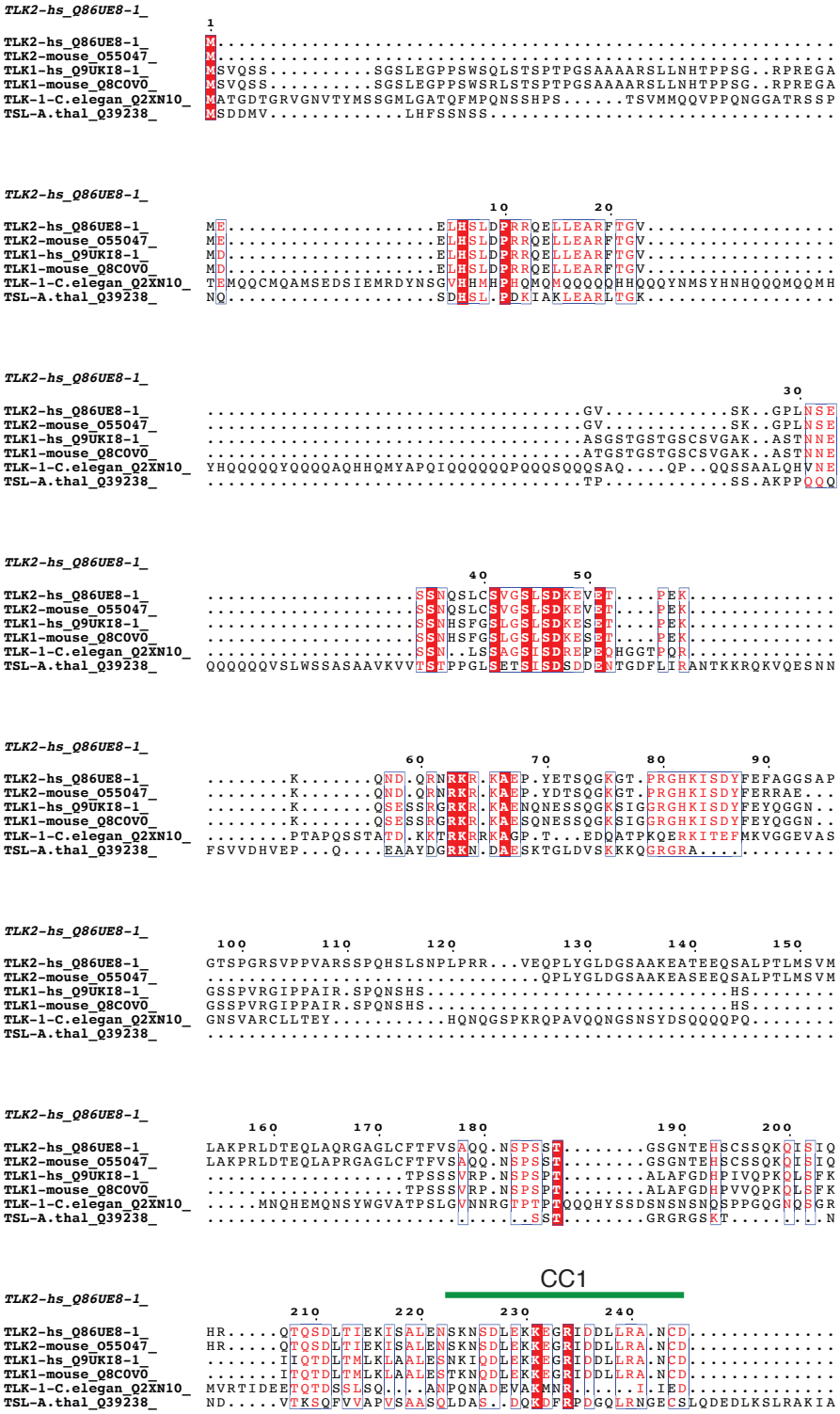
TLK2-hs_Q86UE8-1_
TLK2-hs_Q86UE8-1_
TLK2-mouse_O55047_
TLK1-hs_Q9UKI8-1_
TLK1-mouse_Q8C0V0_
TLK-1-C.elegan_Q2XN10_
TSL-A.thal_Q39238_
CC1

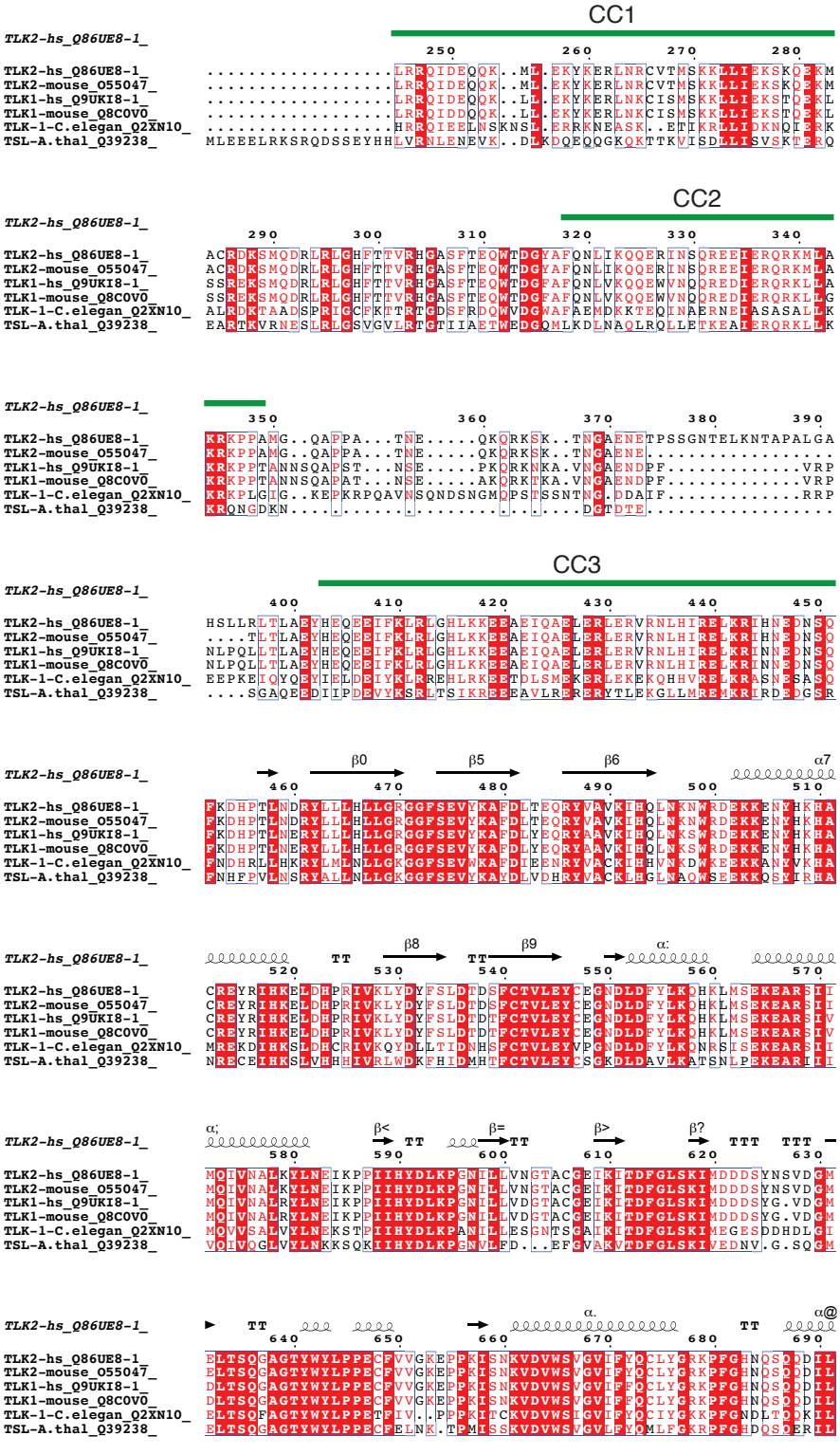
CC1
CC2
CC3
TLK2-hs_Q86UE8-1_
TLK2-hs_Q86UE8-1_
TLK2-mouse_O55047_
TLK1-hs_Q9UKI8-1_
TLK1-mouse_Q8C0V0_
TLK-1-C.elegan_Q2XN10_
TSL-A.thal_Q39238_

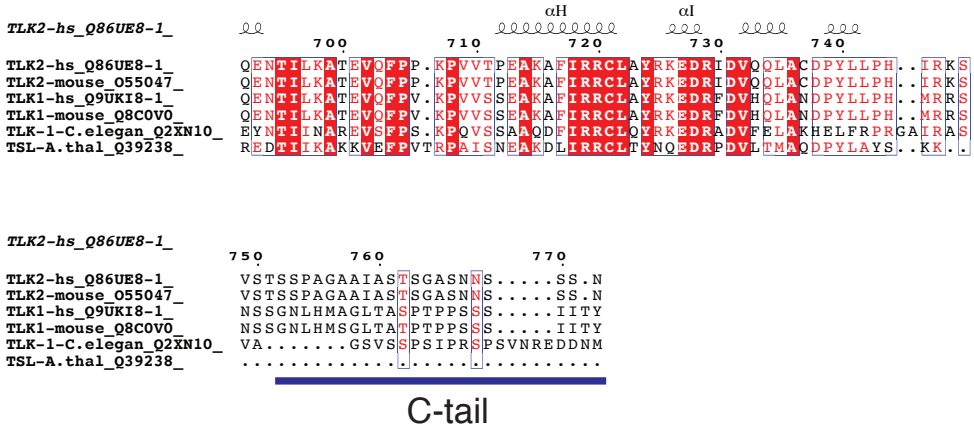

Supplementary Figure 1. TLKs sequence alignment.

Sequence alignment of TLKs from plants to human showing a highly-conserved protein sequence around the predicted coiled-coil regions and the kinase domain. Red box and white residue symbolize strict identity conservation. Red residue symbolizes similar physicochemical properties. Blue frame symbolizes similarity across the group.

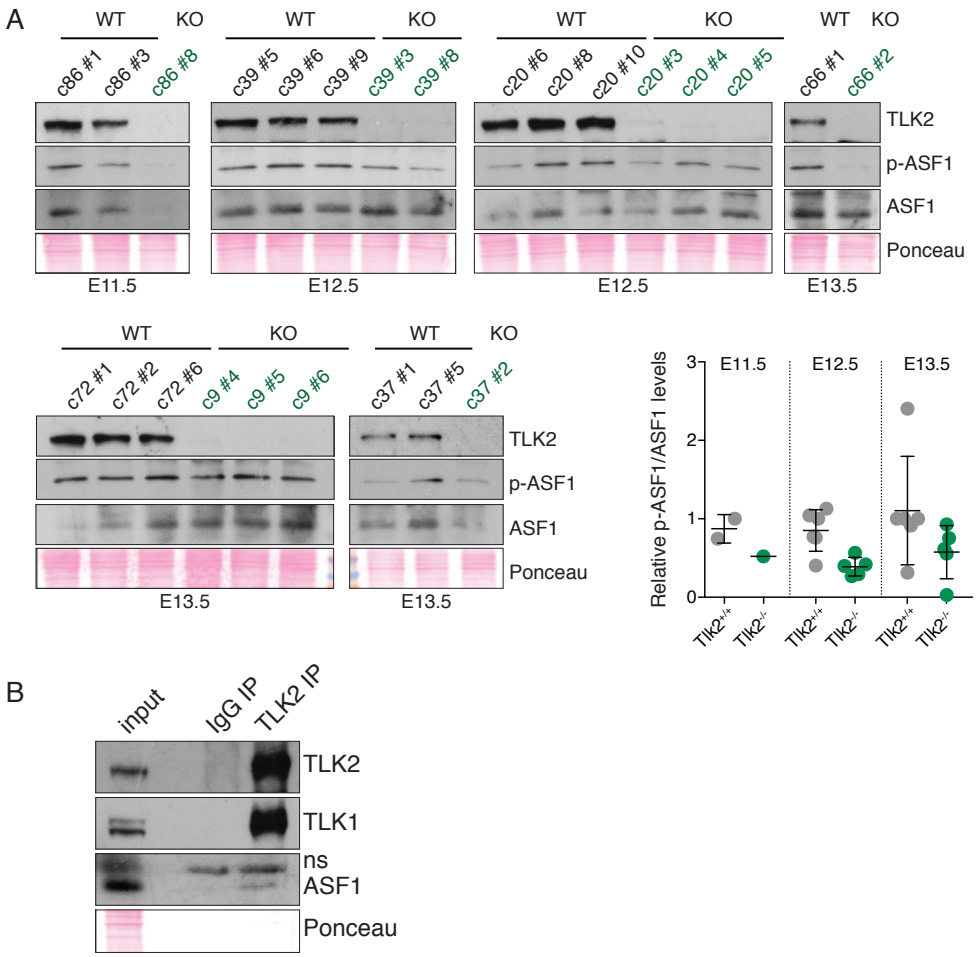

Supplementary Figure 2. Analysis of ASF1 levels and interaction with TLK2.

(A) Analysis of total ASF1 and ASF1-pS166 (p-ASF1) levels in placentas from the indicated genotypes and age. Western blotting results correspond to the same blot for each sample. Compiled quantification of all samples is shown in Figure 17D. ID codes indicate the litter number and embryo number, *Tlk2*$^{-/-}$ placentas are indicated in green font. (B) Additional example of ASF1 Westerns following IP of endogenous TLK2 from placental extracts (related to main Figure 17E). Both TLK1 and ASF1 consistently interact with TLK2 in IPs. A non-specific band is indicated by "ns".

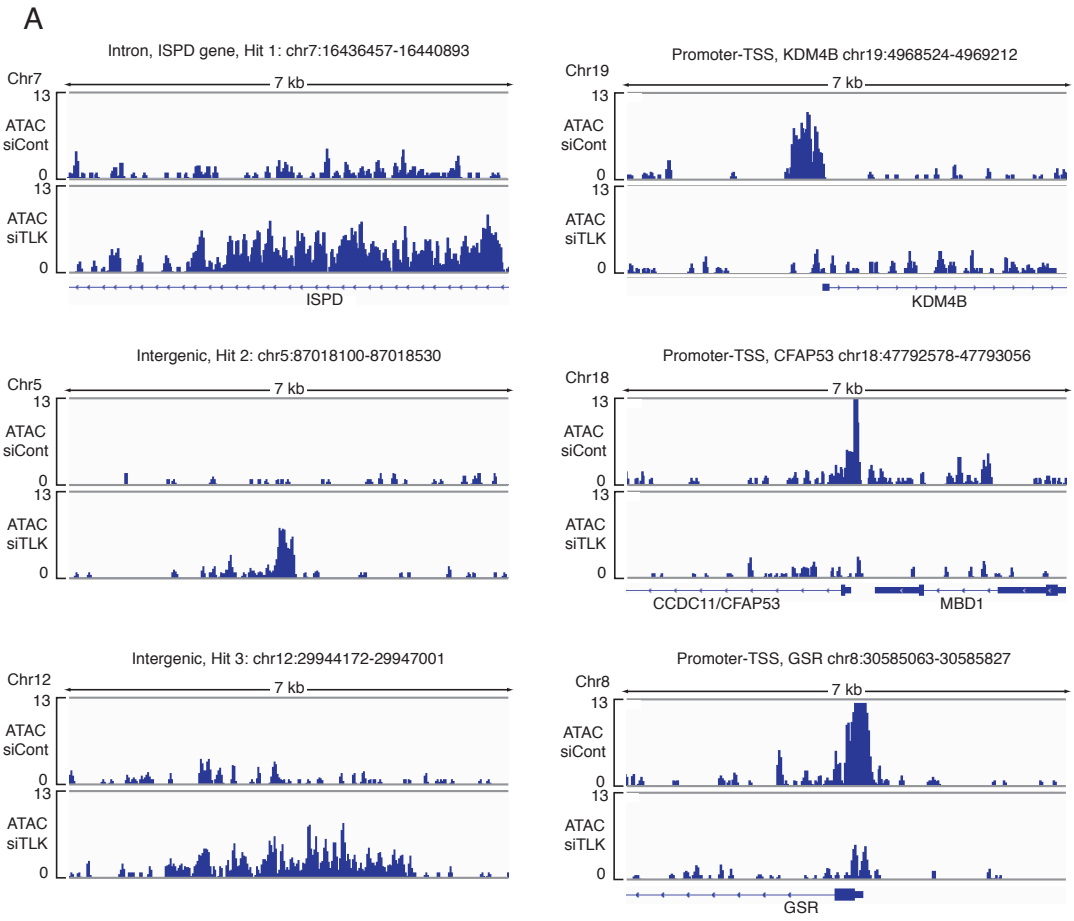

Supplementary Figure 3. ATAC-seq analysis.

(A) IGV tracks of ATAC-seq reads of heterochromatic (left panels) and promoter-TSS (right panels) that become differentially accessible upon TLK loss. Primers for these regions were designed and assayed by ATAC-qPCR in Figure 33C. (B) Venn diagram showing the overlap among differentially accessible peaks at promoter-TSS regions in ATAC-seq and downregulated genes in RNA-seq analysis of siTLK1+2 relative to siCont. Both experiments were done in biological duplicate.

Supplementary Table S1: Results of IP-MS data analysis of Strep-FLAG-TLK2 WT and KD in HEK-293T cells

			Areas (LOG2)								
Accession	Proteins identified with both TLK2 and TLK2-KD baits in 5-6/6 samples and absent in control	Σcoverage	MOCK_1	MOCK_2	TLK2_1	TLK2_2	TLK2_3	TLK2D_1	TLK2D_2	TLK2D_3	CRAP/ratio*
Q86UE8	Serine/threonine-protein kinase tousled-like 2 OS=Homo sapiens GN=TLK2 PE=1 SV=2 - [TLK2_HUMAN] (BAIT)	90,93	NA	NA	3,31E+01	3,31E+01	3,39E+01	3,46E+01	3,54E+01	3,53E+01	0,00243309
Q9UKI8	**Serine/threonine-protein kinase tousled-like 1 OS=Homo sapiens GN=TLK1 PE=1 SV=2 - [TLK1_HUMAN]**	38,51	NA	NA	3,29E+01	3,29E+01	3,37E+01	3,43E+01	3,52E+01	3,50E+01	0
P63167	**Dynein light chain 1, cytoplasmic OS=Homo sapiens GN=DYNLL1 PE=1 SV=1 - [DYL1_HUMAN]**	93,26	NA	NA	2,88E+01	2,99E+01	3,00E+01	2,74E+01	3,15E+01	3,12E+01	0,155717762
Q9Y294	**Histone chaperone ASF1A OS=Homo sapiens GN=ASF1A PE=1 SV=1 - [ASF1A_HUMAN]**	37,25	NA	NA	2,71E+01	2,70E+01	2,76E+01	2,95E+01	2,96E+01	2,97E+01	0,00729927
Q9NVP2	**Histone chaperone ASF1B OS=Homo sapiens GN=ASF1B PE=1 SV=1 - [ASF1B_HUMAN]**	54,95	NA	NA	2,71E+01	2,70E+01	2,66E+01	2,95E+01	2,96E+01	3,01E+01	0,01216545
Q13838	Spliceosome RNA helicase DDX39B OS=Homo sapiens GN=DDX39B PE=1 SV=1 - [DX39B_HUMAN]	29,44	NA	NA	2,65E+01	2,79E+01	2,60E+01	NA	2,70E+01	2,71E+01	0,335766423
P55036	26S proteasome non-ATPase regulatory subunit 4 OS=Homo sapiens GN=PSMD4 PE=1 SV=1 - [PSMD4_HUMAN]	11,94	NA	NA	2,66E+01	2,77E+01	2,64E+01	NA	2,70E+01	2,74E+01	0,177615572
P33993	DNA replication licensing factor MCM7 OS=Homo sapiens GN=MCM7 PE=1 SV=4 - [MCM7_HUMAN]	12,66	NA	NA	2,60E+01	2,66E+01	2,62E+01	NA	2,62E+01	2,65E+01	0,299270073
Q99729	Heterogeneous nuclear ribonucleoprotein A/B OS=Homo sapiens GN=HNRNPAB PE=1 SV=2 - [ROAA_HUMAN]	13,86	NA	NA	2,60E+01	2,67E+01	2,63E+01	NA	2,61E+01	2,63E+01	0,501216545
O00303	Eukaryotic translation initiation factor 3 subunit F OS=Homo sapiens GN=EIF3F PE=1 SV=1 - [EIF3F_HUMAN]	14,29	NA	NA	2,59E+01	2,70E+01	2,66E+01	NA	2,59E+01	2,59E+01	0,272506083
P62280	**40S ribosomal protein S11 OS=Homo sapiens GN=RPS11 PE=1 SV=3 - [RS11_HUMAN]**	15,82	NA	NA	2,63E+01	2,67E+01	2,57E+01	2,53E+01	2,59E+01	2,67E+01	0,367396594
Q6UB35	Monofunctional C1-tetrahydrofolate synthase, mitochondrial OS=Homo sapiens GN=MTHFD1L PE=1 SV=1 - [C1TM_HUMAN	12,47	NA	NA	2,57E+01	2,76E+01	2,56E+01	NA	2,59E+01	2,54E+01	0,182481752
O14979	Heterogeneous nuclear ribonucleoprotein D-like OS=Homo sapiens GN=HNRPDL PE=1 SV=3 - [HNRDL_HUMAN]	8,57	NA	NA	2,60E+01	2,61E+01	2,53E+01	NA	2,56E+01	2,58E+01	0,338199513
Q70IA6	MOB kinase activator 2 OS=Homo sapiens GN=MOB2 PE=1 SV=1 - [MOB2_HUMAN]	10,13	NA	NA	2,56E+01	2,67E+01	2,63E+01	NA	2,55E+01	2,64E+01	0,063260341
P25205	DNA replication licensing factor MCM3 OS=Homo sapiens GN=MCM3 PE=1 SV=3 - [MCM3_HUMAN]	13,74	NA	NA	2,53E+01	2,66E+01	2,59E+01	NA	2,50E+01	2,55E+01	0,291970803
Q7Z417	Nuclear fragile X mental retardation-interacting protein 2 OS=Homo sapiens GN=NUFIP2 PE=1 SV=1 - [NUFP2_HUMAN]	5,04	NA	NA	2,33E+01	2,51E+01	2,64E+01	2,47E+01	NA	2,58E+01	0,228710462

			Areas (LOG2)								
Accession	Proteins identified in all 3 TLK2 bait samples but not TLK2-KD or control	ΣCoverage	MOCK_1	MOCK_2	TLK2_1	TLK2_2	TLK2_3	TLK2D_1	TLK2D_2	TLK2D_3	CRAP/ratio*
P37108	Signal recognition particle 14 kDa protein OS=Homo sapiens GN=SRP14 PE=1 SV=2 - [SRP14_HUMAN]	40,44	NA	NA	2,60E+01	2,71E+01	2,67E+01	NA	NA	NA	0,194647202
Q9GZN8	UPF0687 protein C20orf27 OS=Homo sapiens GN=C20orf27 PE=1 SV=3 - [CT027_HUMAN]	17,24	NA	NA	2,56E+01	2,77E+01	2,64E+01	NA	NA	NA	0,01216545
P30040	Endoplasmic reticulum resident protein 29 OS=Homo sapiens GN=ERP29 PE=1 SV=4 - [ERP29_HUMAN]	14,18	NA	NA	2,52E+01	2,70E+01	2,53E+01	NA	NA	NA	0,065693431
Q9Y6Y0	Influenza virus NS1A-binding protein OS=Homo sapiens GN=IVNS1ABP PE=1 SV=3 - [NS1BP_HUMAN]	12,77	NA	NA	2,49E+01	2,66E+01	2,58E+01	NA	NA	NA	0,248175182
Q9BS26	Endoplasmic reticulum resident protein 44 OS=Homo sapiens GN=ERP44 PE=1 SV=1 - [ERP44_HUMAN]	9,11	NA	NA	2,45E+01	2,57E+01	2,53E+01	NA	NA	NA	0,02676399
P49736	DNA replication licensing factor MCM2 OS=Homo sapiens GN=MCM2 PE=1 SV=4 - [MCM2_HUMAN]	4,76	NA	NA	2,46E+01	2,53E+01	2,48E+01	NA	NA	NA	0,231143552
Q13428	Treacle protein OS=Homo sapiens GN=TCOF1 PE=1 SV=3 - [TCOF_HUMAN]	4,03	NA	NA	2,54E+01	2,69E+01	2,54E+01	NA	NA	NA	0,250608273

*CRAP/ratio score is derived from crapome.org. It indicates the potential likelihood that this is a contaminant based on the number of times the protein has been identified in 411 unrelated experiments (lower value is better) (Mellacheruvu et al., 2013).

Supplementary Table S2: Results of BioID analysis of BirA*- FLAG-TLK2 in AD293 cells

Gene ID	Gene Name	*Full Gene Name*	Top Controls		Technical Replicates				Total	SAINT
11011	TLK2	*tousled like kinase 2*	2	0	1541	4001	2035	2280	9857	N/A
140735	**DYNLL2**	*dynein light chain LC8-type 2*	5	0	83	226	117	115	541	**1**
8655	**DYNLL1**	*dynein light chain LC8-type 1*	0	0	78	208	89	96	471	**1**
9874	**TLK1**	*tousled like kinase 1*	0	0	72	66	128	108	374	**1**
55723	**ASF1B**	*anti-silencing function 1B histone chaperone*	0	0	53	49	47	51	200	**1**
7290	**HIRA**	*histone cell cycle regulator*	0	0	45	19	29	31	124	**1**
25842	**ASF1A**	*anti-silencing function 1A histone chaperone*	0	0	27	29	17	24	97	**1**
54815	**GATAD2A**	*GATA zinc finger domain containing 2A*	0	0	26	7	19	10	62	**1**
29855	**UBN1**	*ubinuclein 1*	0	0	16	9	16	13	54	**1**
254048	**UBN2**	*ubinuclein 2*	0	0	13	4	10	17	44	**1**
3725	**JUN**	*Jun proto-oncogene, AP-1 transcription factor subunit*	0	0	8	6	5	6	25	**1**
4628	**MYH10**	*myosin heavy chain 10*	0	0	20	2	59	58	139	**0,98**
51605	**TRMT6**	*tRNA methyltransferase 6*	0	0	5	2	15	12	34	**0,98**
4627	MYH9	*myosin heavy chain 9*	37	37	136	64	203	208	611	**0**
7175	TPR	*translocated promoter region, nuclear basket protein*	181	156	147	67	180	164	558	**0**
4926	NUMA1	*nuclear mitotic apparatus protein 1*	46	44	87	36	133	110	366	**0**
11083	DIDO1	*death inducer-obliterator 1*	32	24	62	17	101	106	286	**0**
55183	RIF1	*replication timing regulatory factor 1*	29	18	75	23	110	78	286	**0**
871	SERPINH1	*serpin family H member 1*	37	35	37	16	69	68	190	**0**
9329	GTF3C4	*general transcription factor IIIC subunit 4*	19	16	30	15	47	48	140	**0**
11176	BAZ2A	*bromodomain adjacent to zinc finger domain 2A*	6	3	15	7	41	30	93	**0**
51202	DDX47	*DEAD-box helicase 47*	14	11	7	6	40	36	89	**0**
4292	MLH1	*mutL homolog 1*	5	5	15	7	33	33	88	**0**
4637	MYL6	*myosin light chain 6*	10	9	15	6	37	29	87	**0**
51497	TH1L	*negative elongation factor complex member C/D*	7	6	5	4	32	36	77	**0**
29894	CPSF1	*cleavage and polyadenylation specific factor 1*	20	16	28	4	18	23	73	**0**
9328	GTF3C5	*general transcription factor IIIC subunit 5*	8	7	14	5	22	28	69	**0**
57680	CHD8	*chromodomain helicase DNA binding protein 8*	16	10	18	6	26	17	67	**0**
9093	DNAJA3	*DnaJ heat shock protein family (Hsp40) member A3*	16	15	9	4	18	23	54	**0**
84930	MASTL	*microtubule associated serine/threonine kinase like*	10	4	8	0	22	23	53	**0**
728642	CDK11A	*cyclin dependent kinase 11A*	9	6	8	2	17	25	52	**0**
5931	RBBP7	*RB binding protein 7, chromatin remodeling factor*	28	24	11	0	25	8	44	**0**
3315	HSPB1	*heat shock protein family B (small) member 1*	28	28	0	0	20	23	43	**0**
55206	SBNO1	*strawberry notch homolog 1*	6	3	6	3	18	15	42	**0**
25909	AHCTF1	*AT-hook containing transcription factor 1*	25	20	7	0	14	16	37	**0**
11260	XPOT	*exportin for tRNA*	23	17	5	0	15	17	37	**0**
79080	CCDC86	*coiled-coil domain containing 86*	0	0	4	0	15	15	34	**0**
58	ACTA1	*actin, alpha 1, skeletal muscle*	26	22	0	0	33	0	33	**0**
9221	NOLC1	*nucleolar and coiled-body phosphoprotein 1*	9	8	0	0	15	17	32	**0**
4683	NBN	*nibrin*	3	2	10	0	13	9	32	**0**
55299	BRIX1	*BRX1, biogenesis of ribosomes*	4	0	0	0	17	14	31	**0**
4171	MCM2	*minichromosome maintenance complex component 2*	11	8	11	0	11	6	28	**0**
1736	DKC1	*dyskerin pseudouridine synthase 1*	6	6	0	0	10	15	25	**0**
7153	TOP2A	*topoisomerase (DNA) II alpha*	15	15	5	4	7	2	18	**0**
1017	CDK2	*cyclin dependent kinase 2*	13	11	4	0	0	14	18	**0**
5631	PRPS1	*phosphoribosyl pyrophosphate synthetase 1*	5	3	6	0	3	9	18	**0**
3615	IMPDH2	*inosine monophosphate dehydrogenase 2*	11	10	0	0	6	11	17	**0**
22820	COPG1	*coatomer protein complex subunit gamma 1*	6	6	3	0	7	6	16	**0**
10549	PRDX4	*peroxiredoxin 4*	0	0	0	0	15	0	15	**0**
10969	EBNA1BP2	*EBNA1 binding protein 2*	6	6	4	0	7	3	14	**0**
10436	EMG1	*EMG1, N1-specific pseudouridine methyltransferase*	6	3	0	0	6	7	13	**0**
55339	WDR33	*WD repeat domain 33*	0	0	7	0	5	0	12	**0**
196528	ARID2	*AT-rich interaction domain 2*	0	0	0	0	7	5	12	**0**
79784	MYH14	*myosin heavy chain 14*	2	0	0	0	5	6	11	**0**
55756	INTS9	*integrator complex subunit 9*	0	0	11	0	0	0	11	**0**
10898	CPSF4	*cleavage and polyadenylation specific factor 4*	4	4	0	0	8	0	8	**0**
10981	RAB32	*RAB32, member RAS oncogene family*	8	5	3	0	0	4	7	**0**
1717	DHCR7	*7-dehydrocholesterol reductase*	0	0	0	0	0	7	7	**0**
29927	SEC61A1	*Sec61 translocon alpha 1 subunit*	9	3	6	0	0	0	6	**0**
19	ABCA1	*ATP binding cassette subfamily A member 1*	0	0	0	0	6	0	6	**0**
81567	TXNDC5	*thioredoxin domain containing 5*	0	0	0	0	0	5	5	**0**
57082	CASC5	*kinetochore scaffold 1*	10	5	0	0	0	4	4	**0**
1105	CHD1	*chromodomain helicase DNA binding protein 1*	0	0	0	0	4	0	4	**0**
58506	SCAF1	*SR-related CTD associated factor 1*	0	0	0	0	0	4	4	**0**
902	CCNH	*cyclin H*	0	0	0	0	0	4	4	**0**
6520	SLC3A2	*solute carrier family 3 member 2*	0	0	3	0	0	0	3	**0**

Supplementary Table S3: TCGA cohort designations

Abbreviation	Cancer Type
ACC	Adrenocortical carcinoma
BLCA	Bladder Urothelial Carcinoma
BRCA	Breast invasive carcinoma
CESC	Cervical squamous cell carcinoma and endocervical adenocarcinoma
CHOL	Cholangiocarcinoma
CNTL	Controls
COAD	Colon adenocarcinoma
DLBC	Lymphoid Neoplasm Diffuse Large B-cell Lymphoma
ESCA	Esophageal carcinoma
GBM	Glioblastoma multiforme
HNSC	Head and Neck squamous cell carcinoma
KICH	Kidney Chromophobe
KIRC	Kidney renal clear cell carcinoma
KIRP	Kidney renal papillary cell carcinoma
LAML	Acute Myeloid Leukemia
LCML	Chronic Myelogenous Leukemia
LGG	Brain Lower Grade Glioma
LIHC	Liver hepatocellular carcinoma
LUAD	Lung adenocarcinoma
LUSC	Lung squamous cell carcinoma
MESO	Mesothelioma
MISC	Miscellaneous
OV	Ovarian serous cystadenocarcinoma
PAAD	Pancreatic adenocarcinoma
PCPG	Pheochromocytoma and Paraganglioma
PRAD	Prostate adenocarcinoma
READ	Rectum adenocarcinoma
SARC	Sarcoma
SKCM	Skin Cutaneous Melanoma
STAD	Stomach adenocarcinoma
TGCT	Testicular Germ Cell Tumors
THCA	Thyroid carcinoma
THYM	Thymoma
UCEC	Uterine Corpus Endometrial Carcinoma
UCS	Uterine Carcinosarcoma
UVM	Uveal Melanoma

Supplementary Table S4: Chromosome location of indicated genes

Gene ID	Chromosome location
TLK1	2q31.1
TLK2	17q23.2
ASF1B	19p13.12
ASF1A	6q22.31
CHEK1	11q24.2
ATR	3q23
MCM2	3q21.2
MKI67	10q26.2
E2F1	20q11.22
TP53	17p13.1
MYC	8q24.21
PTEN	10q23.31
ATM	11q22.3
EGFR	7p11.2

References

References

Abascal, F., Corpet, A., Gurard-Levin, Z.A., Juan, D., Ochsenbein, F., Rico, D., Valencia, A., and Almouzni, G. (2013). Subfunctionalization via adaptive evolution influenced by genomic context: The case of histone chaperones ASF1a and ASF1b. Mol. Biol. Evol. 30, 1853–1866.

Adam, S., Polo, S., and Almouzni, G. (2013). Transcription recovery after DNA damage requires chromatin priming by the H3. 3 histone chaperone HIRA. Cell 155, 94–106.

Adkins, M.W., and Tyler, J.K. (2004). The histone chaperone Asf1p mediates global chromatin disassembly in vivo. J. Biol. Chem. 279, 52069–52074.

Aguilar-Gurrieri, C., Larabi, A., Vinayachandran, V., Patel, N.A., Yen, K., Reja, R., Ebong, I., Schoehn, G., Robinson, C. V, Pugh, B.F., et al. (2016). Structural evidence for Nap1-dependent H2A–H2B deposition and nucleosome assembly. EMBO J. 35, 1465–1482.

Alabert, C., Barth, T.K., Reverón-Gómez, N., Sidoli, S., Schmidt, A., Jensen, O., Imhof, A., and Groth, A. (2015). Two distinct modes for propagation of histone PTMs across the cell cycle. Genes Dev. 29, 585–590.

Andrews, A.J., Chen, X., Zevin, A., Stargell, L.A., and Luger, K. (2010). The Histone Chaperone Nap1 Promotes Nucleosome Assembly by Eliminating Nonnucleosomal Histone DNA Interactions. Mol. Cell 37, 834–842.

Arnoult, N., Van Beneden, A., and Decottignies, A. (2012). Telomere length regulates TERRA levels through increased trimethylation of telomeric H3K9 and HP1α. Nat. Struct. Mol. Biol. 19, 948–956.

Ashburner, M., Ball, C.A., Blake, J.A., Botstein, D., Butler, H., Cherry, J.M., Davis, A.P., Dolinski, K., Dwight, S.S., Eppig, J.T., et al. (2000). Gene ontology: Tool for the unification of biology. Nat. Genet. 25, 25–29.

Ask, K., Jasencakova, Z., Menard, P., Feng, Y., Almouzni, G., and Groth, A. (2012). Codanin-1, mutated in the anaemic disease CDAI, regulates Asf1 function in S-phase histone supply. EMBO J. 31, 2013–2023.

Banaszynski, L.A., Wen, D., Dewell, S., Whitcomb, S.J., Lin, M., Diaz, N., Elsässer, S.J., Chapgier, A., Goldberg, A.D., Canaani, E., et al. (2013). Hira-dependent histone H3.3 deposition facilitates prc2 recruitment at developmental loci in ES cells. Cell 155, 107–120.

Bao, W., Kojima, K.K., and Kohany, O. (2015). Repbase Update, a database of repetitive elements in eukaryotic genomes. Mob. DNA 6.

Barcaroli, D., Bongiorno-Borbone, L., Terrinoni, A., Hofmann, T.G., Rossi, M., Knight, R.A., Matera, A.G., Melino, G., and De Laurenzi, V. (2006). FLASH is required for histone transcription and S-phase progression. Proc. Natl. Acad. Sci. U. S. A. 103, 14808–14812.

Barlow, C., Hirotsune, S., Paylor, R., Liyanage, M., Eckhaus, M., Collins, F., Shiloh, Y., Crawley, J.N., Ried, T., Tagle, D., et al. (1996). Atm-deficient mice: A paradigm of ataxia telangiectasia. Cell 86, 159–171.

Barrett, T., Wilhite, S.E., Ledoux, P., Evangelista, C., Kim, I.F., Tomashevsky, M., Marshall, K.A., Phillippy, K.H., Sherman, P.M., Holko, M., et al. (2013). NCBI GEO: Archive for functional genomics data sets - Update. Nucleic Acids Res. 41.

Bartkova, J., Hořejší, Z., Koed, K., Krämer, A., Tort, F., Zleger, K., Guldberg, P., Sehested, M., Nesland, J.M., Lukas, C., et al. (2005). DNA damage response as a candidate anti-cancer barrier in early human tumorigenesis. Nature 434, 864–870.

Bartkova, J., Rezaei, N., Liontos, M., Karakaidos, P., Kletsas, D., Issaeva, N., Vassiliou, L.V.F., Kolettas, E., Niforou, K., Zoumpourlis, V.C., et al. (2006). Oncogene-induced senescence is part of the tumorigenesis barrier imposed by DNA damage checkpoints. Nature 444, 633–637.

Behjati, S., Tarpey, P.S., Presneau, N., Scheipl, S., Pillay, N., Van Loo, P., Wedge, D.C., Cooke, S.L., Gundem, G., Davies, H., et al. (2013). Distinct H3F3A and H3F3B driver mutations define chondroblastoma and giant cell tumor of bone. Nat. Genet. 45, 1479–1482.

Bender, S., Tang, Y., Lindroth, A.M., Hovestadt, V., Jones, D.T.W., Kool, M., Zapatka, M., Northcott, P.A., Sturm, D., Wang, W., et al. (2013). Reduced H3K27me3 and DNA Hypomethylation Are Major Drivers of Gene Expression in K27M Mutant Pediatric High-Grade Gliomas. Cancer Cell 24, 660–672.

Bennardo, N., Cheng, A., Huang, N., and Stark, J.M. (2008). Alternative-NHEJ is a mechanistically distinct pathway of mammalian chromosome break repair. PLoS Genet. 4.

Bertoli, C., Skotheim, J.M., and De Bruin, R.A.M. (2013). Control of cell cycle transcription during G1 and S phases. Nat. Rev. Mol. Cell Biol. 14, 518–528.

Bester, A.C., Roniger, M., Oren, Y.S., Im, M.M., Sarni, D., Chaoat, M., Bensimon, A., Zamir, G., Shewach, D.S., and Kerem, B. (2011). Nucleotide deficiency promotes genomic instability in early stages of cancer development. Cell 145, 435–446.

Bishop, A.C., Shah, K., Liu, Y., Witucki, L., Kung, C.Y., and Shokat, K.M. (1998). Design of allele-specific inhibitors to probe protein kinase signaling. Curr. Biol. 8, 257–266.

Blasius, M., Forment, J. V., Thakkar, N., Wagner, S.A., Choudhary, C., and Jackson, S.P. (2011). A phospho-proteomic screen identifies substrates of the checkpoint kinase Chk1. Genome Biol. 12.

Bodor, D.L., Valente, L.P., Mata, J.F., Black, B.E., and Jansen, L.E.T. (2013). Assembly in G1 phaseand Long-Term Stability are Uniqueintrinsic Features of CENP-Anucleosomes. Mol. Biol. Cell.

Bouwman, P., and Jonkers, J. (2012). The effects of deregulated DNA damage signalling on cancer chemotherapy response and resistance. Nat. Rev. Cancer 12, 587–598.

Broughton, B.C., Cordonnier, A., Kleijer, W.J., Jaspers, N.G.J., Fawcett, H., Raams, A., Garritsen, V.H., Stary, A., Avril, M.-F., Boudsocq, F., et al. (2002). Molecular analysis of mutations in DNA polymerase eta in xeroderma pigmentosum-variant patients. Proc. Natl. Acad. Sci. U. S. A. 99, 815–820.

Bruinsma, W., van den Berg, J., Aprelia, M., and Medema, R.H. (2016). Tousled-like kinase 2 regulates recovery from a DNA damage-induced G2 arrest. EMBO Rep. e201540767.

Bryan, T.M., Englezou, A., Dalla-Pozza, L., Dunham, M.A., and Reddel, R.R. (1997). Evidence for an alternative mechanism for maintaining telomere length in human tumors and tumor-derived cell lines. Nat. Med. 3, 1271–1274.

Bryant, H.E., Schultz, N., Thomas, H.D., Parker, K.M., Flower, D., Lopez, E., Kyle, S., Meuth, M., Curtin, N.J., and Helleday, T. (2005). Specific killing of BRCA2-deficient tumours with inhibitors of poly(ADP-ribose) polymerase. Nature 434, 913–917.

Buenrostro, J.D., Giresi, P.G., Zaba, L.C., Chang, H.Y., and Greenleaf, W.J. (2013). Transposition of native chromatin for fast and sensitive epigenomic profiling of open chromatin, DNA-binding proteins and nucleosome position. Nat. Methods 10, 1213–1218.

Buenrostro, J.D., Wu, B., Chang, H.Y., and Greenleaf, W.J. (2015). ATAC-seq: A method for assaying chromatin accessibility genome-wide. Curr. Protoc. Mol. Biol. 2015, 21.29.1-21.29.9.

Bunkenborg, J., García, G.E., Paz, M.I.P., Andersen, J.S., and Molina, H. (2010). The minotaur proteome: Avoiding cross-species identifications deriving from bovine serum in cell culture models. Proteomics 10, 3040–3044.

Buonomo, S.B.C., Wu, Y., Ferguson, D., and De Lange, T. (2009). Mammalian Rif1 contributes to replication stress survival and homology-directed repair. J. Cell Biol. 187, 385–398.

Burgess, R.J., and Zhang, Z. (2014). Histone chaperones in nucleosome assembly and human disease. Nat Struct Mol Biol. 20, 14–22.

Buschbeck, M., and Hake, S.B. (2017). Variants of core histones and their roles in cell fate decisions, development and cancer. Nat. Rev. Mol. Cell Biol. 18, 299–314.

Byun, T.S., Pacek, M., Yee, M.C., Walter, J.C., and Cimprich, K.A. (2005). Functional uncoupling of MCM helicase and DNA polymerase activities activates the ATR-dependent checkpoint. Genes Dev. 19, 1040–1052.

Campos, E.I., Fillingham, J., Li, G., Zheng, H., Voigt, P., Kuo, W.H.W., Seepany, H., Gao, Z., Day, L.A., Greenblatt, J.F., et al. (2010). The program for processing newly synthesized histones H3.1 and H4. Nat. Struct. Mol. Biol. 17, 1343–1351.

Canfield, C., Rains, J., and De Benedetti, A. (2009). TLK1B promotes repair of DSBs via its interaction with Rad9 and Asf1. BMC Mol. Biol. 10, 110.

Carrera, P., Moshkin, Y.M., Grönke, S., Silljé, H.H.W., Nigg, E.A., Jäckle, H., and Karch, F. (2003). Tousled-like kinase functions with the chromatin assembly pathway regulating nuclear divisions. Genes Dev. 17, 2578–2590.

Cerami, E., Gao, J., Dogrusoz, U., Gross, B.E., Sumer, S.O., Aksoy, B.A., Jacobsen, A., Byrne, C.J., Heuer, M.L., Larsson, E., et al. (2012). The cBio Cancer Genomics Portal: An open platform for exploring multidimensional cancer genomics data. Cancer Discov. 2, 401–404.

Chang, F.T.M., McGhie, J.D., Chan, F.L., Tang, M.C., Anderson, M.A., Mann, J.R., Andy Choo, K.H., and Wong, L.H. (2013). PML bodies provide an important platform for the maintenance of telomeric chromatin integrity in embryonic stem cells. Nucleic Acids Res. 41, 4447–4458.

Chang, F.T.M., Chan, F.L., McGhie, J.D.R., Udugama, M., Mayne, L., Collas, P., Mann, J.R., and Wong, L.H. (2015). CHK1-driven histone H3.3 serine 31 phosphorylation is important for chromatin maintenance and cell survival in human ALT cancer cells. Nucleic Acids Res. 43, 2603–2614.

Chapman, J.R., Barral, P., Vannier, J.B., Borel, V., Steger, M., Tomas-Loba, A., Sartori, A.A., Adams, I.R., Batista, F.D., and Boulton, S.J. (2013). RIF1 Is Essential for 53BP1-Dependent Nonhomologous End Joining and Suppression of DNA Double-Strand Break Resection. Mol. Cell 49, 858–871.

Chen, C.C., Carson, J.J., Feser, J., Tamburini, B., Zabaronick, S., Linger, J., and Tyler, J.K. (2008). Acetylated Lysine 56 on Histone H3 Drives Chromatin Assembly after Repair and Signals for the Completion of Repair. Cell 134, 231–243.

Chen, Y.A., Shen, Y.L., Hsia, H.Y., Tiang, Y.P., Sung, T.L., and Chen, L.Y. (2017). Extrachromosomal telomere repeat DNA is linked to ALT development via cGAS-STING DNA sensing pathway. Nat. Struct. Mol. Biol. 24, 1124–1131.

Chiappinelli, K.B., Strissel, P.L., Desrichard, A., Li, H., Henke, C., Akman, B., Hein, A., Rote, N.S., Cope, L.M., Snyder, A., et al. (2015). Inhibiting DNA Methylation Causes an Interferon Response in Cancer via dsRNA Including Endogenous Retroviruses. Cell 162, 974–986.

Chimura, T., Kuzuhara, T., and Horikoshi, M. (2002). Identification and characterization of CIA/ASF1 as an interactor of bromodomains associated with TFIID. Proc. Natl. Acad. Sci. 99, 9334–9339.

Cleaton, M.A.M., Edwards, C.A., and Ferguson-Smith, A.C. (2014). Phenotypic Outcomes of Imprinted Gene Models in Mice: Elucidation of Pre- and Postnatal Functions of Imprinted Genes. Annu. Rev. Genomics Hum. Genet. 15, 93–126.

Clément, C., Vassias, I., Ray-Gallet, D., and Almouzni, G. (2016). Functional Characterization of Histone Chaperones Using SNAP-Tag-Based Imaging to Assess de Novo Histone Deposition. In Methods in Enzymology, pp. 97–117.

Clynes, D., Higgs, D.R., and Gibbons, R.J. (2013). The chromatin remodeller ATRX: A repeat offender in human disease. Trends Biochem. Sci. 38, 461–466.

Clynes, D., Jelinska, C., Xella, B., Ayyub, H., Scott, C., Mitson, M., Taylor, S., Higgs, D.R., and Gibbons, R.J. (2015). Suppression of the alternative lengthening of telomere pathway by the chromatin remodelling factor ATRX. Nat. Commun. 6.

Cong, L., Ran, F.A., Cox, D., Lin, S., Barretto, R., Habib, N., Hsu, P.D., Wu, X., Jiang, W., Marraffini, L.A., et al. (2013). Multiplex Genome Engineering Using CRISPR/Cas Systems. Science (80-.). 339, 819–823.

Conomos, D., Reddel, R.R., and Pickett, H.A. (2014). NuRD-ZNF827 recruitment to telomeres creates a molecular scaffold for homologous recombination. Nat. Struct. Mol. Biol. 21, 760–770.

Cook, A.J.L., Gurard-Levin, Z.A., Vassias, I., and Almouzni, G. (2011). A Specific Function for the Histone Chaperone NASP to Fine-Tune a Reservoir of Soluble H3-H4 in the Histone Supply Chain. Mol. Cell 44, 918–927.

Copeland, N.G., Jenkins, N.A., and Court, D.L. (2001). Recombineering: A powerful new tool for mouse functional genomics. Nat. Rev. Genet. 2, 769–779.

Cornacchia, D., Dileep, V., Quivy, J.P., Foti, R., Tili, F., Santarella-Mellwig, R., Antony, C., Almouzni, G., Gilbert, D.M., and Buonomo, S.B.C. (2012). Mouse Rif1 is a key regulator of the replication-timing programme in mammalian cells. EMBO J. 31, 3678–3690.

Corpet, A., De Koning, L., Toedling, J., Savignoni, A., Berger, F., Lemaître, C., O'Sullivan, R.J., Karlseder, J., Barillot, E., Asselain, B., et al. (2011). Asf1b, the necessary Asf1 isoform for proliferation, is predictive of outcome in breast cancer. EMBO J. 30, 480–493.

Corpet, A., Olbrich, T., Gwerder, M., Fink, D., and Stucki, M. (2014). Dynamics of histone H3.3 deposition in proliferating and senescent cells reveals a DAXX-dependent targeting to PML-NBs important for pericentromeric heterochromatin organization. Cell Cycle 13, 249–267.

Cortez, D. (2015). Preventing replication fork collapse to maintain genome integrity. DNA Repair (Amst). 32, 149–157.

Cortez, D., Guntuku, S., Qin, J., and Elledge, S.J. (2001). ATR and ATRIP: Partners in checkpoint signaling. Science (80-.). 294, 1713–1716.

Coyaud, E., Mis, M., Laurent, E.M.N., Dunham, W.H., Couzens, A.L., Robitaille, M., Gingras, A.-C., Angers, S., and Raught, B. (2015). BioID-based Identification of Skp Cullin F-box (SCF) β-TrCP1/2 E3 Ligase Substrates. Mol. Cell. Proteomics 14, 1781–1795.

Crosio, C., Fimia, G.M., Loury, R., Kimura, M., Okano, Y., Zhou, H., Sen, S., Allis, C.D., and Sassone-Corsi, P. (2002). Mitotic Phosphorylation of Histone H3: Spatio-Temporal Regulation by Mammalian Aurora Kinases. Mol. Cell. Biol. 22, 874–885.

Cross, J.C. (2000). Genetic insights into trophoblast differentiation and placental morphogenesis. Semin. Cell Dev. Biol. 11, 105–113.

Crow, Y.J., Leitch, A., Hayward, B.E., Garner, A., Parmar, R., Griffith, E., Ali, M., Semple, C., Aicardi, J., Babul-Hirji, R., et al. (2006a). Mutations in genes encoding ribonuclease H2 subunits cause Aicardi-Goutières syndrome and mimic congenital viral brain infection. Nat. Genet. 38, 910–916.

Crow, Y.J., Hayward, B.E., Parmar, R., Robins, P., Leitch, A., Ali, M., Black, D.N., Van Bokhoven, H., Brunner, H.G., Hamel, B.C., et al. (2006b). Mutations in the gene encoding the 3′-5′ DNA exonuclease TREX1 cause Aicardi-Goutières syndrome at the AGS1 locus. Nat. Genet. 38, 917–920.

Cui, W., Taub, D.D., and Gardner, K. (2007). qPrimerDepot: A primer database for quantitative real time PCR. Nucleic Acids Res. 35.

Curtis, C., Shah, S.P., Chin, S.F., Turashvili, G., Rueda, O.M., Dunning, M.J., Speed, D., Lynch, A.G., Samarajiwa, S., Yuan, Y., et al. (2012). The genomic and transcriptomic architecture of 2,000 breast tumours reveals novel subgroups. Nature 486, 346–352.

Deeg, K.I., Chung, I., Bauer, C., and Rippe, K. (2016). Cancer Cells with Alternative Lengthening of Telomeres Do Not Display a General Hypersensitivity to ATR Inhibition. Front. Oncol. 6.

Delacroix, S., Wagner, J.M., Kobayashi, M., Yamamoto, K.I., and Karnitz, L.M. (2007). The Rad9-Hus1-Rad1 (9-1-1) clamp activates checkpoint signaling via TopBP1. Genes Dev. 21, 1472–1477.

Delbarre, E., Ivanauskiene, K., Küntziger, T., and Collas, P. (2013). DAXX-dependent supply of soluble (H3.3-H4) dimers to PML bodies pending deposition into chromatin. Genome Res. 23, 440–451.

Delbarre, E., Ivanauskiene, K., Spirkoski, J., Shah, A., Vekterud, K., Moskaug, J., Bøe, S.O., Wong, L.H., Küntziger, T., and Collas, P. (2017). PML protein organizes heterochromatin domains where it regulates histone H3.3 deposition by ATRX/DAXX. Genome Res. 27, 913–921.

Dellino, G.I., Cittaro, D., Piccioni, R., Luzi, L., Banfi, S., Segalla, S., Cesaroni, M., Mendoza-Maldonado, R., Giacca, M., and Pelicci, P.G. (2013). Genome-wide mapping of human DNA-replication origins: Levels of transcription at ORC1 sites regulate origin selection and replication timing. Genome Res. 23, 1–11.

Devbhandari, S., Jiang, J., Kumar, C., Whitehouse, I., and Remus, D. (2017). Chromatin Constrains the Initiation and Elongation of DNA Replication. Mol. Cell 65, 131–141.

Dgany, O., Avidan, N., Delaunay, J., Krasnov, T., Shalmon, L., Shalev, H., Eidelitz-Markus, T., Kapelushnik, J., Cattan, D., Pariente, A., et al. (2002). Congenital Dyserythropoietic Anemia Type I Is Caused by Mutations in Codanin-1. Am. J. Hum. Genet. 71, 1467–1474.

Dilley, R.L., and Greenberg, R.A. (2015). ALTernative Telomere Maintenance and Cancer. Trends in Cancer 1, 145–156.

Dillon, P.J., Gregory, S.M., Tamburro, K., Sanders, M.K., Johnson, G.L., Raab-Traub, N., Dittmer, D.P., and Damania, B. (2013). Tousled-like kinases modulate reactivation of gammaherpesviruses from latency. Cell Host Microbe 13, 204–214.

Dobbelstein, M., and Sørensen, C.S. (2015). Exploiting replicative stress to treat cancer. Nat. Rev. Drug Discov. 14, 405–423.

Drané, P., Ouararhni, K., Depaux, A., Shuaib, M., and Hamiche, A. (2010). The death-associated protein DAXX is a novel histone chaperone involved in the replication-independent deposition of H3.3. Genes Dev. 24, 1253–1265.

Dunham, I., Kundaje, A., Aldred, S.F., Collins, P.J., Davis, C.A., Doyle, F., Epstein, C.B., Frietze, S., Harrow, J., Kaul, R., et al. (2012). An integrated encyclopedia of DNA elements in the human genome. Nature 489, 57–74.

Dunleavy, E.M., Roche, D., Tagami, H., Lacoste, N., Ray-Gallet, D., Nakamura, Y., Daigo, Y., Nakatani, Y., and Almouzni-Pettinotti, G. (2009). HJURP Is a Cell-Cycle-Dependent Maintenance and Deposition Factor of CENP-A at Centromeres. Cell 137, 485–497.

Dyer, M.A., Qadeer, Z.A., Valle-Garcia, D., and Bernstein, E. (2017). ATRX and DAXX: Mechanisms and mutations. Cold Spring Harb. Perspect. Med. 7.

Ehsan, H., Reichheld, J., Durfee, T., Roe, J.L., Kansas, H.E., and Ge, L. (2004). TOUSLED Kinase Activity Oscillates during the Cell Cycle and Interacts with Chromatin Regulators 1. Plant Physiol. 134, 1488–1499.

Elsässer, S.J., Noh, K.M., Diaz, N., Allis, C.D., and Banaszynski, L.A. (2015). Histone H3.3 is required for endogenous retroviral element silencing in embryonic stem cells. Nature 522, 240–244.

Emili, A., Schieltz, D.M., Yates, J.R., and Hartwell, L.H. (2001). Dynamic interaction of DNA damage checkpoint protein Rad53 with chromatin assembly factor Asf1. Mol. Cell 7, 13–20.

Ernst, J., and Kellis, M. (2012). ChromHMM: Automating chromatin-state discovery and characterization. Nat. Methods 9, 215–216.

Falck, J., Petrini, J.H.J., Williams, B.R., Lukas, J., and Bartek, J. (2002). The DNA damage-dependent intra-S phase checkpoint is regulated by parallel pathways. Nat. Genet. 30, 290–294.

Fang, D., Gan, H., Lee, J.H., Han, J., Wang, Z., Riester, S.M., Jin, L., Chen, J., Zhou, H., Wang, J., et al. (2016). The histone H3.3K36M mutation reprograms the epigenome of chondroblastomas. Science (80-.). 352, 1344–1348.

Farmer, H., McCabe, N., Lord, C.J., Tutt, A.N.J., Johnson, D.A., Richardson, T.B., Santarosa, M., Dillon, K.J., Hickson, I., Knights, C., et al. (2005). Targeting the DNA repair defect in BRCA mutant cells as a therapeutic strategy. Nature 434, 917–921.

Fellmann, C., Hoffmann, T., Sridhar, V., Hopfgartner, B., Muhar, M., Roth, M., Lai, D.Y., Barbosa, I.A.M., Kwon, J.S., Guan, Y., et al. (2013). An optimized microRNA backbone for effective single-copy RNAi. Cell Rep. 5, 1704–1713.

Feretzaki, M., and Lingner, J. (2017). A practical qPCR approach to detect TERRA, the elusive telomeric repeat-containing RNA. Methods 114, 39–45.

Fernandez-Vidal, A., Guitton-Sert, L., Cadoret, J.-C., Drac, M., Schwob, E., Baldacci, G., Cazaux, C., and Hoffmann, J.-S. (2014). A role for DNA polymerase θ in the timing of DNA replication. Nat. Commun. 5.

Filipponi, D., Muller, J., Emelyanov, A., and Bulavin, D. (2013). Wip1 Controls Global Heterochromatin Silencing via ATM/BRCA1-Dependent DNA Methylation. Cancer Cell 24, 528–541.

Flynn, R.L., Cox, K.E., Jeitany, M., Wakimoto, H., Bryll, A.R., Ganem, N.J., Bersani, F., Pineda, J.R., Suvà, M.L., Benes, C.H., et al. (2015). Alternative lengthening of telomeres renders cancer cells hypersensitive to ATR inhibitors. Science (80-.). 347, 273–277.

Fokas, E., Prevo, R., Hammond, E.M., Brunner, T.B., McKenna, W.G., and Muschel, R.J. (2014). Targeting ATR in DNA damage response and cancer therapeutics. Cancer Treat. Rev. 40, 109–117.

Foltz, D.R., Jansen, L.E.T., Bailey, A.O., Yates, J.R., Bassett, E.A., Wood, S., Black, B.E., and Cleveland, D.W. (2009). Centromere-Specific Assembly of CENP-A Nucleosomes Is Mediated by HJURP. Cell 137, 472–484.

Fragkos, M., Ganier, O., Coulombe, P., and Méchali, M. (2015). DNA replication origin activation in space and time. Nat. Rev. Mol. Cell Biol. 16, 360–374.

Gaillard, H., García-Muse, T., and Aguilera, A. (2015). Replication stress and cancer. Nat. Rev. Cancer 15, 276–280.

Gao, Y., Davies, S.P., Augustin, M., Woodward, A., Patel, U.A., Kovelman, R., and Harvey, K.J. (2013). A broad activity screen in support of a chemogenomic map for kinase signalling research and drug discovery. Biochem. J. 451, 313–328.

Gavet, O., and Pines, J. (2010). Progressive Activation of CyclinB1-Cdk1 Coordinates Entry to Mitosis. Dev. Cell 18, 533–543.

Gheghiani, L., Loew, D., Lombard, B., Mansfeld, J., and Gavet, O. (2017). PLK1 Activation in Late G2 Sets Up Commitment to Mitosis. Cell Rep. 19, 2060–2073.

Gibbons, R.J., Picketts, D.J., Villard, L., and Higgs, D.R. (1995). Mutations in a putative global transcriptional regulator cause X-linked mental retardation with alpha-thalassemia (ATR-X syndrome). Cell 80, 837–845.

Gibson-Corley, K.N., Olivier, A.K., and Meyerholz, D.K. (2013). Principles for Valid Histopathologic Scoring in Research. Vet. Pathol. 50, 1007–1015.

Gloeckner, C.J., Boldt, K., Schumacher, A., Roepman, R., and Ueffing, M. (2007). A novel tandem affinity purification strategy for the efficient isolation and characterisation of native protein complexes. Proteomics 7, 4228–4234.

Goldberg, A.D., Banaszynski, L.A., Noh, K.M., Lewis, P.W., Elsaesser, S.J., Stadler, S., Dewell, S., Law, M., Guo, X., Li, X., et al. (2010). Distinct Factors Control Histone Variant H3.3 Localization at Specific Genomic Regions. Cell 140, 678–691.

Gorgoulis, V.G., Vassiliou, L.-V.F., Karakaidos, P., Zacharatos, P., Kotsinas, A., Liloglou, T., Venere, M., DiTullio, R.A., Kastrinakis, N.G., Levy, B., et al. (2005). Activation of the DNA damage checkpoint and genomic instability in human precancerous lesions. Nature 434, 907–913.

Green, E.M., Antczak, A.J., Bailey, A.O., Franco, A.A., Wu, K.J., Yates, J.R., and Kaufman, P.D. (2005). Replication-independent histone deposition by the HIR complex and Asf1. Curr. Biol. 15, 2044–2049.

Grigsby, I.F., Rutledge, E.M., Morton, C.A., and Finger, F.P. (2009). Functional redundancy of two C. elegans homologs of the histone chaperone Asf1 in germline DNA replication. Dev. Biol. 329, 64–79.

Groth, A., Lukas, J., Nigg, E.A., Silljé, H.H.W., Wernstedt, C., Bartek, J., and Hansen, K. (2003). Human Tousled like kinases are targeted by an ATM- and Chk1-dependent DNA damage checkpoint. EMBO J. 22, 1676–1687.

Groth, A., Ray-Gallet, D., Quivy, J.P., Lukas, J., Bartek, J., and Almouzni, G. (2005). Human Asf1 regulates the flow of S phase histones during replicational stress. Mol. Cell 17, 301–311.

Groth, A., Corpet, A., Cook, A.J.L., Roche, D., Bartek, J., Lukas, J., and Almouzni, G. (2007). Regulation of replication fork progression through histone supply and demand. Science (80-.). 318, 1928–1931.

Gulen, M.F., Koch, U., Haag, S.M., Schuler, F., Apetoh, L., Villunger, A., Radtke, F., and Ablasser, A. (2017). Signalling strength determines proapoptotic functions of STING. Nat. Commun. 8.

Guy, C.T., Cardiff, R.D., and Muller, W.J. (1992). Induction of mammary tumors by expression of polyomavirus middle T oncogene: a transgenic mouse model for metastatic disease. Mol. Cell. Biol. 12, 954–961.

Hake, S.B., Garcia, B.A., Kauer, M., Baker, S.P., Shabanowitz, J., Hunt, D.F., and Allis, C.D. (2005). Serine 31 phosphorylation of histone variant H3.3 is specific to regions bordering centromeres in metaphase chromosomes. Proc. Natl. Acad. Sci. 102, 6344–6349.

Halazonetis, T.D., Gorgoulis, V.G., and Bartek, J. (2008). An oncogene-induced DNA damage model for cancer development. Science 319, 1352–1355.

Hammond, C.M., Strømme, C.B., Huang, H., Patel, D.J., and Groth, A. (2017). Histone chaperone networks shaping chromatin function. Nat. Rev. Mol. Cell Biol. 18, 141–158.

Han, Z., Saam, J.R., Adams, H.P., Mango, S.E., and Schumacher, J.M. (2003). The C. elegans Tousled-like Kinase (TLK-1) Has an Essential Role in Transcription. Curr. Biol. 13, 1921–1929.

Han, Z., Riefler, G.M., Saam, J.R., Mango, S.E., and Schumacher, J.M. (2005). The C. elegans Tousled-like kinase contributes to chromosome segregation as a substrate and regulator of the Aurora B kinase. Curr. Biol. 15, 894–904.

Harding, S.M., Benci, J.L., Irianto, J., Discher, D.E., Minn, A.J., and Greenberg, R.A. (2017). Mitotic progression following DNA damage enables pattern recognition within micronuclei. Nature 548, 466–470.

Harper, J.W., and Elledge, S.J. (2007). The DNA Damage Response: Ten Years After. Mol. Cell 28, 739–745.

Harrow, J., Frankish, A., Gonzalez, J.M., Tapanari, E., Diekhans, M., Kokocinski, F., Aken, B.L., Barrell, D., Zadissa, A., Searle, S., et al. (2012). GENCODE: The reference human genome annotation for the ENCODE project. Genome Res. 22, 1760–1774.

Hartford, S. a., Luo, Y., Southard, T.L., Min, I.M., Lis, J.T., and Schimenti, J.C. (2011). Minichromosome maintenance helicase paralog MCM9 is dispensible for DNA replication but functions in germ-line stem cells and tumor suppression. Proc. Natl. Acad. Sci. 108, 17702–17707.

Hayano, M., Kanoh, Y., Matsumoto, S., Renard-Guillet, C., Shirahige, K., and Masai, H. (2012). Rif1 is a global regulator of timing of replication origin firing in fission yeast. Genes Dev. 26, 137–150.

Hayashi, S., Lewis, P., Pevny, L., and McMahon, A.P. (2002). Efficient gene modulation in mouse epiblast using a Sox2Cre transgenic mouse strain. Gene Expr. Patterns 2, 93–97.

Heaphy, C.M., De Wilde, R.F., Jiao, Y., Klein, A.P., Edil, B.H., Shi, C., Bettegowda, C., Rodriguez, F.J., Eberhart, C.G., Hebbar, S., et al. (2011). Altered telomeres in tumors with ATRX and DAXX mutations. Science (80-.). 333, 425.

Heinz, S., Benner, C., Spann, N., Bertolino, E., Lin, Y.C., Laslo, P., Cheng, J.X., Murre, C., Singh, H., and Glass, C.K. (2010). Simple Combinations of Lineage-Determining Transcription Factors Prime cis-Regulatory Elements Required for Macrophage and B Cell Identities. Mol. Cell 38, 576–589.

Henson, J.D., Cao, Y., Huschtscha, L.I., Chang, A.C., Au, A.Y., Pickett, H.A., and Reddel, R.R. (2009). DNA C-circles are specific and quantifiable markers of alternative-lengthening-of-telomeres activity. Nat Biotechnol 27, 1181–1185.

Henson, J.D., Lau, L.M., Koch, S., Martin La Rotta, N., Dagg, R.A., and Reddel, R.R. (2017). The C-Circle Assay for alternative-lengthening-of-telomeres activity. Methods 114, 74–84.

Hiraga, S.I., Alvino, G.M., Chang, F., Lian, H.Y., Sridhar, A., Kubota, T., Brewer, B.J., Weinreich, M., Raghuraman, M.K., and Donaldson, A.D. (2014). Rif1 controls DNA replication by directing Protein Phosphatase 1 to reverse Cdc7- mediated phosphorylation of the MCM complex. Genes Dev. 28, 372–383.

Hoek, M., and Stillman, B. (2003). Chromatin assembly factor 1 is essential and couples chromatin assembly to DNA replication in vivo. Proc Natl Acad Sci U S A 100, 12183–12188.

Hoessel, R., Leclerc, S., Endicott, J.A., Nobel, M.E., Lawrie, A., Tunnah, P., Leost, M., Damiens, E., Marie, D., Marko, D., et al. (1999). Indirubin, the active constituent of a Chinese antileukaemia medicine, inhibits cyclin-dependent kinases. Nat. Cell Biol. 1, 60–67.

Holmquist, G., Gray, M., Porter, T., and Jordan, J. (1982). Characterization of Giemsa dark- and light-band DNA. Cell 31, 121–129.

Hu, F., Alcasabas, A.A., and Elledge, S.J. (2001). Asf1 links Rad53 to control of chromatin assembly. Genes Dev. 15, 1061–1066.

Huang, H., Strømme, C.B., Saredi, G., Hödl, M., Strandsby, A., González-Aguilera, C., Chen, S., Groth, A., and Patel, D.J. (2015). A unique binding mode enables MCM2 to chaperone histones H3-H4 at replication forks. Nat. Struct. Mol. Biol. 22, 618–626.

Huang, T.-H., Fowler, F., Chen, C.-C., Shen, Z.-J., Sleckman, B., and Tyler, J.K. (2018). The Histone Chaperones ASF1 and CAF-1 Promote MMS22L-TONSL-Mediated Rad51 Loading onto ssDNA during Homologous Recombination in Human Cells. Mol. Cell 69, 879–892.e5.

Indra, A.K., Warot, X., Brocard, J., Bornert, J.M., Xiao, J.H., Chambon, P., and Metzger, D. (1999). Temporally-controlled site-specific mutagenesis in the basal layer of the epidermis: Comparison of the recombinase activity of the tamoxifen-inducible Cre-ER(T) and Cre-ER(T2) recombinases. Nucleic Acids Res. 27, 4324–4327.

Ivanauskiene, K., Delbarre, E., McGhie, J.D., Kuntziger, T., Wong, L.H., and Collas, P. (2014). The PML-associated protein DEK regulates the balance of H3.3 loading on chromatin and is important for telomere integrity. Genome Res. 24, 1584–1594.

Izquierdo-Bouldstridge, A., Bustillos, A., Bonet-Costa, C., Aribau-Miralbés, P., García-Gomis, D., Dabad, M., Esteve-Codina, A., Pascual-Reguant, L., Peiró, S., Esteller, M., et al. (2017). Histone H1 depletion triggers an interferon response in cancer cells via activation of heterochromatic repeats. Nucleic Acids Res. 45, 11622–11642.

Jasencakova, Z., Scharf, A.N.D., Ask, K., Corpet, A., Imhof, A., Almouzni, G., and Groth, A. (2010). Replication Stress Interferes with Histone Recycling and Predeposition Marking of New Histones. Mol. Cell 37, 736–743.

Jiang, W.Q., Nguyen, A., Cao, Y., Chang, A.C.M., and Reddel, R.R. (2011). HP1-mediated formation of alternative lengthening of telomeres-associated PML bodies requires HIRA but not ASF1a. PLoS One 6.

Kastan, M.B., and Bartek, J. (2004). Cell-cycle checkpoints and cancer. Nature 432, 316–323.

Kelemen, L.E., Wang, X., Fredericksen, Z.S., Pankratz, V.S., Pharoah, P.D.P., Ahmed, S., Dunning, A.M., Easton, D.F., Vierkant, R.A., Cerhan, J.R., et al. (2009). Genetic variation in the chromosome 17q23 amplicon and breast cancer risk. Cancer Epidemiol. Biomarkers Prev. 18, 1864–1868.

Kelly, R., and Davey, S.K. (2013). Tousled-like kinase-dependent phosphorylation of rad9 plays a role in cell cycle progression and G2/M checkpoint exit. PLoS One 8, 1–13.

Kerzendorfer, C., Hannes, F., Colnaghi, R., Abramowicz, I., Carpenter, G., Vermeesch, J.R., and O'Driscoll, M. (2012). Characterizing the functional consequences of haploinsufficiency of NELF-A (WHSC2) and SLBP identifies novel cellular phenotypes in Wolf-Hirschhorn syndrome. Hum. Mol. Genet. 21, 2181–2193.

Khetarpal, P., Das, S., Panigrahi, I., and Munshi, A. (2016). Primordial dwarfism: overview of clinical and genetic aspects. Mol. Genet. Genomics 291.

Kim, H., and D'Andrea, A.D. (2012). Regulation of DNA cross-link repair by the Fanconi anemia/BRCA pathway. Genes Dev. 26, 1393–1408.

Kim, J.-A., Anurag, M., Veeraraghavan, J., Schiff, R., Li, K., and Wang, X.-S. (2016a). Amplification of TLK2 Induces Genomic Instability via Impairing the G2-M Checkpoint. Mol. Cancer Res. 14, 920–927.

Kim, J.A., Tan, Y., Wang, X., Cao, X., Veeraraghavan, J., Liang, Y., Edwards, D.P., Huang, S., Pan, X., Li, K., et al. (2016b). Comprehensive functional analysis of the tousled-like kinase 2 frequently amplified in aggressive luminal breast cancers. Nat. Commun. 7.

Kim, N.W., Piatyszek, M.A., Prowse, K.R., Harley, C.B., West, M.D., Ho, P.L., Coviello, G.M., Wright, W.E., Weinrich, S.L., and Shay, J.W. (1994). Specific association of human telomerase activity with immortal cells and cancer. Science 266, 2011–2015.

Klimovskaia, I.M., Young, C., Strømme, C.B., Menard, P., Jasencakova, Z., Mejlvang, J., Ask, K., Ploug, M., Nielsen, M.L., Jensen, O.N., et al. (2014). Tousled-like kinases phosphorylate Asf1 to promote histone supply during DNA replication. Nat. Commun. 5, 3394.

Kotsantis, P., Silva, L.M., Irmscher, S., Jones, R.M., Folkes, L., Gromak, N., and Petermann, E. (2016). Increased global transcription activity as a mechanism of replication stress in cancer. Nat. Commun. 7.

Krause, D.R., Jonnalagadda, J.C., Gatei, M.H., Sillje, H.H.W., Zhou, B.-B., Nigg, E. a, and Khanna, K. (2003). Suppression of Tousled-like kinase activity after DNA damage or replication block requires ATM, NBS1 and Chk1. Oncogene 22, 5927–5937.

Kurat, C.F., Yeeles, J.T.P., Patel, H., Early, A., and Diffley, J.F.X. (2017). Chromatin Controls DNA Replication Origin Selection, Lagging-Strand Synthesis, and Replication Fork Rates. Mol. Cell 65, 117–130.

Lacoste, N., Woolfe, A., Tachiwana, H., Garea, A., Barth, T., Cantaloube, S., Kurumizaka, H., Imhof, A., and Almouzni, G. (2014). Mislocalization of the Centromeric Histone Variant CenH3/CENP-A in Human Cells Depends on the Chaperone DAXX. Mol. Cell 53, 631–644.

Lallemand-Breitenbach, V., and de Thé, H. (2010). PML nuclear bodies. Cold Spring Harb. Perspect. Biol. 2.

Lam, M.H., Liu, Q., Elledge, S.J., and Rosen, J.M. (2004). Chk1 is haploinsufficient for multiple functions critical to tumor suppression. Cancer Cell 6, 45–59.

Langmead, B., Trapnell, C., Pop, M., and Salzberg, S. (2009). Ultrafast and memory-efficient alignment of short DNA sequences to the human genome. Genome Biol. 10, R25.

Latrick, C.M., Marek, M., Ouararhni, K., Papin, C., Stoll, I., Ignatyeva, M., Obri, A., Ennifar, E., Dimitrov, S., Romier, C., et al. (2016). Molecular basis and specificity of H2A.Z-H2B recognition and deposition by the histone chaperone YL1. Nat. Struct. Mol. Biol. 23, 309–316.

Lazzerini-Denchi, E., and Sfeir, A. (2016). Stop pulling my strings — what telomeres taught us about the DNA damage response. Nat. Rev. Mol. Cell Biol. 17, 364–378.

Le, S., Davis, C., Konopka, J.B., and Sternglanz, R. (1997). Two new S-phase-specific genes from Saccharomyces cerevisiae. Yeast 13, 1029–1042.

Lee, K.Y., Im, J.S., Shibata, E., and Dutta, A. (2017). ASF1a Promotes Non-homologous End Joining Repair by Facilitating Phosphorylation of MDC1 by ATM at Double-Strand Breaks. Mol. Cell 68, 61–75.e5.

Lelieveld, S.H., Reijnders, M.R.F., Pfundt, R., Yntema, H.G., Kamsteeg, E.J., De Vries, P., De Vries, B.B.A., Willemsen, M.H., Kleefstra, T., Löhner, K., et al. (2016). Meta-analysis of 2,104 trios provides support for 10 new genes for intellectual disability. Nat. Neurosci. 19, 1194–1196.

León-Ortiz, A.M., Svendsen, J., and Boulton, S.J. (2014). Metabolism of DNA secondary structures at the eukaryotic replication fork. DNA Repair (Amst). 19, 152–162.

Letessier, A., Millot, G.A., Koundrioukoff, S., Lachagès, A.M., Vogt, N., Hansen, R.S., Malfoy, B., Brison, O., and Debatisse, M. (2011). Cell-type-specific replication initiation programs set fragility of the FRA3B fragile site. Nature 470, 120–124.

Lewis, P.W., Elsaesser, S.J., Noh, K.-M., Stadler, S.C., and Allis, C.D. (2010). Daxx is an H3.3-specific histone chaperone and cooperates with ATRX in replication-independent chromatin assembly at telomeres. Proc. Natl. Acad. Sci. 107, 14075–14080.

Lewis, P.W., Müller, M.M., Koletsky, M.S., Cordero, F., Lin, S., Banaszynski, L.A., Garcia, B.A., Muir, T.W., Becher, O.J., and Allis, C.D. (2013). Inhibition of PRC2 activity by a gain-of-function H3 mutation found in pediatric glioblastoma. Science (80-.). 340, 857–861.

Li, P., Wang, L., Bennett, B.D., Wang, J., Li, J., Qin, Y., Takaku, M., Wade, P.A., Wong, J., and Hu, G. (2017). Rif1 promotes a repressive chromatin state to safeguard against endogenous retrovirus activation. Nucleic Acids Res. 45, 12723–12738.

Li, Y., DeFatta, R., Anthony, C., Sunavala, G., and Benedetti, A. De (2001). A translationally regulated Tousled kinase phosphorylates histone H3 and confers radioresistance when overexpressed. Oncogene 20, 726–738.

Li, Z., Gourguechon, S., and Wang, C.C. (2007). Tousled-like kinase in a microbial eukaryote regulates spindle assembly and S-phase progression by interacting with Aurora kinase and chromatin assembly factors. J. Cell Sci. 120, 3883–3894.

Liang, X., Shan, S., Pan, L., Zhao, J., Ranjan, A., Wang, F., Zhang, Z., Huang, Y., Feng, H., Wei, D., et al. (2016). Structural basis of H2A.Z recognition by SRCAP chromatin-remodeling subunit YL1. Nat. Struct. Mol. Biol. 23, 317–323.

Liberzon, A., Subramanian, A., Pinchback, R., Thorvaldsdóttir, H., Tamayo, P., and Mesirov, J.P. (2011). Molecular signatures database (MSigDB) 3.0. Bioinformatics 27, 1739–1740.

Liberzon, A., Birger, C., Thorvaldsdóttir, H., Ghandi, M., Mesirov, J.P., and Tamayo, P. (2015). The Molecular Signatures Database Hallmark Gene Set Collection. Cell Syst. 1, 417–425.

Lieberman, H.B. (2006). Rad9, an evolutionarily conserved gene with multiple functions for preserving genomic integrity. J. Cell. Biochem. 97, 690–697.

Lindahl, T., and Barnes, D.E. (2000). Repair of endogenous DNA damage. In Cold Spring Harbor Symposia on Quantitative Biology, pp. 127–133.

Liu, W.H., Roemer, S.C., Port, A.M., and Churchill, M.E.A. (2012). CAF-1-induced oligomerization of histones H3/H4 and mutually exclusive interactions with Asf1 guide H3/H4 transitions among histone chaperones and DNA. Nucleic Acids Res. 40, 11229–11239.

Lo, K.W.H., Kan, H.M., Chan, L.N., Xu, W.G., Wang, K.P., Wu, Z., Sheng, M., and Zhang, M. (2005). The 8-kDa dynein light chain binds to p53-binding protein 1 and mediates DNA damage-induced p53 nuclear accumulation. J. Biol. Chem. 280, 8172–8179.

Lopez, M.S., Choy, J.W., Peters, U., Sos, M.L., Morgan, D.O., and Shokat, K.M. (2013). Staurosporine-Derived Inhibitors Broaden the Scope of Analog-Sensitive Kinase Technology. J. Am. Chem. Soc. 135, 18153–18159.

Lopez, M.S., Kliegman, J.I., and Shokat, K.M. (2014). The logic and design of analog-sensitive kinases and their small molecule inhibitors (Elsevier Inc.).

Love, M.I., Huber, W., Anders, S., Lönnstedt, I., Speed, T., Robinson, M., Smyth, G., McCarthy, D., Chen, Y., Smyth, G., et al. (2014). Moderated estimation of fold change and dispersion for RNA-seq data with DESeq2. Genome Biol. 15, 550.

Lovejoy, C.A., Li, W., Reisenweber, S., Thongthip, S., Bruno, J., de Lange, T., De, S., Petrini, J.H.J., Sung, P.A., Jasin, M., et al. (2012). Loss of ATRX, genome instability, and an altered DNA damage response are hallmarks of the alternative lengthening of Telomeres pathway. PLoS Genet. 8, 12–15.

Luijsterburg, M.S., de Krijger, I., Wiegant, W.W., Shah, R.G., Smeenk, G., de Groot, A.J.L., Pines, A., Vertegaal, A.C.O., Jacobs, J.J.L., Shah, G.M., et al. (2016). PARP1 Links CHD2-Mediated Chromatin Expansion and H3.3 Deposition to DNA Repair by Non-homologous End-Joining. Mol. Cell 61, 547–562.

Macheret, M., and Halazonetis, T.D. (2018). Intragenic origins due to short G1 phases underlie oncogene-induced DNA replication stress. Nature.

MacKenzie, K.J., Carroll, P., Martin, C.A., Murina, O., Fluteau, A., Simpson, D.J., Olova, N., Sutcliffe, H., Rainger, J.K., Leitch, A., et al. (2017). CGAS surveillance of micronuclei links genome instability to innate immunity. Nature 548, 461–465.

Malumbres, M. (2014). Cyclin-dependent kinases. Genome Biol. 15.

Marcotte, R., Sayad, A., Brown, K.R., Sanchez-Garcia, F., Reimand, J., Haider, M., Virtanen, C., Bradner, J.E., Bader, G.D., Mills, G.B., et al. (2016). Functional Genomic Landscape of Human Breast Cancer Drivers, Vulnerabilities, and Resistance. Cell 164, 293–309.

Marzec, P., Armenise, C., Pérot, G., Roumelioti, F.M., Basyuk, E., Gagos, S., Chibon, F., and Déjardin, J. (2015). Nuclear-Receptor-Mediated Telomere Insertion Leads to Genome Instability in ALT Cancers. Cell 160, 913–927.

Mejlvang, J., Feng, Y., Alabert, C., Neelsen, K.J., Jasencakova, Z., Zhao, X., Lees, M., Sandelin, A., Pasero, P., Lopes, M., et al. (2014). New histone supply regulates replication fork speed and PCNA unloading. J. Cell Biol. 204, 29–43.

Mellacheruvu, D., Wright, Z., Couzens, A.L., Lambert, J.P., St-Denis, N.A., Li, T., Miteva, Y. V., Hauri, S., Sardiu, M.E., Low, T.Y., et al. (2013). The CRAPome: A contaminant repository for affinity purification-mass spectrometry data. Nat. Methods 10, 730–736.

Mello, J.A., Silljé, H.H.W., Roche, D.M.J., Kirschner, D.B., Nigg, E.A., and Almouzni, G. (2002). Human Asf1 and CAF-1 interact and synergize in a repair-coupled nucleosome assembly pathway. EMBO Rep. 3, 329–334.

Mertins, P., Mani, D.R., Ruggles, K. V., Gillette, M.A., Clauser, K.R., Wang, P., Wang, X., Qiao, J.W., Cao, S., Petralia, F., et al. (2016). Proteogenomics connects somatic mutations to signalling in breast cancer. Nature 534, 55–62.

Messiaen, S., Guiard, J., Aigueperse, C., Fliniaux, I., Tourpin, S., Barroca, V., Allemand, I., Fouchet, P., Livera, G., and Vernet, M. (2016). Loss of the histone chaperone ASF1B reduces female reproductive capacity in mice. Reproduction 151, 477–489.

Meyer, M.J., Fleming, J.M., Lin, A.F., Hussnain, S.A., Ginsburg, E., and Vonderhaar, B.K. (2010). CD44posCD49fhiCD133/2hi defines xenograft-initiating cells in estrogen receptor-negative breast cancer. Cancer Res. 70, 4624–4633.

Min, W., Bruhn, C., Grigaravicius, P., Zhou, Z.W., Li, F., Krüger, A., Siddeek, B., Greulich, K.O., Popp, O., Meisezahl, C., et al. (2013). Poly(ADP-ribose) binding to Chk1 at stalled replication forks is required for S-phase checkpoint activation. Nat. Commun. 4.

Mirkin, E. V., and Mirkin, S.M. (2007). Replication Fork Stalling at Natural Impediments. Microbiol. Mol. Biol. Rev. 71, 13–35.

Moshkin, Y.M., Armstrong, J.A., Maeda, R.K., Tamkun, J.W., Verrijzer, P., Kennison, J.A., and Karch, F. (2002). Histone chaperone ASF1 cooperates with the brahma chromatin-remodelling machinery. Genes Dev. 16, 2621–2626.

Munakata, T., Adachi, N., Yokoyama, N., Kuzuhara, T., and Horikoshi, M. (2000). A human homologue of yeast anti-silencing factor has histone chaperone activity. Genes to Cells 5, 221–233.

Murga, M., Bunting, S., Montãa, M.F., Soria, R., Mulero, F., Cãamero, M., Lee, Y., McKinnon, P.J., Nussenzweig, A., and Fernandez-Capetillo, O. (2009). A mouse model of ATR-Seckel shows embryonic replicative stress and accelerated aging. Nat. Genet. 41, 891–898.

Murga, M., Campaner, S., Lopez-Contreras, A.J., Toledo, L.I., Soria, R., Montaña, M.F., D'Artista, L., Schleker, T., Guerra, C., Garcia, E., et al. (2011). Exploiting oncogene-induced replicative stress for the selective killing of Myc-driven tumors. Nat. Struct. Mol. Biol. 18, 1331–1335.

Neelsen, K.J., and Lopes, M. (2015). Replication fork reversal in eukaryotes: From dead end to dynamic response. Nat. Rev. Mol. Cell Biol. 16, 207–220.

O'Driscoll, M., Ruiz-Perez, V.L., Woods, C.G., Jeggo, P.A., and Goodship, J.A. (2003). A splicing mutation affecting expression of ataxia-telangiectasia and Rad3-related protein (ATR) results in Seckel syndrome. Nat. Genet. 33, 497–501.

O'Sullivan, R.J., and Almouzni, G. (2014). Assembly of telomeric chromatin to create ALTernative endings. Trends Cell Biol. 24, 675–685.

O'Sullivan, R.J., Arnoult, N., Lackner, D.H., Oganesian, L., Haggblom, C., Corpet, A., Almouzni, G., and Karlseder, J. (2014). Rapid induction of alternative lengthening of telomeres by depletion of the histone chaperone ASF1. Nat. Struct. Mol. Biol. 21, 167–174.

Obri, A., Ouararhni, K., Papin, C., Diebold, M.L., Padmanabhan, K., Marek, M., Stoll, I., Roy, L., Reilly, P.T., Mak, T.W., et al. (2014). ANP32E is a histone chaperone that removes H2A.Z from chromatin. Nature 505, 648–653.

Ohzeki, J.I., Bergmann, J.H., Kouprina, N., Noskov, V.N., Nakano, M., Kimura, H., Earnshaw, W.C., Larionov, V., and Masumoto, H. (2012). Breaking the HAC Barrier: Histone H3K9 acetyl/methyl balance regulates CENP-A assembly. EMBO J. 31, 2391–2402.

Pchelintsev, N.A., McBryan, T., Rai, T.S., VanTuyn, J., Ray-Gallet, D., Almouzni, G., and Adams, P.D. (2013). Placing the HIRA Histone Chaperone Complex in the Chromatin Landscape. Cell Rep. 3, 1012–1019.

Pereira, R.D., De Long, N.E., Wang, R.C., Yazdi, F.T., Holloway, A.C., and Raha, S. (2015). Angiogenesis in the placenta: The role of reactive oxygen species signaling. Biomed Res. Int. 2015.

Perez-Garcia, V., Fineberg, E., Wilson, R., Murray, A., Mazzeo, C.I., Tudor, C., Sienerth, A., White, J.K., Tuck, E., Ryder, E.J., et al. (2018). Placentation defects are highly prevalent in embryonic lethal mouse mutants. Nature.

Pierce, A.J., Johnson, R.D., Thompson, L.H., and Jasin, M. (1999). XRCC3 promotes homology-directed repair of DNA damage in mammalian cells. Genes Dev. 13, 2633–2638.

Pilyugin, M., Demmers, J., Peter Verrijzer, C., Karch, F., and Moshkin, Y.M. (2009). Phosphorylation-mediated control of histone chaperone ASF1 levels by tousled-like kinases. PLoS One 4, 1–6.

Poli, J., Tsaponina, O., Crabbé, L., Keszthelyi, A., Pantesco, V., Chabes, A., Lengronne, A., and Pasero, P. (2012). dNTP pools determine fork progression and origin usage under replication stress. EMBO J. 31, 883–894.

Pradhan, S.K., Su, T., Yen, L., Jacquet, K., Huang, C., Côté, J., Kurdistani, S.K., and Carey, M.F. (2016). EP400 Deposits H3.3 into Promoters and Enhancers during Gene Activation. Mol. Cell 61, 27–38.

Prado, F., Cortes-Ledesma, F., and Aguilera, A. (2004). The absence of the yeast chromatin assembly factor Asf1 increases genomic instability and sister chromatid exchange. EMBO Rep. 5, 497–502.

Qvist, P., Huertas, P., Jimeno, S., Nyegaard, M., Hassan, M.J., Jackson, S.P., and Børglum, A.D. (2011). CtIP mutations cause Seckel and Jawad syndromes. PLoS Genet. 7.

R Development Core Team (2016). R: A Language and Environment for Statistical Computing. R Found. Stat. Comput. Vienna Austria 0, {ISBN} 3-900051-07-0.

Rai, T.S., Cole, J.J., Nelson, D.M., Dikovskaya, D., Faller, W.J., Vizioli, M.G., Hewitt, R.N., Anannya, O., McBryan, T., Manoharan, I., et al. (2014). HIRA orchestrates a dynamic chromatin landscape in senescence and is required for suppression of Neoplasia. Genes Dev. 28, 2712–2725.

Ramey, C.J., Howar, S., Adkins, M., Linger, J., Spicer, J., and Tyler, J.K. (2004). Activation of the DNA Damage Checkpoint in Yeast Lacking the Histone Chaperone Anti-Silencing Function 1 Activation of the DNA Damage Checkpoint in Yeast Lacking the Histone Chaperone Anti-Silencing Function 1. Mol. Cell. Biol. 24, 10313–10327.

Rapali, P., Szenes, Á., Radnai, L., Bakos, A., Pál, G., and Nyitray, L. (2011a). DYNLL/LC8: A light chain subunit of the dynein motor complex and beyond. FEBS J. 278, 2980–2996.

Rapali, P., Radnai, L., Süveges, D., Harmat, V., Tölgyesi, F., Wahlgren, W.Y., Katona, G., Nyitray, L., and Pál, G. (2011b). Directed evolution reveals the binding motif preference of the LC8/DYNLL hub protein and predicts large numbers of novel binders in the human proteome. PLoS One 6.

Rappsilber, J., Mann, M., and Ishihama, Y. (2007). Protocol for micro-purification, enrichment, pre-fractionation and storage of peptides for proteomics using StageTips. Nat. Protoc. 2, 1896–1906.

Rattray, A.M.J., and Müller, B. (2012). The control of histone gene expression. Biochem. Soc. Trans. 40, 880–885.

Ray-Gallet, D., Woolfe, A., Vassias, I., Pellentz, C., Lacoste, N., Puri, A., Schultz, D.C., Pchelintsev, N.A., Adams, P.D., Jansen, L.E.T., et al. (2011). Dynamics of Histone H3 Deposition In Vivo Reveal a Nucleosome Gap-Filling Mechanism for H3.3 to Maintain Chromatin Integrity. Mol. Cell 44, 928–941.

Ray Chaudhuri, A., Hashimoto, Y., Herrador, R., Neelsen, K.J., Fachinetti, D., Bermejo, R., Cocito, A., Costanzo, V., and Lopes, M. (2012). Topoisomerase i poisoning results in PARP-mediated replication fork reversal. Nat. Struct. Mol. Biol. 19, 417–423.

Reaper, P.M., Griffiths, M.R., Long, J.M., Charrier, J.D., MacCormick, S., Charlton, P.A., Golec, J.M.C., and Pollard, J.R. (2011). Selective killing of ATM- or p53-deficient cancer cells through inhibition of ATR. Nat. Chem. Biol. 7, 428–430.

Regue, L., Sdelci, S., Bertran, M.T., Caelles, C., Reverter, D., and Roig, J. (2011). DYNLL/LC8 protein controls signal transduction through the Nek9/Nek6 signaling module by regulating Nek6 binding to Nek9. J. Biol. Chem. 286, 18118–18129.

Rein, K., Yanez, D.A., Terré, B., Palenzuela, L., Aivio, S., Wei, K., Edelmann, W., Stark, J.M., and Stracker, T.H. (2015). EXO1 is critical for embryogenesis and the DNA damage response in mice with a hypomorphic Nbs1 allele. Nucleic Acids Res. 43, 7371–7387.

Rhind, N., and Gilbert, D.M. (2013). DNA replication timing. Cold Spring Harb. Perspect. Biol. 5.

Rice, G.I., Bond, J., Asipu, A., Brunette, R.L., Manfield, I.W., Carr, I.M., Fuller, J.C., Jackson, R.M., Lamb, T., Briggs, T.A., et al. (2009). Mutations involved in Aicardi-Goutières syndrome implicate SAMHD1 as regulator of the innate immune response. Nat. Genet. 41, 829–832.

Richet, N., Liu, D., Legrand, P., Velours, C., Corpet, A., Gaubert, A., Bakail, M., Moal-Raisin, G., Guerois, R., Compper, C., et al. (2015). Structural insight into how the human helicase subunit MCM2 may act as a histone chaperone together with ASF1 at the replication fork. Nucleic Acids Res. 43, 1905–1917.

Roe, J.L., Rivin, C.J., Sessions, R.A., Feldmann, K.A., and Zambryski, P.C. (1993). The Tousled gene in A. thaliana encodes a protein kinase homolog that is required for leaf and flower development. Cell 75, 939–950.

Roe, J.L., Durfee, T., Zupan, J.R., Repetti, P.P., McLean, B.G., and Zambryski, P.C. (1997). TOUSLED is a nuclear serine/threonine protein kinase that requires a coiled-coil region for oligomerization and catalytic activity. J. Biol. Chem. 272, 5838–5845.

Ronald, S., Awate, S., Rath, A., Carroll, J., Galiano, F., Dwyer, D., Kleiner-Hancock, H., Mathis, J.M., Vigod, S., and De Benedetti, A. (2013). Phenothiazine Inhibitors of TLKs Affect Double-Strand Break Repair and DNA Damage Response Recovery and Potentiate Tumor Killing with Radiomimetic Therapy. Genes and Cancer 4, 39–53.

Rosado, I. V., Langevin, F., Crossan, G.P., Takata, M., and Patel, K.J. (2011). Formaldehyde catabolism is essential in cells deficient for the Fanconi anemia DNA-repair pathway. Nat. Struct. Mol. Biol. 18, 1432–1434.

Rossant, J., and Cross, J.C. (2001). Placental Development: Lessons From Mouse Mutants. Nat. Rev. Genet. 2, 538–548.

Saldivar, J.C., Cortez, D., and Cimprich, K.A. (2017). The essential kinase ATR: Ensuring faithful duplication of a challenging genome. Nat. Rev. Mol. Cell Biol. 18, 622–636.

Sanematsu, F., Takami, Y., Barman, H.K., Fukagawa, T., Ono, T., Shibahara, K.I., and Nakayama, T. (2006). Asf1 is required for viability and chromatin assembly during DNA replication in vertebrate cells. J. Biol. Chem. 281, 13817–13827.

Saredi, G., Huang, H., Hammond, C.M., Alabert, C., Bekker-Jensen, S., Forne, I., Reverón-Gómez, N., Foster, B.M., Mlejnkova, L., Bartke, T., et al. (2016). H4K20me0 marks post-replicative chromatin and recruits the TONSL–MMS22L DNA repair complex. Nature 534, 714–718.

Schoppy, D.W., Ragland, R.L., Gilad, O., Shastri, N., Peters, A.A., Murga, M., Fernandez-Capetillo, O., Diehl, J.A., and Brown, E.J. (2012). Oncogenic stress sensitizes murine cancers to hypomorphic suppression of ATR. J. Clin. Invest. 122, 241–252.

Schulz, L.L., and Tyler, J.K. (2006). The histone chaperone ASF1 localizes to active DNA replication forks to mediate efficient DNA replication. FASEB J. 20, 488–490.

Schumacher, M.A., Min, J.K., Link, T.M., Guan, Z., Xu, W., Ahn, Y.H., Soderblom, E.J., Kurie, J.M., Evdokimov, A., Moseley, M.A., et al. (2012). Role of Unusual P Loop Ejection and Autophosphorylation in HipA-Mediated Persistence and Multidrug Tolerance. Cell Rep. 2, 518–525.

Schwartzentruber, J., Korshunov, A., Liu, X.Y., Jones, D.T.W., Pfaff, E., Jacob, K., Sturm, D., Fontebasso, A.M., Quang, D.A.K., Tönjes, M., et al. (2012). Driver mutations in histone H3.3 and chromatin remodelling genes in paediatric glioblastoma. Nature 482, 226–231.

Segura-Bayona, S., Knobel, P.A., Gonzalez-Buron, H., Youssef, S.A., Peña-Blanco, A., Coyaud, E., Lopez-Rovira, T., Rein, K., Palenzuela, L., Colombelli, J., et al. (2017). Differential requirements for Tousled-like kinases 1 and 2 in mammalian development. Cell Death Differ. 24.

Sen, S.P., and De Benedetti, A. (2006). TLK1B promotes repair of UV-damaged DNA through chromatin remodeling by Asf1. BMC Mol. Biol. 7.

Shalom, S., and Don, J. (1999). Tlk, a novel evolutionarily conserved murine serine threonine kinase, encodes multiple testis transcripts. Mol. Reprod. Dev. 52, 392–405.

Shaltiel, I.A., Krenning, L., Bruinsma, W., and Medema, R.H. (2015). The same, only different - DNA damage checkpoints and their reversal throughout the cell cycle. J. Cell Sci. 128, 607–620.

Sharp, J.A., Fouts, E.T., Krawitz, D.C., and Kaufman, P.D. (2001). Yeast histone deposition protein Asf1p requires Hir proteins and PCNA for heterochromatic silencing. Curr. Biol. 11, 463–473.

Shay, J.W., and Wright, W.E. (2000). Hayflick, His Limit, and Cellular Ageing. Nat. Rev. Mol. Cell Biol. 1, 72–76.

Shen, J., Peng, Y., Wei, L., Zhang, W., Yang, L., Lan, L., Kapoor, P., Ju, Z., Mo, Q., Shih, I.M., et al. (2015). ARID1A Deficiency Impairs the DNA Damage Checkpoint and Sensitizes Cells to PARP Inhibitors. Cancer Discov. 5, 752–767.

Shi, T., Bunker, R.D., Mattarocci, S., Ribeyre, C., Faty, M., Gut, H., Scrima, A., Rass, U., Rubin, S.M., Shore, D., et al. (2013). Rif1 and Rif2 shape telomere function and architecture through multivalent Rap1 interactions. Cell 153.

Shibahara, K.I., and Stillman, B. (1999). Replication-dependent marking of DNA by PCNA facilitates CAF-1-coupled inheritance of chromatin. Cell 96, 575–585.

Siddiqui, K., On, K.F., and Diffley, J.F.X. (2013). Regulating DNA replication in Eukarya. Cold Spring Harb. Perspect. Biol. 5.

Silljé, H.H.W., and Nigg, E.A. (2001). Identification of human Asf1 chromatin assembly factors as substrates of Tousled-like kinases. Curr. Biol. 11, 1068–1073.

Silljé, H.H.W., Takahashi, K., Tanaka, K., Van Houwe, G., and Nigg, E.A. (1999). Mammalian homologues of the plant Tousled gene code for cell-cycle-regulated kinases with maximal activities linked to ongoing DNA replication. EMBO J. 18, 5691–5702.

Silva, J.C., Gorenstein, M. V., Li, G.-Z., Vissers, J.P.C., and Geromanos, S.J. (2006). Absolute Quantification of Proteins by LCMS E. Mol. Cell. Proteomics 5, 144–156.

Simmons, D.G., and Cross, J.C. (2005). Determinants of trophoblast lineage and cell subtype specification in the mouse placenta. Dev. Biol. 284, 12–24.

Simmons, D.G., Fortier, A.L., and Cross, J.C. (2007). Diverse subtypes and developmental origins of trophoblast giant cells in the mouse placenta. Dev. Biol. 304, 567–578.

Sims, J.K., and Wade, P.A. (2011). Mi-2/NuRD complex function is required for normal S phase progression and assembly of pericentric heterochromatin. Mol. Biol. Cell 22, 3094–3102.

Singh, V., Connelly, Z.M., Shen, X., and De Benedetti, A. (2017). Identification of the proteome complement of humanTLK1 reveals it binds and phosphorylates NEK1 regulating its activity. Cell Cycle 16, 915–926.

Sir, J.H., Barr, A.R., Nicholas, A.K., Carvalho, O.P., Khurshid, M., Sossick, A., Reichelt, S., D'Santos, C., Woods, C.G., and Gergely, F. (2011). A primary microcephaly protein complex forms a ring around parental centrioles. Nat. Genet. 43, 1147–1153.

Sørensen, C.S., and Syljuåsen, R.G. (2012). Safeguarding genome integrity: The checkpoint kinases ATR, CHK1 and WEE1 restrain CDK activity during normal DNA replication. Nucleic Acids Res. 40, 477–486.

Spruijt, C.G., Luijsterburg, M.S., Menafra, R., Lindeboom, R.G.H., Jansen, P.W.T.C., Edupuganti, R.R., Baltissen, M.P., Wiegant, W.W., Voelker-Albert, M.C., Matarese, F., et al. (2016). ZMYND8 Co-localizes with NuRD on Target Genes and Regulates Poly(ADP-Ribose)-Dependent Recruitment of GATAD2A/NuRD to Sites of DNA Damage. Cell Rep. 17, 783–798.

Stetson, D.B., Ko, J.S., Heidmann, T., and Medzhitov, R. (2008). Trex1 Prevents Cell-Intrinsic Initiation of Autoimmunity. Cell 134, 587–598.

Stevens, K.N., Wang, X., Fredericksen, Z., Pankratz, V.S., Cerhan, J., Vachon, C.M., Olson, J.E., and Couch, F.J. (2011). Evaluation of associations between common variation in mitotic regulatory pathways and risk of overall and high grade breast cancer. Breast Cancer Res. Treat. 129, 617–622.

Stracker, T.H., and Petrini, J.H.J. (2011). The MRE11 complex: Starting from the ends. Nat. Rev. Mol. Cell Biol. 12, 90–103.

Subramanian, A., Tamayo, P., Mootha, V.K., Mukherjee, S., Ebert, B.L., Gillette, M.A., Paulovich, A., Pomeroy, S.L., Golub, T.R., Lander, E.S., et al. (2005). Gene set enrichment analysis: a knowledge-based approach for interpreting genome-wide expression profiles. Proc Natl Acad Sci U S A 102, 15545–15550.

Suhasini, A.N., and Brosh, R.M. (2013). Disease-causing missense mutations in human DNA helicase disorders. Mutat. Res. 752, 138–152.

Sukackaite, R., Cornacchia, D., Jensen, M.R., Mas, P.J., Blackledge, M., Enervald, E., Duan, G., Auchynnikava, T., Köhn, M., Hart, D.J., et al. (2017). Mouse Rif1 is a regulatory subunit of protein phosphatase 1 (PP1). Sci. Rep. 7.

Sunavala-Dossabhoy, G., and De Benedetti, A. (2009). Tousled homolog, TLK1, binds and phosphorylates Rad9; TLK1 acts as a molecular chaperone in DNA repair. DNA Repair (Amst). 8, 87–102.

Sunavala-Dossabhoy, G., Li, Y., Williams, B., and De Benedetti, A. (2003). A dominant negative mutant of TLK1 causes chromosome missegregation and aneuploidy in normal breast epithelial cells. BMC Cell Biol. 4, 1–12.

Sunavala-Dossabhoy, G., Balakrishnan, S.K., Sen, S., Nuthalapaty, S., and De Benedetti, A. (2005). The radioresistance kinase TLK1B protects the cells by promoting repair of double strand breaks. BMC Mol. Biol. 6.

Tagami, H., Ray-Gallet, D., Almouzni, G., and Nakatani, Y. (2004). Histone H3.1 and H3.3 Complexes Mediate Nucleosome Assembly Pathways Dependent or Independent of DNA Synthesis. Cell 116, 51–61.

Talbert, P.B., and Henikoff, S. (2017). Histone variants on the move: Substrates for chromatin dynamics. Nat. Rev. Mol. Cell Biol. 18, 115–126.

Tan, B.C.M., Chien, C.T., Hirose, S., and Lee, S.C. (2006). Functional cooperation between FACT and MCM helicase facilitates initiation of chromatin DNA replication. EMBO J. 25, 3975–3985.

Tang, Y., Poustovoitov, M. V., Zhao, K., Garfinkel, M., Canutescu, A., Dunbrack, R., Adams, P.D., and Marmorstein, R. (2006). Structure of a human ASF1a-HIRA complex and insights into specificity of histone chaperone complex assembly. Nat. Struct. Mol. Biol. 13, 921–929.

Técher, H., Koundrioukoff, S., Carignon, S., Wilhelm, T., Millot, G.A., Lopez, B.S., Brison, O., and Debatisse, M. (2016). Signaling from Mus81-Eme2-Dependent DNA Damage Elicited by Chk1 Deficiency Modulates Replication Fork Speed and Origin Usage. Cell Rep. 14, 1114–1127.

Técher, H., Koundrioukoff, S., Nicolas, A., and Debatisse, M. (2017). The impact of replication stress on replication dynamics and DNA damage in vertebrate cells. Nat. Rev. Genet. 18, 535–550.

Toledo, L.I., Murga, M., Zur, R., Soria, R., Rodriguez, A., Martinez, S., Oyarzabal, J., Pastor, J., Bischoff, J.R., and Fernandez-Capetillo, O. (2011). A cell-based screen identifies ATR inhibitors with synthetic lethal properties for cancer-associated mutations. Nat. Struct. Mol. Biol. 18, 721–727.

Toledo, L.I., Altmeyer, M., Rask, M.B., Lukas, C., Larsen, D.H., Povlsen, L.K., Bekker-Jensen, S., Mailand, N., Bartek, J., and Lukas, J. (2014). ATR prohibits replication catastrophe by preventing global exhaustion of RPA. Cell 156, 374.

Tripathi, A.K., Singh, K., Pareek, A., and Singla-Pareek, S.L. (2015). Histone chaperones in Arabidopsis and rice: genome-wide identification, phylogeny, architecture and transcriptional regulation. BMC Plant Biol. 15, 42.

Tubbs, A., and Nussenzweig, A. (2017). Endogenous DNA Damage as a Source of Genomic Instability in Cancer. Cell 168, 644–656.

Tyler, J.K., Adams, C.R., Chen, S.R., Kobayashi, R., Kamakaka, R.T., and Kadonaga, J.T. (1999). The RCAF complex mediates chromatin assembly during DNA replication and repair. Nature 402, 555–560.

Tyler, J.K., Collins, K.A., Prasad-Sinha, J., Amiott, E., Bulger, M., Harte, P.J., Kobayashi, R., and Kadonaga, J.T. (2001). Interaction between the Drosophila CAF-1 and ASF1 Chromatin Assembly Factors. Mol. Cell. Biol. 21, 6574–6584.

Udugama, M., Chang, F.T.M., Chan, F.L., Tang, M.C., Pickett, H.A., McGhie, J.D.R., Mayne, L., Collas, P., Mann, J.R., and Wong, L.H. (2015). Histone variant H3.3 provides the heterochromatic H3 lysine 9 tri-methylation mark at telomeres. Nucleic Acids Res. 43, 10227–10237.

Umehara, T., and Horikoshi, M. (2003). Transcription initiation factor IID-interactive histone chaperone CIA-II implicated in mammalian spermatogenesis. J. Biol. Chem. 278, 35660–35667.

Umehara, T., Chimura, T., Ichikawa, N., and Horikoshi, M. (2002). Polyanionic stretch-deleted histone chaperone cia1/Asf1p is functional both in vivo and in vitro. Genes to Cells 7, 59–73.

Di Virgilio, M., Callen, E., Yamane, A., Zhang, W., Jankovic, M., Gitlin, A.D., Feldhahn, N., Resch, W., Oliveira, T.Y., Chait, B.T., et al. (2013). Rif1 prevents resection of DNA breaks and promotes immunoglobulin class switching. Science (80-.). 339, 711–715.

Wang, Y., Liu, J., Xia, R., Wang, J., Shen, J., Cao, R., Hong, X., Zhu, J.K., and Gong, Z. (2007). The protein kinase TOUSLED is required for maintenance of transcriptional gene silencing in Arabidopsis. EMBO Rep. 8, 77–83.

Welburn, J.P.I., Tucker, J.A., Johnson, T., Lindert, L., Morgan, M., Willis, A., Noble, M.E.M., and Endicott, J.A. (2007). How tyrosine 15 phosphorylation inhibits the activity of cyclin-dependent kinase 2-cyclin A. J. Biol. Chem. 282, 3173–3181.

Winkler, D.D., Muthurajan, U.M., Hieb, A.R., and Luger, K. (2011). Histone chaperone FACT coordinates nucleosome interaction through multiple synergistic binding events. J. Biol. Chem. 286, 41883–41892.

Wong, L.H., Ren, H., Williams, E., McGhie, J., Ann, S., Sim, M., Tam, A., Earle, E., Anderson, M.A., Mann, J., et al. (2009). Histone H3.3 incorporation provides a unique and functionally essential telomeric chromatin in embryonic stem cells. Genome Res. 19, 404–414.

Wong, L.H., Mcghie, J.D., Sim, M., Anderson, M.A., Ahn, S., Hannan, R.D., George, A.J., Morgan, K.A., Mann, J.R., and Choo, K.H.A. (2010). integrity in pluripotent embryonic stem cells ATRX interacts with H3 . 3 in maintaining telomere structural integrity in pluripotent embryonic stem cells. 351–360.

Wu, G., Broniscer, A., McEachron, T.A., Lu, C., Paugh, B.S., Becksfort, J., Qu, C., Ding, L., Huether, R., Parker, M., et al. (2012). Somatic histone H3 alterations in pediatric diffuse intrinsic pontine gliomas and non-brainstem glioblastomas. Nat. Genet. 44, 251–253.

Wu, Y., Wang, C., Sun, H., LeRoith, D., and Yakar, S. (2009). High-Efficient FLPo Deleter Mice in C57BL/6J Background. PLoS One 4.

Yamakawa, a, Kameoka, Y., Hashimoto, K., Yoshitake, Y., Nishikawa, K., Tanihara, K., and Date, T. (1997). cDNA cloning and chromosomal mapping of genes encoding novel protein kinases termed PKU-alpha and PKU-beta, which have nuclear localization signal. Gene 202, 193–201.

Yamane, K., Mizuguchi, T., Cui, B., Zofall, M., Noma, K.I., and Grewal, S.I.S. (2011). Asf1/HIRA facilitate global histone deacetylation and associate with HP1 to promote nucleosome occupancy at heterochromatic loci. Mol. Cell 41, 56–66.

Yamazaki, S., Ishii, A., Kanoh, Y., Oda, M., Nishito, Y., and Masai, H. (2012). Rif1 regulates the replication timing domains on the human genome. EMBO J. 31, 3667–3677.

Ye, X., Franco, A.A., Santos, H., Nelson, D.M., Kaufman, P.D., and Adams, P.D. (2003). Defective S phase chromatin assembly causes DNA damage, activation of the S phase checkpoint, and S phase arrest. Mol. Cell 11, 341–351.

Yeeles, J.T.P., Deegan, T.D., Janska, A., Early, A., and Diffley, J.F.X. (2015). Regulated eukaryotic DNA replication origin firing with purified proteins. Nature 519, 431–435.

Zabaronick, S.R., and Tyler, J.K. (2005). The Histone Chaperone Anti-Silencing Function 1 Is a Global Regulator of Transcription Independent of Passage through S Phase The Histone Chaperone Anti-Silencing Function 1 Is a Global Regulator of Transcription Independent of Passage through S Phase †. Mol. Cell. Biol. 25, 652–660.

Zeman, M.K., and Cimprich, K.A. (2014). Causes and consequences of replication stress. Nat. Cell Biol. 16, 2–9.

Zhang, C., Kenski, D.M., Paulson, J.L., Bonshtien, A., Sessa, G., Cross, J. V., Templeton, D.J., and Shokat, K.M. (2005a). A second-site suppressor strategy for chemical genetic analysis of diverse protein kinases. Nat. Methods 2, 435–441.

Zhang, H., Gan, H., Wang, Z., Lee, J.H., Zhou, H., Ordog, T., Wold, M.S., Ljungman, M., and Zhang, Z. (2017). RPA Interacts with HIRA and Regulates H3.3 Deposition at Gene Regulatory Elements in Mammalian Cells. Mol. Cell 65, 272–284.

Zhang, R., Poustovoitov, M. V., Ye, X., Santos, H.A., Chen, W., Daganzo, S.M., Erzberger, J.P., Serebriiskii, I.G., Canutescu, A.A., Dunbrack, R.L., et al. (2005b). Formation of macroH2A-containing senescence-associated heterochromatin foci and senescence driven by ASF1a and HIRA. Dev. Cell 8, 19–30.

Zhang, S., Xing, H., and Muslin, A.J. (1999). Nuclear localization of protein kinase U-alpha is regulated by 14-3-3. J. Biol. Chem. 274, 24865–72.

Zhang, Y., Liu, T., Meyer, C.A., Eeckhoute, J., Johnson, D.S., Bernstein, B.E., Nussbaum, C., Myers, R.M., Brown, M., Li, W., et al. (2008). Model-based analysis of ChIP-Seq (MACS). Genome Biol. 9.

Zhu, L.J. (2013). Integrative analysis of ChIP-chip and ChIP-seq dataset. Methods Mol. Biol. 1067, 105–124.

Zhu, Q., Pao, G.M., Huynh, A.M., Suh, H., Tonnu, N., Nederlof, P.M., Gage, F.H., and Verma, I.M. (2011). BRCA1 tumour suppression occurs via heterochromatin-mediated silencing. Nature 477, 179–184.

Zou, L., and Elledge, S.J. (2003). Sensing DNA damage through ATRIP recognition of RPA-ssDNA complexes. Science (80-.). 300, 1542–1548.

Van Zundert, G.C.P., Rodrigues, J.P.G.L.M., Trellet, M., Schmitz, C., Kastritis, P.L., Karaca, E., Melquiond, A.S.J., Van Dijk, M., De Vries, S.J., and Bonvin, A.M.J.J. (2016). The HADDOCK2.2 Web Server: User-Friendly Integrative Modeling of Biomolecular Complexes. J. Mol. Biol. 428, 720–725.